Scholars' Mine

Doctoral Dissertations   Student Theses and Dissertations

Fall 2011

Hilbert Transform applications in signal analysis and non-parametric identification of linear and nonlinear systems

Zuocai Wang

Recommended Citation

HILBERT TRANSFORM APPLICATIONS IN SIGNAL ANALYSIS AND NON-

PARAMETRIC IDENTIFICATION OF LINEAR AND NONLINEAR SYSTEMS

by

ZUOCAI WANG

A DISSERTATION

Presented to the Faculty of the Graduate School of the

MISSOURI UNIVERSITY OF SCIENCE AND TECHNOLOGY

In Partial Fulfillment of the Requirements for the Degree

DOCTOR OF PHILOSOPHY

in

CIVIL ENGINEERING

2011

Approved
Genda Chen, Advisor
William Schonberg
Roger A. LaBoube
Ian Prowell
Xiaoping Du

ABSTRACT

Hilbert Huang Transform faces several challenges in dealing with closely-spaced frequency components, short-time and weak disturbances, and interrelationships between two time-varying modes of nonlinear vibration due to its mixed mode problem associated with empirical mode decomposition (EMD). To address these challenges, analytical mode decomposition (AMD) based on Hilbert Transform is proposed and developed for an adaptive data analysis of both stationary and non-stationary responses. With a suite of predetermined bisecting frequencies, AMD can analytically extract the individual components of a structural response between any two bisecting frequencies and function like an adaptive bandpass filter that can deal with frequency-modulated responses with significant frequency overlapping. It is simple in concept, rigorous in mathematics, and reliable in signal processing.

In this dissertation, AMD is studied for various effects of bisecting frequency selection, response sampling rate, and noise. Its robustness, accuracy, efficiency, and adaptability in signal analysis and system identification of structures are compared with other time-frequency analysis techniques such as EMD and wavelet analysis. Numerical examples and experimental validations are extensively conducted for structures under impulsive, harmonic, and earthquake loads, respectively. They consistently demonstrate AMD's superiority to other time-frequency analysis techniques. In addition, to identify time-varying structural properties with a narrow band excitation, a recursive Hilbert Huang Transform method is also developed. Its effectiveness and accuracy are illustrated by both numerical examples and shake table tests of a power station structure.

ACKNOWLEDGMENTS

TABLE OF CONTENTS

LIST OF ILLUSTRATIONS

LIST OF TABLES

1. INTRODUCTION

1.1. STRUCTURAL HEALTH MONITORING AND DAMAGE DETECTION

Structural health monitoring has been an active research field since more than ten years ago. Its overall goal is to provide a diagnosis and prognosis tool for structural condition at any moment during the service life of an engineering structure. It includes several main steps such as sensor deployment, data acquisition, feature extraction, and condition evaluation. Techniques in structural health monitoring can be classified into local and global groups, depending upon the space coverage of damage detection. The local group is used to detect any local damage on a small part of the structure. Often referred to as nondestructive evaluation, this group of techniques includes acoustics emission, hardness testing, and thermal field mapping. These methods all require that the vicinity of the damage is known a priori and that the portion of a structure being inspected must be accessible. Due to these limitations, the local techniques are often limited to the damage detection on or near the surface of the structure. The global group of technologies can be applied to assess the system condition of complex structures. They are dominated by the examination of changes in vibration characteristics.

Vibration-based methods for system identification and damage detection have been widely studied as summarized in a comprehensive review by Doebling et al. (1996; 1998). The basic idea is that the modal parameters such as natural frequencies, mode shapes, and modal damping are functions of the physical properties of the structure such as mass, damping, and stiffness. Therefore, changes in physical property will cause changes in the modal properties. The main advantage of vibration-based methods is that measurements at one location are sufficient to assess the condition of the whole structure.

More recently, Sohn et al. (2004) described the vibration-based structural health monitoring in four parts: (1) operational evaluation, (2) data acquisition, fusion, and cleansing, (3) feature extraction and data compression, and (4) statistical model development for feature discrimination. Operational evaluation begins to understand the purposes of structural monitoring, unique aspects of a structure, and unique features of the damage that is to be detected. The data acquisition process involves selecting the types of sensors, sensor locations, the number of sensors, data acquisition, storage, etc.

Then, data fusion means to integrate information from disparate sources and assess threats on the basis of data coming in from different sources (Klein, 1999). Data cleaning is a process of accepting and rejecting data in the feature selection process. For example, filtering has been widely used to filter out the noise component of measurements. Feature extraction is a process of identifying damage sensitive properties from vibration measurements. These properties can be used to distinguish damage from the undamaged structure.

1.2. STRUCTURAL PARAMETER IDENTIFICATION

A critical step for vibration-based structural health monitoring is to extract dynamic features such as natural frequencies, mode shapes, and damping ratios from structural responses. This step is often referred to as structural parameter identification. Structural parameter identification involves various methods in frequency domain such as frequency response method, in time domain such as least-squares estimation method and stochastic subspace method, and in time-frequency domain such as wavelet transform and Hilbert transform based methods. The identified structural parameters can serve as an index in structural damage detection, condition assessment, vibration mitigation, and long-term health monitoring.

1.2.1. Frequency Domain. With the development of digital signal processing techniques such as Fast Fourier Transform (FFT), modal tests and analysis become competitive in modal property characterization of structures (Alvin et al., 2003). In order to determine modal parameters, the frequency response function of a structure between its excitation and structural response is estimated from the available vibration measurements. It can be readily derived from their Fourier transforms as illustrated in Figure 1.1.
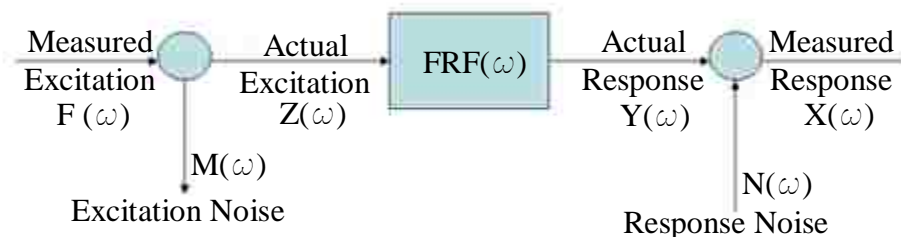
Figure 1.1. Relationship between Excitation and Response

In Figure 1.1, F(ω) and X(ω) represent the Fourier transforms of the measured excitation and the measured response, respectively; Z(ω) = F(ω) - M(ω) is the Fourier transform of the actual excitation and Y(ω) = X(ω) - N(ω) is the Fourier transform of the actual response; M(ω) and N(ω) represent the mechanical and measurement noises to the input and structural response, respectively; FRF(ω) is the frequency response function of the structural system. Mathematically, the response Y(ω) can be related to the excitation Z(ω) by:

$$X(\omega) - N(\omega) = FRF(\omega)[F(\omega) - M(\omega)] \tag{1.1}$$

According to Trendafilova (1998) and Monaco et al. (2000), frequency response functions can be used to quantify and localize minor damage. However, they face difficulties when the input excitation is unknown with ambient vibration of structures. In this case, Brincker et al. (2000; 2001) developed a frequency domain decomposition method under two assumptions: (1) white noise input, and (2) lightly structural damping. Singular value decomposition (SVD) can then be applied to expand the power spectrum density matrix of output responses into the same form as conventional matrix decomposition in modal analysis. Consequently, a first-order linear approximation of the output power spectrum density matrix is used for the estimation of mode shapes and damping coefficient. Although powerful for closed-spaced natural frequency identification, SVD requires the availability of pre-selected natural frequencies and is applicable only when the assumptions are valid.

1.2.2. Time Domain. Structural parameter identification in time domain includes a number of computationally efficient techniques such as least-squares estimation, Auto-Regressive Moving-Average (ARMA), and natural excitation technique (NExT). Least-squares estimation has been widely applied to system identification (Benedettini et al., 1995; Loh et al., 1995; Smyth et al., 1999; Lin et al., 2001; Yang and Lin, 2005). For example, Smyth et al. (1999) presented an adaptive estimation approach for the on-line identification of hysteretic systems under arbitrary dynamic loading. Yang (2005) introduced a new adaptive tracking technique to identify time-varying structural parameters. These methods placed more weight on the current data point and thus introduced a forgetting factor on the previous data so that their effect is reduced.

Natural frequencies, mode shapes, and damping ratios can be identified from a multivariate ARMA model derived from the equation of motion of a structural system. This model has been extensively studied in the last two decades (Lee and Yun, 1991; He and Roeck, 1997). Without knowing the exact degrees of freedom of the system, it often produces more eigenvalues than the actual number of frequencies (Bodeux and Golinval, 2000). Therefore, only some of the estimated eigenvalues are associated with the modes of vibration. To distinguish the physical from nonphysical modes, Bodeux and Golinval (2000) presented a prediction error identification scheme to evaluate the model parameters for vibration-based damage detection.

The NExT method was developed by James et al. (1995; 1996) to effectively extract modal parameters from ambient vibration. Under the white noise excitation, a cross-correlation function between the stationary responses at two degrees of freedom of a system resembles the free vibration of the system and can thus be used to identify the system parameters. For mode shapes, one of the degree of freedom must be used as a reference point. In combination with the Eigen-system Realization Algorithm, Caicedo et al. (2004) further applied this method to the IASC-ASCE benchmark problem. However, two significant issues cannot be overlooked for a proper implementation of this technique: (1) a stationary pink noise excitation, and (2) an independent reference signal of the measured responses. In many applications with ambient vibration, a long record of data is required. However, if the record is too long, the assumption for stationary responses may no longer be justifiable.

1.2.3. Time-Frequency Analysis. Most of the structural parameter identification works in time domain or in frequency domain have been focused on time invariant linear systems. In recent years, researchers embarked on the parameter identification of time-varying linear systems or nonlinear systems that are of great interest in the damage detection of engineering structures. In this case, measured responses are typically non-stationary and modal parameters in frequency domain change over time. As such, time-frequency analysis of measured responses has been developed to decompose and analyze non-stationary signals.

During the last two decades, wavelet analysis and Hilbert transform have been attracting wide attention in the structural health monitoring community. The interest to

the topic of time-frequency analysis is still rising as evidenced by the increasing number of papers published in technical journals and conference proceedings.

Wavelet analysis can be viewed as Fourier spectral analysis with adjustable time windows (Chui, 1992; Flandrin, 1999) for a non-stationary data series. Due to the introduction of adjustable windows, wavelet analysis provides multiple levels of details and approximations in time-frequency domain so that transient features of the data series can be retained in the frequency characteristics. As a result, it has been widely applied to non-stationary dynamic signal analysis (Staszewski, 1997; Ruzzene et al., 1997; Gurly and Karrem, 1999; Hou et al., 2000; Kijewski and Kareem, 2002; 2003). Even so, wavelet analysis still has several issues. For example, wavelet analysis is a non-adaptive data analysis tool since the basic wavelet remains unchanged with the signal characteristics. It also has the so-called leakage problem due to limited length of the basic wavelet function. Therefore, in the time-frequency plane, the frequency curves are often smeared in a large range especially at low frequency. To extract distinct time-frequency curves, Wang and Ren (2007) presented a SVD based wavelet ridge extraction method for further signal analysis and reconstruction. However, according to the Heisenberg-Gabor uncertainty principle, a signal cannot be concentrated on an arbitrary small time-frequency region. In other words, it is impossible to achieve high resolution both in time and frequency domain.

More recently, empirical mode decomposition (EMD) was developed by Huang et al. (1998; 1999; 2003) to decompose a stationary and non-stationary data series into a finite number of intrinsic mode functions (IMFs), each having a well-behaved Hilbert transform. The well-known Hilbert-Huang transform (HHT) combines EMD with Hilbert spectral analysis; it is an adaptive data analysis tool for non-stationary signals. Some HHT applications in engineering, biomedical, financial and geophysical data analyses have been presented by Huang and Shen (2005) and Huang and Attoh-Oine (2005). More research about the EMD applications in signal processing can be found in Chen and Feng (2003), Yang et al. (2004), Peng et al. (2005), Shi and Law (2007), Shi et al. (2009), and Zheng et al. (2009). Although powerful in extracting the properties of non-stationary signals, EMD still faces several challenges in some engineering applications: 1) difficult to decompose signals with closely-spaced frequency components such as wave groups in

ocean engineering, free vibration and beating responses in structural and mechanical systems, 2) difficult to separate a short time weak signal from a stationary strong response, and 3) impossible to deal with the time-varying feature between two modes of vibration for nonlinear systems. Attempts have been made by a few investigators to address these challenges (Chen and Feng, 2003; Peng et al., 2005; and Zheng et al., 2009). However, it is still quite a challenge to consistently and reliably extract individual components from a non-stationary response when their time-varying frequencies are closely spaced, particularly resulting from a nonlinear structural system.

1.3. OBJECTIVES OF THIS STUDY

To address the above challenges, analytical mode decomposition (AMD) is sought to accurately decompose any signal to physically meaningful components in various engineering applications. Therefore, the main objective of this study is to develop a signal decomposition theorem based on the Hilbert transform of a harmonics multiplicative time series, which will serve as the foundation for AMD in structural health monitoring. It decomposes a time series into many signals whose Fourier spectra are non-vanishing over mutually-exclusive frequency ranges separated by constant bisecting frequencies for stationary and non-stationary signals with no overlapping component frequencies, and by time-varying bisecting frequencies for non-stationary signals with overlapping component frequencies.

The performance of AMD with constant bisecting frequencies in dealing with the closely-spaced modes of vibration of linear structures will be investigated with stationary, transient, and intermittent signals both numerically and experimentally. For structural parameter identification, AMD in combination with Hilbert spectral analysis is demonstrated with the free vibration and harmonic vibration of a three degree-of-freedom (DOF) mechanical system and the ambient vibration of a 36-story building with a 4-story light appendage. AMD will then be applied to identify the modal properties of a ¼-scale 3-story building frame with closely-spaced modes due to the presence of multiple tuned mass dampers based on a series of shake table tests.

The performance of AMD with time-varying bisecting frequencies will be investigated with non-stationary, frequency-modulated signals. In this case, each

frequency modulated individual component between any two bisecting frequencies can be analytically extracted. The signal decomposition theorem developed in this study will be demonstrated to function like an adaptive bandpass filter that allows a complete pass of frequency band between two adjacent bisecting frequencies. Parametric studies will be conducted for bisecting frequencies selection, sampling rate and noise effects. Representative engineering applications will be studied with frequency gradually varied, amplitude and frequency modulated, and nonlinear shear buildings under impulsive, harmonic, white noise and earthquake loads. Unlike EMD, AMD is simple in concept, rigorous in mathematics, efficient in computation, and reliable in signal processing. The time-varying bisecting frequencies will be applied to the parametric identification of nonlinear systems.

The secondary objective of this study is to develop a recursive time-varying parameter identification method under narrow band excitations based on Hilbert transform. To validate the proposed method, time-varying parameters will be identified for 1- and 2-story buildings with three scenarios of time-varying parameters: abrupt, gradual, and periodical stiffness variations under earthquake excitations. Noise effects will be taken into account in numerical simulations. The method will be applied to identify a real-world high voltage switch structure from shake table test data. The high voltage switch includes a friction mechanism for opening and closure of the switch.

1.4. RESEARCH SIGNIFICANCE

The critical issue for parameter identification is to extract useful information from the field measured data sets. This requires a robust and high performance signal analysis methodology. Although vibration-based methodologies have been extensively investigated for time-invariant structural systems during the last two decades, there are still several challenges as mentioned above, particularly for systems with closely-spaced modes of vibration. Therefore, a reliable signal processing method is quite necessary to address these challenges.

Recently, parameter identification for time-varying structures has received considerable attention. Some methods such as least-squares based techniques are accurate but inefficient. Other methods such as HHT are inaccurate for MDOF systems.

Therefore, it is highly important to develop a methodology that can accurately and efficiently identify the parameters of time-varying structural systems.

When subjected to extreme loads such as tornados and earthquakes, a structure may experience damage. One of the important objectives in structural health monitoring of civil infrastructures is to identify the state of the structure and to detect damage as it occurs. The damage of the structure is reflected by a local change of structural parameters. Hence, it is important to develop methodologies that are capable of detecting structural parameter changes.

1.5. DISSERTATION ORGANIZATION

This dissertation consists of eight sections. In Section 1, the concepts of structural health monitoring and structural parameter identification are introduced. The objectives and significance of this study are presented. In Section 2, the state-of-the-art development in system identification is reviewed particularly for time-varying parameters of linear and nonlinear systems. In Section 3, a signal decomposition theorem with Hilbert transform or AMD in structural health monitoring is discovered and demonstrated to have addressed the challenges associated with EMD or those of Hilbert vibration decomposition (HVD).

The theorem is applied to identify the time-invariant parameters of various structures with closely-spaced modes from free, harmonic and ambient vibration in Section 4. In particular, AMD is combined with the conventional random decrement technique (RDT) to develop a new system identification method with ambient vibration, referred to as the RDT-AMD method. The new method is applied to a 3-DOF mechanical system and a 36-story building with 4-story appendage system, both with closely-spaced modal frequencies, demonstrating its effectiveness in practical applications. Finally, its accuracy in modal parameter identification is validated with shake table testing of a 3-story building. Parametric studies are conducted to investigate the bisecting frequency selection and frequency resolution of the new method.

In Section 5, AMD is extended to the time-varying parameter identification of from non-stationary responses of both linear and nonlinear systems. Its aim is to lay a mathematical foundation for the decomposition of amplitude- and frequency-modulated

signals and establish admittance requirements for the selection of time-varying bisecting frequencies, one between any two adjacent modulated frequencies. Parametric studies are conducted to understand and quantify the effects of bisecting frequency selection, signal frequency overlapping, sampling rate, and signal noise. Time-varying modal parameters of a nonlinear shear building under impulsive, white noise and earthquake loads will be tracked using the mathematically rigorous theorem.

In Section 6, in order to track the variation of structural parameters under force vibration, a recursive HHT method is developed. It allows the structural identification of a building story-by–story and thus is computationally efficient in the determination of both stiffness and damping coefficients. The method is validated with one- and two-story buildings with three types of time-varying parameters (abruptly, gradually, and periodically) under earthquake excitations even when a simulated measurement noise up to 5% of the signal intensity was injected to the building responses.

In Section 7, the parameter identification and ultimate behavior of a time-varying power station structure are extensively studied based on shake table test results. A series of harmonic tests with constant amplitude and increasing excitation frequency is conducted. Modal parameters are identified for each excitation frequency based on the proposed recursive HHT approach.

In Section 8, the main findings and conclusions of this study are summarized and further researches on AMD and time-varying system identification are recommended.

2. LITERATURE REVIEW

The focus of this study is to develop an adaptive data analysis method for the parameter identification of structures with closely-spaced modes, time-varying properties, and hysteretic behaviors. Therefore, structural dynamic parameters and their role in structural health monitoring are briefly reviewed.

2.1. STRUCTURAL DYNAMICAL PARAMETERS

The actual implementation of a vibration-based structural health monitoring starts with designing a dynamic experiment. The type and number of sensors, and sensor placement are first decided so that physical quantities of interest can be measured. Then, some damage sensitive properties or structural parameters are extracted from the measured dynamic responses. The critical issue in feature extraction is to identify the appropriate dynamic parameters for a particular application, such as natural frequencies, mode shapes, damping, and nonlinear properties. All these parameters play a significant role in system identification and damage detection.

2.1.1. Natural Frequency. Natural frequency is one of the basic dynamic properties of structures. The amount of literature related to system identification and damage detection with frequency shifts is quite large (Loland and Dodds, 1976; Vandiver, 1977; Cawley and Adams, 1979; Ismail, et al., 1990; Stubbs and Osegueda, 1990a; 1990b; Skjaerbaek, et al., 1996; Leutenegger et al., 1999).

The observation that changes in structural properties cause changes in vibration natural frequencies was the impetus for the intensive research works in structural health monitoring. For example, Loand and Dodds (1976) used the changes in the resonant frequencies, mode shapes, and response spectra to identify damage of an offshore oil platform. Frequency changes of 10% to 15% were observed when a structural modification was implemented to resemble a structural failure near the waterline. They concluded that change in response spectrum can be used to monitor structural integrity. However, Farrar, et al. (1994) conducted a dynamic test on the I-40 bridge and found that when the cross-section stiffness at the center of a main plate girder had been reduced 96.4%, no significant reduction in the modal frequencies was observed. In general,

natural frequency represents global behavior of a structural system. Depending on the redundancy, the influence of local damage on the change in natural frequency may change. As such, the appropriateness of using frequency shift as a damage indicator must be evaluated case by case.

2.1.2. Mode Shape, Mode Shape Curvature, and Modal Strain Energy. West (1984) first used the mode shape to locate structural damage without a prior finite element model. The author first used the modal assurance criteria to ensure the level of mode correlation between the conventional test and acoustic test of an undamaged space shuttle orbiter body flap. The mode shapes evaluated from the measured displacements or accelerations of a structure were then used to detect existing damage. Similar approaches have been taken by other researchers such as Stanbridge et al. (1997) and Ettouney (1998). Their research concluded that change in mode shape can be used to detect the location of damage with acceptable accuracy. However, whether this method is applicable for real-world structures is yet to be seen because the number of mode shapes and natural frequencies that can be reliably identified from experiments is quite limited.

Mode shape curvature is basically the second derivative of the mode shape with respect to the location coordinate. Pandey et al. (1991) demonstrated that absolute changes in mode shape curvature can be used for damage detection for beam like structures. It is more sensitive to damage than the mode shape itself. However, the derivative of mode shape is also sensitive to noise. In addition, numerical evaluation on the second derivative of mode shapes sometimes caused unacceptable errors. Therefore, Chance et al. (1994) used the measured strain instead to evaluate curvature directly, improving its accuracy significantly.

Mode strain energy is another potential damage indicator. The ith modal strain energy in the jth element stiffness is defined by the ith mode shape $\emptyset_i$ and element stiffness k_j, which is $\emptyset_i^T k_j \emptyset_i$. Its fraction of the total modal strain energy is defined as the ith modal strain energy ratio for the jth element. The difference in element modal strain energy ratio before and after damage can be used to detect the structural damage. The studies based on the modal strain energy for damage detection (Carrasco et al., 1997; Choi and Stubbs, 1997) demonstrated that the modal strain energy method performed very well for damage location in truss, beam, and plate structures. In all cases, the modal strain energy method

needs information from the undamaged structure. Therefore, a baseline model is required to apply this method.

2.1.3. Damping. Damping is another important dynamic property of structures. Change in damping has been used to detect nonlinear effects caused by cracking (Modena et al., 1999; Adhikari and Woodhouse, 2001). However, damping has not been used as extensively as natural frequencies and mode shapes in structural health monitoring due mainly to its excessive variation. The large variation is likely attributed to the fact that damping effect is a complicated phenomenon in structural dynamics; its mechanism is unclear in many applications. Although viscous or complex damping has been widely considered in structural dynamics textbooks for convenience in mathematical derivation, real-world structures can have significant friction and inelastic deformation effects. Therefore, further research is needed in order to use damping as a damage indicator in structural health monitoring.

2.1.4. Nonlinear Feature. Stiffness and damping force nonlinearities can introduce dynamic phenomena and behaviors that are dramatically different from those predicted by the linear theory. Brandon (1997; 1999) stated that the nonlinear response of a mechanical system was often overlooked and valuable information was lost when one discarded the time series data and focused on the spectral data. Therefore, the author advocated the use of time-domain system identification techniques such as ARMA model and autocorrelation function to retain the important nonlinear information. Although a few attempts were made to take advantage of nonlinear behaviors (Vakakis et al., 2004; Kershenc et al., 2005), it is still a challenge to identify a nonlinear system due to its highly individualistic nature.

2.2. PARAMETER IDENTIFICATION WITH CLOSELY-SPACED MODES

With the development of signal decomposition techniques, such as fast Fourier transform, wavelet transform, and Hilbert transform, various methods in frequency domain and for time-frequency analysis have become competitive in modal property characterization. Over the past decades, a vast amount of literature based on Fourier transform, wavelet transform, and Hilbert transform can be found for the time-invariant modal parameter identification of linear structures (Doebling et al., 1996; Sohn et al.,

2004). Most of them, however, faced a challenge in identifying the modal parameters of a structure with closely-spaced modes, particularly in the presence of measurement noise. Following is a detailed discussion of such a challenge and research needs to address it.

A classical approach in frequency domain is just to take the discrete Fourier transform of dynamic responses and estimate the well separated modes of vibration directly from the peaks of power spectral density functions (Bendat and Piersol, 1993). In the case of close modes, it is difficult to distinguish two nearby peaks. For example, consider a 20 second time duration dynamic response signal of $x(t) = x_1(t) + x_2(t) + x_3(t)$, where $x_1(t) = \cos(2\pi f_1 t)$, $x_2(t) = \cos(2\pi f_2 t + \pi/6)$, and $x_3(t) = \cos(2\pi f_3 t)$. The three frequencies were set to $f_1 = 1.1$ Hz, $f_2 = 1.2$ Hz, and $f_3 = 1.3$ Hz with a frequency spacing of 0.1 Hz. A sampling rate of 50 point per second is used. The original signal and its Fourier spectrum are presented in Figure 2.1.

(a) Original Signal
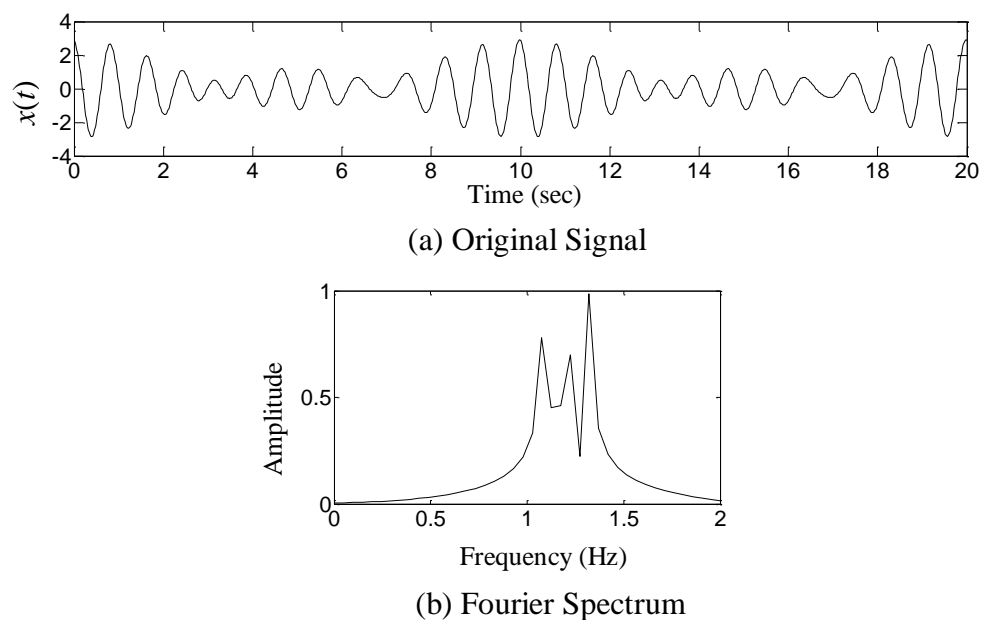
(b) Fourier Spectrum

Figure 2.1. A Signal with Closely-Spaced Frequency and Its Fourier Spectrum

The time series of finite length was first transformed into the frequency domain using the Fourier transform. The Fourier spectrum was then filtered with a bandpass filter to potentially separate the mode information. Finally, the filtered Fourier spectrum was transformed back to the time domain with the inverse Fourier transform. Both in time and

frequency domains, a finite length signal is equivalent to the application of a rectangular window on its corresponding infinite long signal. Both transforms introduce numerical errors in two ways: signal modification by windowing and end effect due to sharp edges or brick walls of the windows. Applying a rectangular window in the frequency/time domain is equivalent to execute a convolution between a sinc function and the time/frequency function over an infinite range. This means that the time/frequency function is now a distorted signal, therefore, the brick wall with the rectangular window or the sudden change of frequency corresponds to an infinitely long oscillation in the time domain that cannot be represented accurately with the Fourier transform and its inverse transform. An improper selection of the beginning and end of a signal could introduce an artificial oscillation as illustrated in Figure 2.2. In the case of splitting closely-spaced frequency components, there is no space to soften the brick wall by designing two smooth edges of a window.
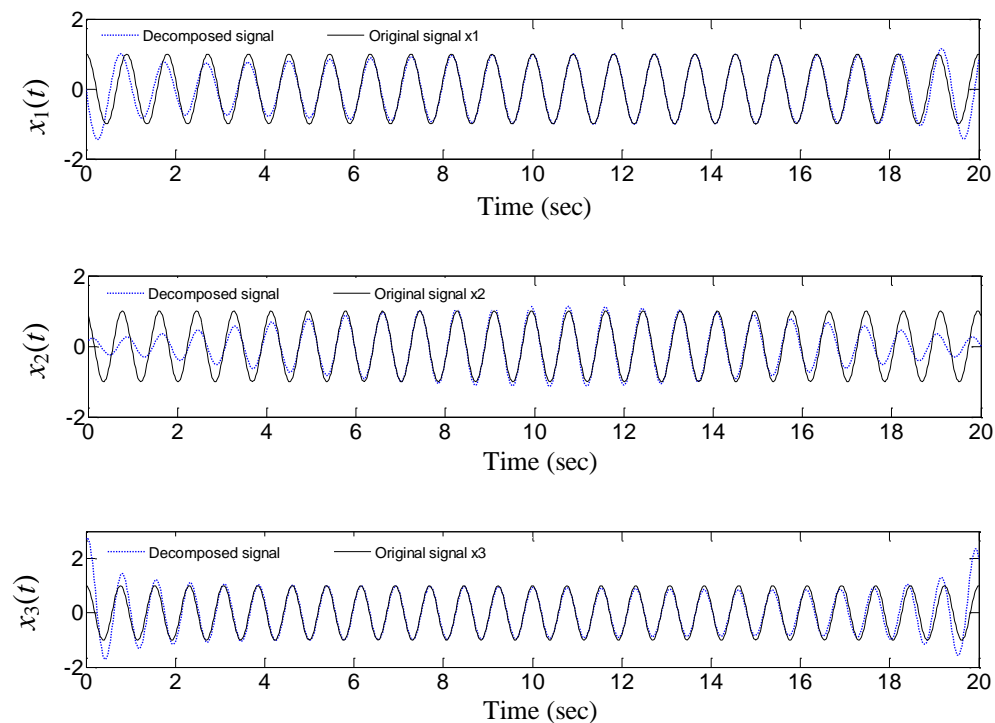
Figure 2.2. Decomposed Signals by Bandpass Filtering versus Exact Signals

In order to detect closely-spaced modes, Brincker et al. (2001) presented a singular value decomposition method in frequency domain under two assumptions: (1) white noise input, and (2) lightly structural damping. In this case, the output power spectrum density matrix can be separated into the effects of a set of single DOF systems, each corresponding to an individual mode from which the mode shapes and damping can be estimated. By using the decomposition technique, closely-spaced modes were identified with high accuracy even in the case of strong noise contamination of the dynamic measurements.

Wavelet transform as one of the time-frequency analysis tools has attracted wide attention in recent years. This method has been widely applied to structural modal parameter identification (Lardies et al., 2002; Kijewski et al., 2003; Yan et al., 2006; Min et al., 2009). However, for a structure with closely-spaced modes, it is difficult to select appropriate wavelet parameters such as center frequency and bandwidth to distinguish the closely-spaced modes. Attempts have been made by a few investigators to identify close-spaced modes with wavelet transform. Teng and Zhu (2010) used an adaptive genetic algorithm to optimize the parameters of wavelet including the center frequency and its bandwidth. The parameters of wavelet were optimized with the adaptive genetic algorithm, whose objective function is the standard deviation between the wavelet ridge and fitting line. In doing so, their numerical simulations with three closely-spaced modes demonstrated that the wavelet transform in combination with the adaptive genetic algorithm can be used to identify the closely-spaced modes of vibration.

HHT is another time-frequency analysis method developed for stationary and non-stationary signal analysis and has been widely applied in structural parameter identification and damaged detection. However, central to HHT, the EMD sift process is unable to decompose signals with closely-spaced modes. With the HHT method, Chen and Xu (2002) explored the possibility to identify the modal parameters of a structure with closely-spaced modes. For the structure with closely-spaced modes, the cutoff frequencies determined from the power spectrum density of the measured response time history were used in the signal sifting process with the intermittency check. The random decrement technique was further applied to each of the modal responses decomposed by EMD with the cutoff frequency intermittency check to obtain the free modal responses.

Then, the modal parameters such as naturel frequencies and damping ratios can be identified. The results of their research show that damping ratios identified using the HHT method is much more accurate than those from the fast Fourier transform analysis.

Wang (2005) presented another HHT based method to decompose a signal with close frequency components. A temporary complex time series was introduced to shift down the frequencies of its components. This can greatly increase the ratio between the higher and lower frequencies so that individual components can be separated with EMD. The key point of this method is to increase the ratio of the frequencies of two components. Consider a signal with two cosine functions:

$$x(t) = \cos(\omega_1 t) + cos(\omega_2 t + \emptyset) \tag{2.1}$$

in which $\omega_2 > \omega_1$ and $\emptyset$ is a phase angle. The ratio of the two frequencies is $\alpha = \omega_2/\omega_1$. It can be increased by subtracting a temporary frequency ω_0 in the numerator and denominator simultaneously. The ratio between the two downshifted frequencies becomes $\alpha = (\omega_2 - \omega_0)/(\omega_1 - \omega_0)$. To achieve this downshifting process, a complex analytic signal $z(t)$ is defined as:

$$z(t) = x(t) + jH[x(t)] \tag{2.2}$$

in which, $H[.]$ represents Hilbert transform of the function in the bracket and $j = \sqrt{-1}$ is an imaginary unit. Downshifting in frequency components can be achieved by multiplying an exponential function, $e^{-j\omega_0 t}$, to yield a new complex signal:

$$Z(t) = z(t)e^{-j\omega_0 t} = e^{j(\omega_1 - \omega_0)t} + e^{j(\omega_2 - \omega_0)t + \emptyset} \tag{2.3}$$

For a proper ω_0, $\alpha = (\omega_2 - \omega_0)/(\omega_1 - \omega_0)$ can be as large as 1.5, and the new complex signal can be easily separated by EMD:

$$Z(t) = \sum_{k=1}^{n} C_k(t) + R_n \tag{2.4}$$

in which $C_k(t)$ is the kth decomposed component named as intrinsic mode function, and R_n is a residual function. The decomposition of the original analytical complex signal can then be upshifted back by multiplying $e^{j\omega_0 t}$ with both sides of Equation (2.4):

$$z(t) = Z(t)e^{j\omega_0 t} = \sum_{k=1}^{n} C_k(t)e^{j\omega_0 t} + R_n e^{j\omega_0 t} \tag{2.5}$$

Therefore, the decomposition of original signal can be expressed as:

$$x(t) = Re[z(t)] = Re[\sum_{k=1}^{n} C_k(t)e^{j\omega_0 t}] + Re[R_n e^{j\omega_0 t}] \tag{2.6}$$

in which, $Re[.]$ represents the real part of the complex function in bracket. Although successful for general systems, this method may still face a challenge as the space

between two frequencies decreases, particularly for flexible structures such as long-span bridges with very low natural frequencies. Overall, it is still a challenge to consistently and reliably identify the properties of structures with closely-spaced modes.

2.3. TIME-VARYING PARAMETER IDENTIFICATION

The measured dynamic responses in structural and mechanical systems are often irregular in amplitude and frequency over time, which is referred to as amplitude- and frequency-modulated signals. Such responses must be characterized with time-varying features such as instantaneous frequency. For example, consider a dynamic response with a sudden drop of frequency: $x(t) = \begin{cases} \cos(6\pi t) & t < 5\ sec \\ \cos(3\pi t) & t \geq 5\ sec \end{cases}$, the original signal and its Fourier spectrum are presented in Figure 2.3. It can be seen from Figure 2.3 that the Fourier spectrum loses the time essence of frequency drop at 5 sec, which is important in real time structural health monitoring. To enable the identification of damage location and occurrence, least-squares based methods in time domain have recently been applied into time-varying parameter identification. Advanced time-frequency analysis techniques such as wavelet transform and Hilbert transform have also been used as summarized below.

(a) Original Signal

(b) Fourier Spectrum
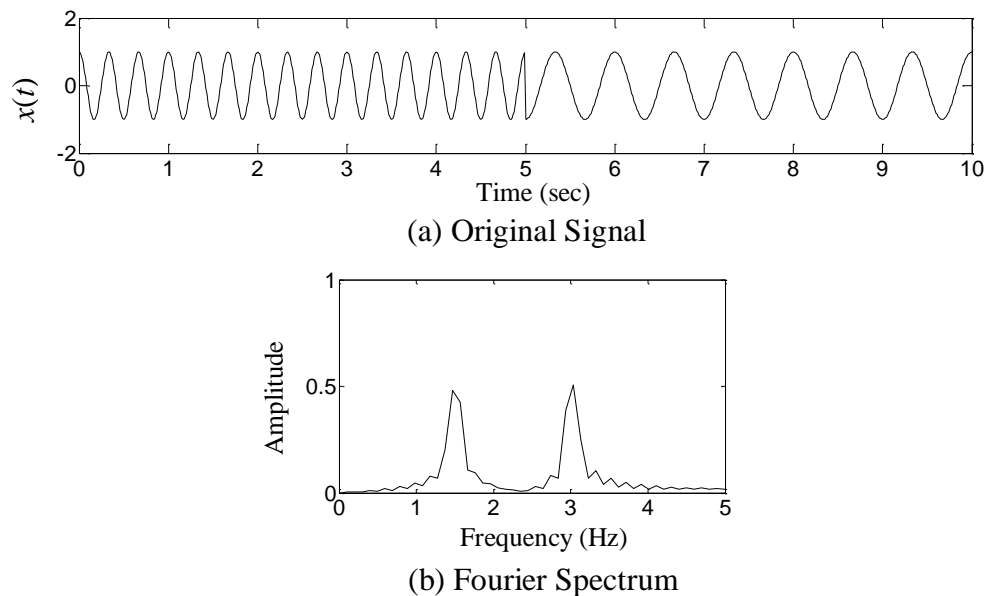
Figure 2.3. A Dynamic Signal with Sudden Drop Frequency

2.3.1. Least-Squares Based Method. Least-squares estimation is a computationally efficient approach in time domain and has been widely applied to structural system identification (Bendedettine et al.; 1995, Bodson, 1995; Loh and Tou, 1995; Smith et al., 1997; Yongkyu, 2002; Ravindra, 2006). A constant forgetting factor is commonly used in the above methods. For example, Smyth et al. (1999; 2002) and Lin et al. (2001) presented a modified least-squares method for the on-line identification of hysteretic systems under arbitrary dynamic loading. The drawback of the constant forgetting factor approach is a trade-off between tracking ability and noise sensitivity. A smaller factor allows a more accurate tracking on the variation of structural parameters but makes the approach more sensitive to noise effect.

Yang and Lin (2005) presented a new adaptive tracking technique based on the least-squares estimation approach to identify time-varying structural parameters. Their method is able to track the abrupt changes of structural parameters due to damage. The tracking algorithm is based on the adaptation of the current measure data to determine the parameter variations and the covariance of the residual error is only contributed by measurement noises. Their proposed approach was applied to linear structures, such as the Phase I ASCE structural health monitoring benchmark building and a nonlinear elastic structure. Yang et al. (2006; 2007) further detected damage to structures using the adaptive tracking technique with unknown excitations. Simulation results for a Duffing-type nonlinear ASCE benchmark building demonstrated that the method is quite effective and accurate for tracking the variations of structural parameters due to damage.

Yang et al. (2009) further proposed a new least-squares based method, referred to as the adaptive quadratic sum-squares error, for the online system identification and damage detection of structures. This new technique can be briefly described as follows. The error vector $\boldsymbol{\varepsilon}_i$ at time $t = i\Delta t$ (Δt is a sampling time) between the observation data and the theoretical data is a nonlinear function of the unknown parametric vector $\boldsymbol{\theta}$. The error vector $\boldsymbol{\varepsilon}_i$ was linearized for $\boldsymbol{\theta}$ at the previous time step $t = (i - 1)\Delta t$, so that $\boldsymbol{\varepsilon}_i$ is a linear function of unknown parametric vector $\boldsymbol{\theta}$. Consequently, the sum-squares error becomes a quadratic function of $\boldsymbol{\theta}$. The analytical recursive solution for the estimate $\widehat{\boldsymbol{\theta}}$ of $\boldsymbol{\theta}$ can then be obtained by minimizing the quadratic sum-squares error. The simulation results, including a two-story steel frame finite element model, a plane truss with finite

element model, and a 5-DOF hysteretic shear beam building, demonstrated the accuracy of the method in tracking the variation of structural parameters such as stiffness degradation due to damage. The adaptive quadratic sum-squares error method was further developed by Huang et al. (2010). The advantage of this method is that the unknown parametric vector is directly estimated and the state vector is updated, thus reducing computational efforts. The accuracy and effectiveness of the proposed method was demonstrated by numerical simulations and the experimental data taken from a scaled three-story building model.

More recently, Wang and Chen (2011) developed a moving-window curve fitting method based on the least-squares estimation in each fixed window. Central to the new method is the transformation from a dynamic to static problem by integrating the dynamic measurements and loads over time. This method can be applied to locate and quantify multiple cracks and sudden reductions in stiffness in beam-like structures. It is a computationally efficient, straightforward identification method for multi-span continuous highway bridges.

2.3.2. Wavelet Transform Based Method. Wavelet transform as an advanced time-frequency analysis technique has been designed for non-stationary time signals of linear systems in the past two decades. Wavelet analysis is essentially an advanced short-time Fourier transform method with adjustable windows at various times. Due to its flexibility in window length selection, wavelet analysis reveals the detail and approximation of a time signal at multiple levels and retains the transient characteristics of the data series with time-frequency spectral decomposition. The integral wavelet transform is the convolution of a signal $x(t)$ and the conjugate of a scaled parent wavelet function $\Psi[(b-t)/a]$ with a dilation scale $a>0$ and translational value b:

$$W(a,b) = \frac{1}{\sqrt{a}} \int_{-\infty}^{\infty} x(t) \, \Psi^* \left(\frac{b-t}{a} \right) dt \tag{2.7}$$

in which a is inversely proportional to frequency, $W(a,b)$ is the wavelet coefficient that represents the similitude between the dilated and shifted parent wavelet and the signal at time b and scale a, and * represents an operation of complex conjugate. The distribution of the wavelet coefficient in time-frequency plane can be used for signal time-frequency analysis. In particular, the extracted ridge lines can be used for signal reconstruction.

Gurly and Kareem (1999) used wavelet transform to decompose a random process into localized orthogonal basis functions, providing a convenient format for the modeling, analysis, and simulation of non-stationary processes. The time-frequency analysis of wavelet transform provided insight into the characteristics of transient signals. The analysis of non-stationary signals including wind, wave and earthquake applications was typically accomplished by the continuous wavelet transform in Equation (2.7).

Staszewski (1997) compared the cross section procedure, impulse response recovery procedure, and ridge detection procedure in damping identification of a dynamic system. The wavelet transform was used to decouple the system into single harmonic modes. The mathematical framework of the decoupling procedure was presented.

Hou et al. (2000) presented a wavelet-based approach for structural health monitoring and damage detection. Both numerical simulation for a simple structural mode with breakage springs and actual recorded data of the building response during an earthquake event were analyzed. The results demonstrated that structural damage or a change in system stiffness can be detected by spikes in the details of the wavelet decomposition of the response data. The locations of the spikes can accurately indicate the time instances when the structural damage occurred.

Kijewski and Kareem (2003) argued that civil engineering structures usually possess long period motions and thus require finer frequency resolution of parent wavelets. Although many parent wavelets are available, the authors focused on the Morlet wavelet due to its unique properties in continuous wavelet transform. The Morlet wavelet is defined by:

$$\varPsi(t) = e^{j\omega_c t} e^{-t^2/2} \tag{2.8}$$

It is essentially a Gaussian-windowed Fourier transform with harmonic oscillations at the central frequency of ω_c. In their study, Kijewski and Kareem (2003) demonstrated that a proper selection of Morlet wavelet central frequencies is required to balance modal separation. In doing so, the instantaneous frequency of a signal can be identified from the wavelet phase or from the ridges of the amplitude.

Although widely used in signal processing, wavelet analysis is non-adaptive to a particular data series. It depends upon the introduction of a predetermined parent wavelet. Therefore, some of the highly transient features in a time signal may be lost in the

process of wavelet transform. In addition, wavelet analysis has end leakages due to the limited length of the basic wavelet function. This often results in a time-frequency ridge pattern with thick and blurred lines, particularly in a low frequency range. To enhance the time and frequency resolution, Wang and Ren (2007) presented a SVD based wavelet ridge extraction method for signal analysis and reconstruction. However, according to the Heisenberg-Gabor uncertainty principle (Flandrin, 1999), a time signal cannot be decomposed and reconstructed in an arbitrarily small time-frequency region. It is difficult, if not impossible, to simultaneously achieve high resolution both in time and frequency domains.

2.3.3. Hilbert Transform Based Method. Perhaps, the most advanced time-frequency analysis technique involves Hilbert transform. Since a decade ago, EMD and Hilbert spectral analysis, called HHT, has been developed for non-stationary and nonlinear data analysis by Huang et al. (1998; 1999; 2003). Over the last two decades, HHT has received wide attention in time-varying system identification, particularly in recent years (Shi and Law, 2007; Shi et al., 2009; Bao et al., 2009).

Shi and Law (2007) proposed an identification algorithm for linear, time-varying systems based on the HHT method. The proposed method was verified with free vibration response data. Three ideal cases of time-varying properties, including smoothly, abruptly and periodically varying systems, were studied. Shi et al. (2009) then further develop this identification algorithm for time-varying systems from the forced vibration response data. Similarly, smoothly, abruptly and periodically varying systems were studied to demonstrate the effectiveness of their identification algorithm.

Consider a linear n-DOF system with time-varying parameters, the equation of motion can be written as:

$$\mathbf{M}(t)\ddot{\mathbf{x}}(t) + \mathbf{C}(t)\dot{\mathbf{x}}(t) + \mathbf{K}(t)\mathbf{x}(t) = \mathbf{f}(t) \tag{2.9}$$

where $\mathbf{M}(t), \mathbf{C}(t)$, and $\mathbf{K}(t)$ are time-varying mass, damping, and stiffness matrices, respectively; $\mathbf{f}(t)$ is the external load vector; $\mathbf{x}(t)$ is the displacement vector. Mass is considered to be constant in this study.

The Hilbert transform of both sides of Equation (2.9) leads to:

$$\mathbf{M}H[\ddot{\mathbf{x}}(t)] + H[\mathbf{C}(t)\dot{\mathbf{x}}(t)] + H[\mathbf{K}(t)\mathbf{x}(t)] = H[\mathbf{f}(t)] \tag{2.10}$$

When $\mathbf{C}(t)$ and $\mathbf{K}(t)$ change slowly in comparison with the building velocity and displacement, the Bedrosian's theorem (Stefan, 1996) can be applied to the second and third terms of Equation (2.10). That is,

$$H[\mathbf{C}(t)\dot{\mathbf{x}}(t)] = \mathbf{C}(t)H[\dot{\mathbf{x}}(t)], \, H[\mathbf{K}(t)\mathbf{x}(t)] = \mathbf{K}(t)H[\mathbf{x}(t)] \tag{2.11}$$

Then, Equation (2.10) becomes:

$$\mathbf{M}H[\ddot{\mathbf{x}}(t)] + \mathbf{C}(t)H[\dot{\mathbf{x}}(t)] + \mathbf{K}(t)H[\mathbf{x}(t)] = H[\mathbf{f}(t)] \tag{2.12}$$

By introducing an analytic signal of $\mathbf{z}(t) = \mathbf{x}(t) + jH[\mathbf{x}(t)]$, Equations (2.9) and (2.12) can be combined into:

$$\mathbf{M}(t)\ddot{\mathbf{z}}(t) + \mathbf{C}(t)\dot{\mathbf{z}}(t) + \mathbf{K}(t)\mathbf{z}(t) = \mathbf{g}(t) \tag{2.13}$$

where $\mathbf{g}(t) = \mathbf{f}(t) + jH[\mathbf{f}(t)]$ is the analytic signal of the external load vector.

The key of the identification algorithm by Shi et al. (2009) is to decompose the response $\mathbf{x}(t)$ into n modal responses by the EMD process:

$$\mathbf{x}(t) = \sum_{i=1}^{n} \mathbf{x}_i(t) + \boldsymbol{r}(t) \tag{2.14}$$

The analytic signal $\mathbf{z}(t) = \sum_{i=1}^{n} \mathbf{z}_i(t) = \sum_{i=1}^{n}\{\mathbf{x}_i(t) + jH[\mathbf{x}_i(t)]\}$ can then be formulated, and Equation (2.13) can be written into:

$$\mathbf{M}(t)\sum_{i=1}^{n}\ddot{\mathbf{z}}_i(t) + \mathbf{C}(t)\sum_{i=1}^{n}\dot{\mathbf{z}}_i(t) + \mathbf{K}(t)\sum_{i=1}^{n}\mathbf{z}_i(t) = \mathbf{g}(t) \tag{2.15}$$

By left multiplying $\mathbf{z}_i^T(t)$ on both sides of Equation (2.15) and using the orthogonal properties of IMF, the following equation can be obtained:

$$\mathbf{z}_i^T(t)\mathbf{M}(t)\ddot{\mathbf{z}}_i(t) + \mathbf{z}_i^T(t)\mathbf{C}(t)\dot{\mathbf{z}}_i(t) + \mathbf{z}_i^T(t)\mathbf{K}(t)\mathbf{z}_i(t) = \mathbf{z}_i^T(t)\mathbf{g}(t) \tag{2.16}$$

For an n-story shear-type building, Equation (2.16) contains *2n* equations for the evaluation of *2n* time-varying parameters at any time instant *t* with a given mass matrix. An important advantage of the proposed algorithm is that only one set of IMFs is required to solve all the time-varying unknown system parameters. However, the identification results of time-varying parameters using one set of IMFs are inaccurate since the orthogonality of two IMFs is defined over the entire duration of a signal rather than at each time step.

More recently, Bao et al. (2009) used the auto-correlation functions of various structural responses to reduce noise effects so that the accuracy of the HHT method can be improved. In essence, a bandpass filter and an effective IMF selection procedure were combined to overcome the modal perturbation issue of time-varying systems. The

robustness and effectiveness were verified both by numerical simulations and laboratory measured vibration data on a scaled concrete steel composite beam model.

Although powerful in extracting the time-varying properties of non-stationary signals, EMD faces several challenges in some engineering applications as presented in the previous section. For a dynamic response signal, the decomposed IMFs by EMD may be equivalent to the modal responses when the modes of vibration are well separated. As the spacing of two vibration modes is reduced to sufficiently small, the corresponding two IMFs may be inseparable and thus cannot represent the modal responses. Shi and Law (2007) and Shi et al. (2009) considered that each IMF represents a modal response and concluded that only one set of IMFs is required to solve all the time-varying parameters. Obviously, simply using an IMF to represent a modal response may not be justifiable. Therefore, to extract each modal response by EMD, a bandpass filter was used to pre-process the dynamic response (Chen and Xu, 2002; Yang et al. 2003; Bao et al. 2009).

More recently, Feldman (2006; 2008; 2011) introduced a new signal decomposition formulation, called Hilbert Vibration Decomposition (HVD), for non-stationary signals. It includes three steps: 1) to estimate the instantaneous frequency of the largest energy vibration component, 2) to extract the envelope of the largest energy vibration component, and 3) to subtract the largest energy component from the original signal and repeat the whole process for the remaining signal. The key idea behind HVD is that the instantaneous frequency of an analytic signal is dominated by the largest energy component. Therefore, the instantaneous frequency can be extracted by using a lowpass filter. Once the instantaneous frequency is detected, the so-called coherent demodulation or phase lock-in amplifier detection technique is used to extract the envelope of the largest energy vibration component. According to Braun and Feldman (2011), HVD faces serious challenges when applied to separate low amplitude harmonics from significant noise additions; its inaccuracy is greatly amplified even with insignificant noise. Overall, it is still quite a challenge to consistently and reliably extract individual components from a data series, particularly when its time-varying frequencies are closely-spaced.

3. ANALYTICAL MODE DECOMPOSITION

3.1. HILBERT TRANSFORM AND ANALYTIC SIGNAL

Hilbert transform is one of the integral transform like Laplace and Fourier transform. It is named after David Hilbert, who first introduced it to solve a special case of integral equations in the area of mathematical physics (Korpel, 1982). The Hilbert transform of a function $x(t)$ is defined by an integral transform (Titchmarsh, 1950; Hahn, 1996):

$$H[x(t)] = \frac{1}{\pi} P \int_{-\infty}^{\infty} \frac{x(\tau)}{t-\tau} d\tau \qquad (3.1)$$

in which P indicates the Cauchy principal value around $t = \tau$. Physically, Hilbert transform is equivalent to a special kind of linear filter, where all the amplitudes of spectral components remain unchanged, but their phases are shifted by $\pi/2$. Mathematically, the Hilbert transform $H[x(t)]$ of the original function represents a convolution of $x(t)$ and $\frac{1}{\pi t}$, which can be written as:

$$H[x(t)] = x(t) * \left(\frac{1}{\pi t}\right) \qquad (3.2)$$

Note that the Hilbert transform of a time signal $x(t)$ is another signal in time domain. If $x(t)$ is real valued, $H[x(t)]$ is also real valued.

As defined in Equation (2.2), an analytic signal is the complex signal whose imaginary part is the Hilbert transform of the real part (Vakman, 1998; Huang and Shen, 2005; Schreier and Scharf, 2010; Feldman, 2011). The analytic signal can be viewed as a vector at the origin of the complex plane having a length $a(t)$ and an angle $\theta(t)$. The projection on the real axis is the original signal $x(t)$ and the projection on the imaginary axis is the Hilbert transform of the original signal. The traditional representation of the analytic signal in its exponential form can be written as (Gabor, 1946; Hartmann, 2004):

$$z(t) = a(t)e^{j\theta(t)} \qquad (3.3)$$

$$a(t) = \sqrt{x^2(t) + \{H[x(t)]\}^2}, \text{ and } \theta(t) = \arctan\left(\frac{H[x(t)]}{x(t)}\right) \qquad (3.4)$$

Here, $a(t)$ is the instantaneous amplitude, and $\theta(t)$ is the phase function. The instantaneous frequency is simply defined as:

$$\omega(t) = \frac{d\theta}{dt} \qquad (3.5)$$

It can also be expressed into:

$$\omega(t) = \frac{x(t)\dot{H}[x(t)] - \dot{x}(t)H[x(t)]}{a^2(t)} \tag{3.6}$$

For any signal, there is a unique value of the instantaneous phase at any given time. For a non-stationary signal whose spectral contents vary with time, the instantaneous frequency plays an important role in the understanding of signal characteristics. The instantaneous amplitude, phase angle and frequency can be expressed by a phasor rotating in the complex plane, as shown in Figure 3.1. A phasor can be viewed as a vector at the original of the complex plane having a length $a(t)$ and a phase angle $\theta(t)$ with an angle speed of $\omega(t)$. The projections on the real and imaginary axle are the original signal and Hilbert transform of the original signal, respectively.
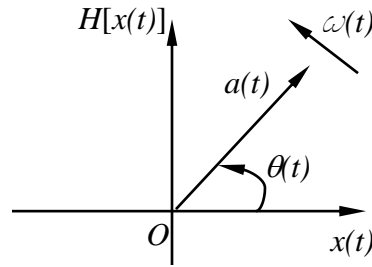
Figure 3.1. Instantaneous Amplitude, Phase Angle and Frequency in Complex Plane

3.2. HILBERT SPECTRAL ANALYSIS

To have a physical meaning for instantaneous frequency, Cohen (1995) presented the Hilbert transform of a mono-component function. In this case, the instantaneous characteristics agree with the intuitive meaning of the signal amplitude, phase and frequency.

3.2.1. Hilbert Spectrum. The original signal can be expressed as the real part $Re[.]$ of an analytic signal:

$$x(t) = Re[a(t)e^{j\int_0^t \omega(\tau)d\tau}] \tag{3.7}$$

The Hilbert spectrum $HS(\omega, t)$ of the signal $x(t)$ is then defined by:

$$HS(\omega, t) = \begin{cases} a(t) & \omega = \omega(t) \\ 0 & \omega \neq \omega(t) \end{cases} \tag{3.8}$$

3.2.2. Hilbert Spectra of Simple Functions. A sine frequency modulated signal $x(t)$ is a frequency modulated cosine signal as defined by:

$$x(t) = \cos[6\pi t + \sin(2\pi t)] \qquad (3.9)$$

The instantaneous frequency in Hz can then be calculated as:

$$f(t) = \frac{1}{2\pi}\frac{d[6\pi t + \sin(2\pi t)]}{dt} = 3 + \cos(2\pi t) \qquad (3.10)$$

The frequency of the original signal ranges from 2 Hz to 4 Hz. The original signal and its Hilbert transform are presented in Figure 3.2. The Fourier spectrum and Hilbert spectrum are compared in Figure 3.3. It can be clearly seen that Fourier spectrum cannot detect the instantaneous frequency modulation over time since it represents the total energy distribution over time in frequency domain. On the other hand, the Hilbert spectrum accurately delineates the instantaneous frequency as a function of time.
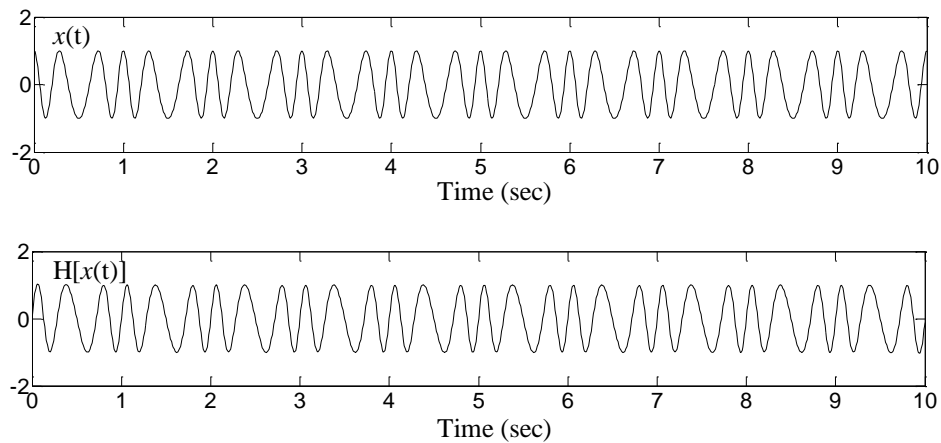
Figure 3.2. Original Signal and Its Hilbert Transform
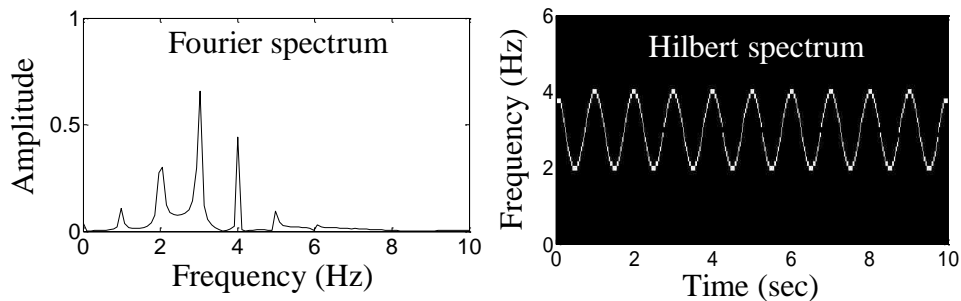
Figure 3.3. Fourier and Hilbert Spectra

Consider another example signal with a sudden drop of frequency as defined by:

$$x(t) = \begin{cases} \cos(6\pi t) & t < 5\ sec \\ \cos(3\pi t) & t \geq 5\ sec \end{cases} \qquad (3.11)$$

The frequency drops from 3 Hz to 1.5 Hz at 5 sec. The original signal and its Hilbert transform are shown in Figure 3.4. The Fourier spectrum and Hilbert spectrum are shown in Figure 3.5. It can be clearly seen from Figure 3.5, the instantaneous frequency can be detected from the Hilbert spectrum of the analytic signal. On the other hand, Fourier spectrum loses the time essence at 5 sec.
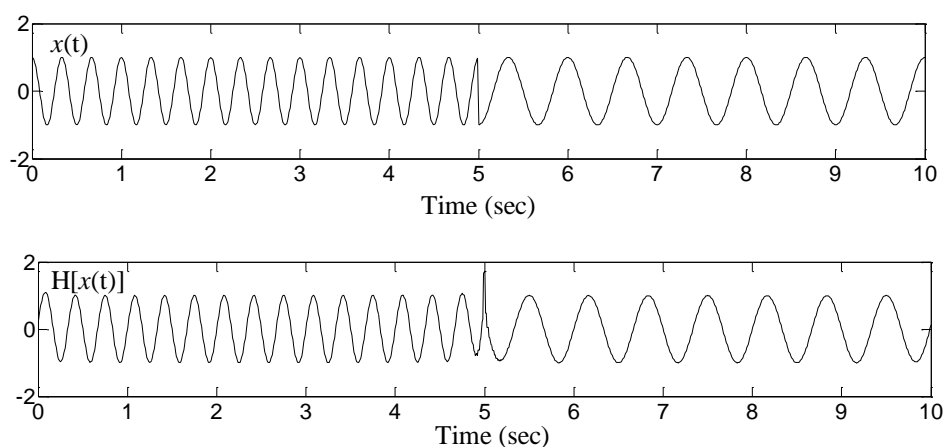
Figure 3.4. Original Signal and Its Hilbert Transform
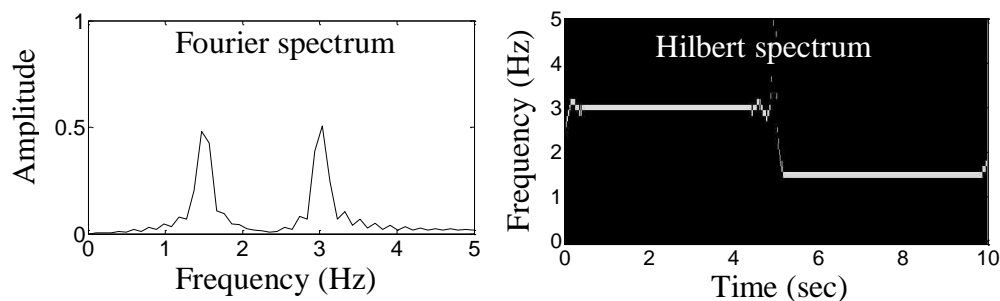
Figure 3.5. Fourier and Hilbert Spectra

3.3. EMD AND HHT

    3.3.1. EMD. A description of the Hilbert transform with emphasis on its multiple mathematical formulations can be found in Hahn (1996). However, the instantaneous frequency defined in Equations (3.5) and (3.6) is applicable to narrowband signals or mono-component functions that have well-behaved Hilbert transform. To decompose a general time series into many narrowband signals, Huang et al. (1998) introduced the EMD process.

    As discussed by Huang et al. (1998, 1999), the EMD method is necessary to deal with data from non-stationary processes associated with nonlinear phenomena and systems. In contrast to the previous methods, EMD is intuitive and adaptive to the original data. The main underlying assumption is that any data series consists of a series of intrinsic modes of vibration. Each intrinsic mode represents a simple oscillation which will have the same number of extrema and zero-crossing points or different number by one only. According to Huang et al. (1998, 1999), a general signal $x(t)$ can be decomposed into a summation of l intrinsic mode functions (IMFs): $c_i(t)$ $(i = 1, 2, ..., l)$ and a residual signal $r(t)$ after EMD process.

$$x(t) = \sum_{i=1}^{l} c_i(t) + r_l(t) \qquad (3.12)$$

    The EMD process decomposes a signal $x(t)$ by the following sifting steps:

(1) Identify all the local maxima and minima of the signal and represent the upper and lower envelopes of the signal by two cubic spline lines.

(2) Compute the average of the upper and lower envelopes, $m_{1k}(t)$, and subtract it from the signal, $h_{1(k-1)}(t)$ $(= x(t)$ when $k=1)$,

$$h_{1k}(t) = h_{1(k-1)}(t) - m_{1k}(t) \qquad (3.13)$$

(3) Repeat Steps (1) and (2) for the remaining function, $h_{1k}(t)$ *(k=1,2,…)*, until it satisfies the two IMF conditions: (a) for the whole dataset, the number of extrema (maxima or minima) and the number of zero-crossings must either equal or differ at most by one; (b) at any point, the average value of the envelopes defined by the local maxima and by the local minima is zero. Then, $h_{1k}(t)$ becomes the first IMF. That is,

$$c_1(t) = h_{1k}(t) \tag{3.14}$$

The first IMF found by Equation (3.14) contains the highest frequency component of the original signal $x(t)$. It can be separated from the original signal, leaving a residue $r_1(t)$ that can be calculated by:

$$r_1(t) = x(t) - c_1(t) \tag{3.15}$$

Since the residue $r_1(t)$ still contains low frequency components in the data series, it can be treated as a new signal and subjected to the same sifting steps as described above. This procedure can be repeated with all the subsequent residues $r_i(t)$:

$$r_i(t) = r_{i-1}(t) - c_i(t) \ (i = 2, \dots, l) \tag{3.16}$$

The EMD process stops when it satisfies the two criteria established by Huang et al. (1999; 2003): either when the residue becomes so small that it is less than the predetermined value of any substantial consequence, or when the residue becomes a monotonic function from which no more IMFs can be extracted. Equation (3.12) is finally obtained by summing up all the terms in Equations (3.15) and (3.16).

As an example to illustrate the EMD process, a frequency modulated signal is considered:

$$x(t) = \cos[3.5\pi t + 0.5\sin(2\pi t)] + \cos[2\pi t + 0.5\sin(\pi t)] \tag{3.17}$$

The exact instantaneous frequencies of the high and low frequency components are: 1.75+0.5cos(2πt) and 1.0+0.25cos(πt) in Hz. The signal was analyzed over a period of 30 sec with a sampling rate of 20 Hz. The original signal and its IMFs are presented in Figure 3.6 and Figure 3.7, respectively. It can be seen from Figure 3.7 that four IMFs are obtained with dominant frequencies decreasing as the EMD process proceeds.
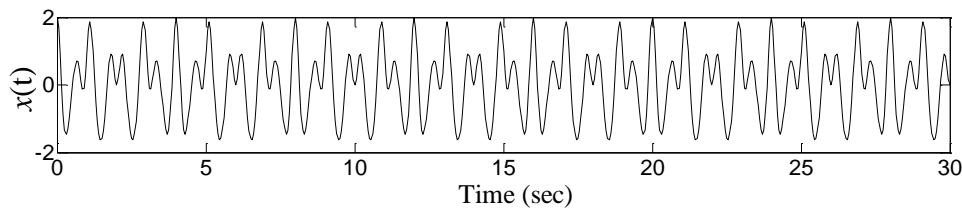
Figure 3.6. Original Signal with Two Cosine Frequency Modulated Components
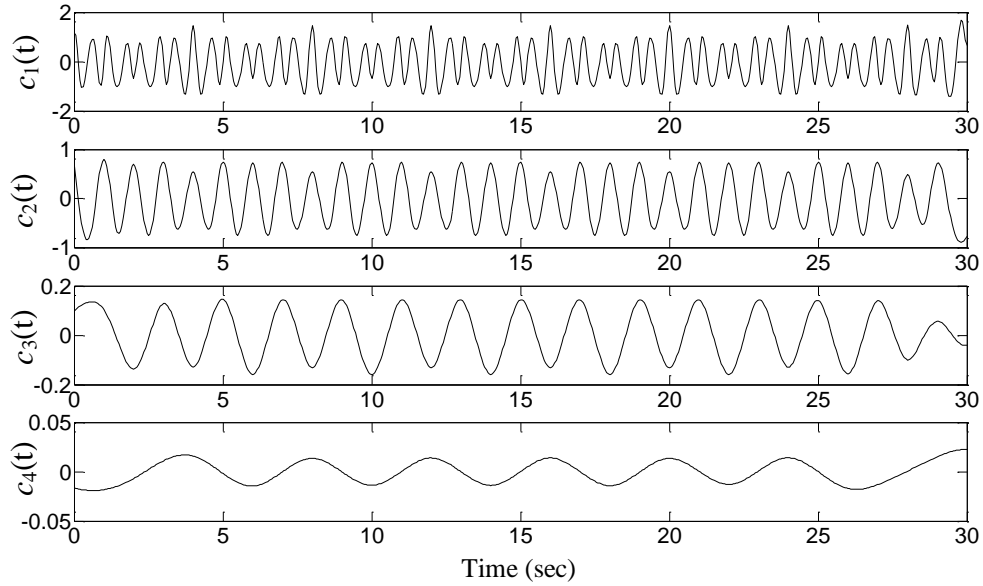
Figure 3.7. First Four IMFs of the Original Signal

3.3.2. HHT. The IMFs decomposed by the EMD process have well-behaved Hilbert transform since each IMF is a narrowband signal and can be considered as a mono-component function. The combination of EMD and Hilbert spectral analysis is often referred to as HHT (Huang et al., 1998; 1999). The Hilbert transform and analytic signal of each IMF can be computed as:

$$H[c_i(t)] = \frac{1}{\pi} PV \int_{-\infty}^{\infty} \frac{c_i(\tau)}{t-\tau} d\tau \tag{3.18}$$

$$z_i(t) = c_i(t) + jH[c_i(t)] = a_i(t)e^{j\theta_i(t)} \tag{3.19}$$

in which $a_i(t) = \sqrt{c_i^2(t) + H^2[c_i(t)]}$ and $\theta_i(t) = arctan\frac{H[c_i(t)]}{c_i(t)}$ are instantaneous amplitude and phase for the ith IMF.

The instantaneous frequency of the ith IMF can be expressed as:

$$\omega_i(t) = \frac{d\theta_i(t)}{dt} = \frac{c_i(t)\dot{H}[c_i(t)] - \dot{c}_i(t)H[c_i(t)]}{a_i^2(t)} \tag{3.20}$$

The ith IMF $c_i(t)$ can thus be expressed into:

$$c_i(t) = Re[a_i(t)e^{j\int_0^t \omega_i(\tau)d\tau}] \tag{3.21}$$

The Hilbert spectrum of the ith IMF $c_i(t)$ is then defined as:

$$HS_i(\omega, t) = \begin{cases} a_i(t) & \omega = \omega_i(t) \\ 0 & \omega \neq \omega_i(t) \end{cases} \tag{3.22}$$

The original signal can also be expressed into the real part of all the analytic functions of the IMFs. That is,

$$x(t) = Re[\sum_{i=1}^{l} a_i(t)e^{j\int_0^t \omega_i(\tau)d\tau}] \tag{3.23}$$

Here, the residue $r_l(t)$ is intentionally left out since it is either negligible or a monotonic function. The energy remained in the residual term represents a mean offset. Finally, the Hilbert spectrum of the original signal is defined by:

$$HS(\omega, t) = \sum_{i=1}^{l} HS_i(\omega, t) \tag{3.24}$$

The entire HHT process can be summarized in a block diagram as shown in Figure 3.8.
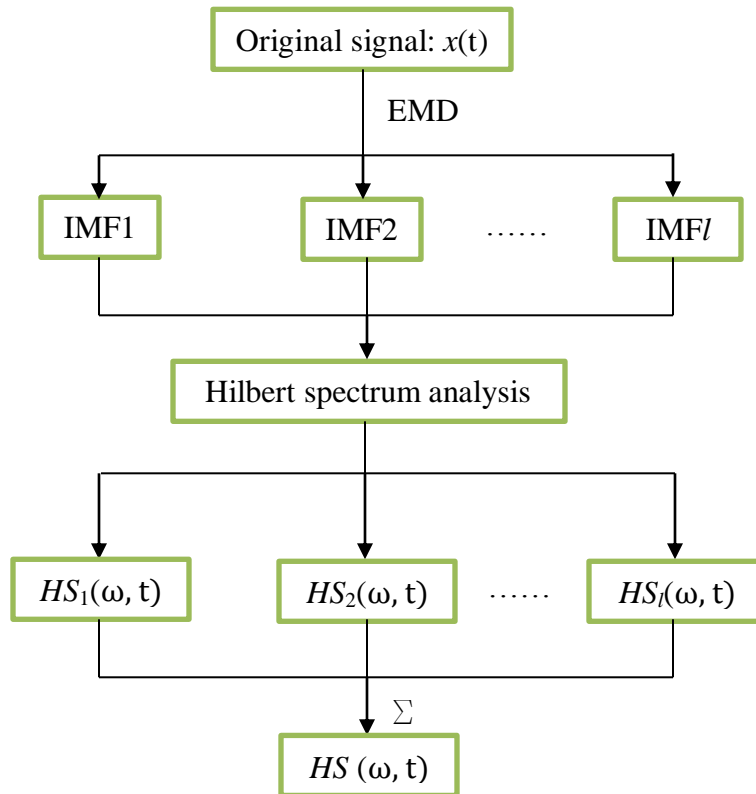
Figure 3.8. Block Diagram of the HHT Process

To illustrate the HHT process, the Hilbert spectrum of the example defined by Equation (3.17) was determined and presented in Figure 3.9. It can be clearly seen from Figure 3.9 that HHT can distribute the energy on the time-frequency plane. The instantaneous frequency of each IMF can be detected from the Hilbert spectrum. There is

no need to introduce spurious harmonics in order to represent non-stationary and nonlinear waveform deformations as the case with Fourier transform and wavelet transform. Therefore, HHT is a superior tool for time-frequency analysis of non-stationary signals particularly when they carry nonlinear features of a physical phenomenon or a mechanical system.
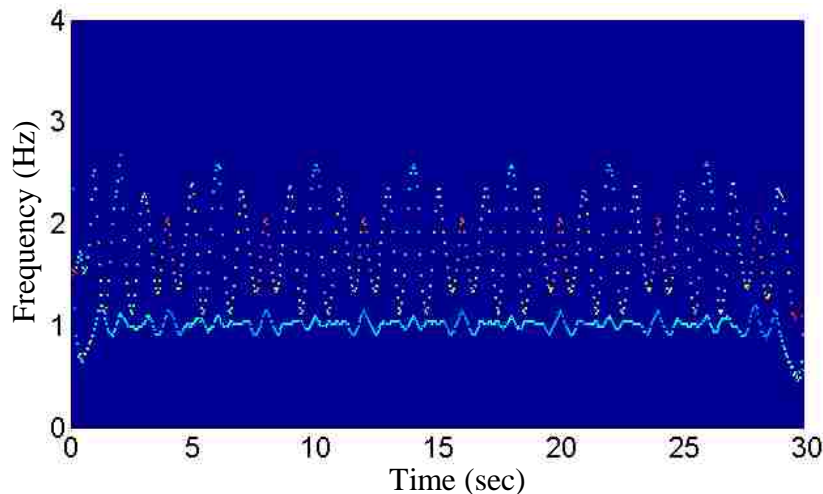
Figure 3.9. Hilbert Spectrum of Two Cosine Frequency Modulated Components

3.3.3. HHT Issues. As pointed out in Section 1.2.3, HHT faces several challenges in some engineering applications. Here, these challenges are elaborated further: (1) unable to decompose signals with closely-spaced frequency components such as wave groups in ocean engineering, free vibration and beating responses in structural and mechanical systems, (2) unable to separate small intermittent fluctuations from a large ocean wave, and (3) unable to track the time-varying change between two modes of vibration for nonlinear structural and mechanical systems.

Attempts have been made by a few investigators to address these challenges. With the HHT method, Chen and Xu (2002) identified the modal parameters of a linear system with closely-spaced modes of vibration. They established the minimum cutoff frequency criteria in the EMD sifting process to ensure that the frequency bandwidths of IMFs be separated. Wang (2005) decomposed a small intermittent fluctuation around a large ocean wave by injecting a known time function into the original signal for two purposes. The first purpose was to introduce a series of additional maxima/minima when the added time

function is rich in high frequency. The second purpose is to down shift the frequency components of the signal using so that the ratio of two close frequencies in a wave group can be increased for a smooth EMD process. Overall, it is still quite a challenge to consistently and reliably identify the properties of structures with closely-spaced modes.

To illustrate the issue with time-varying feature extractions of a nonlinear system, a signal $x(t)$ with two frequency modulated cosine components is considered:

$$x(t) = x_1(t) + x_2(t) \tag{3.25}$$

in which $x_1(t) = \cos[3.5\pi t + 0.5\sin(0.5\pi t)]$ and $x_2(t) = \cos[2.6\pi t + 0.8\sin(0.4\pi t)]$ ($0 \leq t \leq 30$ sec). The frequency of $x_1(t)$ component is $f_1 = 1.75 + 0.125\cos(0.5\pi t)$ Hz, and the frequency of $x_2(t)$ component is $f_2 = 1.3 + 0.16\cos(0.4\pi t)$ Hz. The signal was analyzed with a sampling rate of 20 Hz. The first two IMFs using the conventional EMD are presented in Figure 3.10. It can be clearly seen that the first IMF has two components that are mixed together. The two instantaneous frequencies obtained from Hilbert spectral analysis are presented in Figure 3.11. In comparison with their exact values, also shown in Figure 3.11, the instantaneous frequencies obtained from HHT are incorrect since the two components are not completely separated.
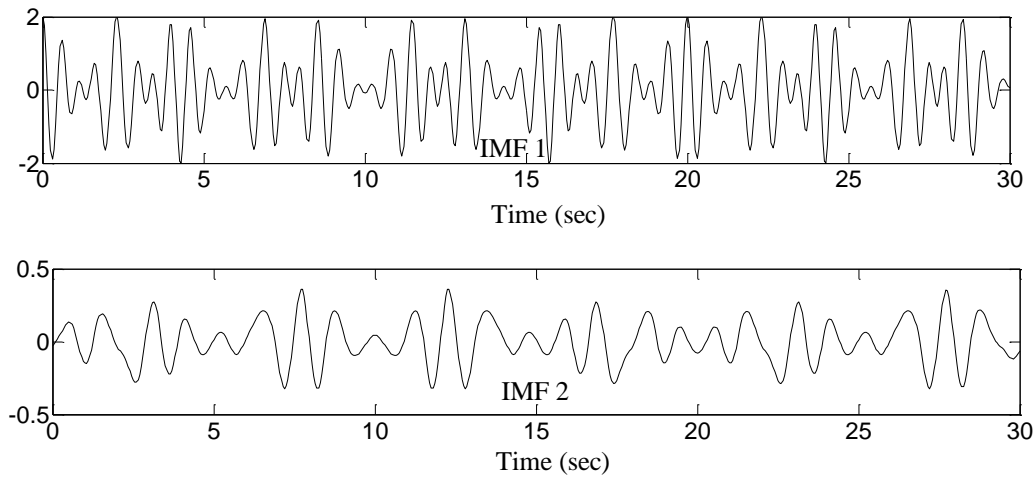
Figure 3.10. The First Two IMFs by EMD
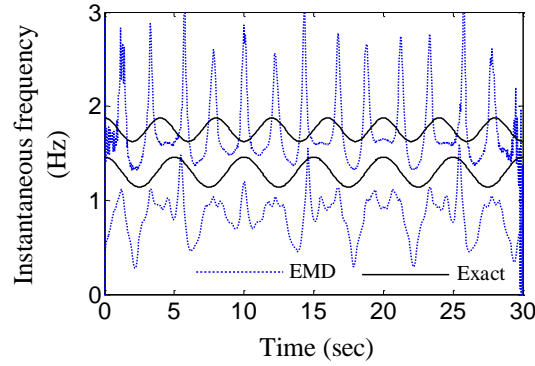
Figure 3.11. Two Instantaneous Frequencies by HHT

3.4. HILBERT VIBRATION DECOMPOSITION

Another technique called Hilbert vibration decomposition (HVD) was developed by Feldman (2006; 2011) for decomposition of non-stationary and multicomponent dynamic signals. Its main idea is to decompose a signal into a sum of components with slowly-varying instantaneous amplitudes and frequencies:

$$x(t) = \sum_i a_i(t)\cos(\int \omega_i(t)dt) \tag{3.26}$$

where $a_i(t)$ and $\omega_i(t)$ are the instantaneous amplitude and instantaneous frequency of the ith component. Each mono-component $a_i(t)\cos(\int \omega_i(t)dt)$ is an intrinsic mode of the original signal with a simple oscillatory waveform. If only one term is needed in Equation (3.26), $x(t)$ is called a mono-component signal. Otherwise, it is referred to as a multi-component signal with a broadband spectrum.

3.4.1. Instantaneous Frequency of the Largest Energy Component. Consider a multi-component signal with two harmonics as described by Equation (3.26). Its analytic function can be derived as:

$$z(t) = a_1(t)e^{j\int_0^t \omega_1(\tau)d\tau} + a_2(t)e^{j\int_0^t \omega_2(\tau)d\tau} = a(t)e^{j\int_0^t \omega(\tau)d\tau} \tag{3.27}$$

The instantaneous amplitude $a(t)$ and instantaneous frequency $\omega(t)$ of the analytic signal can be related to individual component parameters by:

$$a(t) = \{a_1^2(t) + a_2^2(t) + 2a_1(t)a_2(t)\cos\{\int_0^t [\omega_2(\tau) - \omega_1(\tau)]d\tau\}\}^{1/2} \tag{3.28}$$

$$\omega(\text{t}) = \omega_1(\text{t}) + \frac{[\omega_2(\text{t})-\omega_1(\text{t})]\left[a_2^2(\text{t})+2a_1(t)a_2(t)\cos\left\{\int_0^t[\omega_2(\tau)-\omega_1(\tau)]d\tau\right\}\right]}{a^2(t)} +$$

$$\frac{[a_1(t)a_2'(t)-a_1'(t)a_2(t)]sin\left\{\int_0^t[\omega_2(\tau)-\omega_1(\tau)]d\tau\right\}}{a^2(t)} \tag{3.29}$$

The signal envelope a(t) consists of a slowly varying part, including the sum of the squared of individual component amplitudes, and a rapidly varying (oscillating) part. The instantaneous frequency $\omega(t)$ also has two parts: a slowly varying part ω_1 and a rapidly varying asymmetrical oscillating part. The rapidly oscillating part of the instantaneous frequency has an important feature (Vakman, 1998; Feldman, 2006; 2010). When the derivatives of both $a_1(t)$ and $a_2(t)$ are negligible and $a_1(t)$ is significantly larger than $a_2(t)$, the integration of the oscillatory part of the instantaneous frequency in one cycle related to the frequency difference of two components is approximately equal to zero. Therefore, the instantaneous frequency of the largest energy component can be extracted by a low-pass filter. For a more general case of three and more quasi-harmonics in the signal, the instantaneous frequency has a more complicated form. However, lowpass filtering can still be used to extract the instantaneous frequency of the largest energy component.

3.4.2. Envelope of the Largest Energy Component. Once the instantaneous frequency is extracted, the envelope of the largest energy component can be readily estimated by a well-known technique (Fink, 1975) as called differently in various applications: synchronous detection, coherent demodulation, and lock-in amplifier detection. The essence of this technique is to extract the amplitude of a signal with a known frequency by multiplying the initial signal by two reference signals that are exactly 90° out of phase with one another. For convenience, the two reference signals are selected to be $cos(\int \omega_r(t)dt)$ and $sin(\int \omega_r(t)dt)$ whose frequency is exactly the same as that of the rth component of the original signal.

When the original signal, Equation (3.26) with an explicit phase angle φ_i for each component, is multiplied by the reference signal $cos(\int \omega_r(t)dt)$, the combined signal is equal to:

$$x_{i=r}(t) = \sum_i \{a_i(t)\cos[\int \omega_i(t)dt + \varphi_i]\}\cos[\int \omega_r(t)dt]$$

$$\approx \frac{1}{2}a_r(t)\{\cos(\varphi_r) + \cos[\int 2\omega_r(t)dt + \varphi_i]\} \qquad (3.30)$$

in which, φ_i is the initial phase angle of the r component. Similarly, when the initial signal is multiplied by the reference signal $sin(\int \omega_r(t)dt)$, the combined signal becomes,

$$\tilde{x}_{i=r}(t) \approx \frac{1}{2}a_r(t)\{-\sin(\varphi_r) + sin[\int 2\omega_r(t)dt + \varphi_r]\} \qquad (3.31)$$

Each of the obtained parts consists of a slowly varying function, which includes the amplitude and the initial phase, and a rapidly oscillatory part. Therefore, a low-pass filter can be used to extract the slowly varying function. The amplitudes of the slowly varying parts in Equations (3.30) and (3.31) can then be written as:

$$a_{i=r}(t) = \frac{1}{2}a_r(t)\cos(\varphi_r) \text{ and } \tilde{a}_{i=r}(t) = \frac{1}{2}a_r(t)\sin(\varphi_r) \qquad (3.32)$$

Finally, the amplitude of the largest energy component of the original signal can be expressed with:

$$a_r(t) = \sqrt{[a_{i=r}(t)]^2 + [\tilde{a}_{i=r}(t)]^2} \qquad (3.33)$$

Once fully extracted, the largest energy component can be subtracted from the original signal and the HVD process can be repeated until all of the individual components are separated. The HVD process can be represented by a block diagram as illustrated in Figure 3.12.
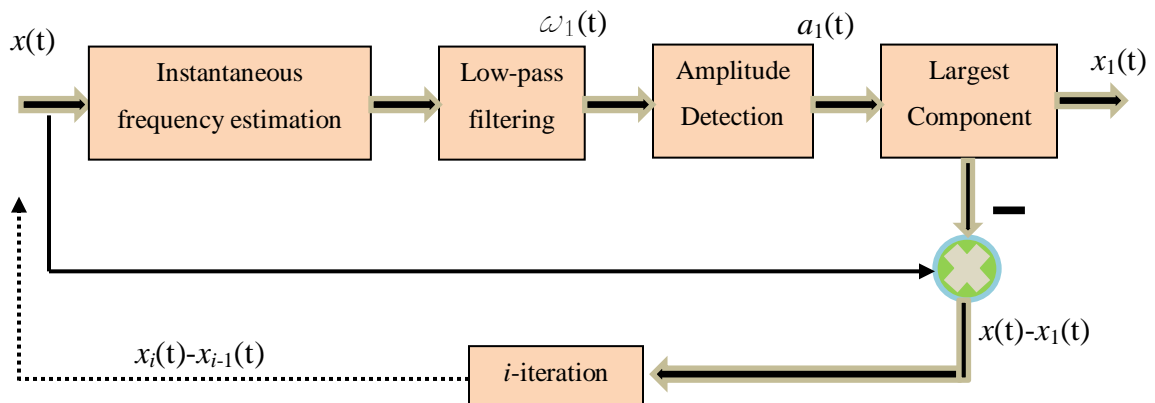
Figure 3.12. Block Diagram of Hilbert Vibration Decomposition

3.5. BEDROSIAN THEOREM

3.5.1. Bedrosian Theorem Derivation. Bedrosian theorem is also called the product theorem of Hilbert transform. Discovered by Bedrosian (1962), it can be stated as follows:

Let $x(t)$ and $y(t)$ denote two generally complex functions in $L^2(-\infty, \infty)$ of the real variable t. If

- (a) The Fourier transform $\hat{x}(u)$ of $x(t)$ vanishes for $|u| > a$, and the Fourier transform $\hat{y}(v)$ of $y(t)$ vanishes for $|v| < a$ where a is an arbitrary positive constant, or

- (b) $x(t)$ and $y(t)$ are analytic (i.e., their real and imaginary parts are Hilbert pairs),

the Hilbert transform of the product of $x(t)$ and $y(t)$ is given by:

$$H[x(t)y(t)] = x(t)H[y(t)] \tag{3.34}$$

The theorem can be proved by examining the inverse Fourier transform of both sides of Equation (3.34). The inverse Fourier transform of the product $x(t)y(t)$ can be written as:

$$x(t)y(t) = \frac{1}{(2\pi)^2} \int_{-\infty}^{\infty} du \int_{-\infty}^{\infty} dv\, \hat{x}(u)\hat{y}(v)e^{j(u+v)t} \tag{3.35}$$

Applying Hilbert transform on both sides of Equation (3.35) yields:

$$H[x(t)y(t)] = \frac{1}{(2\pi)^2} \int_{-\infty}^{\infty} du \int_{-\infty}^{\infty} dv\, \hat{x}(u)\hat{y}(v)H[e^{j(u+v)t}] \tag{3.36}$$

The Hilbert transform of $e^{j(u+v)t}$ is:

$$H[e^{j(u+v)t}] = jsgn(u + v)e^{j(u+v)t} \tag{3.37}$$

where $sgn(.)$ is a sign function. Therefore, substituting Equation (3.37) into Equation (3.36) gives:

$$H[x(t)y(t)] = \frac{1}{(2\pi)^2} \int_{-\infty}^{\infty} du \int_{-\infty}^{\infty} dv\, \hat{x}(u)\hat{y}(v)jsgn(u + v)e^{j(u+v)t} \tag{3.38}$$

Figure 3.13 illustrates the integration plane. Under the first condition of the theorem, the product $\hat{x}(u)\hat{y}(v)$ is non-vanishing only in the shaded region in Figure 3.13. In this case, $sgn(u + v) = sgn(v)$. Equation (3.38) can then be expressed into:

$$H[x(t)y(t)] = \frac{1}{(2\pi)^2} \int_{-\infty}^{\infty} du \int_{-\infty}^{\infty} dv \, \hat{x}(u)\hat{y}(v)jsgn(v)e^{j(u+v)t}$$

$$= x(t)\frac{1}{2\pi}\int_{-\infty}^{\infty} dv \, \hat{y}(v)jsgn(v)e^{jvt} = x(t)H[(y(t)] \qquad (3.39)$$
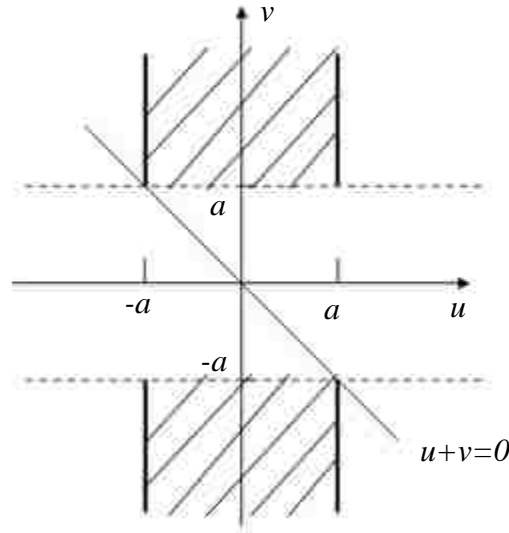
Figure 3.13. Integration Region

3.5.2. Illustrative Examples. To illustrate accuracy of the Bedrosian theory, several functions are tested and taken as examples.

Let $x_0(t) = \sin(2\pi f_0 t)$, $f_0 = 5$ Hz, and $0 \le t \le 10$ sec., and $x_i(t)$ ($i = 1, 2, ..., 6$) be:

$$x_1(t) = \begin{cases} 1, & 0 \le t \le 4 \text{ sec} \\ 0.5, & 4 \le t \le 10 \text{ sec} \end{cases} \qquad (3.40)$$

$$x_2(t) = \begin{cases} 1, & 0 \le t \le 4 \text{ sec} \\ 1.5 - t/8, & 4 \le t \le 8 \text{ sec} \\ 0.5, & 8 \le t \le 10 \text{ sec} \end{cases} \qquad (3.41)$$

$$x_i(t) = \frac{\cos(2\pi f_i t)+1}{2} \ (i = 3, 4, 5, 6)$$

$$f_3 = 1 \text{ Hz}, f_4 = 2 \text{ Hz}, \ f_5 = 5 \text{ Hz}, \text{and } f_6 = 10 \text{ Hz} \qquad (3.42)$$

Figure 3.14 compares the Hilbert transforms of the product $x_i(t)x_0(t)$ ($i = 1, 2, ..., 6$) evaluated by its definition and the Bedrosian theorem. For $i \le 4$, the

frequency component of $x_i(t)$ is less than that of $x_0(t)$ the frequency of $x_i(t)$ that of $x_0(t)$

(a) Bedrosian theory   (b) Exact signal
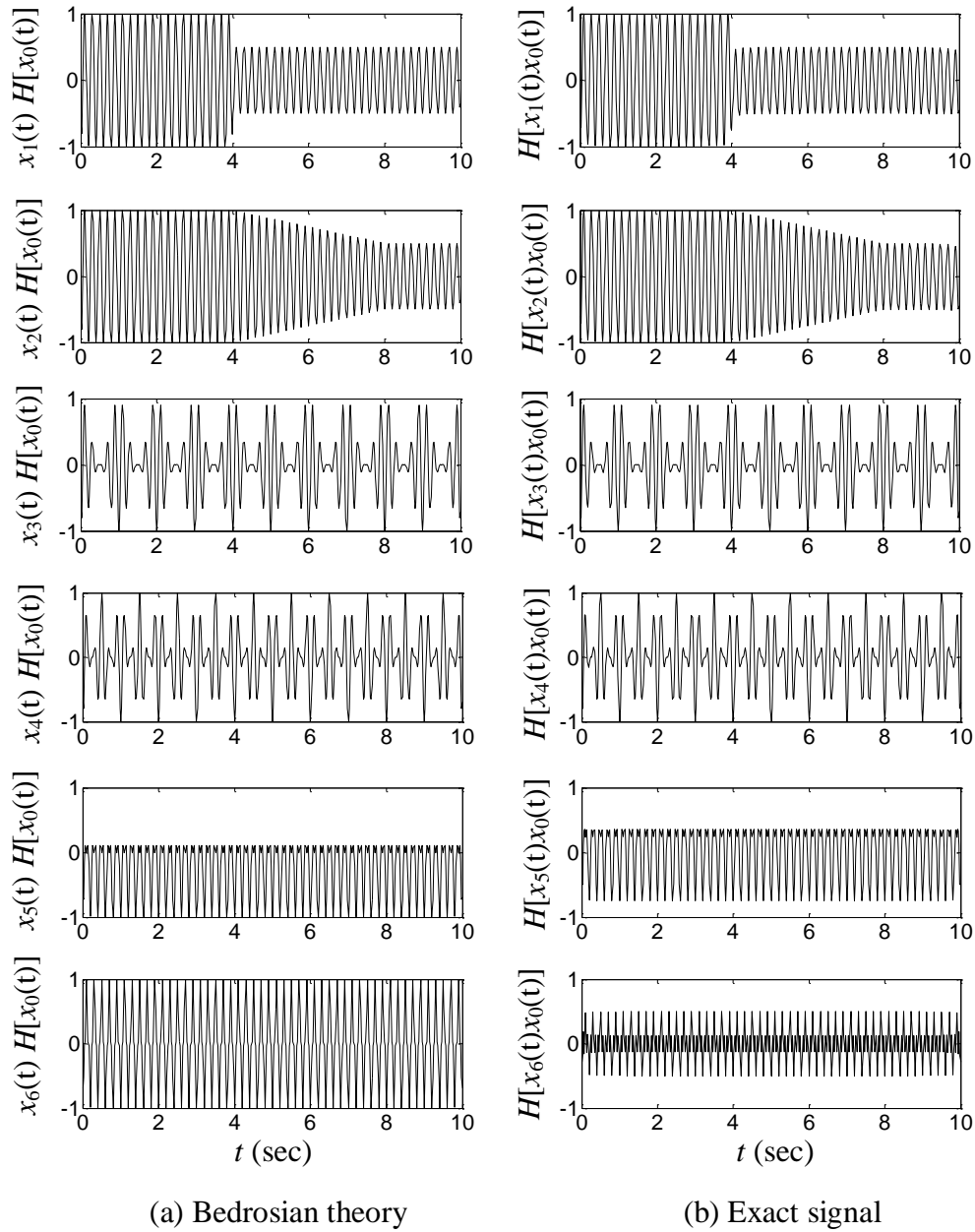
Figure 3.14. Hilbert Transform of Product Signals

3.6. A NEW SIGNAL DECOMPOSITION THEOREM

A new signal decomposition theorem based on Hilbert transform of a harmonics multiplicative time series was recently discovered by Chen and Wang (2011). In structural health monitoring, this theorem leads to the development of analytical mode decomposition (AMD) for stationary and non-stationary dynamic responses. Following is a presentation of the theorem and its proof. For simplicity and clarity, this section is focused on signals with time-invariant frequencies.

3.6.1. AMD Theorem and Proof. Let $x(t)$ denote a real time series of n significant frequency components $(\omega_1, \omega_2, \cdots, \omega_n$; all positive and invariant over time) in $L^2(-\infty, +\infty)$ of the real time variable t. It can be decomposed into n signals $x_i^{(d)}(t)$ *(i=1,2,...,n)* whose Fourier spectra are equal to $\hat{X}(\omega)$ over n mutually exclusive frequency ranges $(|\omega| < \omega_{b1})$, $(\omega_{b1} < |\omega| < \omega_{b2})$, $\cdots$, $(\omega_{b(n-2)} < |\omega| < \omega_{b(n-1)})$, and $(\omega_{b(n-1)} < |\omega|)$. That is,

$$x(t) = \sum_{i=1}^{n} x_i^{(d)}(t) \tag{3.43}$$

Here, $\hat{X}(\omega)$ is the Fourier transform of $x(t)$, ω represents a frequency variable, and $\omega_{bi} \in (\omega_i, \omega_{i+1})$ $(i = 1,2,\cdots,n-1)$ are *n-1* bisecting frequencies. Each signal has a narrow bandwidth in the frequency domain and can be determined by:

$$x_1^{(d)} = s_1(t), \cdots, x_i^{(d)}(t) = s_i(t) - s_{i-1}(t), \cdots, x_n^{(d)}(t) = x(t) - s_{n-1}(t) \tag{3.44}$$

$$s_i(t) = \sin(\omega_{bi}t) H[x(t)cos(\omega_{bi}t)] - \cos(\omega_{bi}t) H[x(t) \sin(\omega_{bi}t)]$$

$$(i = 1, 2, \cdots, n-1) \tag{3.45}$$

The AMD theorem is proven in two steps. The first step is to split a time series into two signals whose Fourier spectra are non-vanishing over two mutually exclusive frequency ranges about a bisecting frequency. The second step is to apply the bisecting process to derive the decomposed signals $x_i^{(d)}(t)$ *(i=1,2,...,n)* as stated in the theorem.

A time series can generally be expressed into a summation of two signals:

$$x(t) = s_1(t) + \bar{s}_1(t) \tag{3.46}$$

whose Fourier transforms $\hat{s}_1(\omega)$ and $\hat{\bar{s}}_1(\omega)$ vanish for $|\omega| > \omega_b$ and $|\omega| < \omega_b$, respectively. Here, ω_b is an arbitrary positive value referred to as the bisecting frequency.

Due to the Parseval's theorem in Fourier transforms and the fact that $\hat{s}_1(\omega)$ and $\hat{\bar{s}}_1(\omega)$ are equal to $\hat{X}(\omega)$ over two mutually exclusive frequency ranges of $(-\infty, \omega_b)$ and $(\omega_b, +\infty)$, respectively:

$$\int_{-\infty}^{+\infty} |s_1(t)|^2\, dt = \int_{-\infty}^{+\infty} |\hat{s}_1(\omega)|^2\, d\omega/2\pi \leq \int_{-\infty}^{+\infty} \left|\hat{X}(\omega)\right|^2 d\omega/2\pi = \int_{-\infty}^{+\infty} |x(t)|^2\, dt < \infty$$

(3.47)

$$\int_{-\infty}^{+\infty} |\bar{s}_1(t)|^2\, dt = \int_{-\infty}^{+\infty} |\hat{\bar{s}}_1(\omega)|^2\, d\omega/2\pi \leq \int_{-\infty}^{+\infty} \left|\hat{X}(\omega)\right|^2 d\omega/2\pi = \int_{-\infty}^{+\infty} |x(t)|^2\, dt < \infty$$

(3.48)

Therefore, both $s_1(t)$ and $\bar{s}_1(t)$ are real functions in $L^2(-\infty, +\infty)$.

Let $s_c(t) = \cos(\omega_b t)$ and $s_s(t) = \sin(\omega_b t)$. The Hilbert transform of $s_k(t)x(t)$ ($k=c, s$) can be expressed into:

$$H[s_k(t)x(t)] = H[s_k(t)s_1(t)] + H[s_k(t)\bar{s}_1(t)]$$

(3.49)

Since the Fourier transforms of $s_c(t)$ and $s_s(t)$ vanish at all frequencies except for $|\omega| = \omega_b$, they are non-vanishing over mutually exclusive frequency ranges with the Fourier transforms $s_1(t)$ and $\bar{s}_1(t)$. The first term on the right-hand side of Equation (3.49) has a low-pass function of $s_1(t)$ and a high-pass function of $s_k(t)$. The second term has a low-pass function of $s_k(t)$ and a high-pass function of $\bar{s}_1(t)$. According to the Bedrosian theorem, Equation (3.49) can be rewritten as:

$$H[s_k(t)x(t)] = s_1(t)H[s_k(t)] + s_k(t)H[\bar{s}_1(t)]$$

(3.50)

When k is set to c and s, respectively, two algebraic equations for two unknowns, $s_1(t)$ and $H[\bar{s}_1(t)]$, can be obtained, leading to

$$s_1(t) = \frac{s_s(t)H[s_c(t)x(t)] - s_c(t)H[s_s(t)x(t)]}{s_s(t)H[s_c(t)] - s_c(t)H[s_s(t)]}$$

(3.51)

$$H[\bar{s}_1(t)] = \frac{H[s_c(t)]H[s_s(t)x(t)] - H[s_s(t)]H[s_c(t)x(t)]}{s_s(t)H[s_c(t)] - s_c(t)H[s_s(t)]}$$

(3.52)

The Hilbert transforms of $s_c(t)$ and $s_s(t)$ can be expressed into:

$$H[s_c(t)] = \sin(\omega_b t) \text{ and } H[s_s(t)] = -\cos(\omega_b t)$$

(3.53)

They meet the following relation:

$$s_s(t)H[s_c(t)] - s_c(t)H[s_s(t)] = 1$$

(3.54)

Equations (3.51) and (3.52) then become:

$$s_1(t) = \sin(\omega_b t)\, H[x(t)cos(\omega_b t)] - \cos(\omega_b t)\, H[x(t)\sin(\omega_b t)]$$

(3.55)

$$H[\bar{s}_1(t)] = \sin(\omega_b t)\, H[x(t)sin(\omega_b t)] + \cos(\omega_b t)\, H[x(t)\cos(\omega_b t)]$$

(3.56)

The signal $\bar{s}_1(t)$ and the Hilbert transform of $s_1(t)$ can be derived from Equation (3.46) and expressed into:

$$\bar{s}_1(t) = x(t) - s_1(t) \tag{3.57}$$

$$H[s_1(t)] = H[x(t)] - H[\bar{s}_1(t)] \tag{3.58}$$

By selecting $\omega_b = \omega_{b1}, \omega_{b2}, \cdots, \omega_{b(n-1)}$, a time series can be bisected into two signals in various ways as follows:

$$x(t) = s_1(t) + \bar{s}_1(t) = s_2(t) + \bar{s}_2(t) = \cdots = s_{n-1}(t) + \bar{s}_{n-1}(t) \tag{3.59}$$

Each decomposed signal can be expressed into:

$$x_1^{(d)} = s_1(t), x_i^{(d)}(t) = s_i(t) - s_{i-1}(t), (i = 2, 3, \cdots, n - 1), x_n^{(d)}(t) = \bar{s}_{n-1}(t) \tag{3.60}$$

in which $s_i(t)$ $(i = 1, 2, \cdots, n - 1)$ and $\bar{s}_{n-1}(t)$ can be evaluated by using Equation (3.55) and Equation (3.57) with $\omega_b = \omega_{bi}$ and $\omega_{b(n-1)}$, respectively, and the AMD theorem is proven.

3.6.2. Lowpass and Bandpass Filter Based on AMD Theorem. The component in a signal with frequency less than the bisecting frequency can be analytically extracted by Equation (3.45). This process operates like a lowpass filter, which requires only the Hilbert transform and the bisecting frequency. The block diagram of such a heterodyne-like filter is shown in Figure 3.15. With multiple steps of bisecting, an original time series with multiple closely-spaced frequency components can be decomposed into many signals, each component with frequency between two adjacent bisecting frequencies. This process operates like a bandpass filter. The diagram of such a bandpass filter is presented in Figure 3.16.
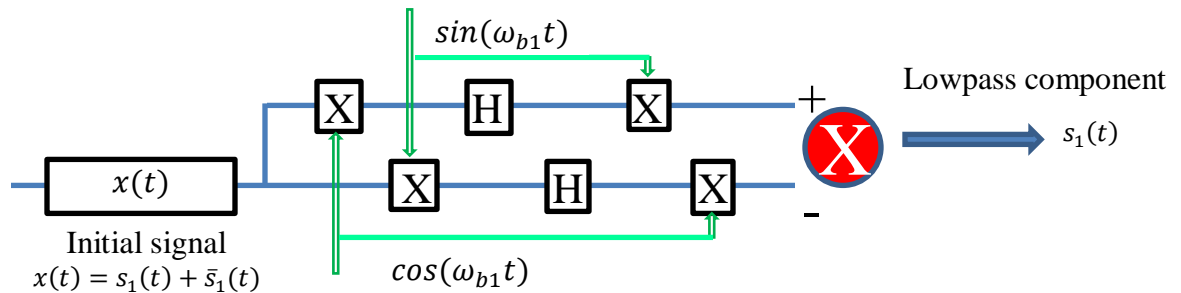
Figure 3.15. Block Diagram of a Lowpass Filter with a Bisecting Frequency ω_{b1}
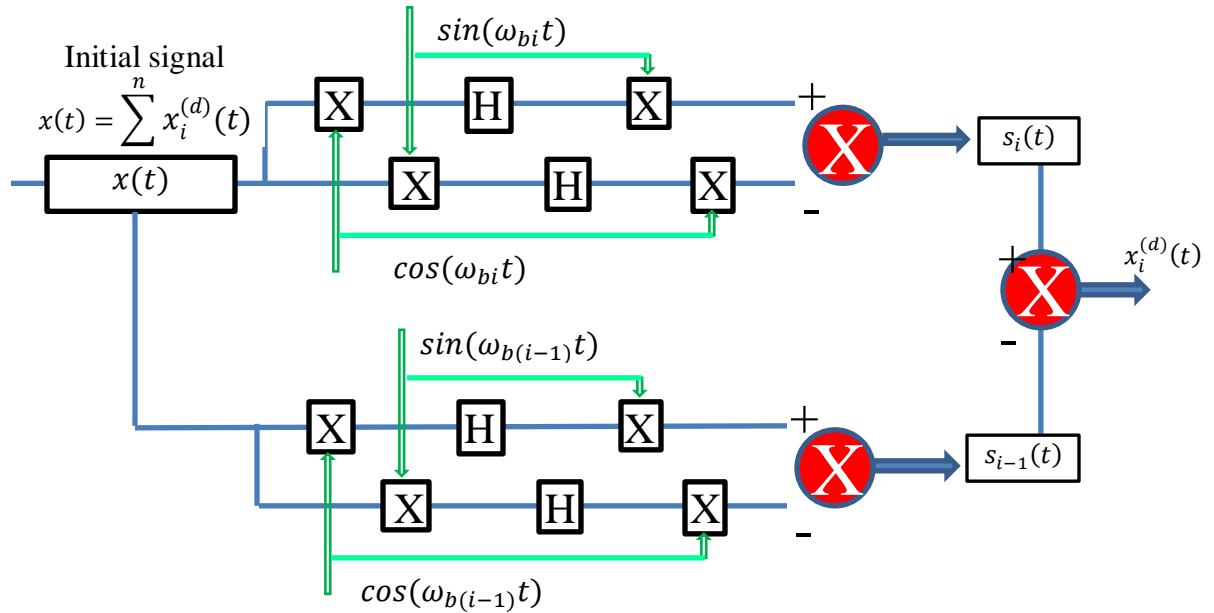
Figure 3.16. Block Diagram of a Bandpass Filter with Two Bisecting Frequencies: $\omega_{b(i-1)}$ and ω_{bi}

3.6.3. Comparison with a Frequency Filtering Technique. The signal decomposition theorem is developed to split a time series into *n* signals whose frequency contents are mutually exclusive about *n-1* bisecting frequencies. This process appears somewhat similar to a bandpass filtering technique with multiple rectangular windows in the frequency domain. Therefore, a comparative study was conducted to understand their difference. For fair comparisons, the cutoff frequencies in frequency bandpass filters were set to equal the bisecting frequencies used with the AMD method.

A time series with three close frequency components was considered: $x(t) = x_1(t) + x_2(t) + x_3(t)$. The three frequencies were set to $f_1 = 1.1$ Hz, $f_2 = 1.2$ Hz, and $f_3 = 1.3$ Hz with a frequency spacing of 0.1 Hz. A time step of 0.02 sec was used in numerical simulations. The three individual components were selected as: $x_1(t) = \cos(2\pi f_1 t)$, $x_2(t) = \cos(2\pi f_2 t + \pi/6)$, and $x_3(t) = \cos(2\pi f_3 t)$. The decomposed signals obtained following the AMD procedure and their Fourier transforms (normalized by the number of data points in the time series) are presented in Figures. 3.17 and 3.18, respectively.
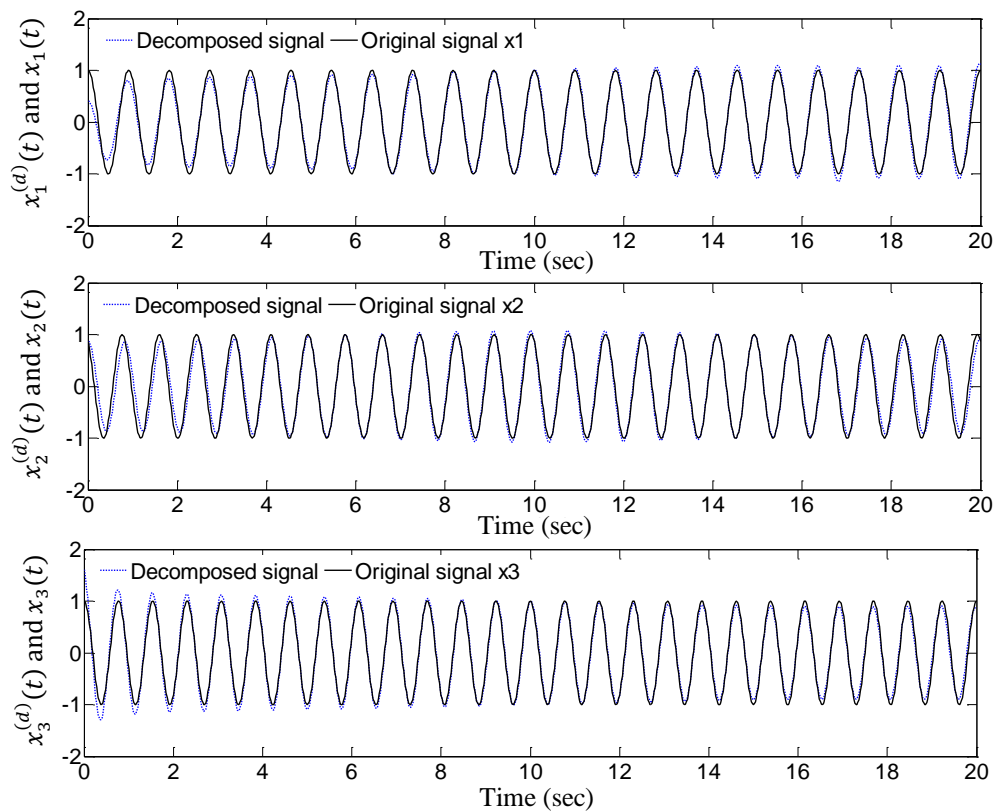
Figure 3.17. Decomposed Signals by AMD
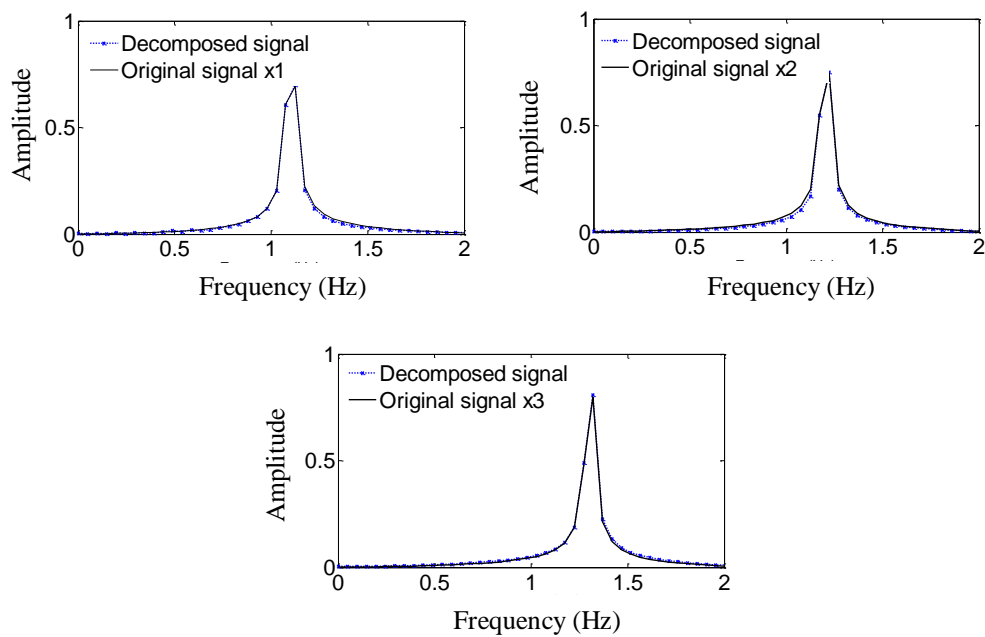
Figure 3.18. Fourier Spectra of the Decomposed Signals by AMD

It can be seen from Figures. 3.17 and 3.18 that the decomposed signals are in excellent agreement with the exact signals both in time and frequency domains. The AMD method can accurately separate the three components. Note that a slight difference observed at the beginning and end of the time series is due to the end effect of Hilbert transforms as a result of a finite time series. In this study, the mirror image technique about the first or the last maxima/minima of the original signal was used to minimize the end effect in the numerical integration of Hilbert transforms (Huang et al., 2003)

Figure 3.19 compares the decomposed signals of the time series used in Figure 3.17 by bandpass filtering with the original signals with $\Delta f = 0.05$ Hz. It can be clearly seen from Figure 3.19 that the decomposed signals are significantly weaker than the original signals at the ends of signal. In comparison with Figure 3.17, the bandpass filtering technique is considerably less accurate than the AMD method. The transient oscillations at the beginning and end of the signals due to filtering are substantially more significant than those by the AMD method.

With bandpass filtering, a time series of finite length in engineering applications is first transformed into the frequency domain (Fourier transform). In the time domain, the finite length signal is equivalent to the application of a rectangular window into the infinite long time series. After having been multiplied by a rectangular window in the frequency domain, the Fourier spectrum is transformed back to the time domain (inverse Fourier transform). Both transforms introduce numerical errors in two ways: signal modification by windowing and end effect due to sharp edges or brick walls of the windows. Applying a rectangular window in the frequency/time domain is equivalent to execute a convolution between a sinc function and the time/frequency function over an infinite range. This means that the time/frequency function is now a distorted signal as indicated in Figure 3.19. The brick wall with the rectangular window or the sudden change of frequency corresponds to an infinitely long oscillation in the time domain that cannot be represented accurately with the Fast Fourier Transform and its inverse transform. An improper selection of the beginning and end of a signal could introduce an artificial oscillation as illustrated in Figure 3.19. In the case of splitting closely-spaced frequency components, there is no space to soften the brick wall by designing two smooth edges of a window.

On the other hand, the AMD method splits a time series into two signals in two mutually exclusive frequency ranges that extend to the negative and positive infinity, respectively. It only involves two Hilbert transforms that were evaluated with the inverse Fourier transforms of one-sided spectra without rectangular windows. Therefore, the problems associated with frequency bandpass filtering don't exist with the AMD method.
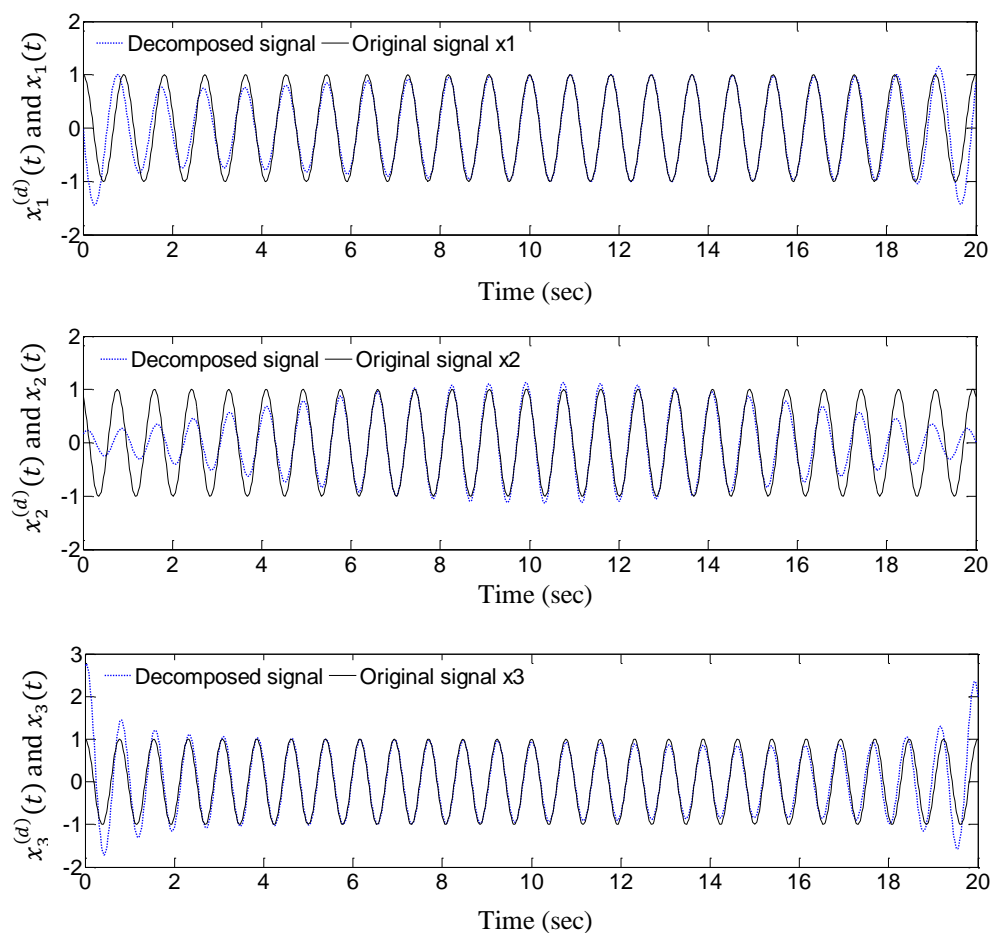
Figure 3.19. Decomposed Signals by Frequency Filtering and Exact Signals

3.7. AMD FOR NONSTATIONARY SIGNALS

In this section, the AMD Theorem is extended to the processing of non-stationary signals with time-varying frequencies. For simplicity, frequency modulated signals are considered here. The goal is to decompose each frequency modulated individual component from a general non-stationary time series by properly selecting two time-

varying bisecting frequencies that cover the component frequency at any time instant. The essence of the AMD theorem for non-stationary signal processing is basically an adaptive bandpass filter, whose bandpass frequency depends on the frequency characteristics of the signal over time.

3.7.1. AMD Theorem for Non-stationary Signals. For a non-stationary time series, particularly associated with nonlinear dynamic systems, the dominant frequencies can vary with time. Depending upon the dynamic characteristics of an engineering system, they may overlap over the duration of the signal as illustrated in Figure 3.20 for ω_{1t} and ω_{2t}. Here the subscript t signifies a parameter in time domain. Specifically, ω_{2t} is always larger than ω_{1t} at each time instant but can be smaller than ω_{1t} if they are compared at two different times. To successfully separate the frequency components, time-varying bisecting frequencies must be used.
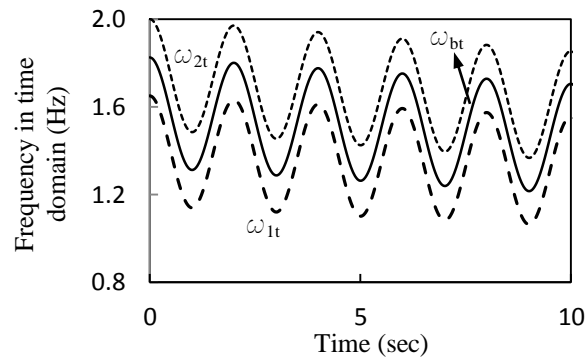
Figure 3.20. Illustration on Varying Bisecting Frequencies in Time Domain

The AMD theorem presented in Section 3.6 was proven in two steps: bisecting of a time series and its decomposition by repeating the bisecting process. The second step is the same both for stationary and non-stationary signals. Following is a brief derivation for the first step with necessary modifications.

Let $x(t)$ denote a real time series in $L^2(-\infty, +\infty)$ of the real time variable t. Consider a time-varying bisecting frequency of $\omega_{bt}(t)$, as illustrated in Figure 3.20, for the decomposition of the time series into a lowpass and a highpass component:

$$x(t) = s_1(t) + \bar{s}_1(t). \tag{3.61}$$

For clarity, $\omega_{bt}(t)$ is referred to as the bisecting frequency in time domain as indicated by its subscript t. Corresponding to the time-varying bisecting frequency, we can define a phase angle in phase domain by:

$$\theta = \int_0^t \omega_{bt}(\tau)d\tau = f(t) \tag{3.62}$$

Since $\omega_{bt}(t) > 0$ at all times, Equation (3.62) is a non-decreasing function. In this case, the phase and time domains are mapped by a unique one-to-one relation. Therefore, the time variable can be expressed into a function of the phase angle. The original time series can then be written as a function of phase angle, $x(\theta)$, which also belongs to L^2($-\infty$, $+\infty$) of the real phase angle θ because:

$$\int_{-\infty}^{+\infty}|x(\theta)|^2\,d\theta = \int_{-\infty}^{+\infty}|x(t)|^2\omega_{bt}(t)dt \le \omega_{bt,max}\int_{-\infty}^{+\infty}|x(t)|^2\,dt \le \infty \tag{3.63}$$

in which $\omega_{bt,max}$ represents the maximum bisecting frequency in time domain that is less than the maximum natural frequency (finite value) of an engineering system. In this case, the AMD theorem is directly applicable to $x(\theta)$ if a bisecting frequency in phase domain is defined and designated as $\omega_{b\theta}$ as illustrated in Figure 3.21. That is, $x(\theta)$ can be decomposed into two components whose Fourier spectra are equal to $\hat{X}(\omega_{\theta})$ over two mutually exclusive frequency ranges $(|\omega_{\theta}| < \omega_{b\theta})$ and $(\omega_{b\theta} < |\omega_{\theta}|)$. The lowpass component can then be evaluated by:

$$s_1(\theta) = \sin(\omega_{b\theta}\theta)\,H[x(\theta)cos(\omega_{b\theta}\theta)] - \cos(\omega_{b\theta}\theta)\,H[x(\theta)\sin(\omega_{b\theta}\theta)] \tag{3.64}$$

where $\omega_{b\theta} = 1$. After Equation (3.62) has been introduced, Equation (3.64) can be expressed into a function of time. Note that ω_{1t} and ω_{2t} in Figure 3.20 are two time-varying frequencies of a time series while $\omega_{1\theta}$ and $\omega_{2\theta}$ in Figure 3.21 are their corresponding frequencies in phase domain, which vary with the phase angle. As illustrated in Figures 3.20 and 3.21 the bisecting frequency fluctuates significantly in time domain but is equal to one in phase domain. The constant bisecting frequency in phase domain can be obtained regardless of how rapidly the time-varying frequencies change in time domain.
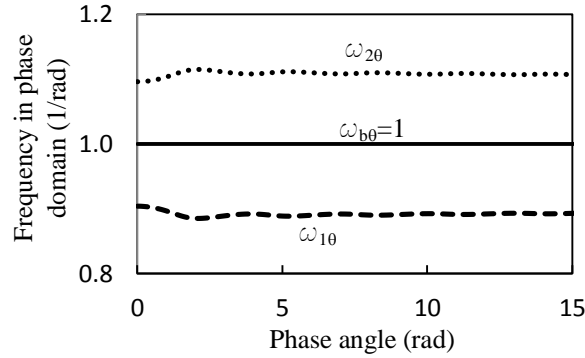
Figure 3.21. Illustration on Varying Bisecting Frequencies in Phase Domain

3.7.2. Role of Transform from Time Domain to Phase Domain. Equation (3.64) differs from Equation (3.45) in Section 3.6 in that it involves Hilbert transform in phase domain instead of time domain. It is thus desirable to examine the condition under which their difference is small. As defined in Equation (3.1), the Hilbert transforms of a real time series $y(t)$ and $y(\theta)$ can be respectively expressed into:

$$H[y(t)] = \frac{1}{\pi} P \int_{-\infty}^{+\infty} \frac{y(r)}{t-r} dr \tag{3.65}$$

$$H[y(\theta)] = \frac{1}{\pi} P \int_{-\infty}^{+\infty} \frac{y(\rho)}{\theta-\rho} d\rho \tag{3.66}$$

After Equation (3.62) has been introduced, $\theta = \int_0^t \omega_{bt}(\tau)d\tau$ and $\rho = \int_0^r \omega_{bt}(\tau)d\tau$, Equation (3.66) can be rewritten as:

$$H[y(\theta)] = \frac{1}{\pi} P \int_{-\infty}^{+\infty} \frac{y(r)}{\int_r^t \omega_{bt}(\tau)d\tau/\omega_{bt}(r)} dr \tag{3.67}$$

In general, Equation (3.67) differs from Equation (3.66) unless $\omega_{bt}(\tau)$ is constant. To understand their similarity and difference in other cases, four signals were analyzed over 30 sec, including:

Case 1: $x(t) = \cos[3.5\pi t + 5\sin(0.1\pi t)] + \cos[2.8\pi t + 5\sin(0.1\pi t)]$,

Case 2: $x(t) = \cos[3.5\pi t + 0.5\sin(\pi t)] + \cos[2.8\pi t + 0.5\sin(\pi t)]$,

Case 3: $x(t) = \cos[3.5\pi t + 0.1\sin(5\pi t)] + \cos[2.8\pi t + 0.1\sin(5\pi t)]$, and

Case 4: $x(t) = \cos[3.5\pi t + \sin(0.5\pi t)] + \cos[2.8\pi t + 2\sin(0.25\pi t)]$.

Each of the first three series has two time-varying frequency components in parallel; they represent slow, medium, and fast fluctuations of frequencies over time. The last series has two non-parallel time-varying frequencies. In all cases, the time-varying

bisecting frequency is taken to be the average of the frequencies of the two components. The frequency of individual components and the bisecting frequency are presented in Figure 3.22. For clarity, the slowly and fast varying frequencies are presented for 30 and 2 seconds, respectively, while all other cases are shown in 10 seconds.
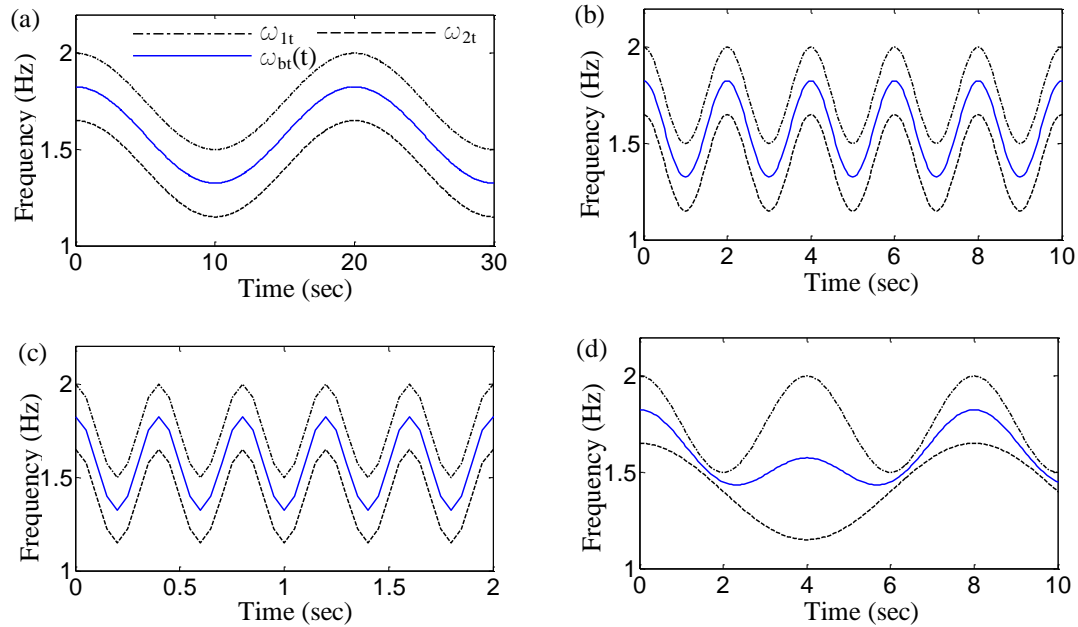
Figure 3.22. Component Frequencies and Bisecting Frequency: (a) Case 1, (b) Case 2, (c) Case 3, and (d) Case 4

Equation (3.64) is directly applied in phase domain. It can also be used in time domain if Equation (3.62) is introduced before the Hilbert transform is executed. The decomposed lowpass component is compared with its original signal in Figure 3.23 in time domain and in Figure 3.24 in phase domain. It is clearly observed from Figures 3.23 and 3.24 that the decomposed component and the exact signal are all in excellent agreement for the first three cases with parallel component frequencies as shown in Figure 3.22(a-c), being in time or phase domains. The decomposed lowpass component in the fourth case with nonparallel component frequencies, Figure 3.22(d), is more accurate in phase domain than in time domain. This is mainly attributed to the two close-spaced frequencies and incomplete cycle at the end of 30 sec, as indicated in Figure 3.22(d). Overall, the difference in time and phase domains is small since the singularity in Hilbert transform likely dominates the principal value integral as shown in Equations.

(3.65-3.67) and thus results in a small variation of $\int_r^t \omega_{bt}(\tau)d\tau/[\omega_{bt}(r)(t-r)]$ as r approaches t around the singular point as illustrated in Figure 3.25. As expected, the more rapid the change in modulated frequencies, the larger the variation of the integration. Note that effort was made to compensate the end effect in Hilbert transform by mirror imaging the time function from the first and last maxima/minima of a time signal.

Furthermore, the Fast Fourier Transform was performed for each of the four cases. The Fourier spectra are presented in Figure 3.26 for the signal in time domain and in Figure 3.27 for the signal in phase domain. It can be observed from Figure 3.26 that there is a strong overlapping between two frequency components in time domain. Once transferred to phase domain, the two frequency components are well separated as shown in Figure 3.27. The difference in frequency overlapping in time and phase domains was illustrated in Figures 3.20 and 3.21.
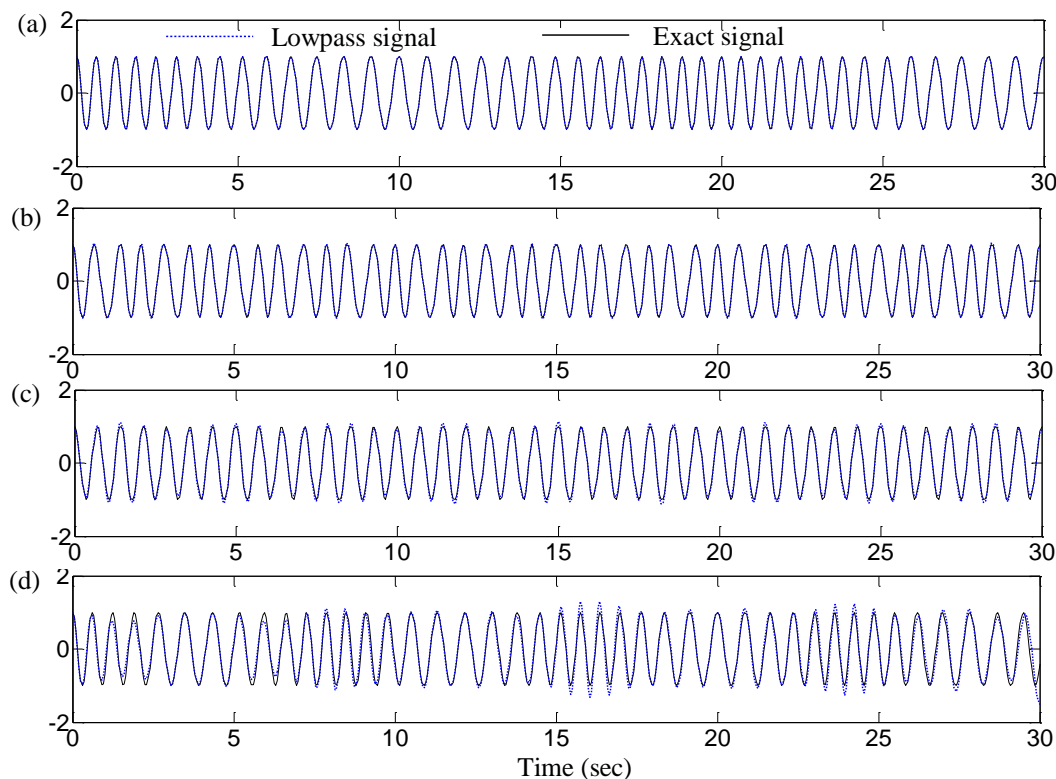
Figure 3.23. The Decomposed Lowpass and Exact Signal in Time Domain: (a) Case 1, (b) Case 2, (c) Case 3, and (d) Case 4
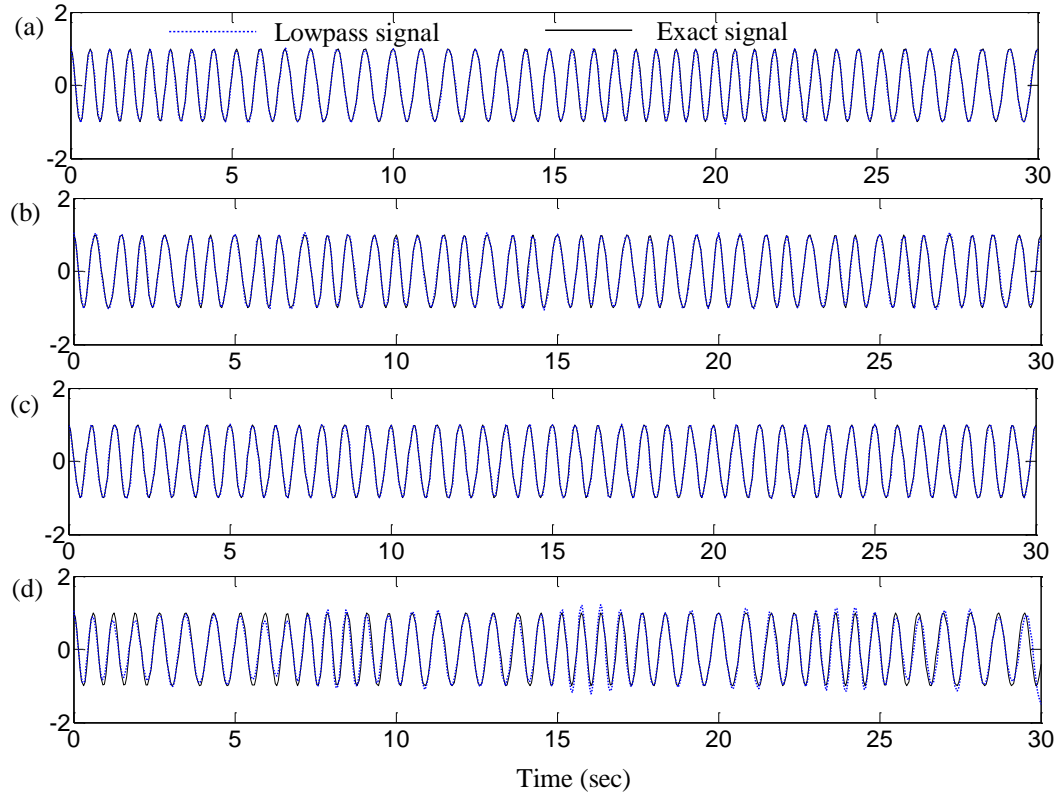
Figure 3.24. The Decomposed Lowpass and Exact Signal in Phase Domain: (a) Case 1, (b) Case 2, (c) Case 3, and (d) Case 4
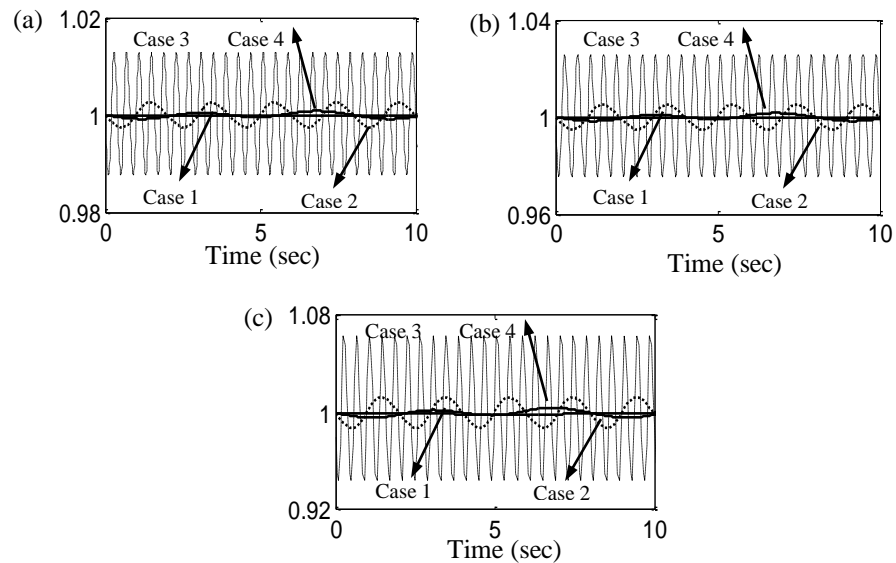
Figure 3.25. Variation of $\int_r^t \omega_{bt}(\tau)d\tau /[\omega_{bt}(r)(t-r)]$ with Bisecting Frequency Selection: (a) $t - r = 0.001$sec, (b) $t - r = 0.01$sec, and (c)) $t - r = 0.05$sec.
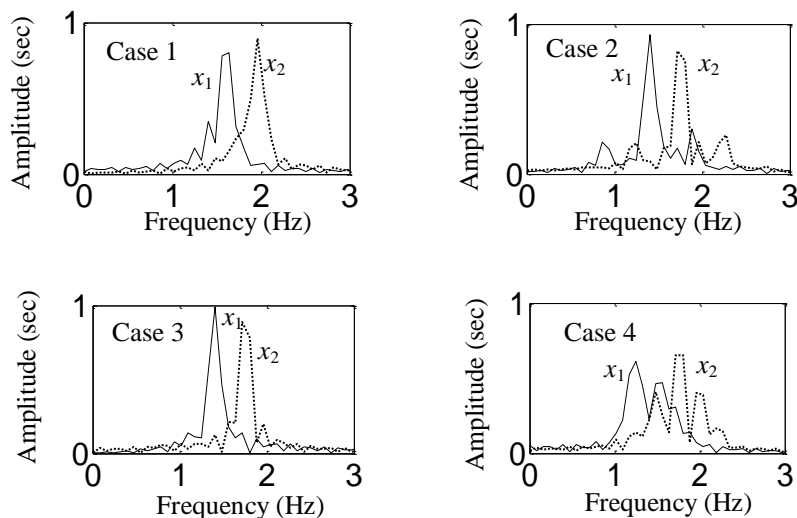
Figure 3.26. Fourier Spectra of Individual Components in Time Domain
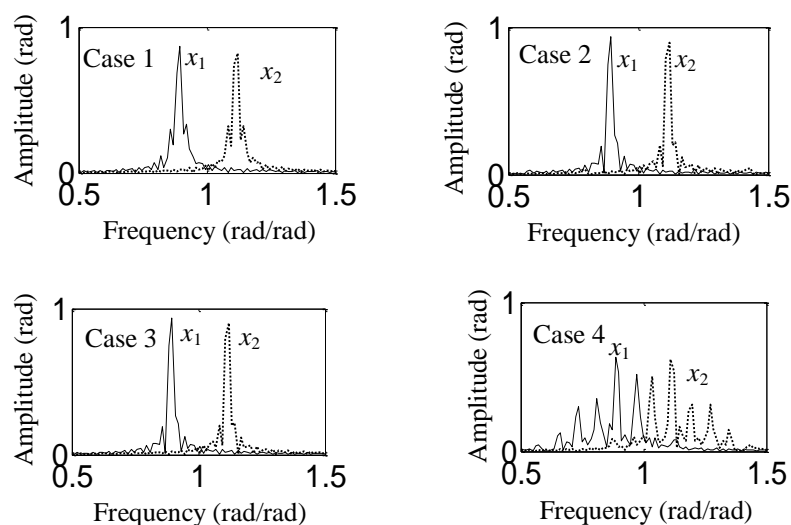
Figure 3.27. Fourier Spectra of Individual Components in Phase Domain

3.7.3. Adaptive Lowpass and Bandpass Filter for Signals with Time-Varying Frequencies. As observed in Section 3.6, AMD functions like a suite of "perfect" bandpass filters. Since the bisecting frequency varies with time, reflecting the time-frequency analysis of a data series, the related filter with a time-varying bisecting frequency $\omega_{bt}(t)$ is referred to as an adaptive lowpass filter in this study.

Due to significant overlapping of the frequency contents in time domain, it is recommended that an adaptive lowpass filter be applied in phase domain as schematically illustrated in Figure 3.28 and an adaptive bandpass filter is presented in Figure 3.29.
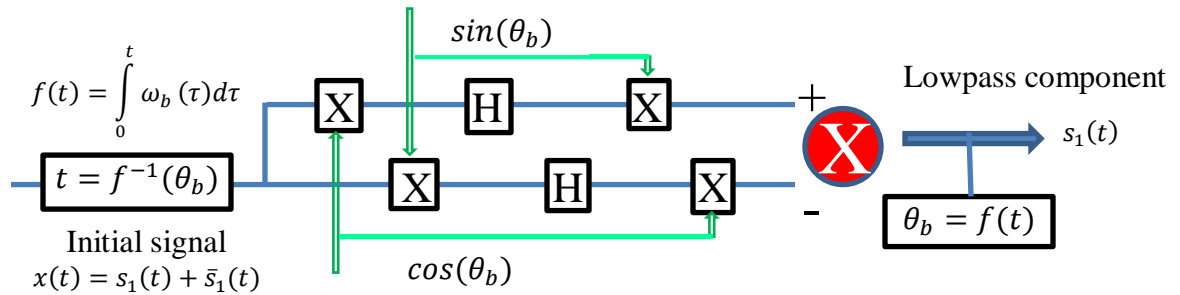
Figure 3.28. Block Diagram of an Adptive Lowpass Filter with a Time Varying Bisecting Frequency $\omega_b(t)$
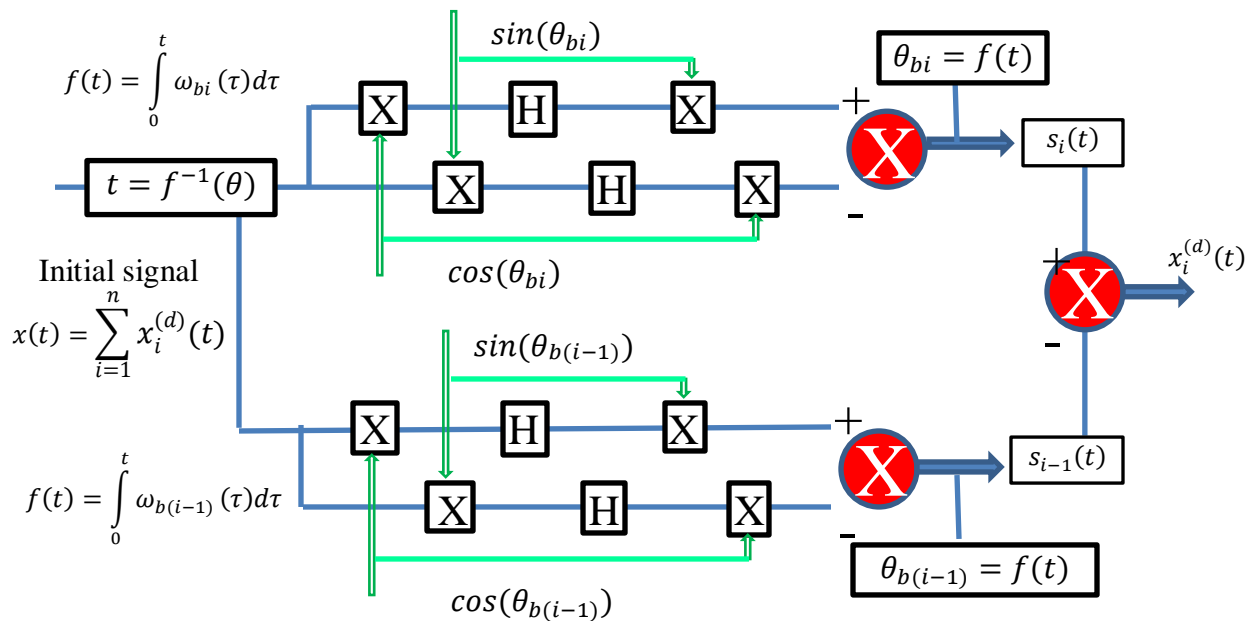
Figure 3.29. Block Diagram of an Adaptive Bandpass Filter with Two Time Varying Bisecting Frequencies: $\omega_{b(i-1)}(t)$ and $\omega_{bi}(t)$

3.8. SUMMARY

In this section, Hilbert transform, analytic signal, and Hilbert spectral analysis were first introduced. To execute a well-behaved Hilbert transform in Hilbert spectrum analysis, two signal decomposition methods (EMD and HVD) were then described briefly. Although powerful in adaptive data analysis, these methods still face several challenges in engineering applications.

To address these challenges for both stationary and non-stationary signal analysis, a new signal decomposition theorem was discovered and proven in this study. The essence of this theorem is the exact separation of a general time series into two time functions whose Fourier spectra are non-vanishing over two mutually-exclusive frequency ranges separated by a bisecting frequency. With multiple steps of bisecting, an original time series with multiple closely-spaced frequency components can be decomposed into many signals, each dominated by a narrowband frequency component. Therefore, AMD functions like a suite of "perfect" bandpass filters. Unlike frequency filtering techniques in frequency domain, this bandpass filter decomposes signals directly in time domain, eliminating the problems associated with frequency bandpass filtering. For stationary and non-stationary signals with invariant frequencies, constant bisecting frequencies are selected. For non-stationary signals with varying frequencies, time-varying bisecting frequencies were introduced to deal with significant frequency overlapping in the entire time domain, though separated at any time instant. In this case, it is recommended that the AMD theorem be applied in phase domain.

4. PARAMETER IDENTIFICATION OF TIME INVARIANT SYSTEMS WITH AMD-HILBERT SPECTRAL ANALYSIS

Emphasis in this section is placed on the understanding of the minimum spacing between two discernible frequencies, the effect of a bisecting frequency selection on the AMD accuracy, and the application of the AMD theorem in various engineering systems.

4.1. BISECTING FREQUENCY SELECTION

To investigate the effect of bisecting frequency selections on the accuracy of signal decompositions, two frequency resolutions were considered: $\Delta f = 0.05$ Hz and $\Delta f = 0.025$ Hz. They correspond to a time series of 20 sec and 40 sec, respectively. Furthermore, three relative intensities of the three frequency components were chosen to understand their potential influence on the selection of the bisecting frequency. Therefore, a total of six cases were analyzed with the following original signals: (1) $x_1(t) = \cos(2\pi f_1 t)$, $x_2(t) = \cos(2\pi f_2 t + \pi/6)$, and $x_3(t) = \cos(2\pi f_3 t)$; (2) $x_1(t) = 0.5\cos(2\pi f_1 t)$, $x_2(t) = \cos(2\pi f_2 t + \pi/6)$, and $x_3(t) = 0.5\cos(2\pi f_3 t)$; and (3) $x_1(t) = \cos(2\pi f_1 t)$, $x_2(t) = 0.5\cos(2\pi f_2 t + \pi/6)$, and $x_3(t) = \cos(2\pi f_3 t)$.

The Fourier spectra for the above six cases are presented in Figure 4.1. The amplitudes of the pulses depend upon the frequency resolution used in numerical integrations. As the resolution improves from 0.05 Hz to 0.025 Hz, the three pulses in each case become narrower and higher and their relative amplitudes are more accurate. This is mainly due to the decreasing aliasing effect and the decreasing impact by the incomplete data set whose total number of points is not equal to the multiplier of 2 in the Fast Fourier Transform. However, selection in the frequency resolution has little effect on the Fourier spectrum comparison between the decomposed signal and the exact signal so long as they use the same resolution. Therefore, all examples to illustrate the superiority of the AMD theorem over existing technologies were analyzed with the minimum frequency resolution of 0.05 Hz. For system identification and damage detection, 0.025 Hz frequency resolution is recommended to ensure the accurate representation of various frequency components in a structural response. Note that a weak signal in between two strong signals requires a higher frequency resolution to detect.
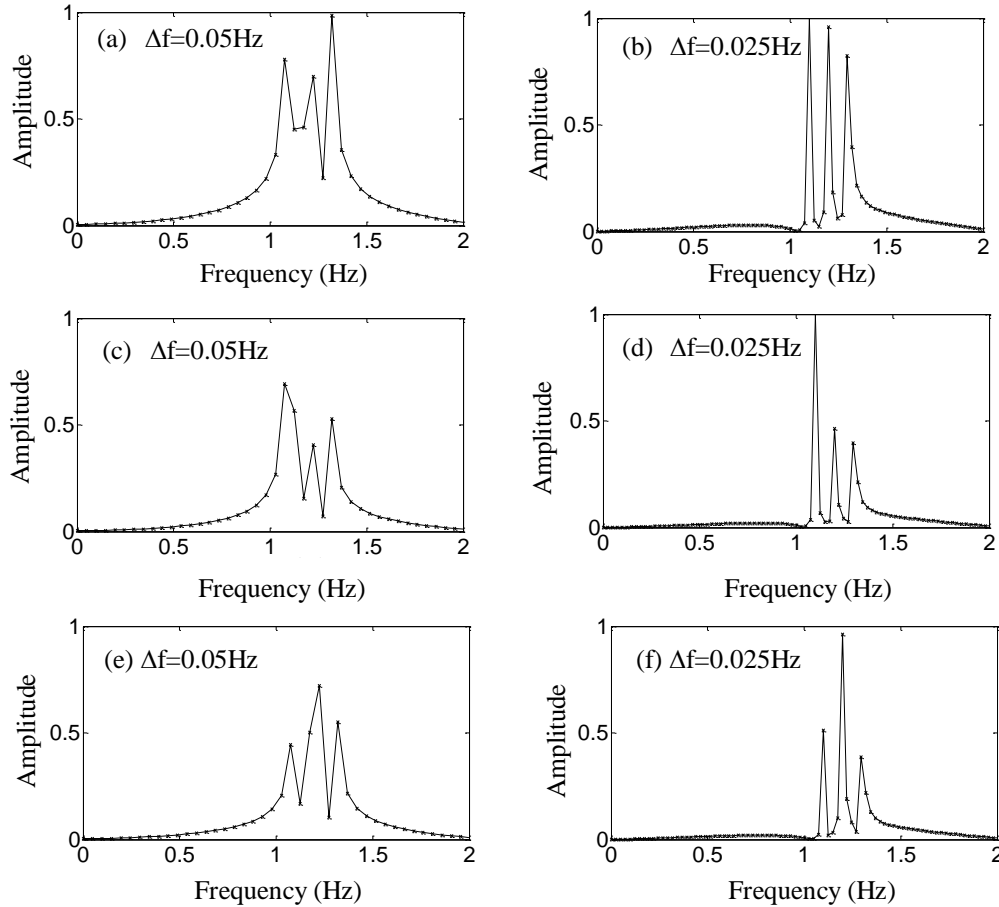
Figure 4.1. Fourier Spectra of Time Series in Six Cases: (a, b) for $x(t) = cos(2\pi f_1 t) + cos(2\pi f_2 t + \pi/6) + cos(2\pi f_3 t)$, (c, d) for $x(t) = 0.5cos(2\pi f_1 t) + cos(2\pi f_2 t + \pi/6) + 0.5cos(2\pi f_3 t)$, and (e, f) for $x(t) = cos(2\pi f_1 t) + 0.5\,cos(2\pi f_2 t + \pi/6) + cos(2\pi f_3 t)$. $(f_1 = 1, f_2 = 1.2, and\ f_3 = 1.3)$

The amplitude ratio between the Fourier transforms of the decomposed signal $\hat{x}_i^{(d)}(\omega_i)$ and the original signal $\hat{x}_i(\omega_i)$ is presented in Figure 4.2 for $i = 1, 2, 3$ in each of the six cases. The bisecting frequency was considered as a weighted average of the beginning and end frequencies of a range: $\omega_{b1}/2\pi = \alpha f_1 + (1 - \alpha)f_2$ and $\omega_{b2}/2\pi = \alpha f_3 + (1 - \alpha)f_2$, in which $1 - \alpha$ represents the weight factor on the center frequency f_2. It can be seen from Figure 4.2 that the relative error in signal decomposition is nearly independent of the relative signal amplitudes and less than 3.3% when the bisecting frequency takes 80%~120% of the frequency at $\alpha = 0.5$. Therefore, the bisecting frequency can be selected to be the average of the lower and higher frequencies and the accuracy in mode decomposition is insensitive to this selection.
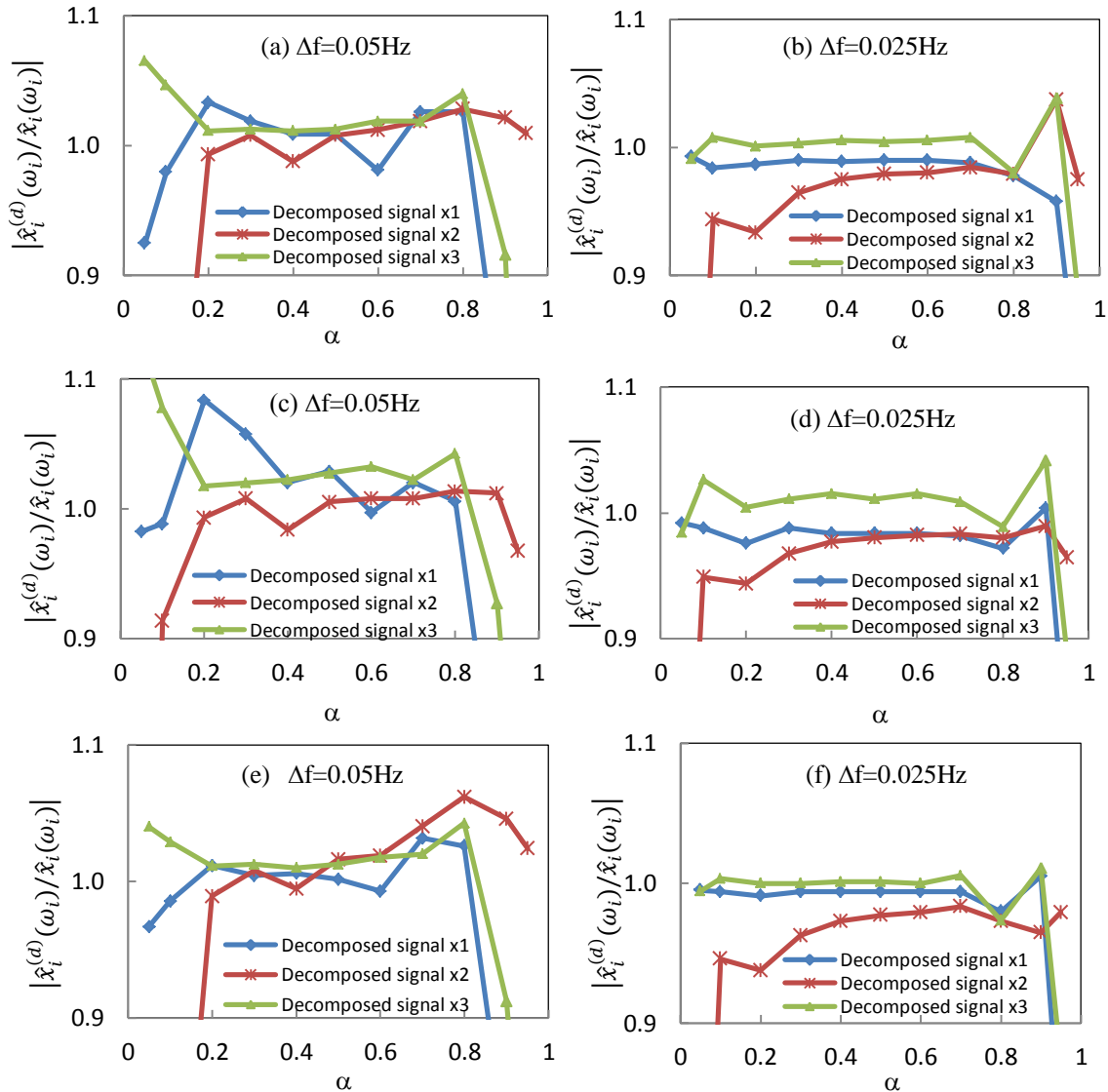
Figure 4.2. Effect of Bisecting Frequency Selection on Amplitude Ratio: (a, b), $x(t) = cos(2\pi f_1 t) + cos(2\pi f_2 t + \pi/6) + cos(2\pi f_3 t)$, (c, d), $x(t) = 0.5cos(2\pi f_1 t) + cos(2\pi f_2 t + \pi/6) + 0.5cos(2\pi f_3 t)$, and (e, f), $x(t) = cos(2\pi f_1 t) + 0.5\ cos(2\pi f_2 t + \pi/6) + cos(2\pi f_3 t)$. $(f_1 = 1, f_2 = 1.2, and\ f_3 = 1.3)$

4.2. SIGNAL DECOMPOSITION IN ENGINEERING APPLICATIONS

To demonstrate the sensitivity to noise and the performance advantage over existing techniques in the literature, the AMD method was applied to analyze four examples representing various engineering applications. The results are compared with those from the existing techniques.

4.2.1. Noise Effects. Consider a 20-sec, two-frequency time series $x(t) = x_1(t) + x_2(t) + rand(\sigma)$ with the Gaussian white noise $rand(\sigma)$: $x_1(t) = \sin(2\pi f_1 t)$ and $x_2(t) = \sin(2\pi f_2 t)$ where $f_1 = 1.0$ Hz and $f_1 = 1.5$ Hz. The ratio of the two frequencies is $f_2/f_1 = 1.5$. The standard deviation of the mean-zero white noise is 10% of the signal strength. That is, $\sigma = 0.1 \times max|x_1(t) + x_2(t)|$. A time step of 0.02 sec was used in simulations.

Following the EMD process, four IMFs were determined from the time series. The first two IMFs had wideband frequency components that were mainly contributed by the white noise. The 3rd and 4th IMFs, IMF3 and IMF4, and their Fourier transforms are compared with their respective exact signals in Figures 4.3 and 4.4, respectively. It can be clearly seen that both IMFs have significant errors and the two frequency components are still mixed after the application of EMD.

To apply the proposed AMD method, $\omega_b = 2\pi(f_1 + f_2)/2 = 2.5\pi$ rad/sec was selected. Figures 4.5 and 4.6 present the decomposed signals and their Fourier transforms, respectively. As one can see, the two frequency components were completely separated and the decomposed signals are in excellent agreement with their respective exact signals. Therefore, the proposed AMD is superior to the EMD.
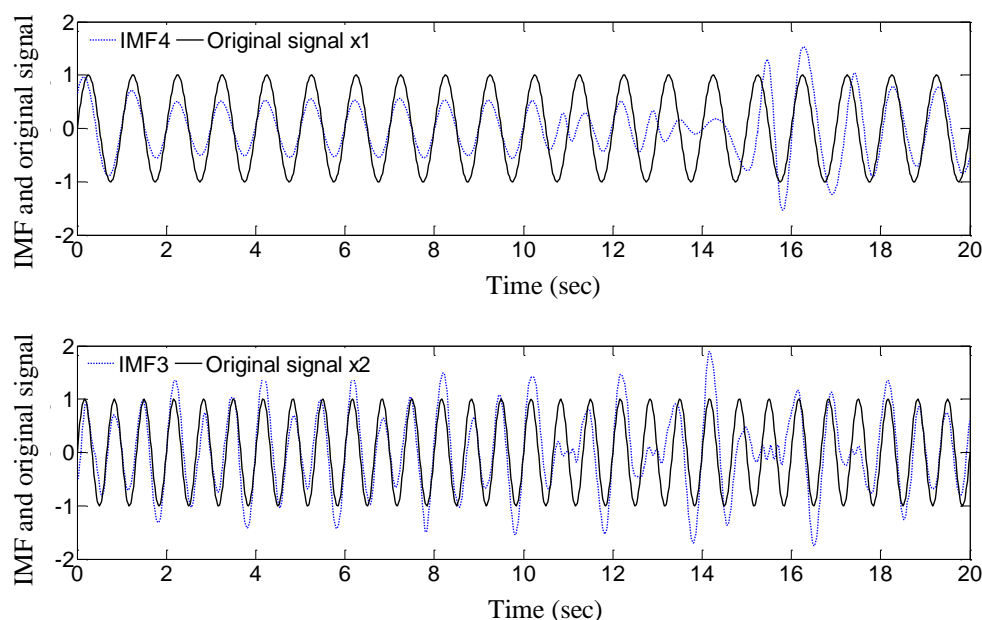
Figure 4.3. IMF3 and IMF4 by EMD versus Exact Signals
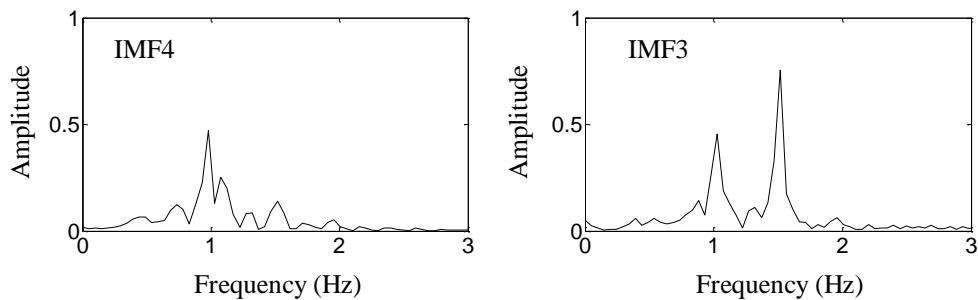
Figure 4.4. Fourier Spectra of IMF3 and IMF4 by EMD

Figure 4.5. Decomposed Signals by AMD versus Exact Signals
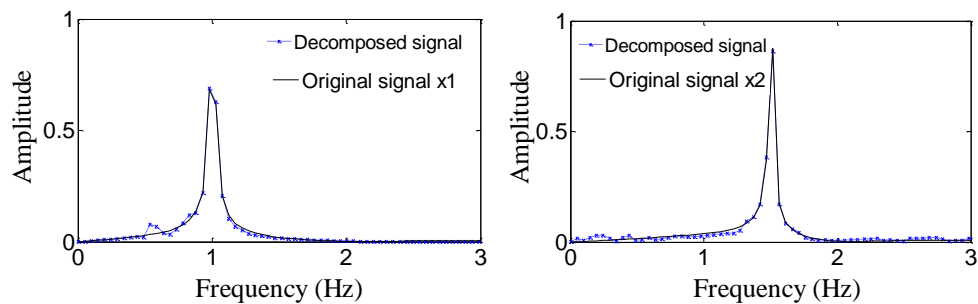
Figure 4.6. Fourier Spectra of the Decomposed Signals by AMD versus Exact Signals

4.2.2. Closely-Spaced Frequency Components. A two frequency component signal was considered: $x(t) = x_1(t) + x_2(t)$, $x_1(t) = \cos(2\pi f_1 t + \pi/6)$ and $x_2(t) = \cos(2\pi f_2 t)$. Both long period ocean wave and short period mechanical wave were analyzed.

4.2.2.1 Long period ocean wave. The processing of an ocean wave data was considered (Wang, 2005). A time step of 0.1 sec was adopted in this example. The two frequencies were taken to be $f_1 = 1/32$ Hz and $f_2 = 1/30$ Hz. Their ratio was $f_2/f_1 = 1.067$. Figures 4.7 and 4.8 present the 1st and 2nd IMFs, IMF1 and IMF2, and their Fourier transforms based on the wave group method with a downshift frequency of 1/28 Hz (Wang, 2005). Similarly, Figures 4.9 and 4.10 show the decomposed signals and their Fourier transforms obtained from the proposed AMD method. The results indicate that both the wave group method with EMD and the AMD method can effectively separate the two frequency components in this case. However, the Fourier spectra in Figure 4.10 are still cleaner than those in Figure 4.8 outside the two frequency components f_1 and f_2.
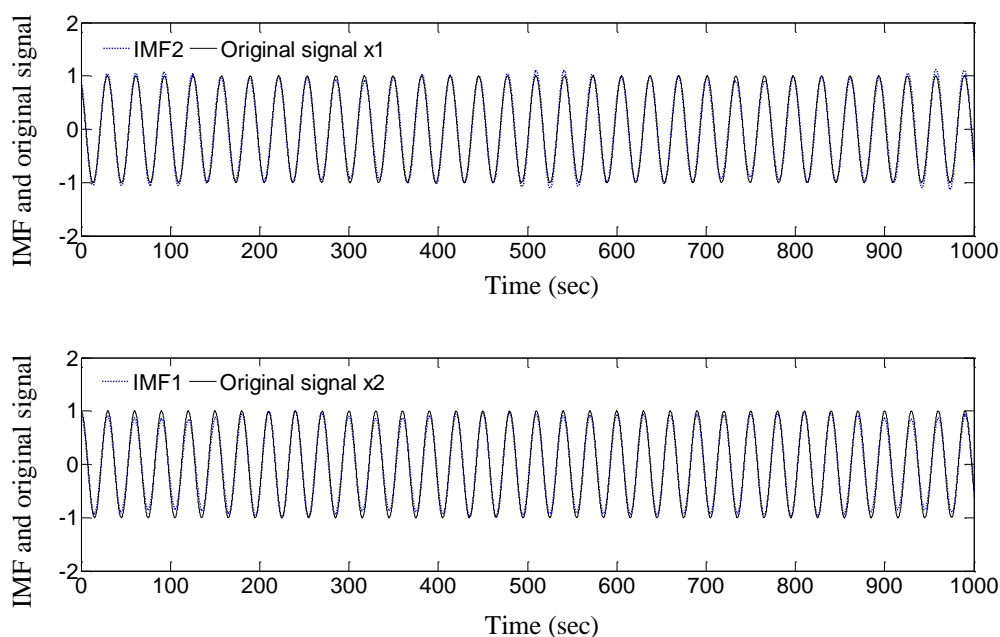
Figure 4.7. IMF1 and IMF2 by the Wave Group Method with EMD versus Exact Signals
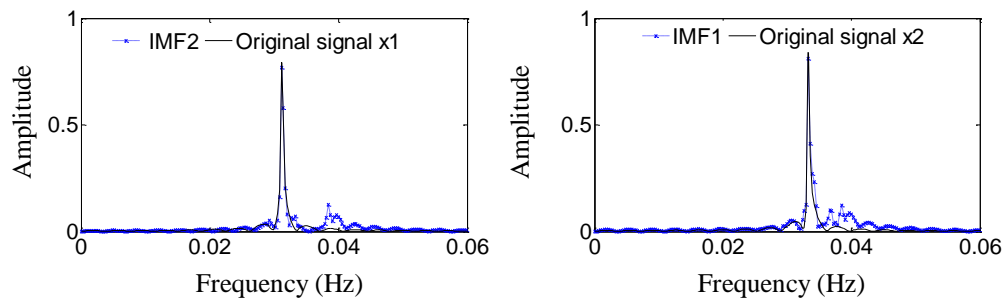
Figure 4.8. Fourier Spectra of IMF1 and IMF2 by Wave Group Method with EMD and Exact Signals
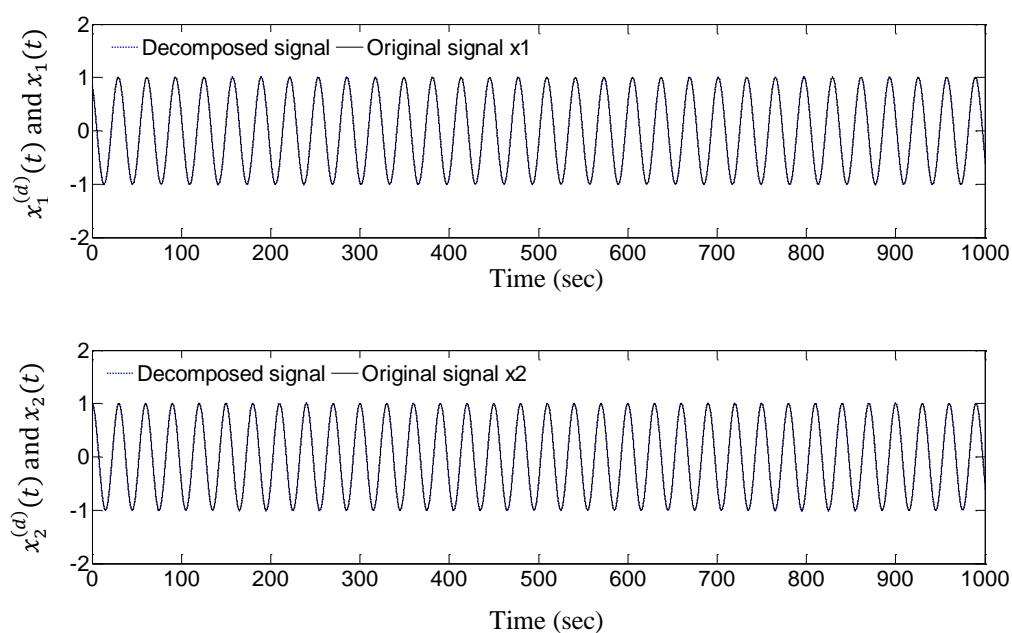
Figure 4.9. Decomposed Signals by AMD versus Exact Signals
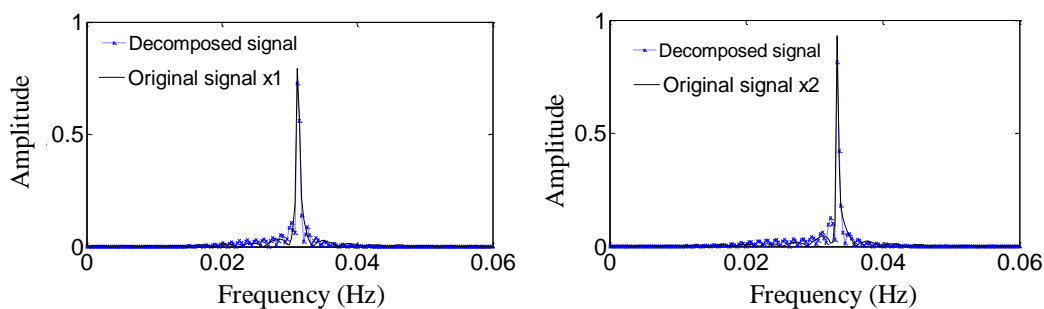
Figure 4.10. Fourier Spectra of the Decomposed Signals by AMD versus Exact Signals

4.2.2.2 Short period mechanical wave. A 20-sec signal with $f_1 = 1.1\,Hz$ and $f_2 = 1.2\,Hz$ was considered. The ratio of the two frequencies was $f_2/f_1 = 1.091$. A time step of 0.02 sec was used. Figures 4.11 and 4.12 present the first two IMFs and their Fourier spectra based on the wave group method with a downshift frequency of 1.3 Hz. Figures 4.13 and 4.14 depict the decomposed signals and their Fourier spectra based on the proposed AMD method. It can be clearly seen that the wave group method cannot completely separate the two frequency components even though the frequency ratio of 1.091 is greater than 1.067 in Section 4.2.2.1. This indicates that the wave group method with EMD cannot ensure that reasonable solution be achieved for general cases due to the inherent issue with EMD. On the other hand, the proposed AMD can consistently separate the two close frequency components with high accuracy.
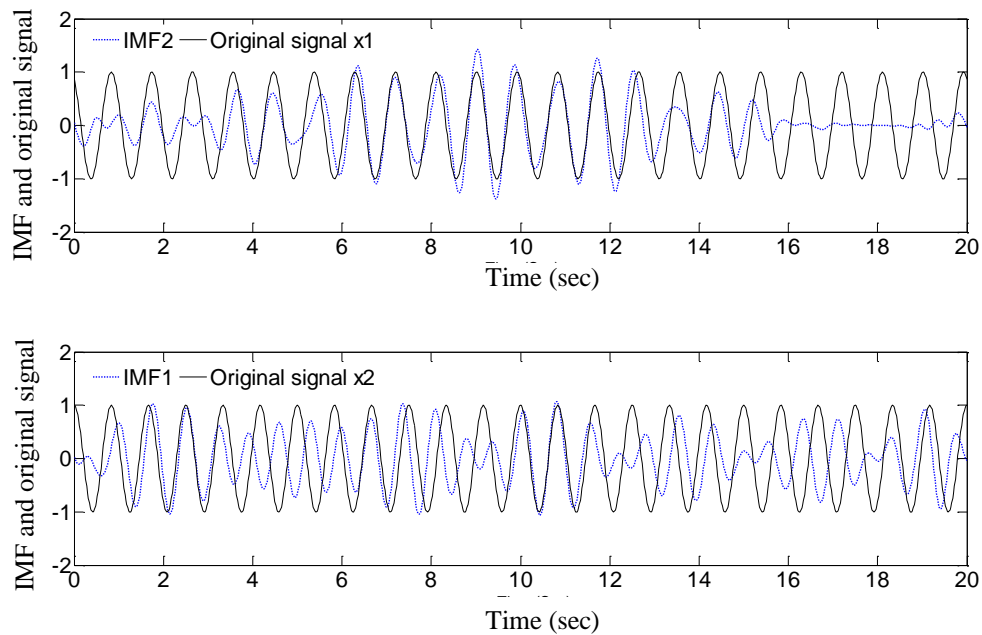
Figure 4.11. IMF1 and IMF2 by the Wave Group Method with EMD versus Exact Signals
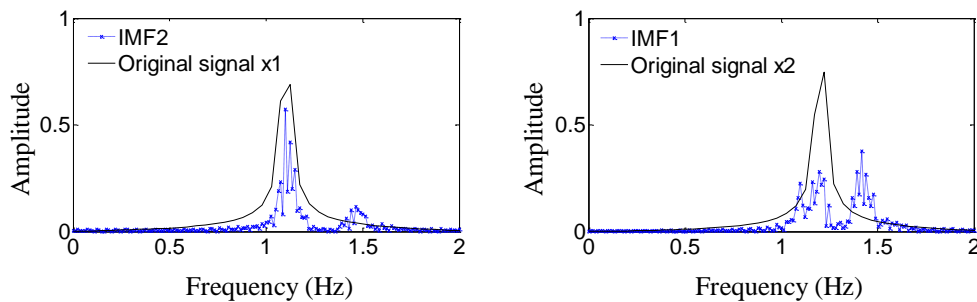
Figure 4.12. Fourier Spectra of IMF1 and IMF2 by Wave Group Method with EMD and Exact Signals
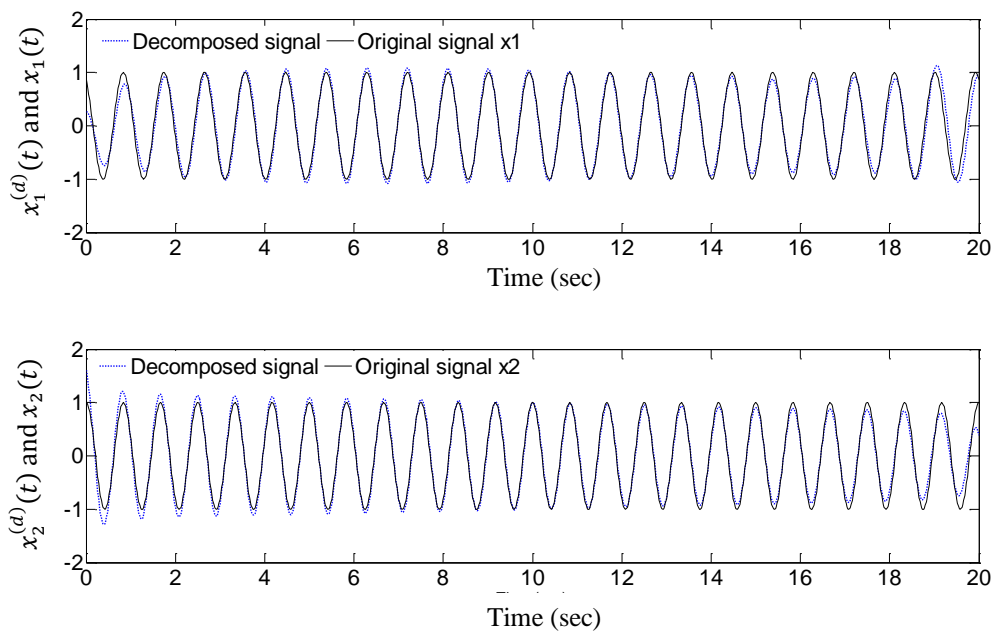
Figure 4.13. Decomposed Signals by AMD versus Exact Signals
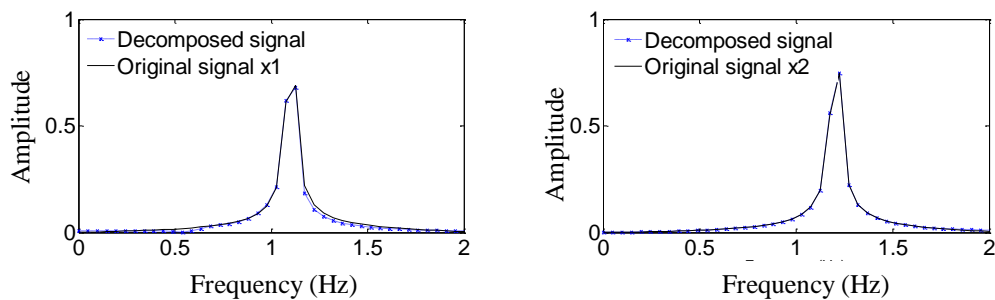
Figure 4.14. Fourier Spectra of the Decomposed Signals by AMD versus Exact Signals

4.2.3. Amplitude Decaying Signals. Consider a two frequency component amplitude decaying signal: $x(t) = x_1(t) + x_2(t)$, $x_1(t) = 10e^{-\zeta 2\pi f_1 t}\cos(2\pi f_1 t)$, and $x_2(t) = 1.8e^{-\zeta 2\pi f_2 t}\cos(2\pi f_2 t)$. Here, $f_1 = 2.0\ Hz$, $f_2 = 4.3\ Hz$, and $\zeta = 0.02$. A time step of 0.02 sec was used. Figures 4.15 and 4.16 present the two decomposed signals and their Fourier spectra by introducing a temporary signal of $x_{temp}(t) = 20\cos(8\pi t)$ (Wang, 2005). Similarly, Figure 4.17 and 4.18 show the decomposed signals and their Fourier spectra based on the AMD method. Figures 4.15 and 4.16 indicate that the existing method (Wang, 2005) cannot completely separate the two frequency components. Figures 4.17 and 4.18 clearly demonstrate that the two close frequency components have been separated successfully by AMD.
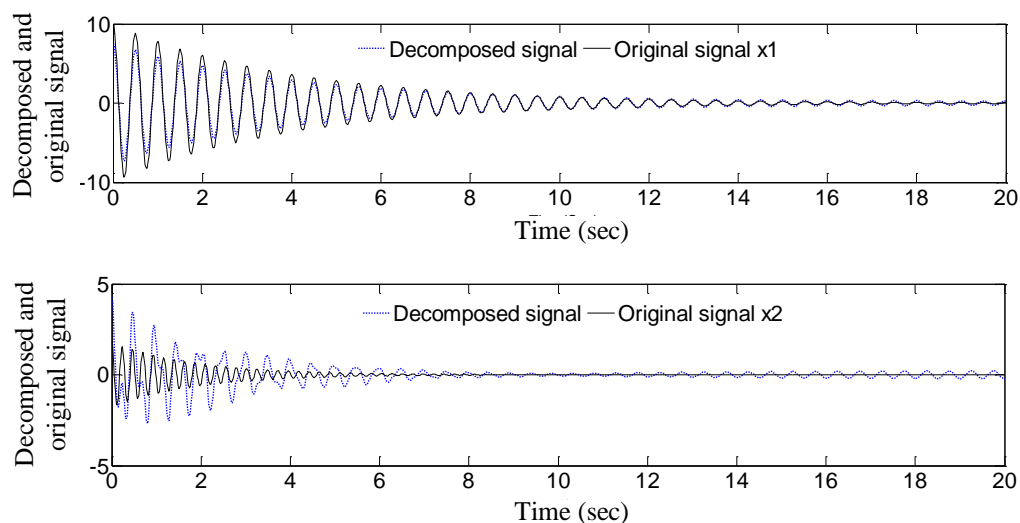
Figure 4.15. Decomposed Signals by Adding a Temp-Signal versus Exact Signals
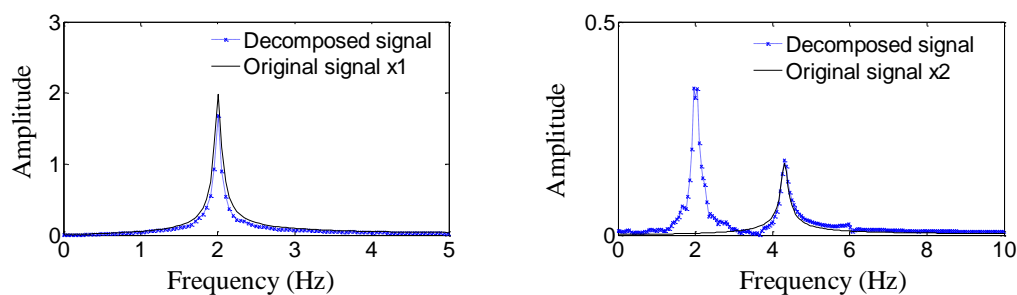
Figure 4.16. Fourier Spectra of the Decomposed Signals by Adding a Temp-Signal versus Exact Signals
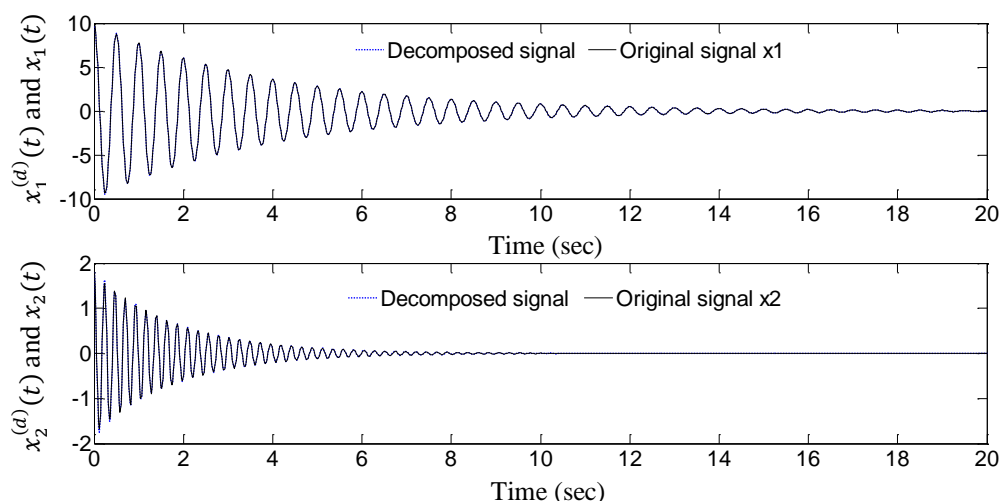
Figure 4.17. Decomposed Signals by AMD versus Exact Signals
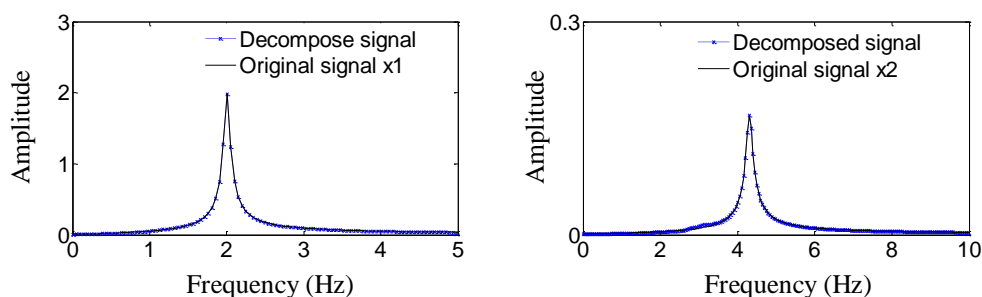
Figure 4.18. Fourier Spectra of the Decomposed Signals by AMD versus Exact Signals

4.2.4. Small Intermittent Fluctuations around a Large Standing Wave. The two frequency component signal (Wang, 2005) was considered: $x(t) = x_1(t) + x_2(t)$, $x_1(t) = cos(2\pi t/640)$ (0<t<3200 sec), and, $x_2(t) = 0.02\ sin(2\pi t/32)$ (1264 ≤ t ≤ 1296 sec). The time step in this case was taken to be 0.1 sec.

Figures 4.19 and 4.20 present the decomposed signals and their Fourier transforms that were determined by EMD with an added temporary signal of $x_{temp}(t) = 0.2\cos(2\pi t/60)$. Figures 4.21 and 4.22 show the decomposed signals and Fourier spectra by the AMD theorem with three bisecting frequencies of $f_b = \omega_b/2\pi = 0.003\ Hz$, $0.0075\ Hz$ and $0.0164\ Hz$, respectively. The last bisecting frequency represents the average of the frequencies of signals $x_1(t)$ and $x_2(t)$. For this example, both methods can decompose the small intermittent fluctuation from the large long period

wave. However, the decomposed signal $x_2(t)$ by the EMD method is greatly affected by the signal $x_1(t)$ as shown in Figure 4.20. The proposed AMD theorem gives clean, well separate, and significantly more accurate results as illustrated in Figure 4.22. Figures 4.21 and 4.22 also illustrate that in this case, the optimum bisecting frequency in the AMD should weight more of the large wave frequency due mainly to the distributive nature of the Fourier spectrum of a short time intermittent signal. As indicated in Figure 4.21, more accurate results can be obtained if the bisecting frequency is reduced to slightly above the frequency of $x_1(t)$, such as 0.003 Hz.
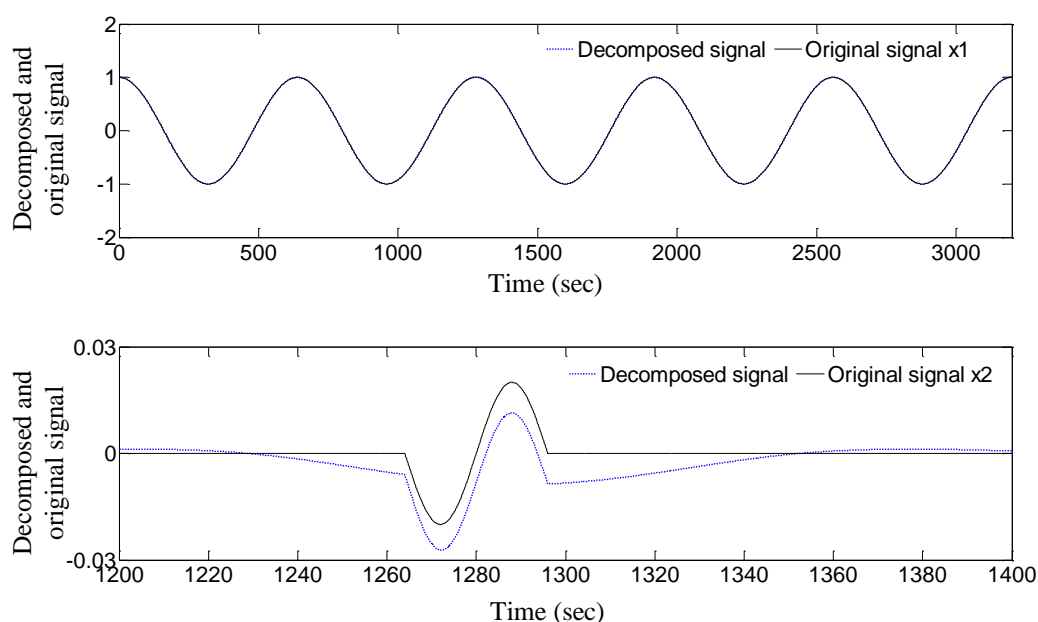
Figure 4.19. Decomposed Signals by Adding a Temp-Signal versus Exact Signals
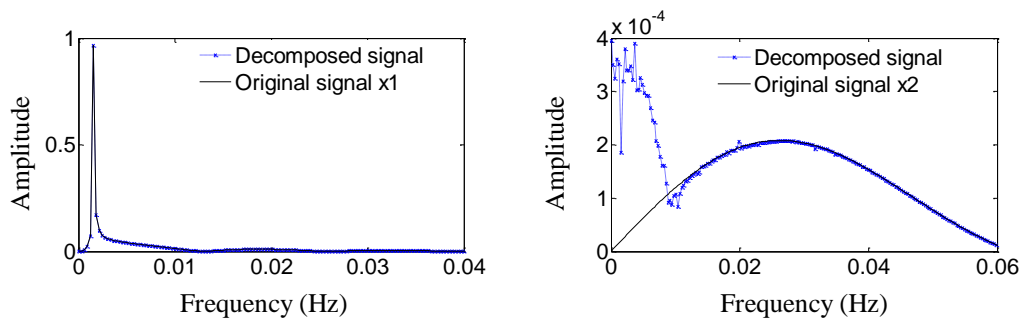
Figure 4.20. Fourier Spectra of the Decomposed Signals by Adding a Temp-Signal versus Exact Signals
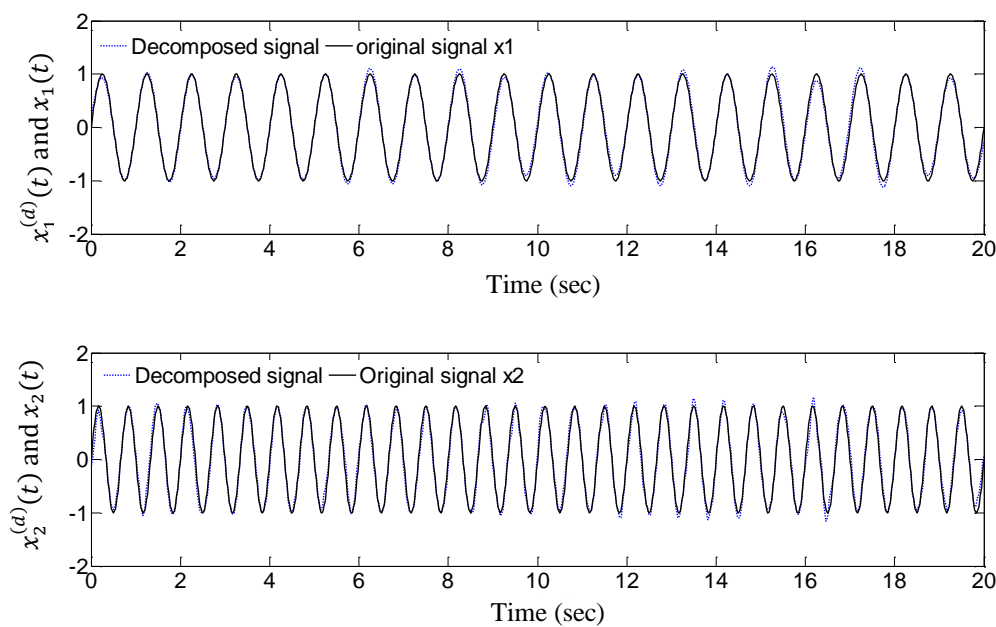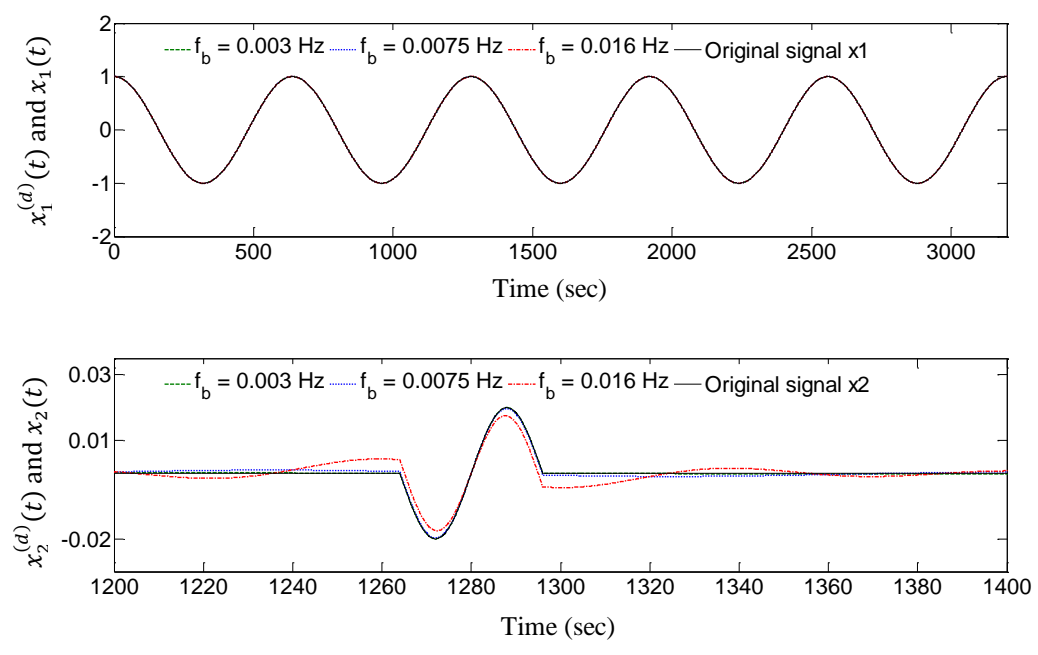
Figure 4.21. Decomposed Signals by AMD versus Exact Signals
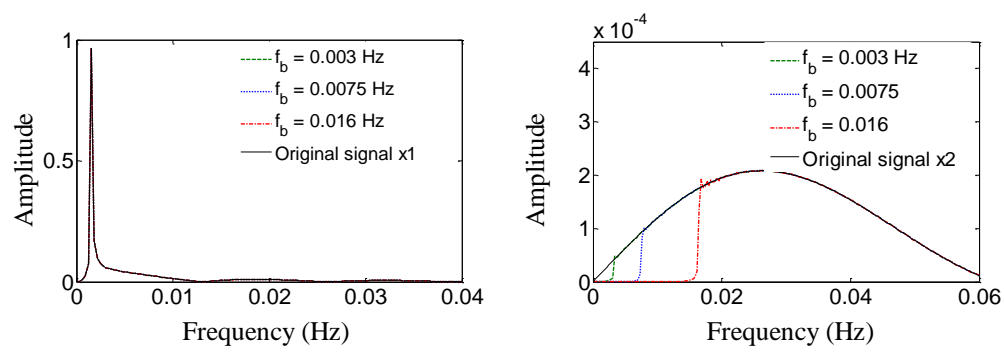
Figure 4.22. Fourier Spectra of the Decomposed Signals by AMD versus Exact Signals

4.3. MODAL PARAMETER IDENTIFICATION FROM FREE VIBRATION

4.3.1. Modal Parameter Identification. For the system identification of an n-DOF structure, the Fourier transform of an original measured response, such as structural displacement or acceleration, can be plotted as illustrated in Figure 4.23 for the case of $n=3$.

The frequencies ω_1, ω_2, $\cdots$, ω_n correspond to the peaks of the Fourier transform and can be estimated from Figure 4.23. The bisecting frequencies $\omega_{b1}, \omega_{b2}, \cdots, \omega_{b(n-1)}$

can then be selected in between any two natural frequencies of the structure as shown in Figure 4.23.
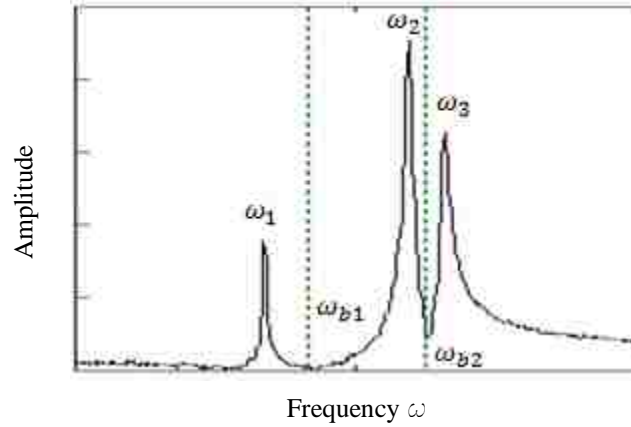
Figure 4.23. Representative Fourier Spectrum of a Structural Response

Each decomposed signal by AMD has a narrow frequency band corresponding to one mode of vibration. Similar to the HHT method (Yang et al., 2003), the instantaneous amplitude $A_{pi}(t)$ and phase angle $\theta_{pi}(t)$ of the ith decomposed mode $x_{pi}^{(d)}(t)$ at the pth DOF can be determined from:

$$A_{pi}(t)e^{j\theta_{pi}(t)} = x_{pi}^{(d)}(t) + j\, H[x_{pi}^{(d)}(t)] \tag{4.1}$$

If the structure is subjected to an impulsive load, the frequency and damping ratio can be detected using the least-squares fit procedure:

$$\omega_i = \frac{d\theta_{pi}(t)}{dt} \text{ and } \varsigma_i = -\frac{d\left[\ln\left(A_{pi}(t)\right)\right]}{\omega_i dt} \tag{4.2}$$

In general, the response of the pth DOF $x_p(t)$ can be expanded into a summation of modal contributions, each being the product of the pth modal element φ_{pi} and the modal coordinate $g_i(t)$ ($i = 1, 2, \cdots, n$). That is,

$$x_p(t) = \sum_{i=1}^{n} x_{pi}^{(d)}(t) = \sum_{i=1}^{n} \varphi_{pi}g_i(t) \tag{4.3}$$

Considering the ith modal contributions from the pth and q^{th} DOFs, $\varphi_{pi}g_i(t)$ and $\varphi_{qi}g_i(t)$, the instantaneous mode shape can be described by:

$$\left|\frac{\varphi_{pi}}{\varphi_{qi}}\right| = \frac{A_{pi}(t)}{A_{qi}(t)} \tag{4.4}$$

The difference between the phase angles of the pth and q^{th} modal elements φ_{pi} and φ_{qi} can be expressed into $\varphi_{pq}^{i} = \theta_{pi}(t) - \theta_{qi}(t)$, which is in theory equal to either $\pm 2m\pi$ or $\pm(2m+1)\pi$ (m is an integer). In frequency domain, the modal elements can be directly evaluated by:

$$\frac{\varphi_{pi}}{\varphi_{qi}} = \frac{Im[\hat{x}_{pi}^{(d)}(\omega_i)]}{Im[\hat{x}_{qi}^{(d)}(\omega_i)]} \tag{4.5}$$

In Equation (4.5), $\hat{x}_{pi}^{(d)}(\omega_i)$ and $\hat{x}_{qi}^{(d)}(\omega_i)$ are the Fourier transforms of $x_{pi}^{(d)}(t)$ and $x_{qi}^{(d)}(t)$ ($i = 1, 2, \cdots, n$) and *Im[.]* represents the imaginary part of the complex argument inside the square bracket.

4.3.2. Numerical Simulation. Consider a 3-DOF mass-spring-dashpot representation of a classically-damped mechanical system with closely-spaced modes. As shown in Figure 4.24, the system has three masses of $m_1 = m_2 = m_3 = 1000$ kg, four springs with stiffness of $k_1 = k_4 = 40$ kN/m and $k_2 = k_3 = 15$ kN/m, and four dashpots with damping coefficients of $c_1 = c_4 = 120$ N·sec/m and $c_2 = c_3 = 45$ N·sec/m. The system has three natural frequencies of $f_1 = 0.673$ Hz, $f_2 = 1.180$ Hz, and $f_3 = 1.304$ *Hz*. Three damping ratios of the classically-damped system are $\zeta_1 = 0.63\%$, $\zeta_2 = 1.11\%$, and $\zeta_3 = 1.23\%$. The 2nd and 3rd natural frequencies are closely spaced. An impulsive force of 10 kN over 0.02 sec was applied on the mass m_3 at *t*=0 sec. The displacement time histories at three masses were analytically evaluated and used for system identification. A time step of 0.02 sec was used in numerical integrations.

The EMD of the displacement at mass m_3 separated the 1st mode from the 2nd and 3rd, but failed to further separate the 2nd and 3rd modes. With the proposed AMD method, all three modes decomposed from the displacement at the third mass can be separated as indicated in Figures 4.25 and 4.26 in time and frequency domains, respectively. Figure 4.27 presents the amplitude and phase angle of each mode from which the natural frequencies and damping ratios are identified as given in Table 4.1. It is seen from Table 4.1 that the modal parameters of the 2nd mode cannot be identified from the displacement at mass m$_2$ since m$_2$ happens to be the node of the 2nd mode. In comparison with the exact

natural frequencies and damping ratios given in Table 4.1, the identified results are accurate to 1.6% for frequency and less than 1% for damping ratio.
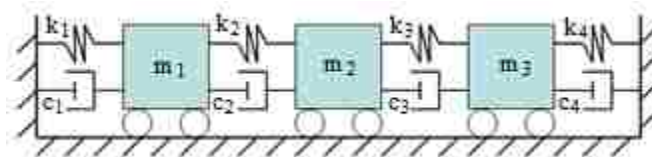
Figure 4.24. 3-DOF Representation of a Mechanical System
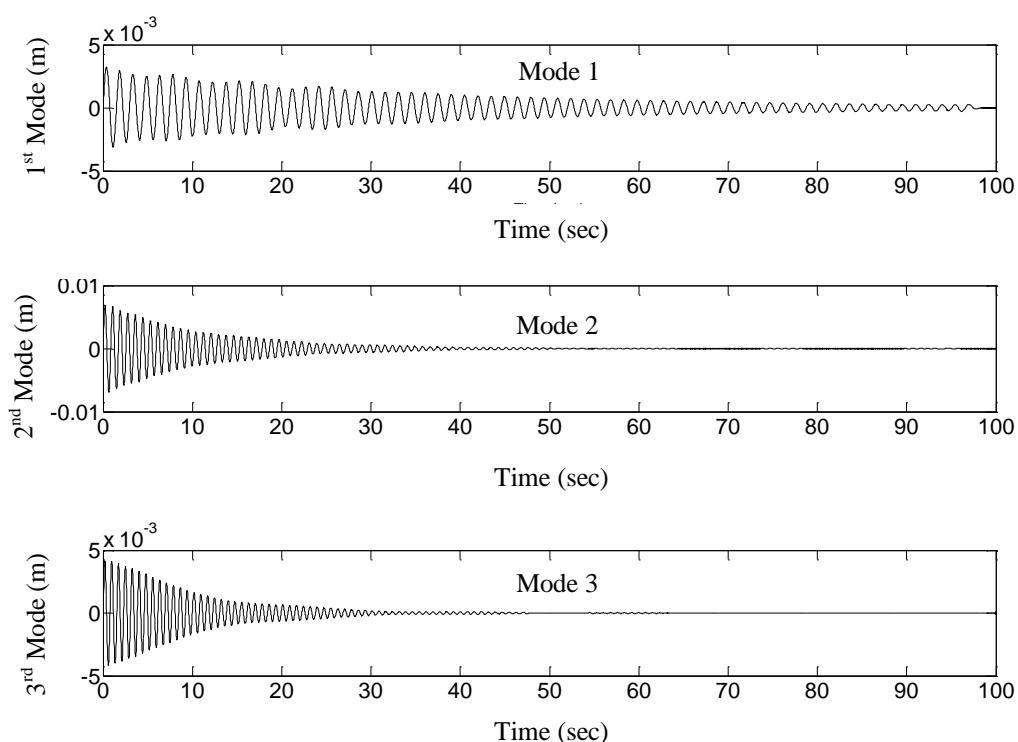
Figure 4.25. Three Modes of Vibration Decomposed by AMD

The instantaneous mode shape identified is presented in Figure 4.28 over different periods of time. This can be explained by the modal responses of vibration as shown in Figure 4.25. The vibration of the 1st mode lasts significantly longer than that of the 2nd mode, which is in turn longer than that of the 3rd mode. The 1st mode shape is more stable after the 2nd and 3rd modes decay for 30 sec. This indicates that, though not visible in Figures 4.25 and 4.26, the 1st mode of vibration decomposed from the system responses was slightly disturbed by the presence of the 2nd and 3rd modes. The accuracy and sign of

the identified modal elements were verified by the difference in phase angles between any two modes. The results presented in Figure 4.28 indicated that the phase difference between any two modes is approximately either $0°$ or $180°$.

For the time-invariant system as shown in Figure 4.24, the modal elements can be directly determined with Equation (4.5). The real and imaginary parts of the Fourier transforms of all DOF displacements are presented in Figure 4.29 for each decomposed mode of vibration. Based on the ratio of the peak value of the imaginary part, the mode matrix $\mathbf{\Phi}$ of the 3-DOF system was identified and compared with its theoretical values below:

$$\mathbf{\Phi}_{identified} = \begin{bmatrix} 1.0 & -1.0 & 1.0 \\ 2.48 & 0 & -0.80 \\ 1.0 & 1.0 & 1.0 \end{bmatrix} \text{ and } \mathbf{\Phi}_{theoretical} = \begin{bmatrix} 1.0 & -1.0 & 1.0 \\ 2.47 & 0 & -0.81 \\ 1.0 & 1.0 & 1.0 \end{bmatrix}$$

It is clearly seen that the identified mode matrix is accurate with a maximum error of 1.25%. The 2nd mode is symmetric about mass m_2 due to the symmetry of the 3-DOF system. The 1st and 3rd modes have masses m_1 and m_3 moving in the same amount but mass m_2 in the same or opposite direction as m_1 and m_3.
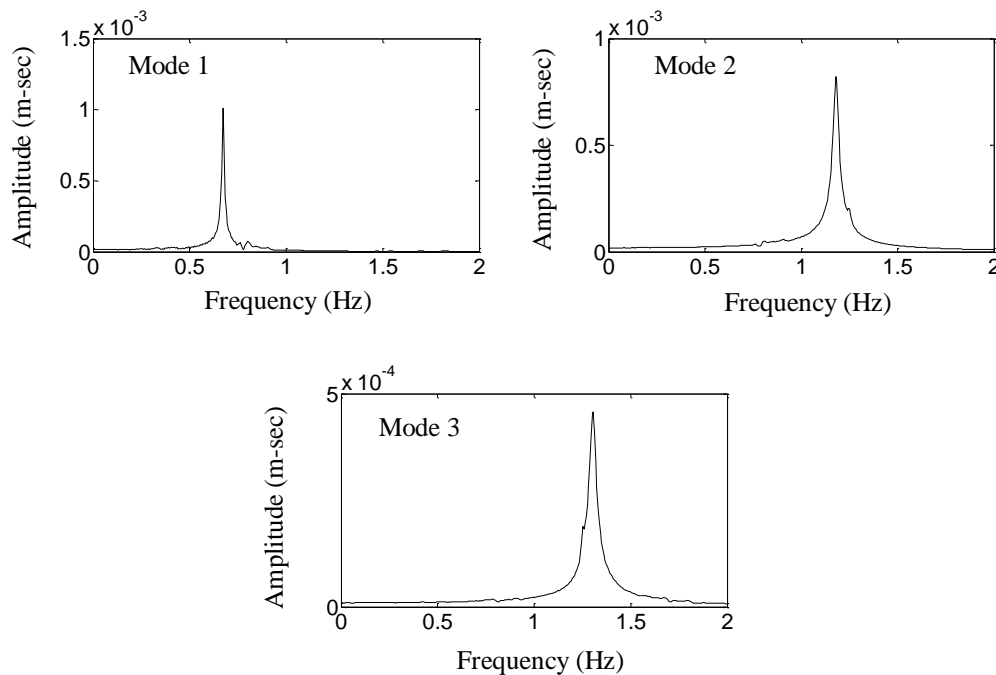
Figure 4.26. Fourier Spectra of the Decomposed Modes of Vibration by AMD

(a) Mode 1

(b) Mode 2

(c) Mode 3
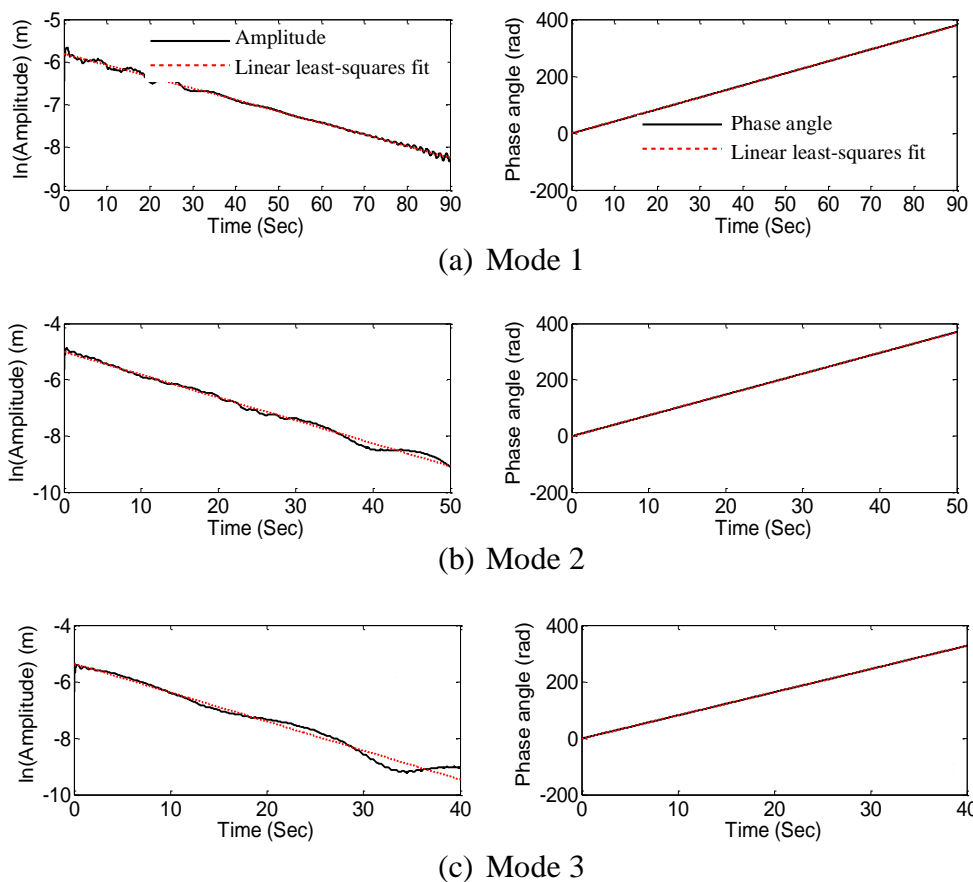
Figure 4.27. Amplitude and Phase angle of Hilbert Transforms

Table 4.1. Identified Natural Frequencies and Damping Ratios by AMD

Mode	Displacement on m_1		Displacement on m_2		Displacement on m_3		Exact	
	Damping ratio (%)	Frequency (Hz)	Damping ratio (%)	Frequency (Hz)	Damping ratio (%)	Frequency (Hz)	Damping ratio (%)	Frequency (Hz)
1	0.63	0.673	0.64	0.673	0.64	0.673	0.63	0.673
2	1.11	1.180	-	-	1.11	1.181	1.11	1.180
3	1.24	1.304	1.24	1.304	1.23	1.304	1.23	1.304
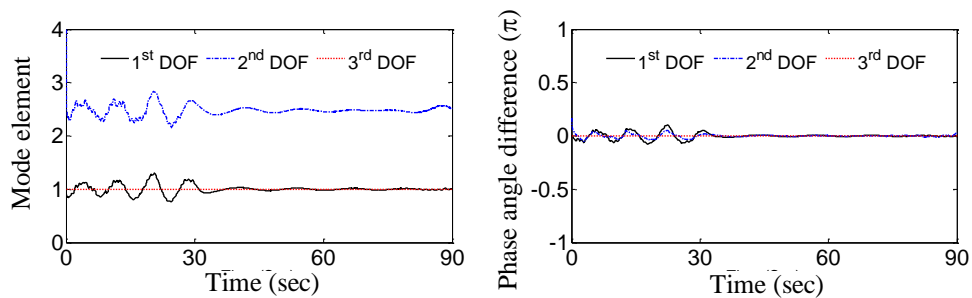
(a) Mode 1
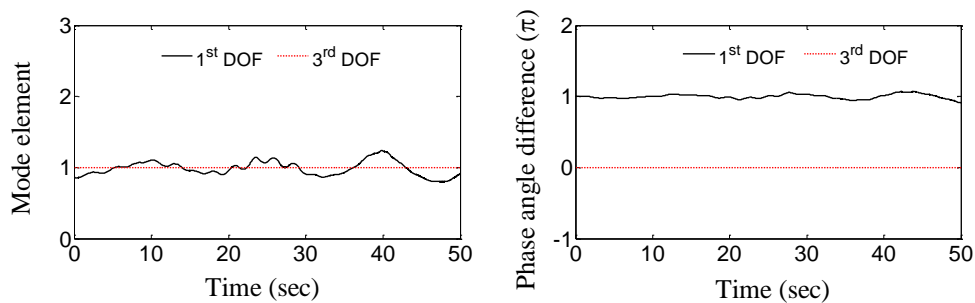
(b) Mode 2
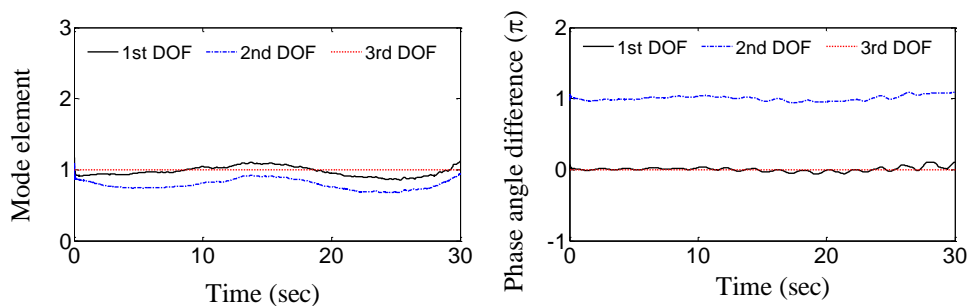
(c) Mode 3

Figure 4.28. Instantaneous Mode Shapes Identified From the Amplitude of Hilbert Transforms

(a) Mode 1

(b) Mode 2

(c) Mode 3
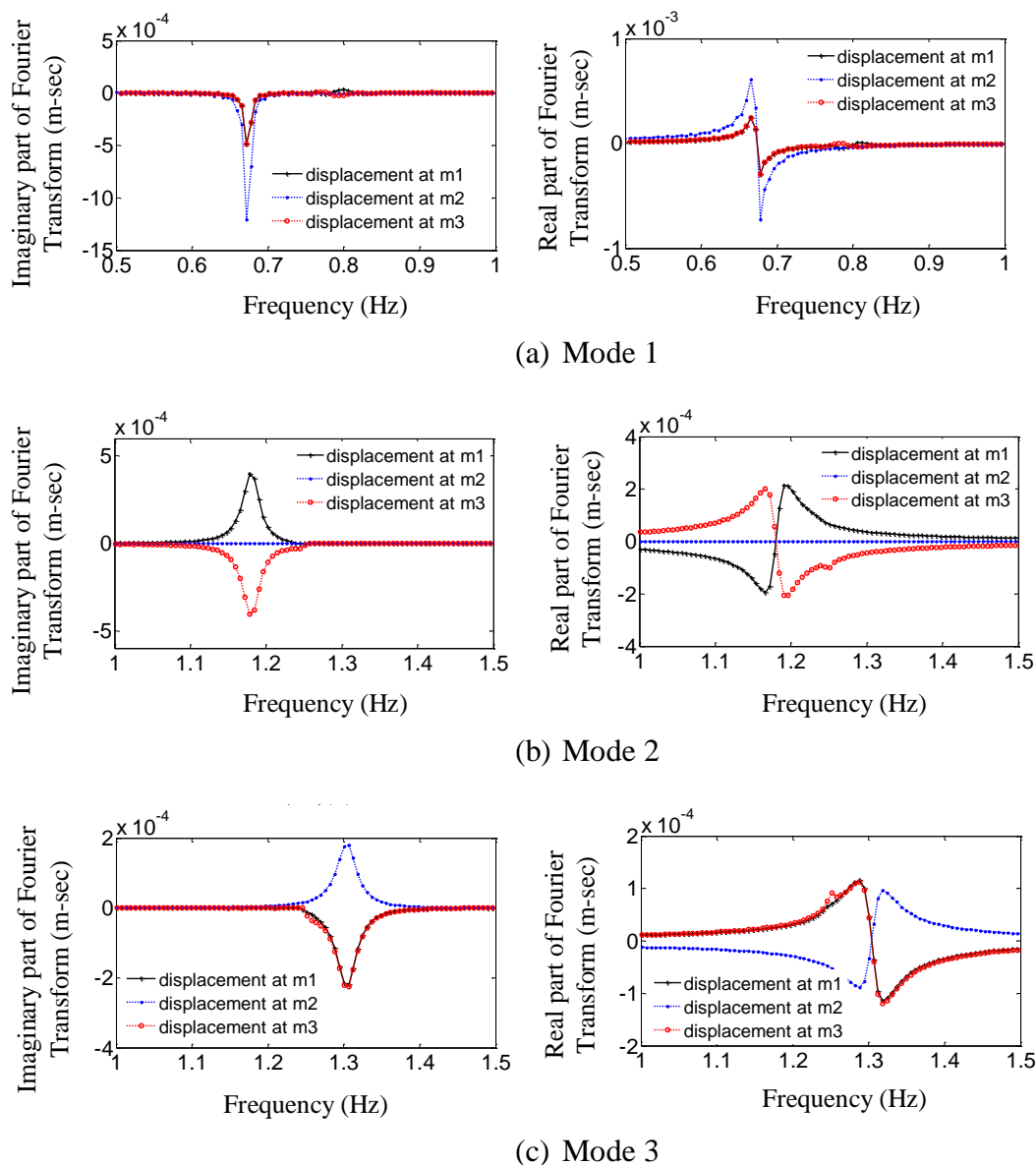
Figure 4.29. Fourier Transform of Three Modes of Vibration Decomposed by AMD

4.4. MODAL PARAMETER IDENTIFICATION FROM FORCE VIBRATION

4.4.1. Transient Response. Consider a single-DOF system with mass, damping and stiffness coefficients equal to $m, c,$ and k, respectively. Under a harmonic excitation $f(t) = F_0 sin(\omega t)$, the equation of motion can be expressed into:

$$m\ddot{x}(t) + c\dot{x}(t) + kx(t) = f(t) \tag{4.6}$$

The complete solution for the displacement response $x(t)$ can be written as (Chopra, 2007):

$$x(t) = e^{-\zeta \omega_n t}[A\cos(\omega_D t) + B\sin(\omega_D t)] + C\sin(\omega t) + D\cos(\omega t) \quad (4.7)$$

in which $\omega_n = \sqrt{k/m}$ is the natural frequency, $\omega_D = \omega_n\sqrt{1-\zeta^2}$, and ζ is the damping ratio, which is equal to $\zeta = c/2m\omega_n$.

As a particular solution of Equation (4.6), the second term of Equation (4.7) represents the steady state response of the system, denoted by $x_s(t)$:

$$x_s(t) = C\sin(\omega t) + D\cos(\omega t) \quad (4.8)$$

The coefficients C and D can be solved by substituting Equation (4.8) into Equation (4.6), which yields:

$$C = \frac{F_0}{k}\frac{1-(\frac{\omega}{\omega_n})^2}{[1-(\frac{\omega}{\omega_n})^2]^2+[2\zeta\frac{\omega}{\omega_n}]^2} \quad \text{and} \quad D = \frac{F_0}{k}\frac{-2\zeta\frac{\omega}{\omega_n}}{[1-(\frac{\omega}{\omega_n})^2]^2+[2\zeta\frac{\omega}{\omega_n}]^2} \quad (4.9)$$

As a general solution of Equation (4.6), the first term of Equation (4.7) represents the transient response of the system, designated by $x_t(t)$:

$$x_t(t) = e^{-\zeta \omega_n t}[A\cos(\omega_D t) + B\sin(\omega_D t)] \quad (4.10)$$

The coefficients A and B can be solved based on the initial displacement $x(0)$ and initial velocity $\dot{x}(0)$. They are written as:

$$A = x(0) - \frac{F_0}{k}\frac{-2\zeta\frac{\omega}{\omega_n}}{[1-(\frac{\omega}{\omega_n})^2]^2+[2\zeta\frac{\omega}{\omega_n}]^2} \text{ and } B = \frac{\dot{x}(0)+\zeta\omega_n x(0)}{\omega_D} - \frac{F_0}{k}\frac{\omega}{\omega_D}\frac{-2\zeta^2+[1-\left(\frac{\omega}{\omega_n}\right)^2]}{[1-(\frac{\omega}{\omega_n})^2]^2+[2\zeta\frac{\omega}{\omega_n}]^2} \quad (4.11)$$

When the excitation frequency is not equal to the natural frequency, AMD can be used to extract the transient response from a displacement measurement. The extracted transient response can then be used for the identification of natural frequency and damping ratio of the system following Equation (4.2).

For a linear *n*-DOF system, the equation of motion can be written as:

$$\mathbf{M}\ddot{x}(t) + \mathbf{C}\dot{x}(t) + \mathbf{K}x(t) = \mathbf{f}(t) \quad (4.12)$$

where $\mathbf{M}$, $\mathbf{C}$, and $\mathbf{K}$ are mass, damping, and stiffness matrices, respectively; $\mathbf{f}(t)$ is the external load vector; $\mathbf{x}(t)$ is the displacement vector. By introducing modal coordinate vector $\mathbf{q} = \{q_1, q_2, \ldots, q_n\}^T$, the displacement vector can be expressed into:

$$\mathbf{x}(t) = \mathbf{\Phi}\mathbf{q} \quad (4.13)$$

in which $\mathbf{\Phi}$ is the mode shape matrix. When classical damping is considered, each of the *n* decoupled equations in modal space can be written as:

$$M_i \ddot{q}_i + C_i \dot{q}_i + K_i q_i = F_i \quad (i = 1, 2, \ldots, n) \tag{4.14}$$

where M_i, C_i, K_i, and F_i are the ith modal mass, damping, stiffness and excitation, which in turn can be expressed into:

$$M_i = \emptyset_i^T \mathbf{M} \emptyset_i \ , \ C_i = \emptyset_i^T \mathbf{C} \emptyset_i \ , \ K_i = \emptyset_i^T \mathbf{K} \emptyset_i \ , \ F_i = \emptyset_i^T \mathbf{f} \tag{4.15}$$

in which $\emptyset_i$ is the ith mode shape vector.

Under a harmonic excitation, $\mathbf{f}(t) = \mathbf{F}_0 \sin(\omega t)$, the steady state response $q_i^s(t)$ of Equation (4.14) can be expressed into:

$$q_i^s(t) = C_i \sin(\omega t) + D_i \cos(\omega t) \tag{4.16}$$

$$C_i = \frac{\emptyset_i^T \mathbf{F}_0}{K_i} \frac{1 - (\frac{\omega}{\omega_i})^2}{[1 - (\frac{\omega}{\omega_i})^2]^2 + [2\zeta_i \frac{\omega}{\omega_i}]^2} \ , \qquad D_i = \frac{\emptyset_i^T \mathbf{F}_0}{K_i} \frac{-2\zeta_i \frac{\omega}{\omega_i}}{[1 - (\frac{\omega}{\omega_i})^2]^2 + [2\zeta_i \frac{\omega}{\omega_i}]^2} \tag{4.17}$$

in which $\omega_i = \sqrt{K_i/M_i}$ is the ith natural frequency, $\zeta_i = c_i/2M_i\omega_i$ is the ith damping ratio, and $\omega_{Di} = \omega_i \sqrt{1 - \zeta_i^2}$ is the ith natural frequency with damping effect.

The transient response of Equation (4.14) is given by:

$$q_i^t(t) = e^{-\zeta_i \omega_i t}[A_i \cos(\omega_{Di} t) + B_i \sin(\omega_{Di} t)] \tag{4.18}$$

$$A_i = q_i(0) - \frac{\emptyset_i^T \mathbf{F}_0}{K_i} \frac{-2\zeta_i \frac{\omega}{\omega_i}}{[1 - (\frac{\omega}{\omega_i})^2]^2 + [2\zeta_i \frac{\omega}{\omega_i}]^2} \text{ and } B_i = \frac{\dot{q}_i(0) + \zeta_i \omega_i q_i(0)}{\omega_{Di}} - \frac{\emptyset_i^T \mathbf{F}_0}{K_i} \frac{\omega}{\omega_{Di}} \frac{-2\zeta_i^2 + [1 - (\frac{\omega}{\omega_i})^2]}{[1 - (\frac{\omega}{\omega_i})^2]^2 + [2\zeta_i \frac{\omega}{\omega_i}]^2}$$

$$\tag{4.19}$$

The initial modal displacement $q_i(0)$ and initial modal velocity $\dot{q}_i(0)$ can be solved from the initial displacement $\mathbf{x}(0)$ and velocity $\dot{\mathbf{x}}(0)$:

$$q_i(0) = \frac{\emptyset_i^T \mathbf{M} \mathbf{x}(0)}{M_i}, \ \dot{q}_i(0) = \frac{\emptyset_i^T \mathbf{M} \dot{\mathbf{x}}(0)}{M_i} \tag{4.20}$$

The complete solution of Equation (4.12) can then be written as:

$$\mathbf{x}(t) = \sum_{i=1}^{n} \emptyset_i \ q_i^t(t) + \sum_{i=1}^{n} \emptyset_i \ q_i^s(t) \tag{4.21}$$

The steady state response can first be extracted from a displacement measurement by AMD. The remaining transient response in Equation (4.21) can further be decomposed into a summation of the modal responses. Finally, the modal parameters (natural frequency and damping ratio) can be identified using Equation (4.2).

4.4.2. Numerical Examples with Harmonic Excitations. In this section, a single-DOF system and a 3-DOF system are analyzed as numerical examples to illustrate modal parameter identification from transient response.

4.4.2.1 Single-DOF system. A single-DOF system with mass m = 1000 kg, damping coefficient c = 200 N · sec/m and stiffness k = 40 kN/m is subjected to a harmonic excitation $f(t) = 10sin(3\pi t)$ kN. The system has natural frequency $f = 1.0\ Hz$ and damping ratio $\zeta = 1.58\%$. The numerically simulated displacement, velocity and acceleration responses and their Fourier spectra are presented in Figure 4.30 and Figure 4.31, respectively. It can be clearly seen from Figure 4.30 that the responses at the beginning include the transient components related to free vibration. Indeed, two peaks can be clearly seen in Figure 4.31. They represent the steady state response at the excitation frequency of 1.5 Hz and the transient response with natural frequency of 1.0 Hz, respectively. A sampling rate of 50 Hz was used in simulation.
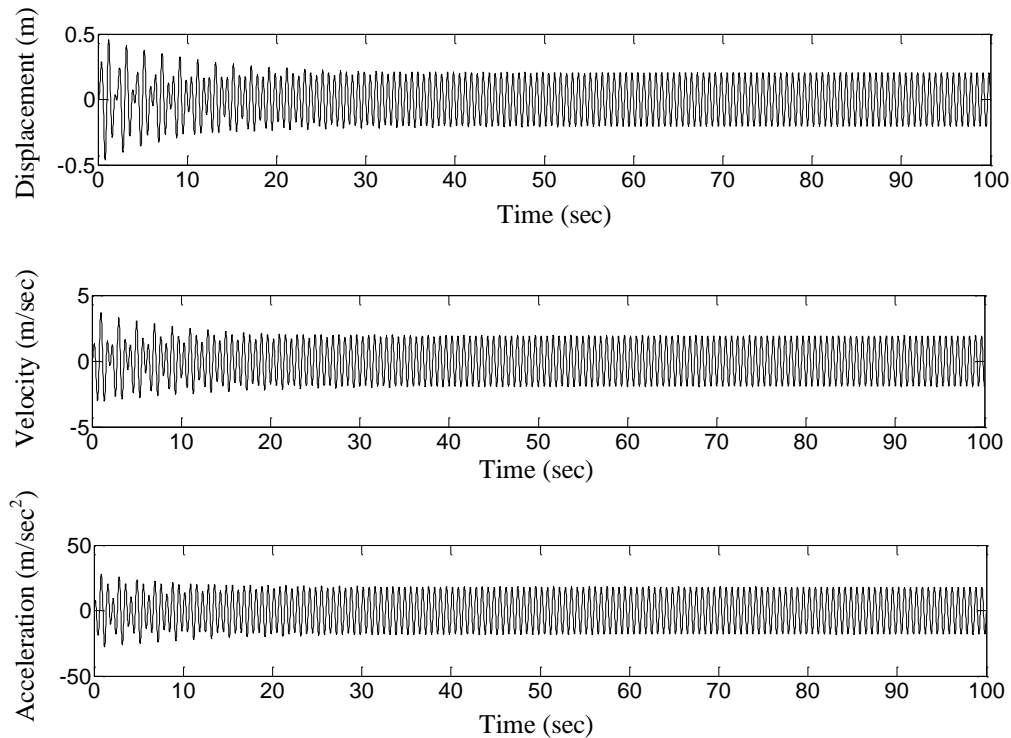
Figure 4.30. Displacement, Velocity, and Acceleration Responses
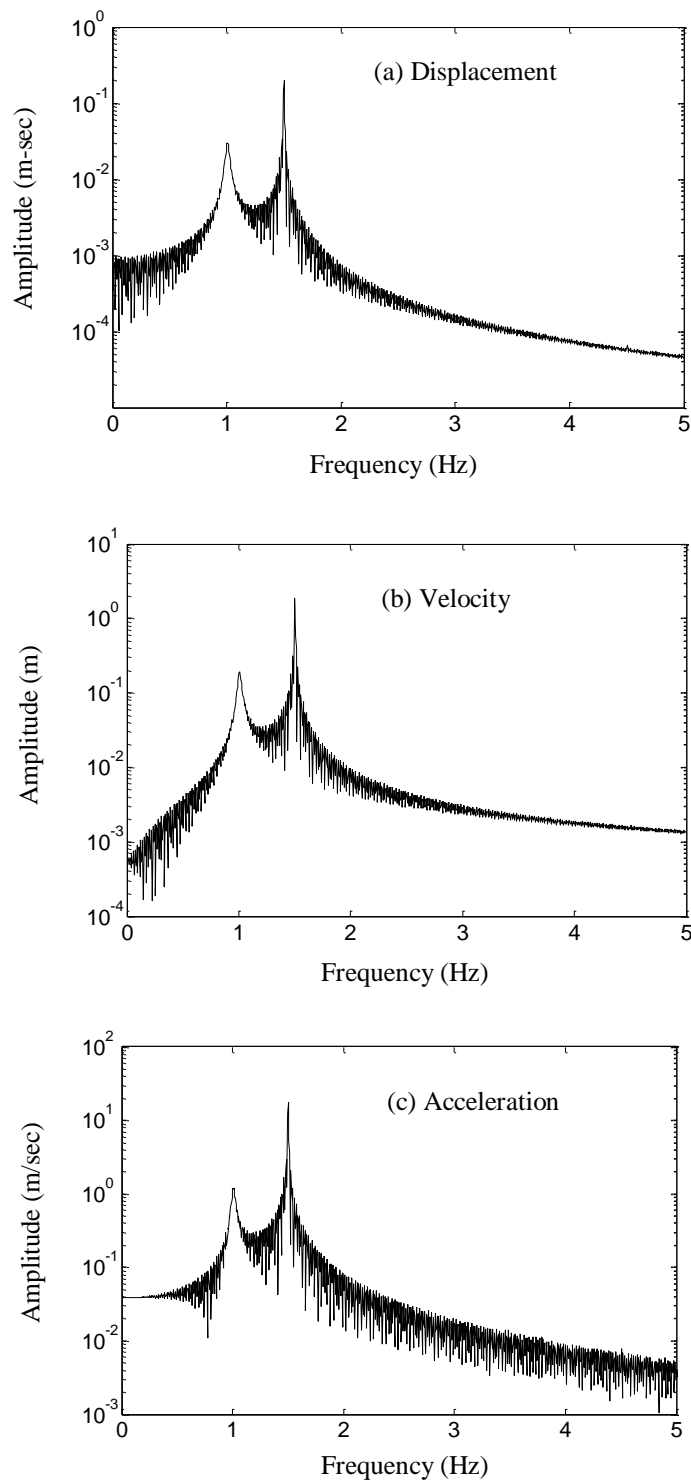
Figure 4.31. Fourier Spectra of Displacement, Velocity, and Acceleration Responses

To separate the transient response from the steady state response, a bisecting frequency of 1.25 Hz was taken as the average of the excitation and theoretical natural frequencies. The decomposed transient and steady state responses by AMD are presented in Figure 4.32 and their Fourier spectra are in Figure 4.33. Figure 4.34 shows the amplitude and phase angle of the transient response, from which the natural frequency and damping ratio are determined to be 1.0 Hz and 1.59%, respectively. The identified results are in excellent agreement with the exact natural frequency and damping ratio.
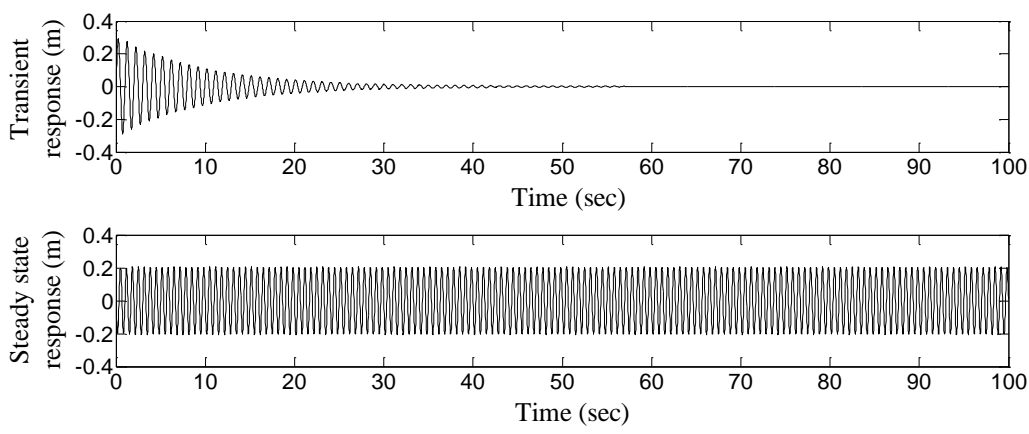
Figure 4.32. Extracted Transient and Steady State Displacement by AMD
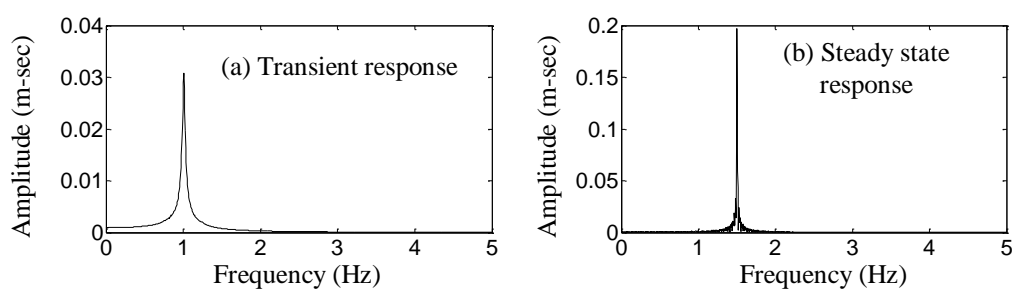
Figure 4.33. Fourier Spectra of Transient and Steady State Displacement
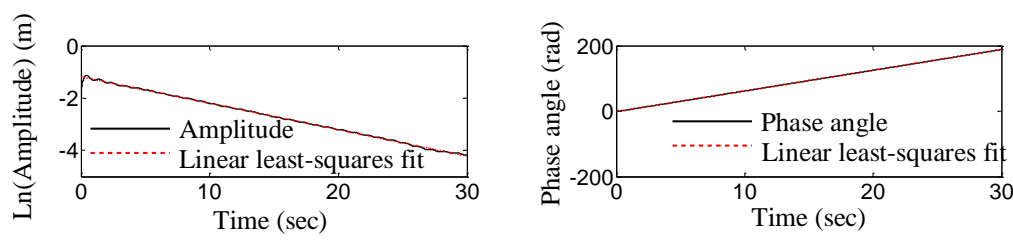
Figure 4.34. Amplitude and Phase Angle of Analytic Signal

To study the noise effect, a Gaussian white noise with a noise-to-signal ratio of 10% was injected to the simulated displacement. The noise contaminated displacement is presented in Figure 4.35. The decomposed transient response and steady state response from the contaminated displacement with a bisecting frequency of 1.25 Hz are presented in Figure 4.36, and their Fourier spectra are in Figure 4.37. Figure 4.38 shows the amplitude and phase angle of the noise contaminated transient response, from which the natural frequency and damping ratio are identified to be 1.0 Hz and 1.55%. Once again, they are in excellent agreement with the exact values. Therefore, the modal parameters can be identified with high accuracy from the transient response of force vibration even with the presence of significant noise.
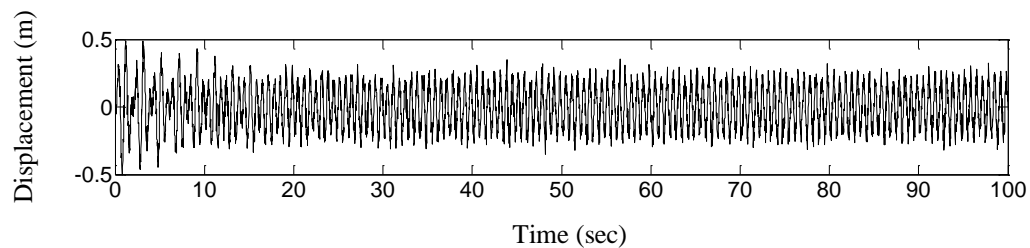
Figure 4.35. Displacement Response with 10% Gaussian White Noise
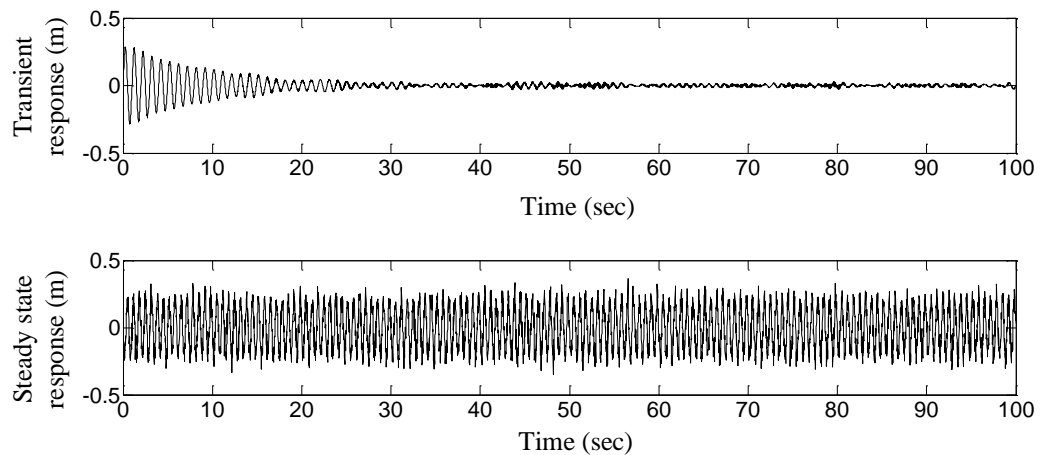
Figure 4.36. Extracted Noise Polluted Transient and Steady State Displacement by AMD
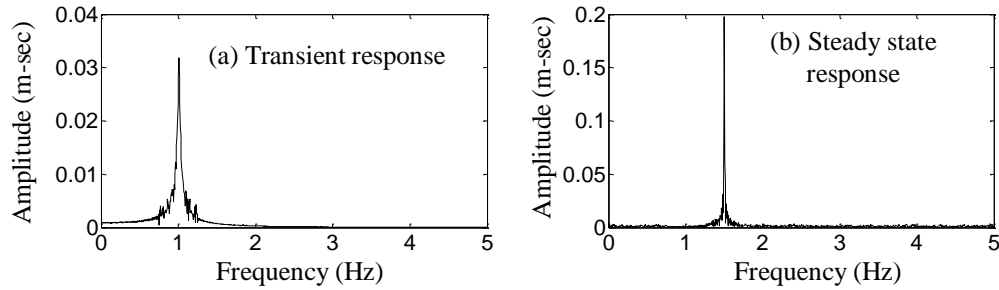
Figure 4.37. Fourier Spectra of Noise Polluted Transient and Steady State Displacement
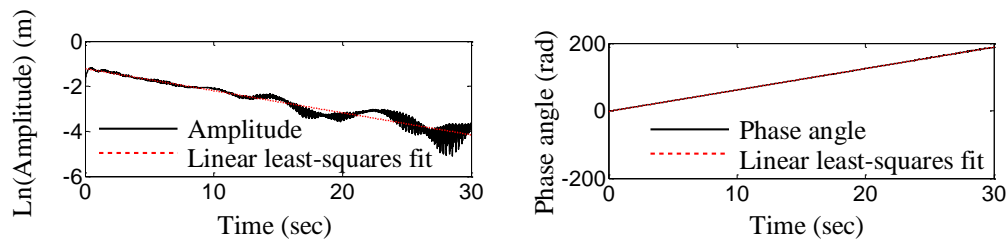
Figure 4.38. Amplitude and Phase Angle of Analytic Signal with 10% Noise

4.4.2.2 3-DOF mechanical system. The same 3-DOF mechanical system as presented in Section 4.3.2 was subjected to a harmonic excitation $f(t) = 10sin(3\pi t)$ kN applied on m_3. Initially, the system was in equilibrium position at rest. The numerically simulated displacement responses at various masses, as shown in Figure 4.39 for m_3 with a sample rate of 50 Hz, were used for parameter identification. The Fourier spectrum of the displacement at m_3 is presented in Figure 4.40. It can be clearly seen from Figures 4.39 and 4.40 that the displacement response includes the steady state response component with the excitation frequency and the transient response component with three natural frequencies. To extract the transient modal responses, the steady state response component was first extracted from the total displacement. Since the transient response component attenuates rapidly over time, the later displacement response represents the steady state response component from which the excitation frequency can be easily identified. In this example, the excitation frequency is 1.5 Hz, corresponding to the maximum peak in the Fourier spectrum.
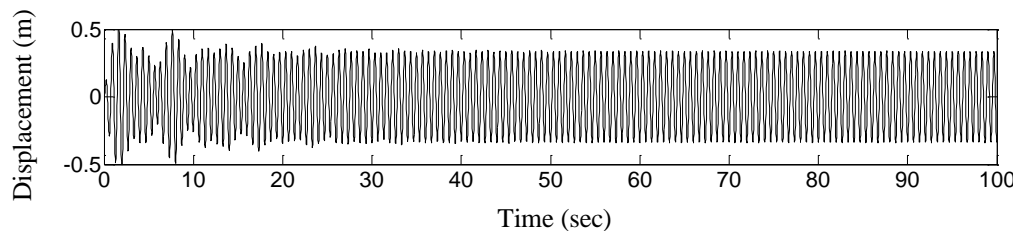
Figure 4.39. Displacement at m_3
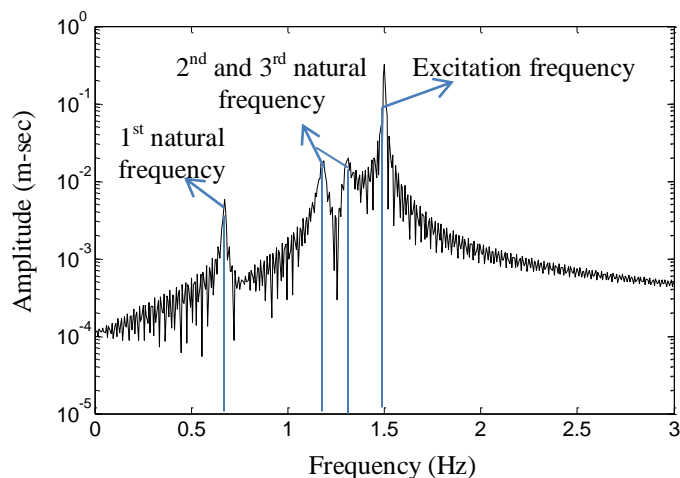
Figure 4.40. Fourier Spectrum of Displacement at m_3

A bisecting frequency of 1.4 Hz in AMD was selected to separate the transient and steady state response components as presented in Figure 4.41. The transient response was further decomposed into three modes by AMD with two bisecting frequencies of 0.92 Hz and 1.25 Hz, respectively. The extracted modal responses or free vibration are shown in Figure 4.42. The amplitude $A_{3i}(\tau)$ and phase angle $\theta_{3i}(\tau)$ (i =1, 2, 3) of each modal response are shown in Figure 4.43. The natural frequencies and damping ratios are further identified and listed in Table 4.2. It is seen from Table 4.2 that the modal parameters of the 2nd mode cannot be identified from the displacement at mass m_2 since m_2 happens to be at the node of the 2nd mode. In comparison with the exact natural frequencies and damping ratios given in Table 4.1, the identified results are accurate to 2% for frequency and less than 24% for damping ratio.
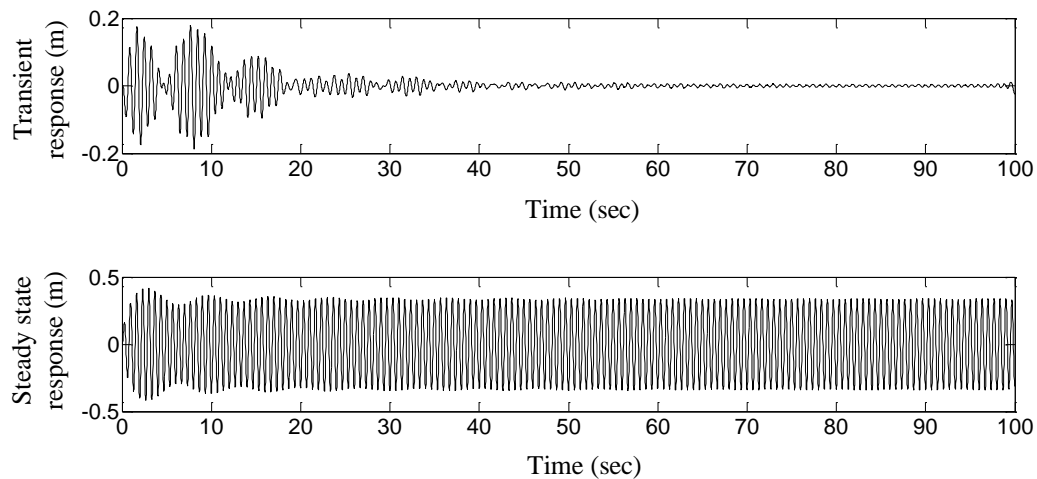
Figure 4.41. Extracted Transient and Steady State Displacement using AMD
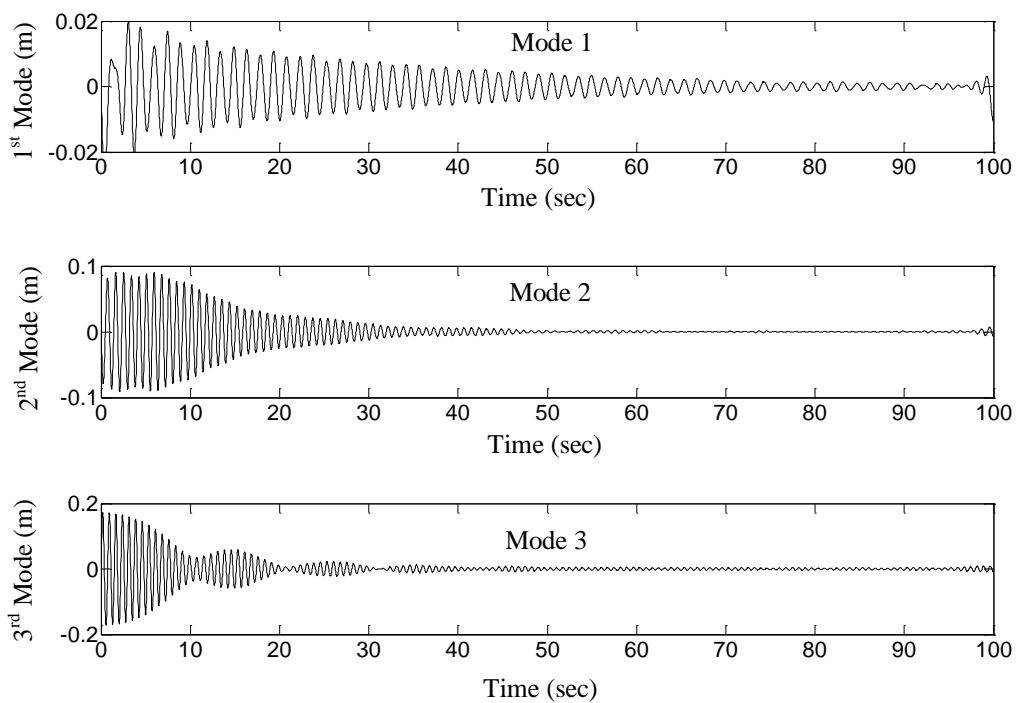
Figure 4.42. Extracted Modal Responses from the Transient Displacement using AMD

(a) Amplitude   (b) Phase Angle (rad)
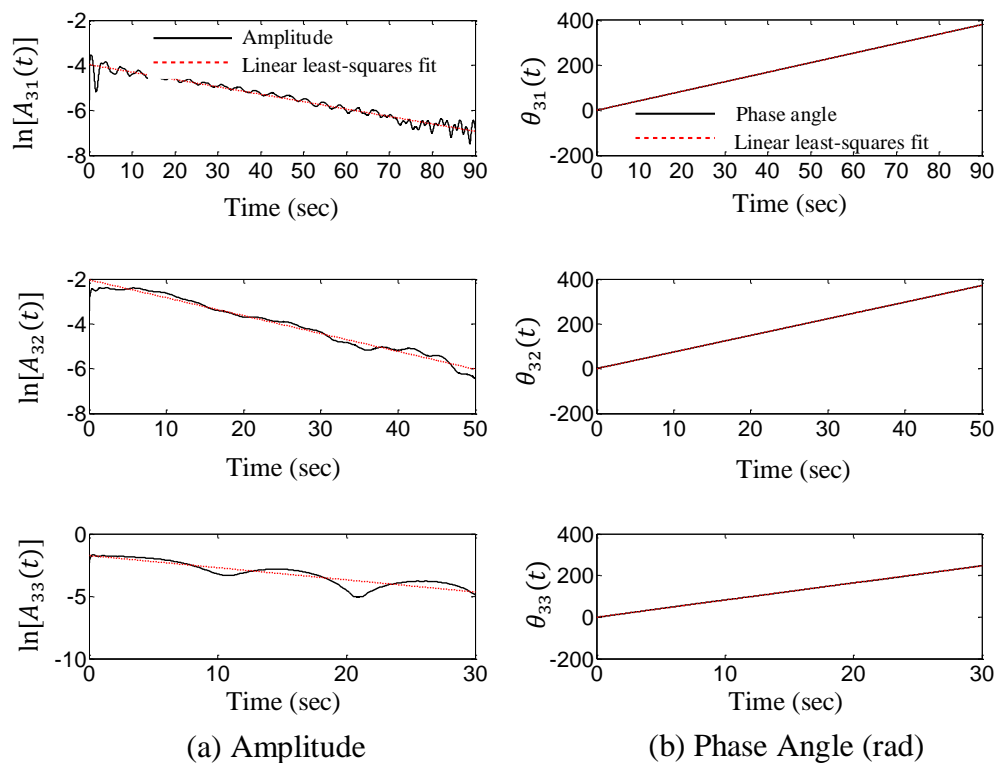
Figure 4.43. Amplitude and Phase Angle of the Modal Responses

Table 4.2. Identified Natural Frequencies and Damping Ratios from Force Vibration

Mode	Displacement on m_1		Displacement on m_2		Displacement on m_3		Exact	
	Damping ratio (%)	Frequency (Hz)	Damping ratio (%)	Frequency (Hz)	Damping ratio (%)	Frequency (Hz)	Damping ratio (%)	Frequency (Hz)
1	0.73	0.673	0.71	0.673	0.78	0.673	0.63	0.673
2	1.10	1.183	-	-	1.08	1.181	1.11	1.180
3	1.12	1.300	1.16	1.302	1.18	1.308	1.23	1.304

4.5. MODAL PARAMETER IDENTIFICATION FROM AMBIENT VIBRATION

The modal parameters of structures can be identified from ambient vibration in three steps by combining EMD with the random decrement technique (RDT) (Chen and Xu, 2002; Yang and Lei, 2000; Cole, 1968). First, a structural response is decomposed into many modal responses using a signal decomposition method such as EMD. Each modal response is then sampled to obtain a large number of short-time responses starting

at a common threshold value, whose average response resembles the free vibration of the structure. Finally, the average response (free vibration) is used to identify modal parameters. In this section, AMD will be used in combination with RDT, called RDT-AMD method, to identify the parameters of closely-spaced modes from ambient vibration.

4.5.1. The RDT-AMD Method. Under a broadband excitation, each modal response is narrow banded in frequency domain. As the two natural frequencies of a building approach to each other, their corresponding frequency response functions overlap in a certain frequency range. Under ambient vibration, this modal interaction cannot be properly taken into account in AMD though AMD is effective to separate close natural modes (or natural frequencies) included in free vibration. Therefore, this study proposes that RDT be first introduced to the ambient responses so that the interaction effect between closely-spaced vibration modes can be removed from the extracted free vibration.

The RDT process outputs the average free vibration response over a significantly shorter period of time than the duration of a structural response. As a result, the frequency resolution after RDT is significantly reduced. To further separate closely-spaced modes from the free vibration, an advanced signal decomposition technique such as AMD is required. Therefore, the proposed RDT-AMD method combines the advantages of RDT and AMD in dealing with modal interaction and accurate decomposition issues in system identification from ambient vibration.

In the RDT-AMD method, a displacement response time history at each time instant is considered to result from three effects: initial displacement, initial velocity, and white noise excitation. The effect from the random input will disappear as a large number of the short-time response segments, sampled with the same initial condition, are taken and averaged. Therefore, the average response segment represents the free vibration of the structure due to the initial condition. In applications, a threshold displacement level is preset and N response segments starting at the threshold displacement are taken. The free vibration response can be obtained by:

$$x^f(\tau) = \frac{1}{N}\sum_{i=1}^{N} x^t(t_i + \tau) \ (0 \leq \tau \leq t_{Seg}) \tag{4.22}$$

where $x^t(t_i + \tau)$ is the ambient vibration response, t_i is the starting time for each segment, t_{Seg} is the duration of all segments, and $x^f(\tau)$ represents the free vibration due to the combined modal responses.

AMD is then applied to decompose the free vibration response $x^f(\tau)$ into many components, each with a single frequency corresponding to one modal response of free vibration. Similar to Section 4.3, the instantaneous amplitude and phase angle of each decomposed mode can be determined, from which the instantaneous frequency and damping ratio of the structure can be evaluated using the least-square fit procedure. The instantaneous mode shape is also related to the ratio between two instantaneous amplitude.

4.5.2. Parametric Study of RDT-AMD Method. In this section, sensitivity analyses are conducted to address the effectiveness of the proposed RDT-AMD method for closely-spaced modal parameter identification from ambient vibration.

4.5.2.1 Frequency space index. The same frequency space index γ as defined by Chen and Xu (2002) is used here. That is:

$$\gamma = \frac{\omega_{i+1} - \omega_i}{\omega_{i+1} + \omega_i} \tag{4.23}$$

where ω_i and ω_{i+1} are two close natural frequencies. The smaller the space index, the closer the two corresponding modes of vibration. To measure the accuracy of a decomposed response, an energy error index is introduced and defined by:

$$Error = \frac{\int_0^T [x_i^{(d)}(t) - x_{i,exact}(t)]^2 dt}{\int_0^T [x_{i,exact}(t)]^2 dt} \tag{4.24}$$

where $x_i^{(d)}(t)$ and $x_{i,exact}(t)$ represent the ith decomposed response and exact response. Use of the response difference in the numerate of Equation (4.24) ensures that it accounts for the effect of both amplitude and phase of the decomposed response.

To quantify the frequency resolution of the AMD between two modes of vibration, a two-story building with closely-spaced natural frequencies was analyzed under an impulsive load or a Gaussian white noise excitation applied on the top floor. As shown in Figure 4.44, m_1 and m_2 represent the masses of the first and second floors, k_1 and k_2 represent the interval stiffness coefficients of the first and second stories, and c_1 and c_2 are corresponding damping coefficients. In this study, Rayleigh damping was

considered with a damping ratio of ζ for both modes of vibration. The first and second natural frequencies are represented by f_1 and f_2, respectively. Various cases with different building properties are given in Table 4.3.
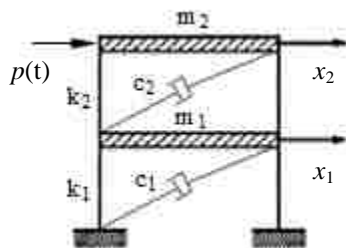
Figure 4.44. Two-Story Building Example

Table 4.3. Properties of the Two-Story Building

Case	k_1 (N-m)	k_2 (N-m)	m_1 (kg)	m_2 (kg)	f_1 (Hz)	f_2 (Hz)	ζ	γ
1		50		0.167	2.544	2.886		0.063
2		40		0.133	2.562	2.872		0.057
3	3256	30	11.6	0.100	2.579	2.850	1%	0.050
4		20		0.067	2.598	2.823		0.042
5		15		0.050	2.612	2.814		0.037
6		10		0.033	2.629	2.810		0.033

For ambient vibration, the Gaussian white noise excitation $p(t)$ has zero mean and a standard deviation of 1 N. The responses of the building were simulated for 1000 sec. at 0.05 sec. interval. For comparison with the ambient vibration effect on the frequency resolution, an impulsive load $p(t)$ of 1 N was suddenly applied at t=0 to generate free vibration. The time duration of all free vibration simulations was considered 20 sec. with a time interval of 0.01 sec.

The decomposed modal responses by the AMD method and by the bandpass filtering technique with multiple rectangular windows in the frequency domain are compared with the exact modal responses based on the energy error index defined in Equation (4.24). The cutoff frequencies selected in bandpass filters were equal to the bisecting frequencies used with the AMD method. The decomposed responses of the first mode with AMD and bandpass filtering methods are compared in Figure 4.45 with the

exact modal response for free and ambient vibration, respectively. In general, the AMD is more accurate than the bandpass filtering technique, particularly at the beginning and end of the free vibration.
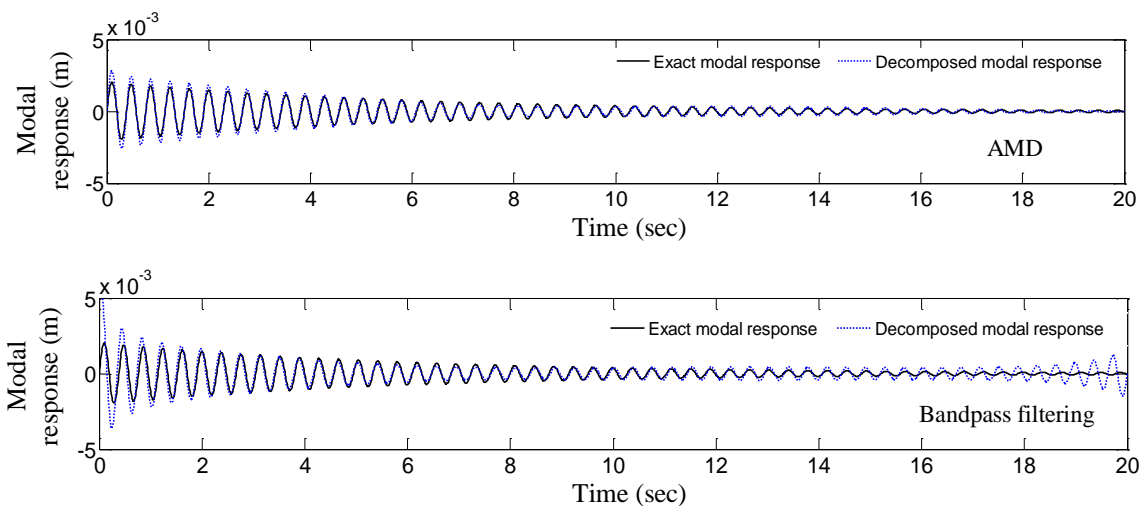
(a) Free Vibration
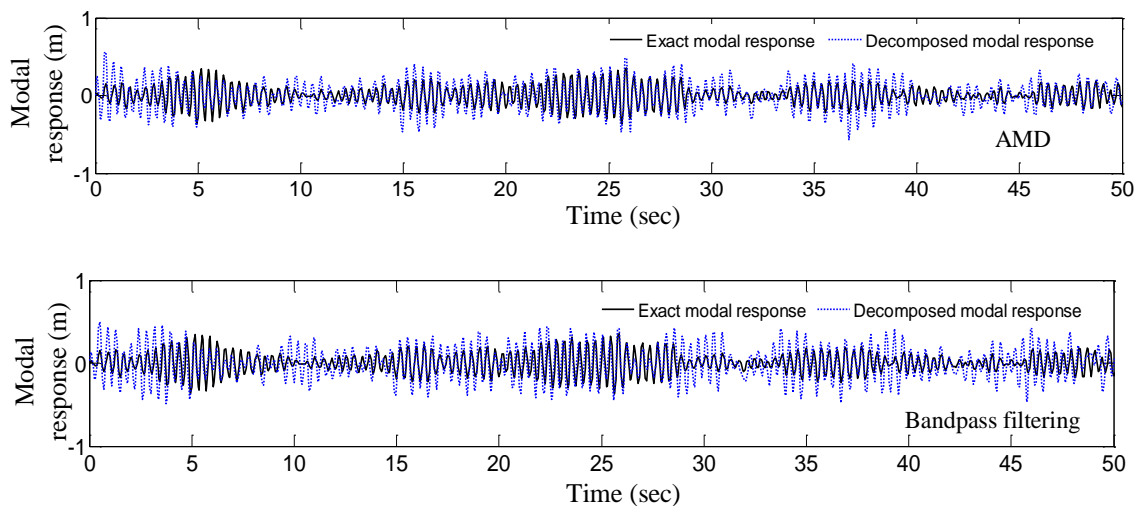
(b) Ambient Vibration

Figure 4.45. Exact and Decomposed Responses of the First Mode from AMD and Bandpass Filtering Methods

The energy error index for each mode of vibration is plotted in Figure 4.46 as a function of frequency space index. For free vibration as shown in Figure 4.46(a), the AMD method results in an energy error index of approximately 7.5% for Mode 1 and 1%

for Mode 2 when $\gamma = 0.033$, while the bandpass filtering method leads to 77% for Mode 1 and 7% for Mode 2. The main difference between the two methods is attributed to the brick wall effect at the two ends of a bandpass filter. Use of a 20-sec. time series corresponds to the frequency resolution of 0.05 Hz. As such, applying a rectangular window in frequency domain distorts the time series with an infinite duration. The brick wall effect associated with the frequency bandpass filtering doesn't exist with the AMD method. If 5% is set for an acceptable energy error index, the AMD and the bandpass filtering methods can separate two natural frequencies with $\gamma = 0.037$ and 0.063, respectively.

For ambient vibration as shown Figure 4.46(b), the AMD method gives an energy error index of 88% for Mode 1 and 10% for Mode 2 when $\gamma = 0.033$, while the bandpass filtering method results in 118% for Mode 1 and 14% for Mode 2. Corresponding to a 5% energy error index, two natural frequencies with $\gamma < 0.063$ cannot be discerned with both methods. Overall, the energy error index for ambient vibration is significantly larger than that for free vibration. This is because, unlike free vibration, the modal response under ambient excitations is actually a narrow band response instead of a mono-frequency response. Therefore, as γ becomes small, the two closely-spaced modal responses overlap each other over a certain frequency range. Figure 4.47 illustrates this point with the Fourier spectra of Modes 1 and 2. The Fourier spectrum of Mode 2 significantly affects that of Mode 1 at the fundamental frequency; the amplitude from Mode 2 is larger than 50% of the amplitude from Mode 1. However, at the second natural frequency, the amplitude from Mode 1 is negligible compared to that of Mode 2. This is the reason why the energy error for Mode 1 is significantly greater than that for Mode 2 in all cases as shown in Figure 4.46.

(a) Free Vibration

(b) Ambient Vibration
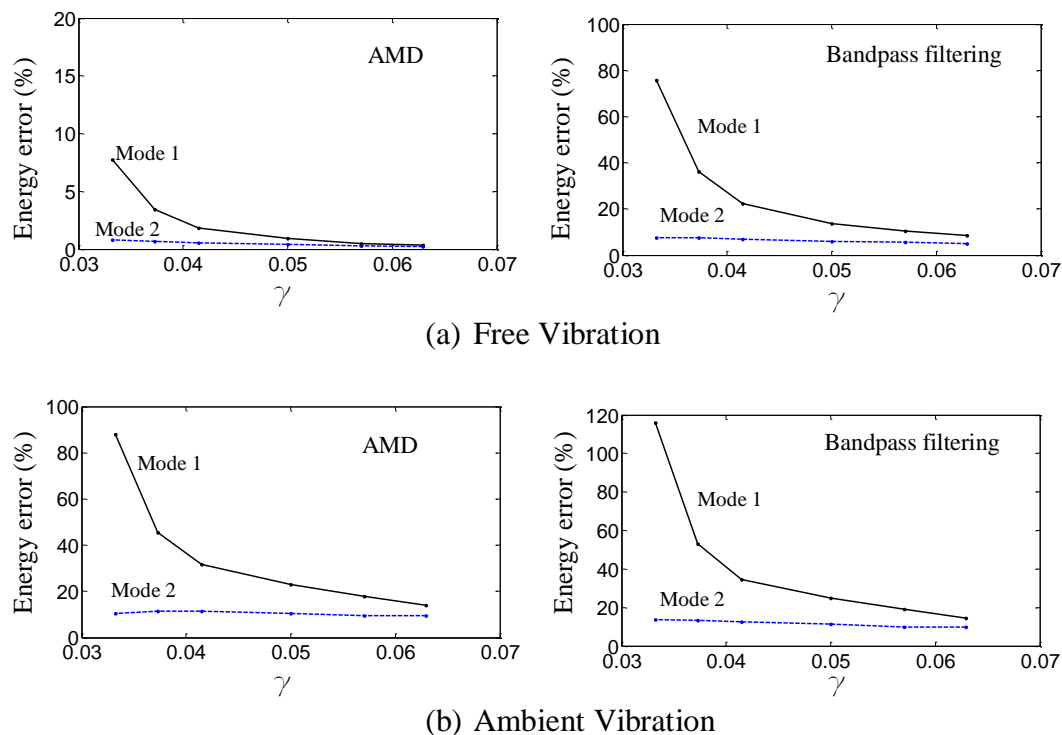
Figure 4.46. Energy Error Indices Associated with AMD and Bandpass Filtering Methods

(a) Fourier Spectra   (b) Modal Response Overlapping
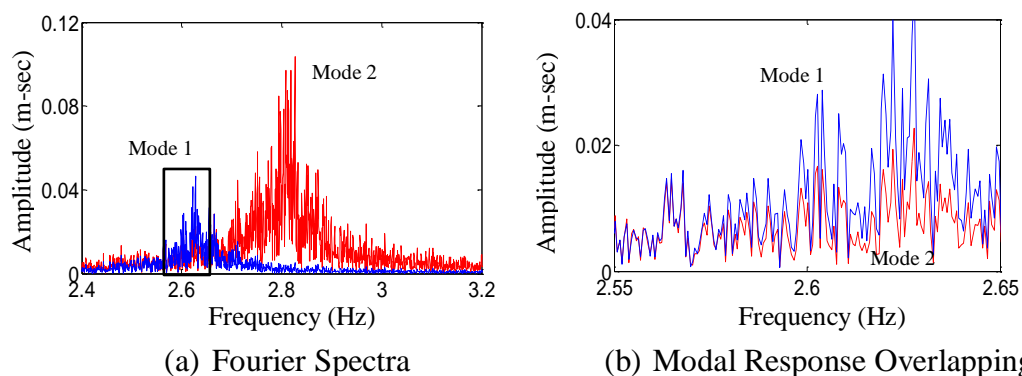
Figure 4.47. Fourier Spectra of the Exact Responses of Modes 1 and 2 and Their
Overlapping

4.5.2.2 Effect of free vibration time duration. To eliminate or minimize the
frequency overlapping effect between modes of vibration under ambient vibration, RDT
will be first applied on the measured response to extract the free vibration response in
application of AMD for modal parameter identification. However, the time duration of
the free vibration from RDT is often significantly shorter than that of the original

measured response. Therefore, the frequency resolution of the free vibration response is much lower. Take the two-story building as an example. When γ =0.033, the Fourier spectra of the ambient displacement response at the top floor $x_2(t)$ and its corresponding free vibration after RDT with all available 8-sec. time segments at a displacement threshold of one standard deviation are presented in Figures 4.48(a) and (b), respectively. It can be clearly seen from Figure 4.48 that the frequency resolution of the free vibration is much lower than that of the ambient vibration.

As discussed in Section 4.5.2.1, the AMD method is less sensitive to the use of finite duration time series in comparison with the bandpass filtering method. To quantify the effect of response duration, the two-story building with γ=0.05 was investigated. Towards this endeavor, the free vibration response $x_2(t)$ at the top floor was simulated for 1 to 20 sec with time interval of 1 sec. A time step of 0.01 sec and a sampling frequency of 100 Hz were used. The bisecting frequency in AMD took the average of two natural frequencies, which is also used as the cutoff frequency in the bandpass filtering method. The energy error indices for the AMD method and bandpass filtering method are compared in Figure 4.49. The decomposed and exact responses are compared in Figure 4.50 for a time duration of 1, 5, 10, and 20 sec. It can be clearly seen from Figure 4.49 that the energy error index is overall larger with the bandpass filtering method, particularly as the time duration becomes shorter. AMD results in an energy error index of less than 20% with 1-sec time duration and less than 5% with 7-sec time duration, while the bandpass filtering method gives an energy error index of greater than 60% and 20%, respectively. This is because the error for the bandpass filtering method not only results from the incomplete cycles of responses, but also from the introduction of a rectangular window in the frequency domain. The error for the AMD method only comes from the incomplete cycles of responses. It can also be seen from Figure 4.50 that the decomposed signal by AMD is much more accurate than that by the bandpass filtering method as the time duration becomes shorter.

(a) Ambient Vibration　　　　　　　　(b) Free Vibration after RDT
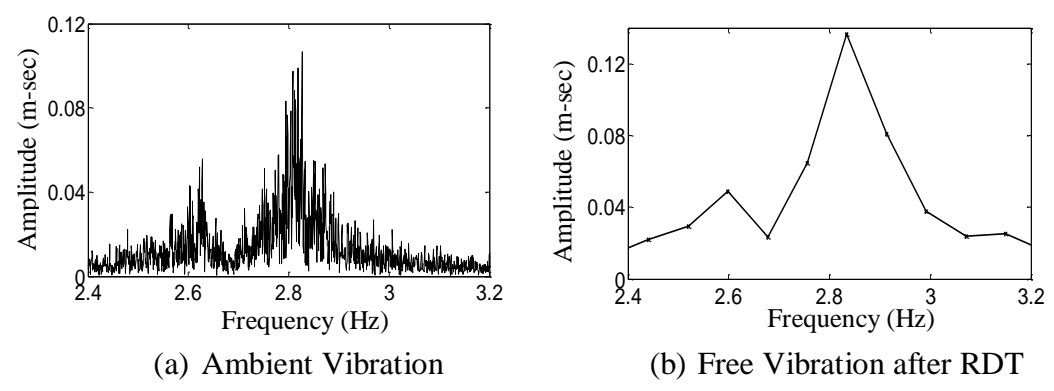
Figure 4.48. Fourier Spectra of Ambient Vibration and Free Vibration after RDT
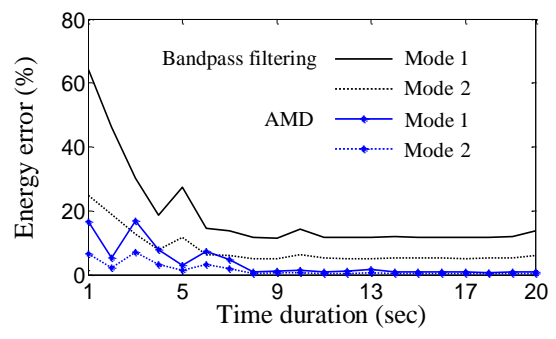
Figure 4.49. Energy Error Indices under Free Vibration

(a) AMD Method　　　　　　　　(b) Bandpass Filtering Method
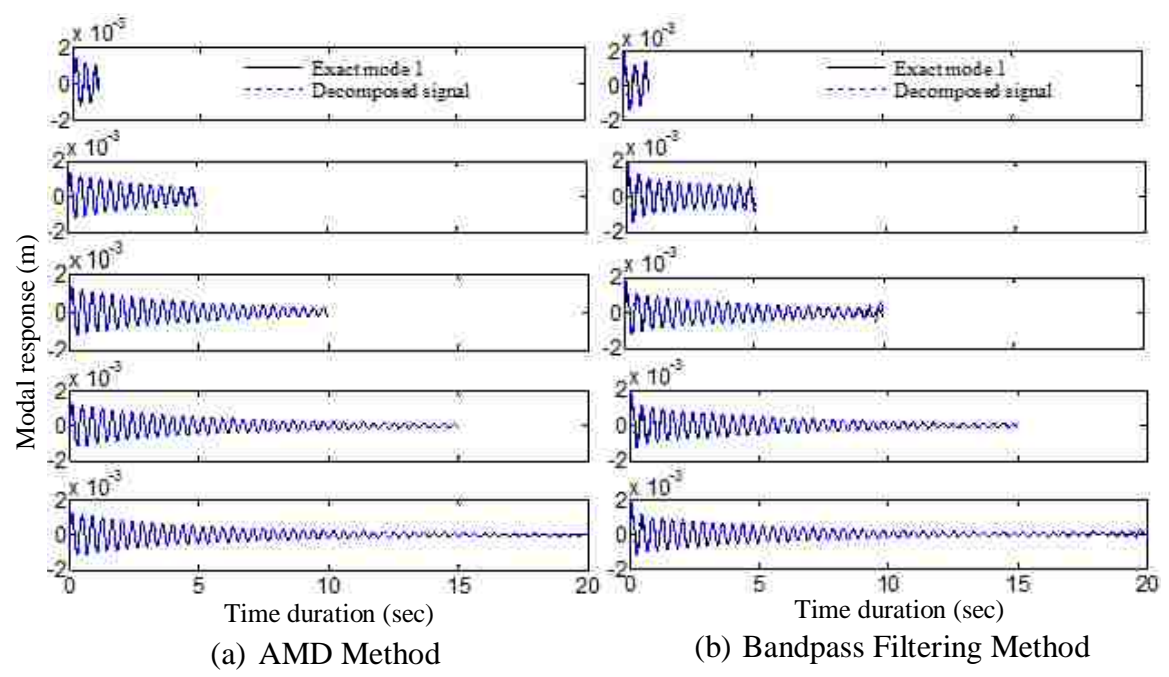
Figure 4.50. Decomposed and Exact Mode 1 Response with Time Duration: 1, 5, 10, 15, and 20 sec.

4.5.3. Application of the RDT-AMD Method. In this section, a 3-DOF system and a 36-story building are analyzed as numerical examples to illustrate modal parameter identification from ambient vibration using the proposed RDT-AMD method.

4.5.3.1 3-DOF mechanical system with closely-spaced modes. The same 3-DOF mechanical system as presented in Section 4.3.2 was analyzed. The Gaussian white noise with a standard deviation of $0.1g$ (g is gravity acceleration) was applied on m_3. The displacement response at m_3 was numerically calculated and sampled at a frequency of 20 Hz, which is presented in Figure 4.51(a).

RDT was first applied to the displacement response with a time segment length of 20 sec and a threshold value of standard deviation of the ambient response. The free response extracted by RDT and its Fourier spectrum are shown in Figure 4.51(b).
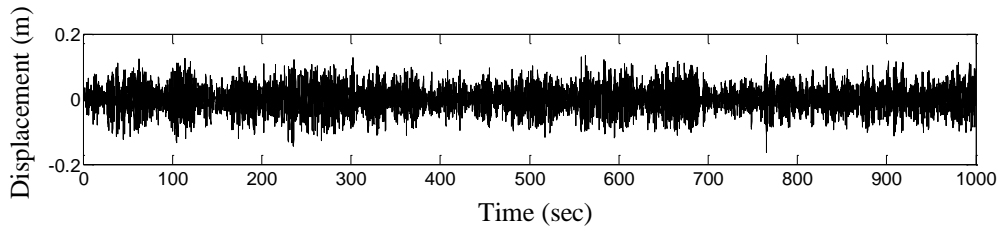
(a) Ambient Displacement at m_3
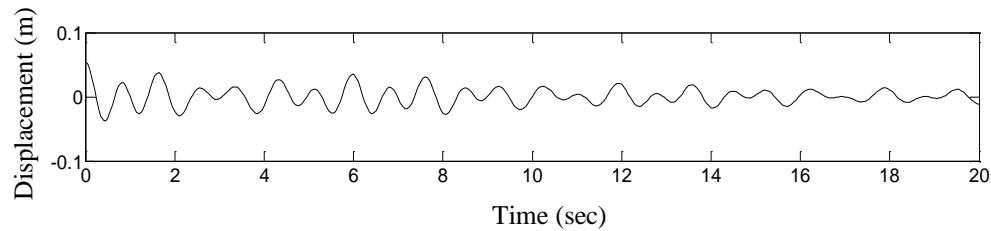
(b) Free Response Extracted from Ambient Displacement

Figure 4.51. Ambient Displacement and Extracted Free Response

The Fourier spectra of the original ambient response and extracted free response are shown in Figure 4.52(a, b). The extracted free response was decomposed into three components by AMD with a bisecting frequency of 0.92 Hz and 1.25 Hz, respectively, as shown in Figure 4.53. The amplitude $A_{3i}(\tau)$ and phase angle $\theta_{3i}(\tau)$ (i =1, 2, 3) of mode i are shown in Figure 4.54. The natural frequency and damping ratio are further identified and listed in Table 4.4. In comparison with the exact natural frequencies and damping ratios given in Table 4.1, the identified results are accurate to 2% for frequency and less

than 24% for damping ratio. The results show that the identified damping ratios from ambient vibration are not as accurate as that from free vibration. The mode shape identified using the ratio of imaginary peak value at natural frequency between each DOF is:

$$\emptyset_1 = \{0.97 \quad 2.45 \quad 1.00\}^T, \emptyset_2 = \{-0.98 \quad 0 \quad 1.00\}^T, \emptyset_3 = \{0.98 \quad -0.83 \quad 1.00\}^T.$$

(a) Ambient displacement   (b) Extracted free response
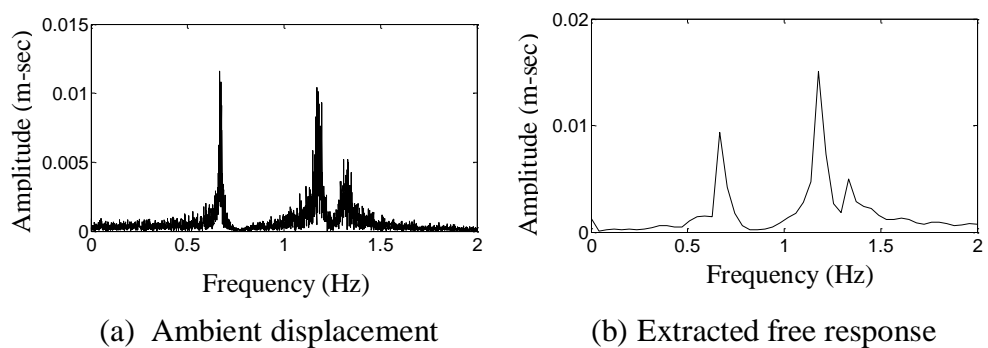
Figure 4.52. Fourier Spectra of Ambient Displacement and Extracted Free Response
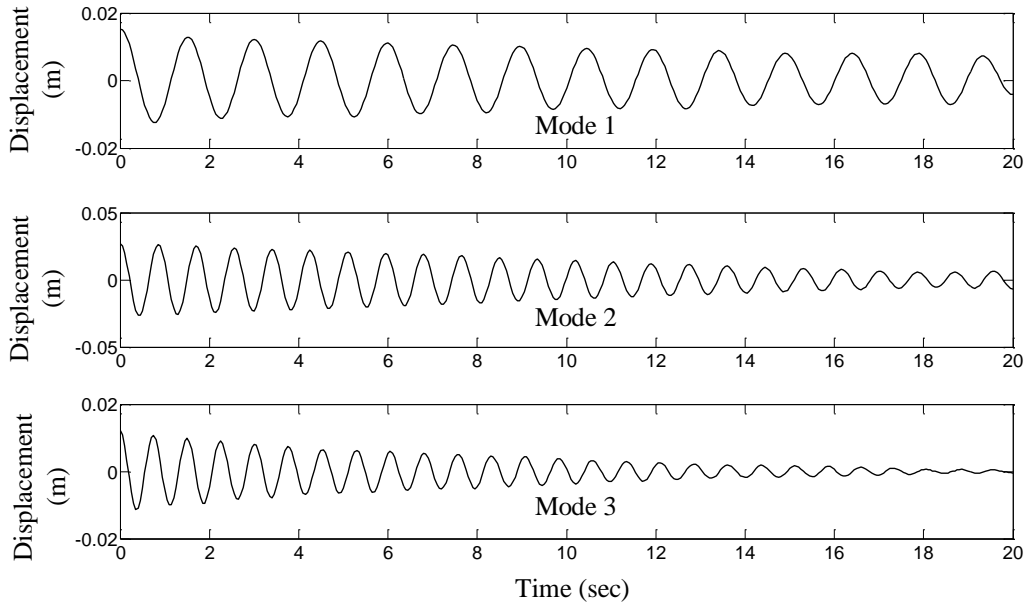
Figure 4.53. Decompose Modes from Extracted Free Response using AMD

(a) Amplitude
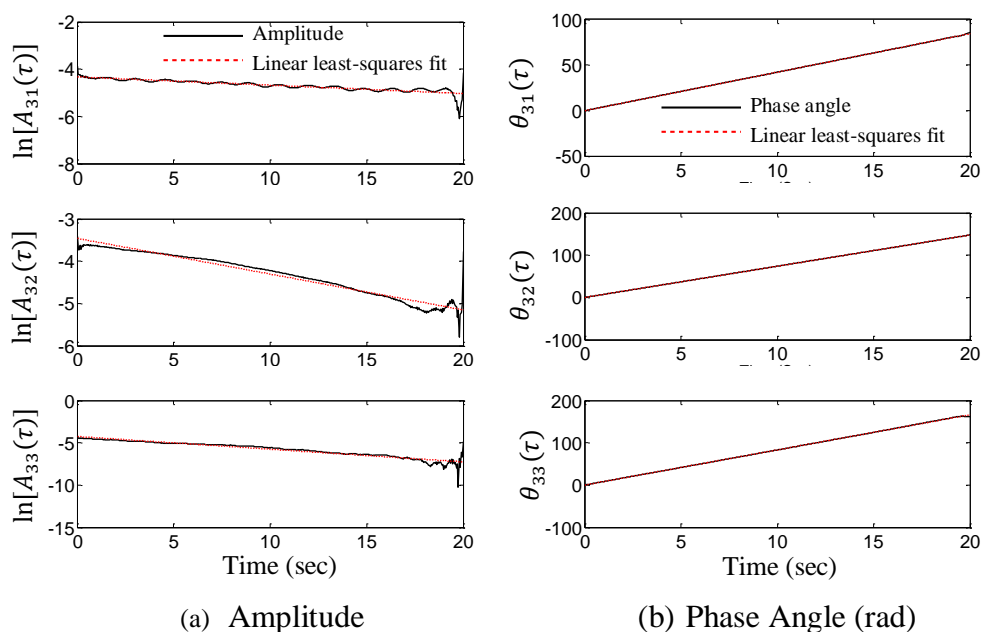
(b) Phase Angle (rad)

Figure 4.54. Amplitude and Phase Angle of Hilbert Transform of the Free Response
Obtained by RDT

Table 4.4. Identified Natural Frequencies and Damping Ratios from Ambient Vibration

Mode	Displacement on m_1		Displacement on m_2		Displacement on m_3		Exact	
	Damping ratio (%)	Frequency (Hz)	Damping ratio (%)	Frequency (Hz)	Damping ratio (%)	Frequency (Hz)	Damping ratio (%)	Frequency (Hz)
1	0.73	0.672	0.71	0.672	0.78	0.672	0.63	0.673
2	1.15	1.179	-	-	1.18	1.175	1.11	1.180
3	1.20	1.328	1.24	1.320	1.19	1.330	1.23	1.304

4.5.3.2 36-story shear building with light appendage. The same 36-story shear-
type building with a 4-story light appendage (Figure 4.55) as used in Chen and Xu (2002)
was analyzed as an application example of the proposed method.

The main building was assumed to be uniform with a floor mass of 1.29×10^6 kg
and interval stiffness of 1.0×10^9 N/m. The light appendage was modeled with a 4-DOF
substructure. The mass ratio between each appendage DOF and each building floor is
0.02. The story stiffness of the appendage is 0.03% of the interval shear stiffness of the
main building. The first four undamped natural frequencies are 0.184, 0.196, 0.542, and
0.573 Hz. Classical damping was considered (Chen and Xu 2002; Clough and Penzien
1993). The modal damping ratios of the first four modes are assumed to be 1% and the

other modal damping ratios are zero. The building was subjected to ground motion, which is assumed to be a Gaussian white noise with a standard deviation of $0.001g$ (g is the gravitational acceleration). The acceleration response at the top of the appendage, as shown in Figure 4.56 together with the ground motion, was considered to be the measured response sampled at 20 Hz.
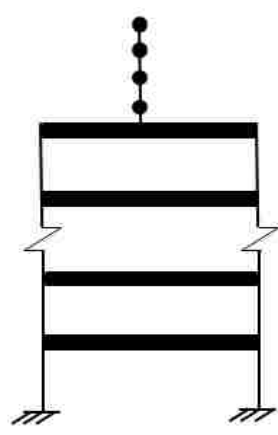
Figure 4.55. Shear Building with Light Appendage
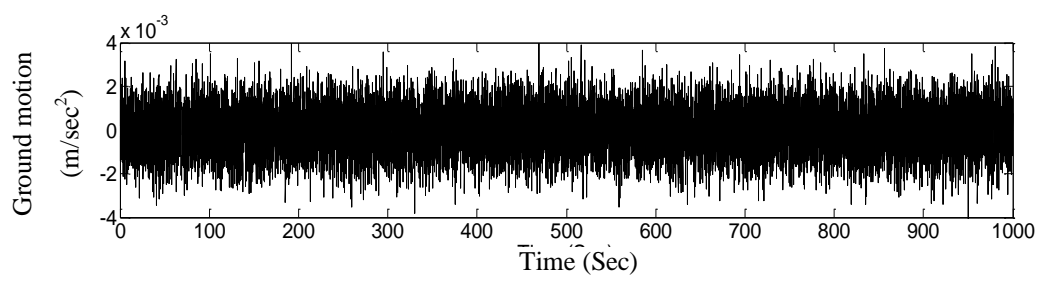
(a) Ground Motion
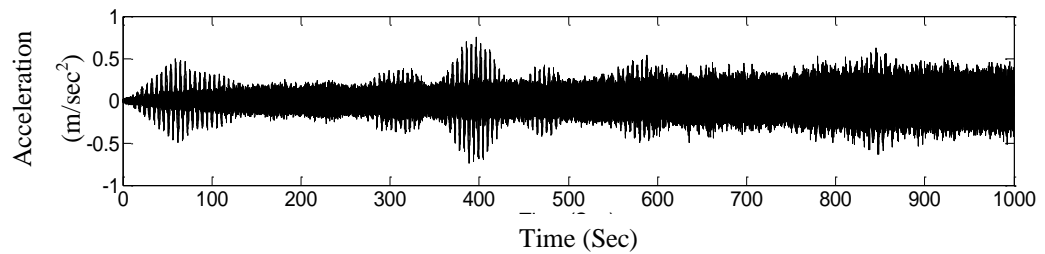
(b) Acceleration Response at the Top of Appendage

Figure 4.56. Simulated Excitation and Response

As presented in Figure 4.57, its Fourier spectra indicate that Modes 1 and 2 as well as Modes 3 and 4 are closely-spaced. Before RDT was applied to eliminate the frequency overlapping effect between closely-spaced modes, the first two modes were separated from the remaining modes by AMD with a bisecting frequency of 0.4 Hz. This is because these two groups of vibration modes are well separated with negligible frequency overlapping. The acceleration response from Modes 1 and 2, and the response from Modes 3 and 4 are presented in Figure 4.58 with their corresponding Fourier spectra shown in Figure 4.59.

To further decompose the closely-spaced Modes 1 and 2 or Modes 3 and 4, RDT was first applied to extract the free vibration response as shown in Figure 4.60 at a threshold of one standard deviation of their group acceleration. AMD was then applied with a bisecting frequency equal to the average of the two closely-spaced natural frequencies. The instantaneous amplitude $A_{pi}(\tau)$ and phase angle $\theta_{pi}(\tau)$ ($p = 40, i = 1, 2,$ 3, and 4) from each mode of the extracted free vibration are presented in Figure 4.61. The natural frequency and damping ratio identified from Figure 4.61 are given in Table 4.5. The maximum errors for damping ratio identification and frequency identification are 6% and 1%, respectively. These results demonstrated high accuracy of the proposed RDT-AMD method for modal parameter identification of closely-spaced modes in practical applications.
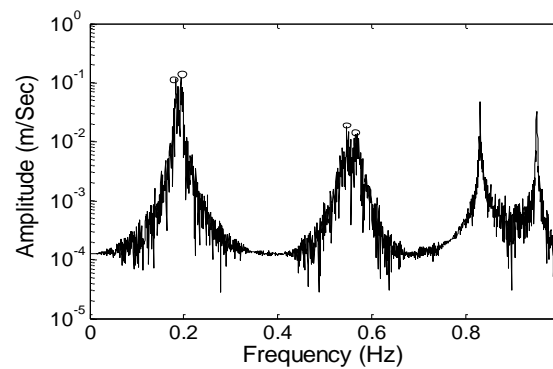
Figure 4.57. Fourier Spectrum of the Acceleration at the Top of Appendage
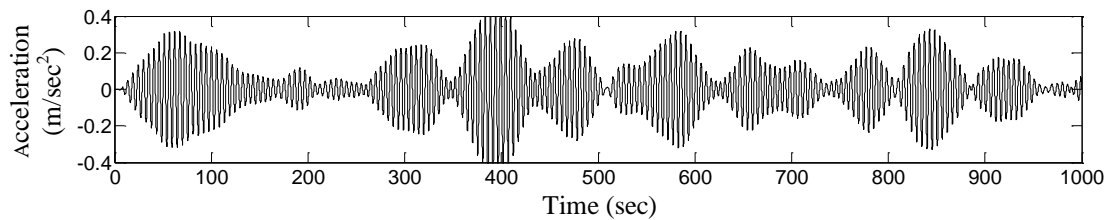
(a) Mode 1 and 2
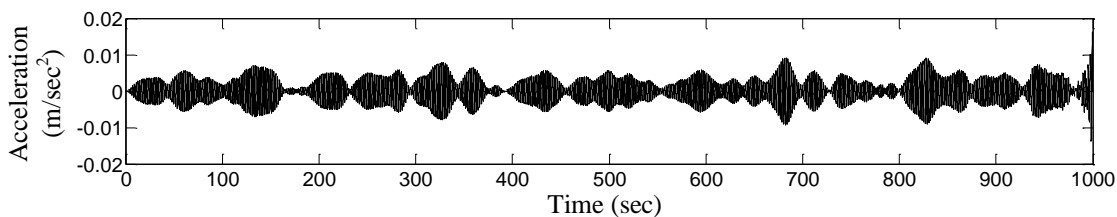
(b) Mode 3 and 4

Figure 4.58. Closely-Spaced Modal Responses
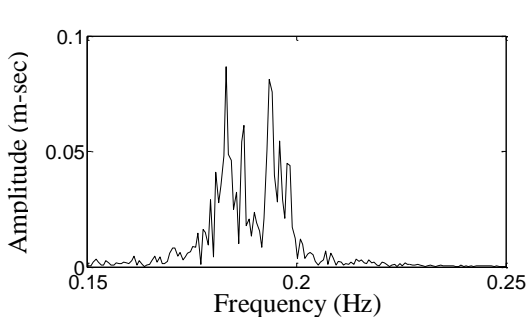
(a) Mode 1 and 2
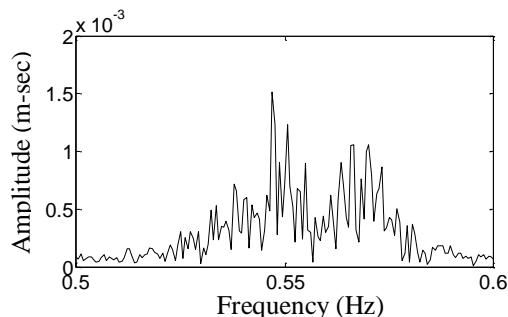
(b) Mode 3 and 4

Figure 4.59. Fourier Spectra of Closely-Spaced Modal Response

Mode 1 and 2

Mode 3 and 4
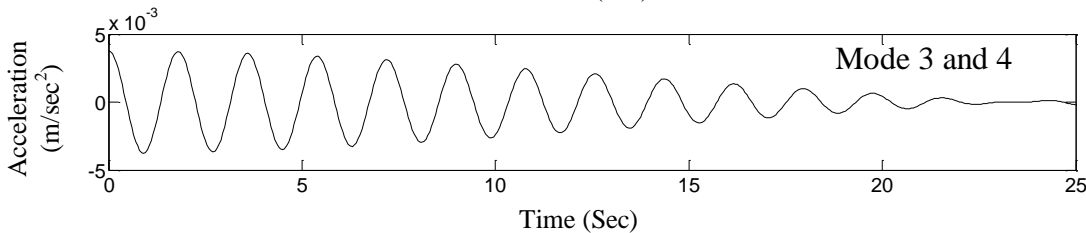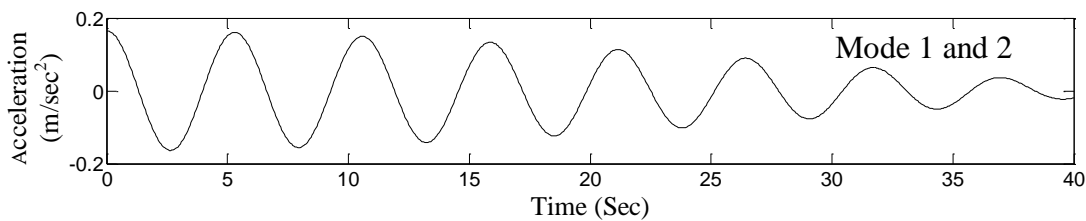
Figure 4.60. Extracted Free Response using RDT

(a) Amplitude (b) Phase Angle (rad)
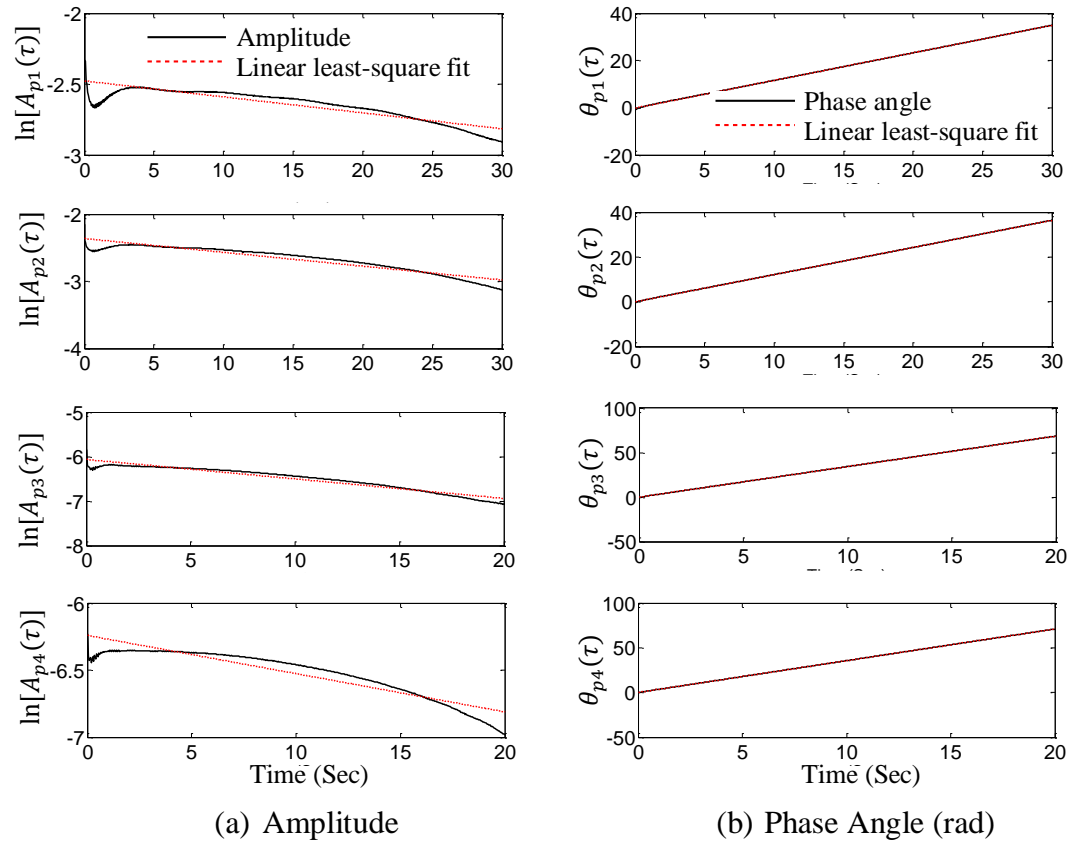
Figure 4.61. Amplitude and Phase Angle of the Free Vibration Response Extracted from Ambient Vibration

Table 4.5. Identified Natural Frequency and Damping Ratio of Building-Appendage System

Mode	Identified		Theoretical		Error	
	Damping ratio (%)	Frequency (Hz)	Damping ratio (%)	Frequency (Hz)	Damping ratio	Frequency
1	0.96	0.186	1.00	0.184	-4%	1.0%
2	1.02	0.194	1.00	0.196	2%	-1.0%
3	1.06	0.545	1.00	0.542	6%	0.6%
4	0.94	0.569	1.00	0.573	-6%	-0.7%

4.6. SHAKE TABLE TEST VALIDATION

To validate the RDT-AMD method for parameter identification, a ¼-scale, 3-story steel frame installed with a single tuned mass damper on the top floor is considered as illustrated in Figure 4.62 (Chen and Wu, 2001). The damper was tuned into the fundamental frequency of the structure that is 1.22 m long, 0.61 m wide, and 2.54 m tall. Therefore, the structure-damper system has two closely-spaced natural frequencies. A series of shake table tests of the structure-damper system were conducted. The modal and structural properties of the individual steel frame and damper are summarized in Table 4.6.

For comparison, the structure-damper system was excited by a 20 second mean-zero white noise acceleration with a standard deviation of 0.001g (g is the gravitational acceleration) and by a compressed component of the 1952 Taft earthquake with a time factor of 3/4. Sampled at 100 Hz, the two base accelerations are shown in Figure 4.63 and their corresponding top floor accelerations are presented in Figure 4.64 in time histories or Figure 4.65 in Fourier spectra.

Figure 4.65 consistently indicated the presence of four natural frequencies. Two closely-spaced frequency components are observed around the fundamental frequency of the structure. Before RDT was applied to eliminate the frequency overlapping effect, the first two closely-spaced modes of the structure-damper system were separated by AMD with a bisecting frequency of 7 Hz since they are well separated from the remaining two modes with negligible frequency overlapping.

With a threshold acceleration of one standard deviation of the combined response of Modes 1 and 2, RDT was first applied to extract the 3.5-sec free vibration response as illustrated in Figure 4.66. The free vibration responses were then decomposed by AMD with a bisecting frequency equal to the average of the two-closely-spaced frequencies.

(a) 3-Story Steel Frame
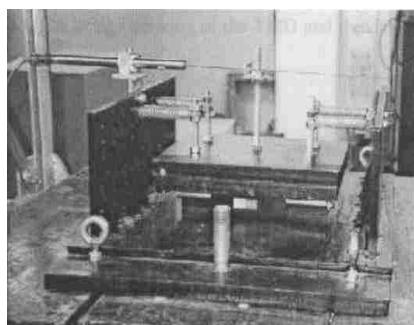
(b) Tuned Mass Damper

Figure 4.62. The Shake Table Test Setup

Table 4.6. Modal and Physical Properties of Steel Frame and Damper

	Mode number (3-story steel frame)			Damper
	1	2	3	
Frequency (Hz)	2.743	9.45	18.84	2.72
Damping ratio (%)	0.48	1.15	1.45	1.40
Mass or Mass matrix (kg)	$\begin{bmatrix} 445 & 0 & 0 \\ 0 & 394 & 0 \\ 0 & 0 & 388 \end{bmatrix}$			39.3
Damping coefficient or damping matrix (N-sec/m)	$\begin{bmatrix} 777.0 & -468.3 & 25.7 \\ -468.3 & 859.4 & -422.4 \\ 25.7 & -422.4 & 405.7 \end{bmatrix}$			18.8
Stiffness coefficient or stiffness matrix ($\times 10^6$ N/m)	$\begin{bmatrix} 2.669 & -2.118 & 0.452 \\ -2.118 & 3.397 & -1.645 \\ 0.452 & -1.645 & 1.26 \end{bmatrix}$			0.0114
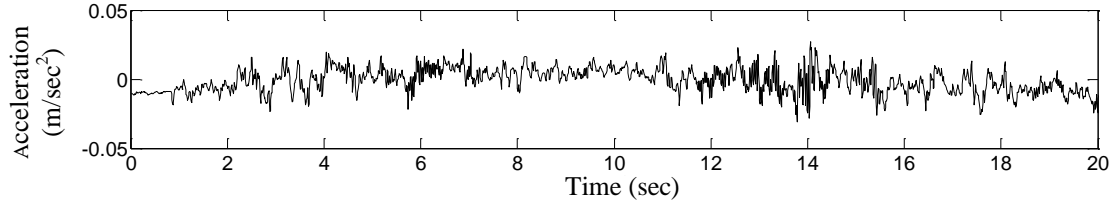
(a) White Noise Excitation
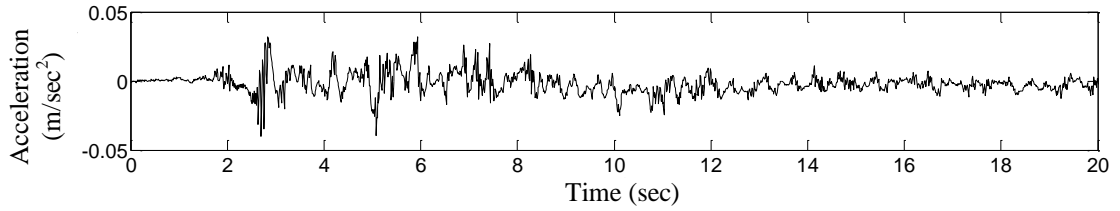
(b) Compressed Taft Earthquake

Figure 4.63. Base Motions to the Structure with Various Excitations
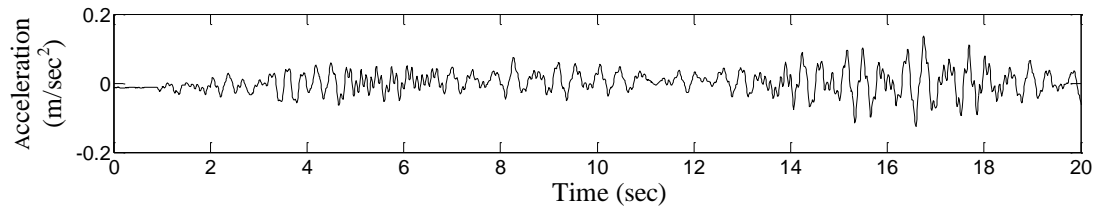
(a) White Noise Excitation
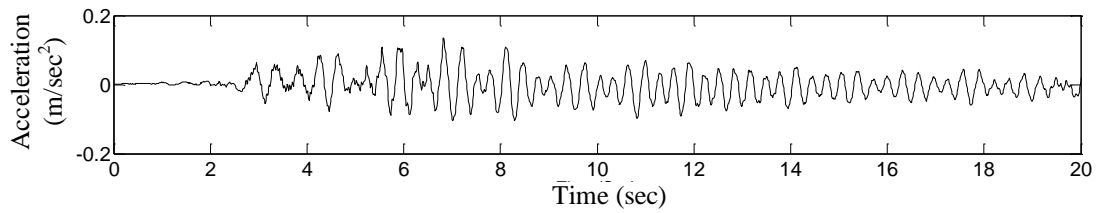
(b) Compressed Taft Earthquake

Figure 4.64. Measured Top Floor Accelerations of the Structure: (a) White Noise
Excitation and (b) Compressed Taft Earthquake Excitation
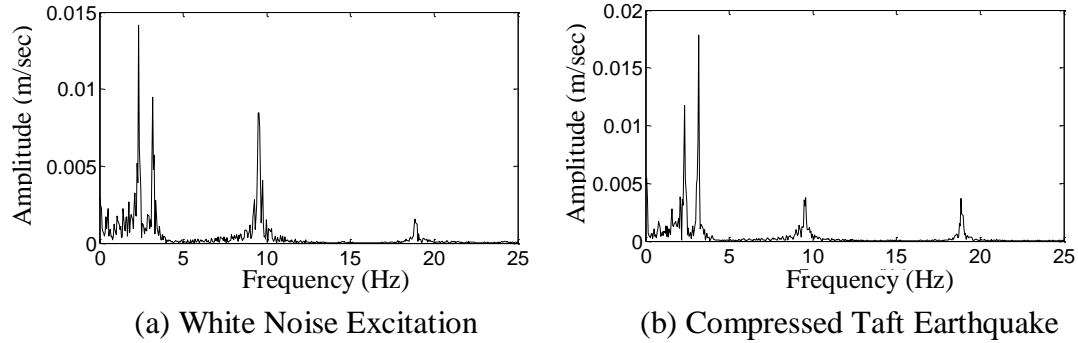
Figure 4.65. Fourier Spectra of the Measured Top Floor Accelerations
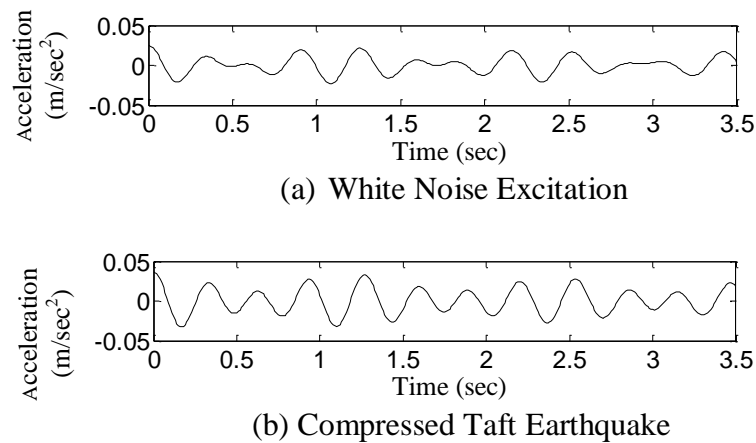
Figure 4.66. Extracted Free Vibration Responses

The instantaneous amplitude $A_{pi}(\tau)$ and phase angle $\theta_{pi}(\tau)$ of the third floor acceleration ($p = 3$) for each mode i (i =1 and 2) are presented in Figure 4.67. Finally, the natural frequency and damping ratio were evaluated with the least-squares fitting process; the identified results are listed in Table 4.7. It is clearly seen from Table 4.7 that the proposed method can consistently identify the closely-spaced natural frequencies with high accuracy. However, for the steel frame structure, the damping ratios identified from the two tests are somewhat inconsistent due mainly to the fact that the damping mechanism of the tuned mass damper is neither purely viscous nor frictional (Chen and Wu, 2001).
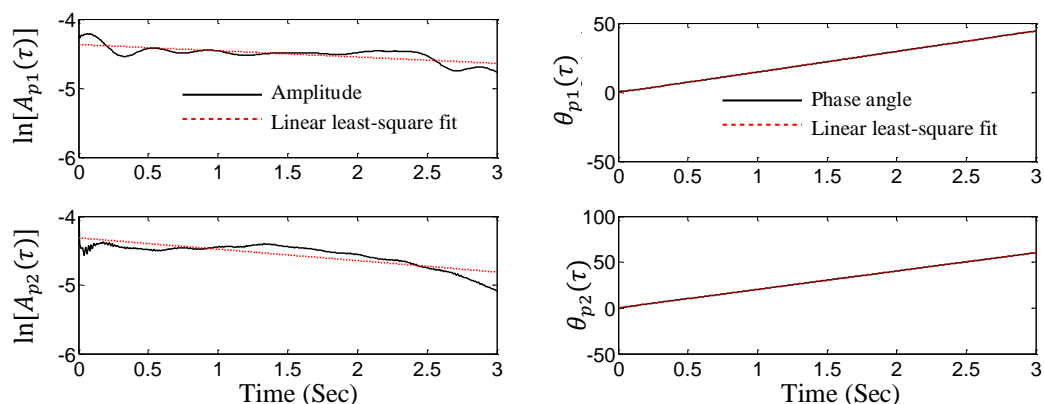
(a) White Noise Excitation
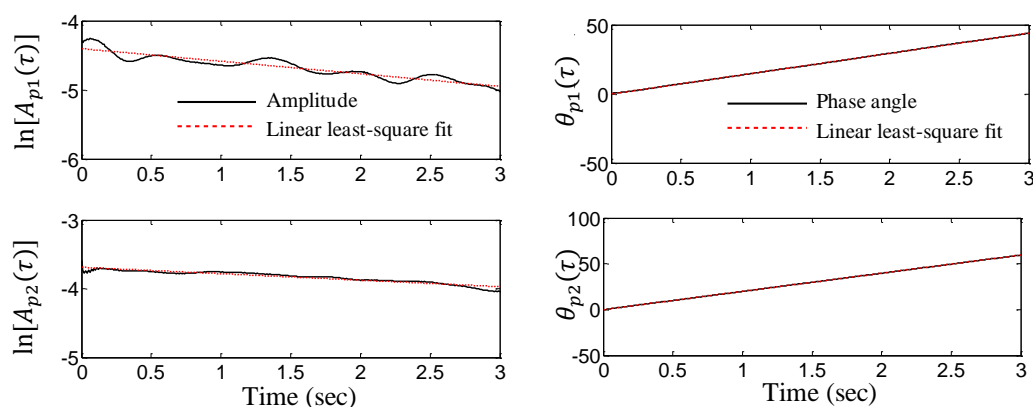
(b) Compressed Taft Earthquake

Figure 4.67. Amplitude and Phase Angle of the Free Vibration Response Extracted from the Third Floor Acceleration

Table 4.7. Identified Natural Frequencies and Damping Ratios from the Top Floor Acceleration

Mode	White noise		Compressed Taft earthquake	
	Damping ratio (%)	Frequency (Hz)	Damping ratio (%)	Frequency (Hz)
1	0.61	2.36	0.50	2.34
2	0.84	3.20	1.01	3.16

4.7. SUMMARY

The bisecting frequency in the AMD theorem can theoretically be selected as any value between the two frequencies of interest but practically be recommended to take the average of the two frequencies due to the finite length of signals in applications. It is insensitive to other choices in 80%~120% of the average value so long as the frequency

resolution in the Fast Fourier Transform does not exceed 50% of the spacing of the two frequencies. This translates into a discernible frequency spacing of twice the frequency resolution of a time series or the required duration of the time series that is equal to two divided by the minimum frequency spacing.

Numerical examples for four representative engineering applications indicate that the new theorem is superior to existing techniques: the filtering technique, wave-group method, and tempered signal approach that are currently available in the literature to deal with the decomposition of closely-spaced modes, beating effects, and small intermittent fluctuations. It is simple in concept, efficient in computation, consistent in performance, and reliable in signal processing.

Free modal responses can be simply extracted from the free vibration, and the modal parameters can then be readily estimated based on the least-squares procedure. Under harmonic excitations, the response can be separated into the transient and the steady state response component. Since the transient response decays quickly, the energy of the vibration is dominated by the steady state response. Therefore, the steady state response can be first extracted using AMD theorem based on the dominant response at later time. The transient signal can be obtained by subtracting the steady state response from the total response. Then, the free modal responses can be extracted from the transient response and used for modal parameter identification. The results of the 3-DOF mechanical system simulation demonstrate that the proposed method can accurately identify the modal parameters from free or harmonic vibration even with significant noise effects.

For systems with ambient vibration, a new system identification method with ambient vibration, combining the advantages of the AMD theorem and the conventional RDT, named as RDT-AMD method was developed. In the proposed RDT-AMD method, RDT was first applied to extracting the free vibration information from an ambient response time history with closely-spaced modes. The extracted free vibration response was then decomposed by the theorem into individual modal responses from which modal parameters are evaluated.

An energy error index is defined as the ratio between the squared modal response error and the exact modal energy over the response duration. It accounts for the effects of

both amplitude and phase. For a 20-sec ambient vibration response, AMD induces an energy error index of 88% for a frequency space index of 0.033. For a 20-sec free vibration response, AMD results in an energy error index of approximately 7.5% for a frequency space index of 0.033. Even when the duration of free vibration is reduced to 1 sec, the energy error induced by AMD is less than 20% for a frequency space index of 0.05.

While RDT can eliminate modal overlapping effects as two natural frequencies approach each other, AMD can accurately separate two closely-spaced frequencies with no brick wall effects associated with bandpass filtering. Together, they provide a system identification method (RDT-AMD) of high accuracy from ambient vibration. The application examples include a 3-DOF mechanical system and a 36-story building with 4-story appendage system. Finally, shake table tests validated high accuracy of the proposed method in modal parameter identification of a building system based on actual measurement data.

5. IDENTIFICATION OF TIME-VARYING AND WEAKLY NONLINEAR SYSTEMS WITH AMD-HILBERT SPECTRAL ANALYSIS

The AMD developed in Section 3 can decompose signals with amplitude and frequency modulations over time. This section applies it for the adaptive analysis of non-stationary time series that is commonly seen in time-varying and nonlinear engineering systems. Its aims are to establish admittance requirements for the selection of time-varying bisecting frequencies and quantify the effects of bisecting frequency selection, signal frequency overlapping, sampling rate, and signal noise. For nonlinear systems, a non-parametric identification method is developed and applied to a simple Duffing oscillator and a building system with hysteretic behaviors.

5.1. HHT, WAVELET AND AMD-HILBERT SPECTRAL ANALYSIS

For time-varying and nonlinear systems, the system properties changes over time. Therefore, advanced time-frequency analysis must be conducted to identify their characteristics. In this study, the AMD-Hilbert spectral analysis is compared with HHT and wavelet analysis. Both HHT and wavelet analysis has been reviewed in Sections 2 to 4.

5.1.1. AMD-Hilbert Spectral Analysis. AMD-Hilbert spectral analysis is similar to the HHT method. The main difference is the use of AMD instead of EMD in signal decomposition. Specifically, the IMFs by EMD are replaced by the decomposed signal components by AMD. Therefore, as discussed before for the HHT method, the AMD-Hilbert spectral analysis can be used to identify the instantaneous amplitude, phase, and frequency of a time series through the formation of an analytic function of the signal.

5.1.2. Comparative Study on Instantaneous Frequency. To compare the above three time-frequency analysis methods, a signal $x(t)$ with two frequency-modulated components was considered:

$$x(t) = x_1(t) + x_2(t) \qquad (5.1)$$

in which $x_1(t) = \cos[3.5\pi t + 0.5\sin(0.5\pi t)]$ and $x_2(t) = \cos[2.6\pi t + 0.8\sin(0.4\pi t)]$ ($0 \leq t \leq 30\ sec$). Frequencies of the two components are $f_1 = 1.75 + 0.125\cos(0.5\pi t)$

and $f_2 = 1.3 + 0.16\cos(0.4\pi t)$ Hz, respectively. In all simulations, a sampling rate of 20 Hz was used.

For time-frequency analysis with HHT, the first two IMFs by EMD are presented in Figure 5.1. Clearly, the first IMF still includes the frequency information from both components, a mixed mode problem that is often associated with EMD. As shown in Figure 5.2, the instantaneous frequencies identified from the first two IMFs rapidly fluctuate over time and quite deviate from their respective exact values. They are incorrect because of the mixed mode problem of the two frequency components.
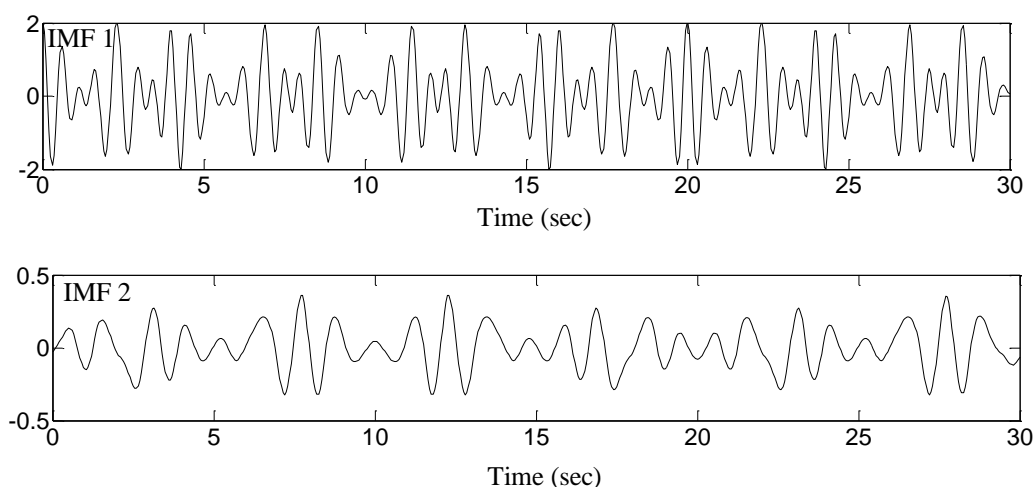
Figure 5.1. First Two IMFs from EMD
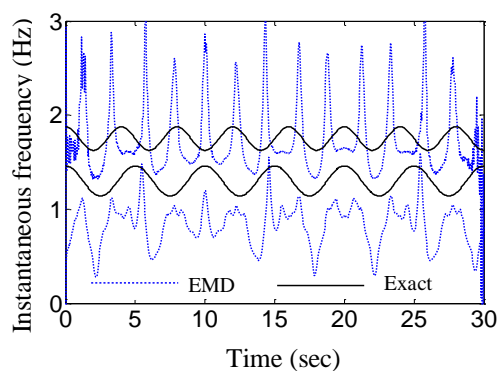
Figure 5.2. Instantaneous Frequency from HHT

For wavelet analysis, a simplified complex Morlet wavelet was selected as a parent wavelet function. It is defined by:

$$\Psi(t) = \frac{1}{\sqrt{\pi k_b}} e^{-\frac{t^2}{k_b}} e^{j2\pi f_c t} \tag{5.2}$$

in which k_b is a bandwidth parameter and f_c is the center frequency of the wavelet. To have various frequency and time resolutions, three center frequencies of 0.5, 1.0, and 1.5 Hz with the same bandwidth parameter $k_b = 5\ sec^2$ were selected. Corresponding to each of the center frequency f_c, Figure 5.3(a-c) plots the wavelet coefficients W(a, b), Equation (2.7) in Section 2.3.2, as a function of b (in sec) and $f_c/a/\Delta$ (in Hz) in time-frequency plane. Here Δ denotes the sampling period and time interval of a data series. It can be clearly observed from Figures 5.3 that the smaller the center frequency or the dilation scale a, the higher the time resolution and the lower the frequency resolution so that the two frequency components cannot be separated. On the other hand, the larger the center frequency or the dilation scale a, the higher the frequency resolution and the lower the time resolution so that the two frequency components can be separated. In this case, the time information is lost and the frequency of each component appears a constant over time. By using an appropriate center frequency, the two components can be separated with relatively high time resolution as shown in Figure 5.3(b). However, according to the Heisenberg-Gabor uncertainty principle, a signal can never be concentrated on an arbitrarily small time-frequency region. It is impossible to simultaneously achieve high resolutions both in time and frequency domains.

For AMD-Hilbert spectral analysis, a constant bisecting frequency of 1.53 Hz can be selected from Figure 5.3(c). As presented in Figure 5.4, the decomposed signals by AMD are in excellent agreement with their respective exact signals, particularly in frequency content.

(a) $f_c = 0.5$ Hz

(b) $f_c = 1.0$ Hz

(c) $f_c = 1.5$ Hz
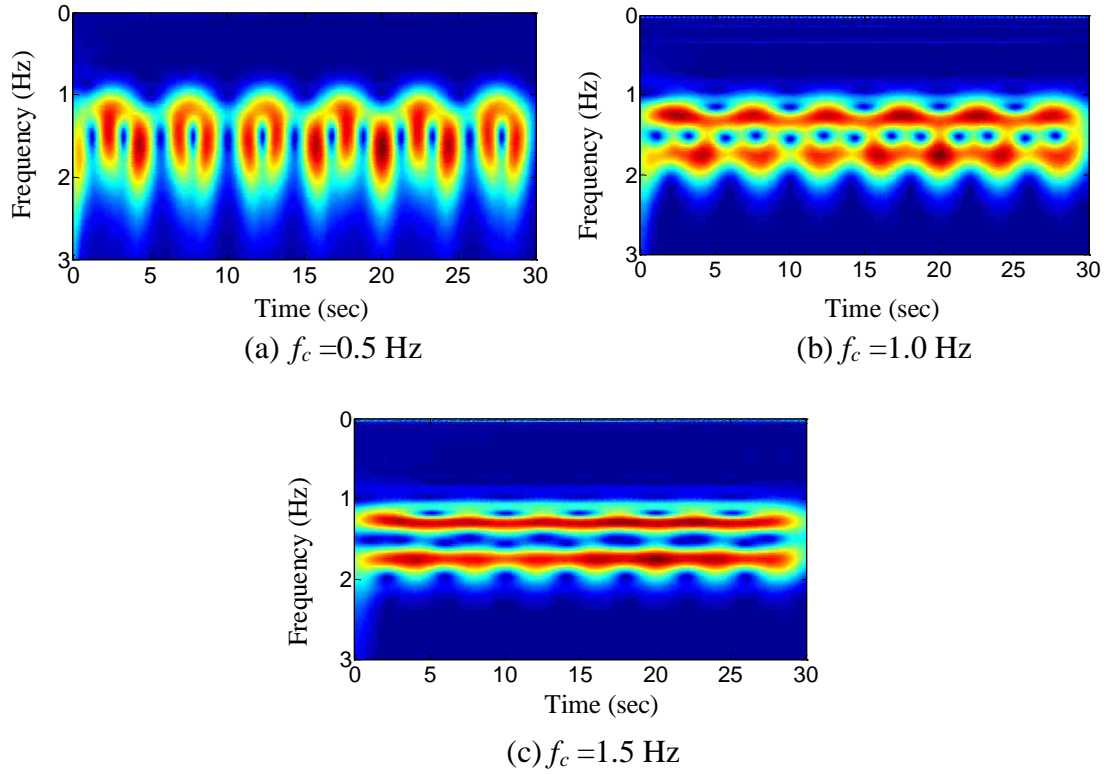
Figure 5.3. Wavelet Transform Scalograms for Various Center Frequencies
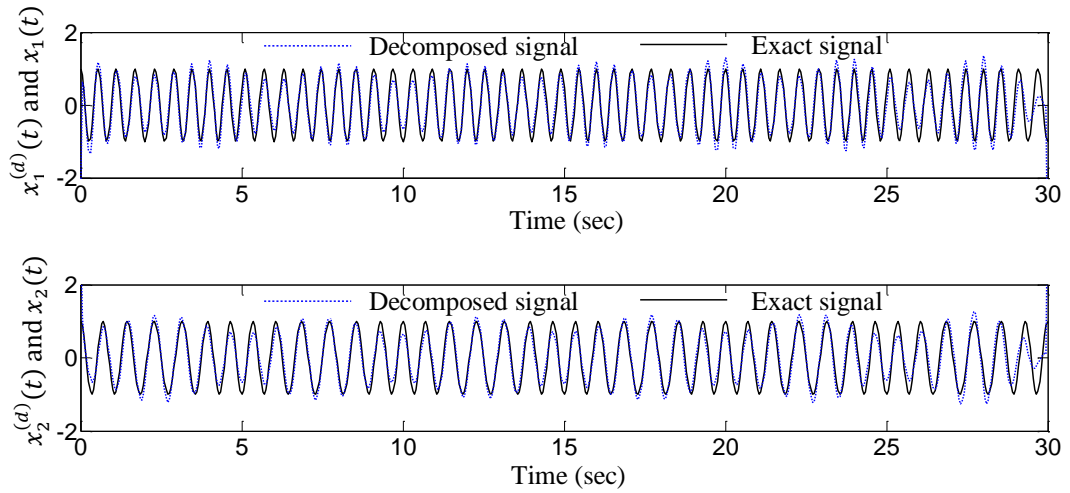
Figure 5.4. Decomposed Signals using AMD

5.2. PARAMETRIC STUDIES

In this section, sensitivity analyses are conducted to address several practical issues with AMD. They include the selection of bisecting frequency, mitigation of the end effect associated with Hilbert transform, and the effects of sampling rate and noise.

5.2.1. Bisecting Frequency Selection. For a stationary signal process, bisecting frequencies can be selected as constants from the Fourier transform of the signal. For non-stationary signals, bisecting frequencies change over time and can be estimated from time-frequency analysis tools such as wavelet analysis using the wavelet ridge extraction method (Staszewski, 1997, Kijewski and Kareem, 2002, Wang and Ren, 2007). In this case, the main differences between AMD-Hilbert spectrum analysis and wavelet analysis are summarized below:

(1) In AMD-Hilbert spectral analysis, wavelet analysis with high frequency resolution only is needed for the estimation of time-varying bisecting frequencies. Each individual component of a non-stationary signal will then be extracted analytically and analyzed with Hilbert spectrum to simultaneously achieve high resolution in evaluating component characteristics such as instantaneous frequencies both in time and frequency domains.

(2) In the conventional wavelet analysis, a tradeoff must be made to simultaneously achieve reasonable resolution both in time and frequency domains as illustrated in Figure 5.3. As the frequency resolution increases, the time resolution decreases so that the frequency variation is unable to track over time. On the other hand, as the time resolution increases, the frequency resolution decreases so that the components of a non-stationary signal cannot be decomposed appropriately.

To study the effect of bisecting frequency selection on the time-frequency analysis, the same signal as used in Equation (5.6) was analyzed with three choices of bisecting frequency (BF): (a) constant, (b) time-varying, and (c) random. The constant BF was set to 1.53 Hz from the wavelet scalogram in Figure 3(c). The time-varying BF was taken to be the average of the two wavelet ridges in Figure 5.5. The random BF was generated from a Gaussian distribution with a mean of 1.53 Hz and coefficient of

variation of 1%. These choices of bisecting frequency are shown in Figure 5.6(a). Their corresponding instantaneous frequencies obtained by AMD-Hilbert spectrum analysis are presented in Figure 5.6(b). It can be clearly seen from Figure 5.6(b) that the differences among the three choices of bisecting frequency are negligible. In comparison with their exact values, the instantaneous frequencies from AMD-Hilbert spectrum analysis are sufficiently accurate in engineering applications.
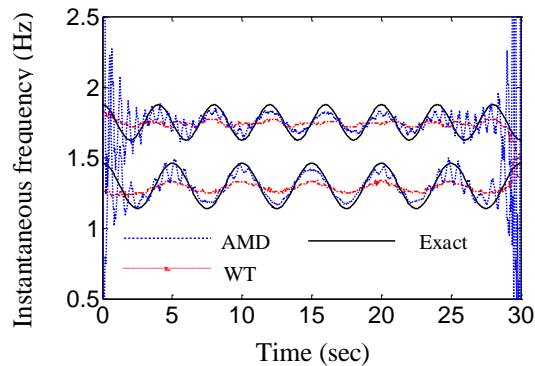
Figure 5.5. Instantaneous Frequency from AMD-Hilbert Spectral Analysis and Wavelet Analysis

(a) Bisecting Frequency

(b) Instantaneous Frequency
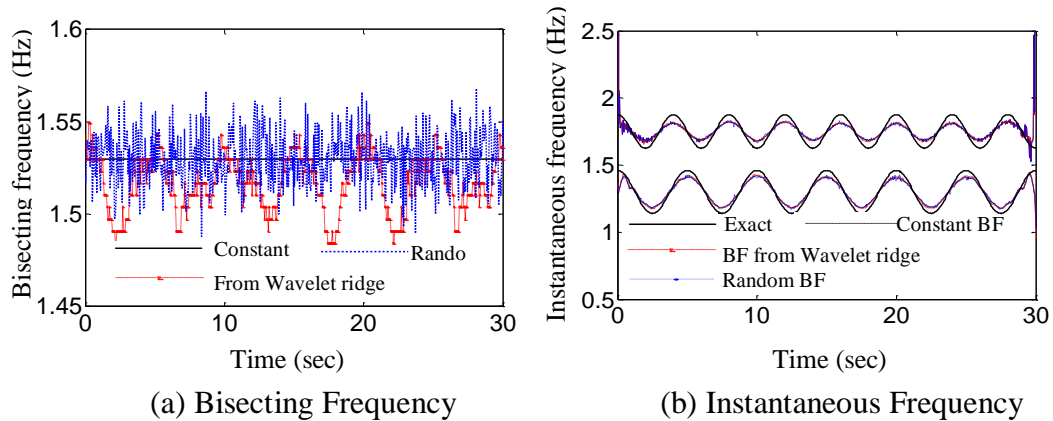
Figure 5.6. AMD-Hilbert Spectrum Analysis with Various Bisecting Frequency Selections

5.2.2. End Effect Reduction. As indicated in Figure 5.5, AMD-Hilbert spectrum analysis has significant end effects due to finite length and incomplete cycle included in a non-stationary signal. Although several techniques are available (Qing and Zhong, 2006, Feldman, 2008, Xun and Yan, 2008, Cheng et al., 2007), the end effects associated with Hilbert transform for a frequency-modulated signal of finite length can never be eliminated since the instantaneous frequencies vary with time and it is impossible for the signal to end exactly at its complete cycles. In this study, a simple mirror image technique about the first and last maxima/minima of the signal was used to extend the 30-sec signal at its beginning and end to a nearly 90-sec signal. While the original 30-sec signal was used in Figure 5.5, the extended nearly 90-sec signal was considered in Figure 5.6(b). Clearly, the end effects have been significantly reduced by the mirror image technique.

5.2.3. Sampling Rate Selection and Noise Effect. To understand the sampling rate and noise effects on the signal decomposition by AMD, the signal in Equation (5.1) was discretized at 0.05 sec interval and contaminated with a Gaussian white noise with zero mean and a standard deviation of 10% of the amplitude of the signal $x_1(t) + x_2(t)$. The contaminated signal and the noise component are shown in Figure 5.7. To select bisecting frequencies, wavelet analysis using the signified complex Morlet wavelet in Equation (5.2) with a center frequency of 1.5 Hz and bandwidth parameter of 5 sec^2 was conducted to produce the wavelet scalogram as shown in Figure 5.8. It can be seen that three bisecting frequencies were marked in Figure 5.8. The first and third bisecting frequencies were used to filter out noises outside the signal frequency range and the second frequency was used to decompose the two signal components.

When a sampling rate of 20 Hz is used, the frequency components of the contaminated signal can be accurately reconstructed up to 10 Hz according to the Nyquist-Shannon sampling theory. In this case, the noise above 10 Hz due to Gibbs' effects from a 1-10 Hz bandpass filter cannot be represented appropriately. This misrepresentation will distort the reconstruction of the contaminated signal since the one-sided Fourier transform is used to evaluate the Hilbert transforms in the proposed AMD; the contaminated signal thus cannot be completely decomposed into two components with mutually exclusive frequency spectra. To account for the Gibb's effects, a higher

sampling rate must be used. To illustrate this point, the 30-sec contaminated signal (similar to the measured data in engineering applications) was resampled by a linear interpolation between any two adjacent data points. For example, the original 0.05 sec time interval can be reduced to 0.025 and 0.0125 sec to increase the sampling rate from 20 Hz to 40 Hz and 80 Hz, respectively.

Figures 5.9(a-c) show the instantaneous frequencies obtained by AMD for a sampling rate of 20 Hz, 40 Hz, and 80 Hz, respectively. The use of 20 Hz sampling rate results in significant errors in the estimation of instantaneous frequencies but both 40 Hz and 80 Hz sampling rates lead to accurate results in comparison with the exact instantaneous frequencies. To help explain the difference in sampling rate effect from 20 Hz to 40 Hz, the Fourier spectra of the white noise with 0.05-sec and 0.025-sec time intervals are compared in Figure 5.10. Figure 5.10(b) confirms that the Gibbs' effect was significant above 10 Hz. To further support the above explanation, Figures 5.11(a, b) show the Fourier spectra of the two decomposed signals with 20 Hz and 40 Hz sampling rates, respectively. Indeed, as illustrated in Figure 5.11(a), the spectra of the decomposed signals are nonzero around 8-9 Hz when the data series was sampled at 20 Hz sampling rate. As the sampling rate was increased to 40 Hz, Figure 5.11(b), AMD can accurately extract each individual component.

Figure 5.11 (b) also demonstrated that AMD is a "perfect" adaptive bandpass filter for any data series that is appropriately sampled. Referred to Figure 5.8, the noises of the contaminated signal below the first and above the third bisecting (cutoff) frequencies have been successfully filtered out. To further illustrate the effects of noise level, two Gaussian white noises with zero means and standard deviations of 5% and 20% of the amplitude of the signal $x_1(t) + x_2(t)$ were respectively injected to the signal in Equation (5.1). With a 0.025-sec time interval (by a linear interpretation of the 0.05-sec data series), the instantaneous frequencies with different noise levels are presented in Figure 5.12. In comparison with Figure 5.9(b), all the instantaneous frequencies obtained from AMD-Hilbert spectral analysis are in an excellent agreement with their respective exact values even with 20% noise. Various levels of noise have been effectively filtered out by the proposed AMD.
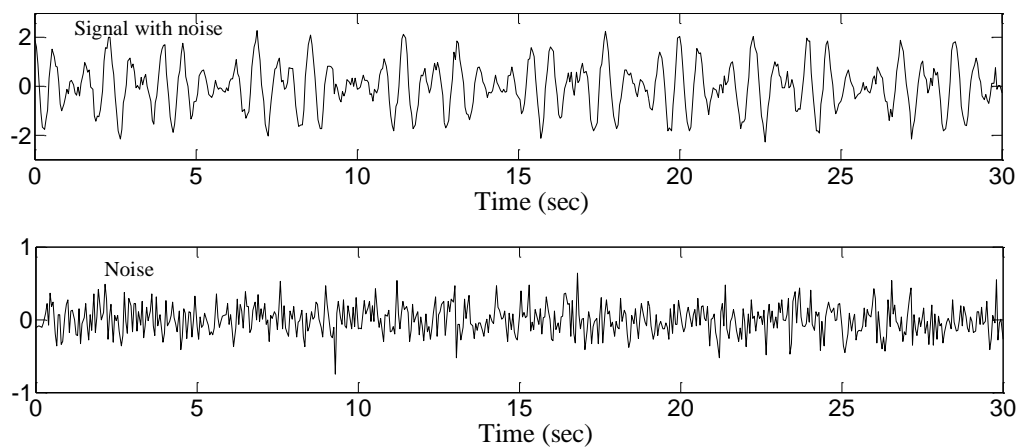
Figure 5.7. Contaminated Signal with Noise and the Gaussian White Noise
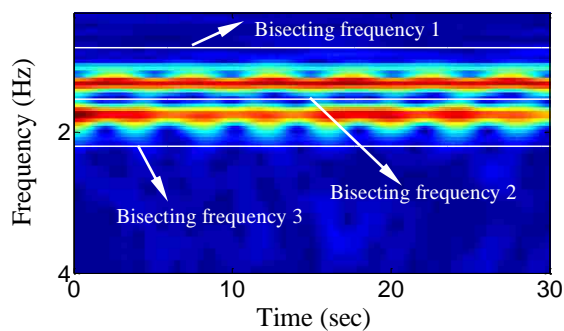
Figure 5.8. Continuous Wavelet Analysis: Scalogram and Bisecting Frequencies
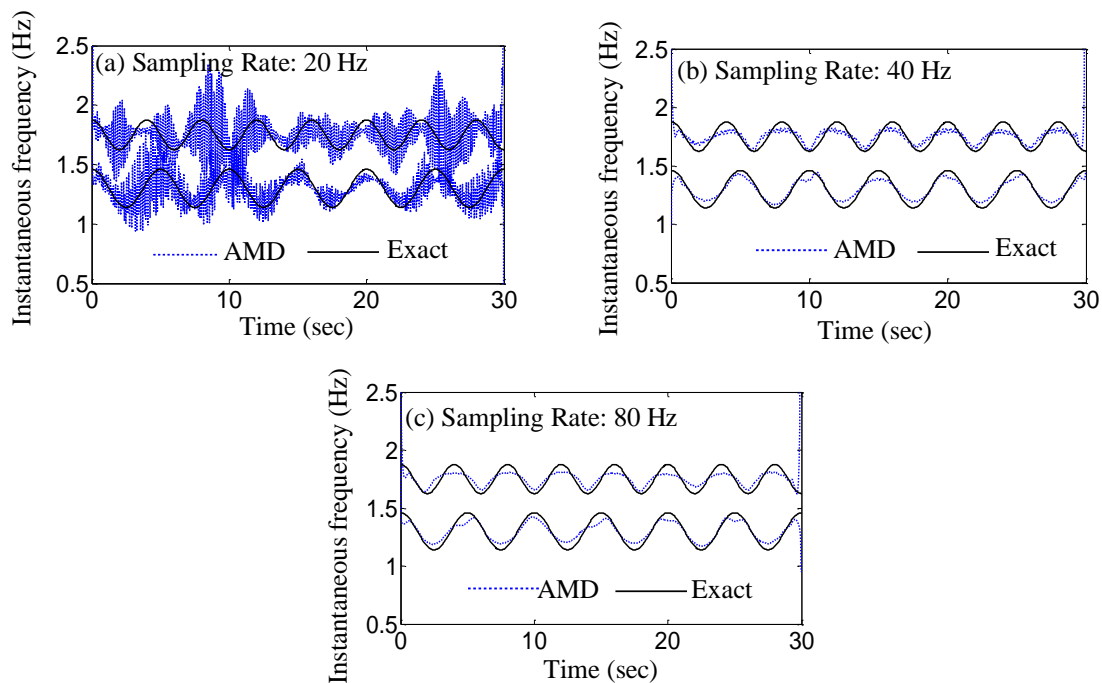
Figure 5.9. Instantaneous Frequencies with Various Sampling Rates

(a) Sampling Rate: 20 Hz   (b) Sampling Rate: 40 Hz
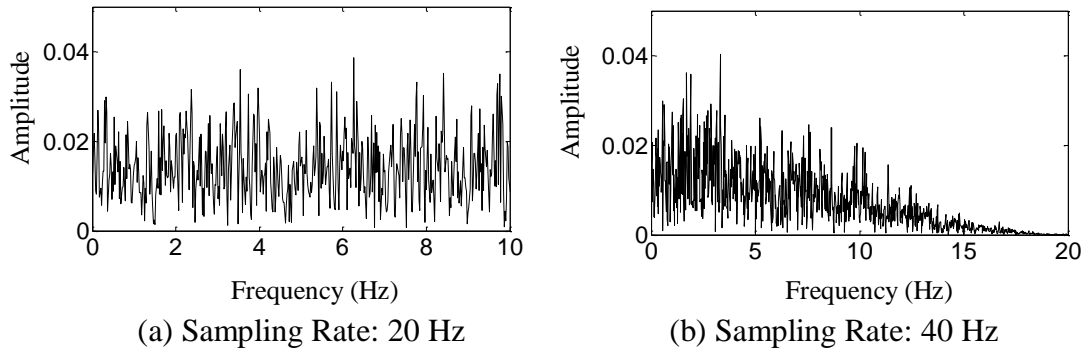
Figure 5.10. Fourier Spectra of the Gaussian Noise with Different Sampling Rates

(a) Sampling Frequency: 20 Hz

(b) Sampling Frequency: 40 Hz
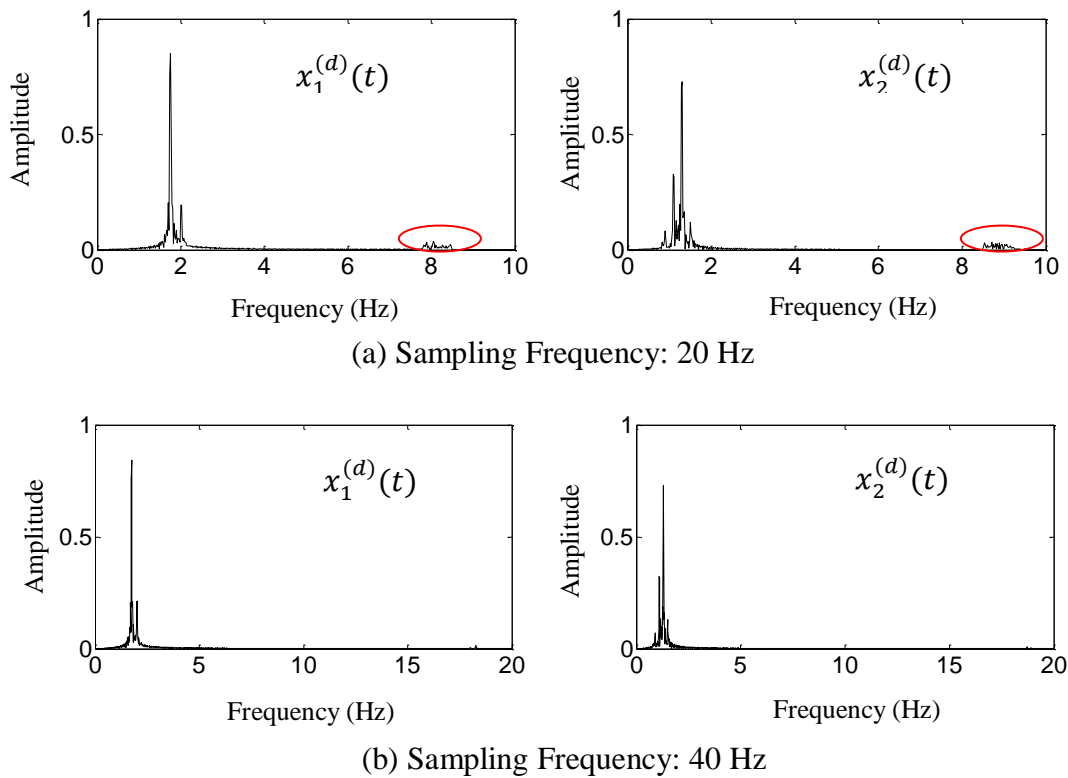
Figure 5.11. Fourier Spectra of the Decomposed Signals with Different Sampling Frequencies

(a) 5% White Noise   (b) 20% White Noise
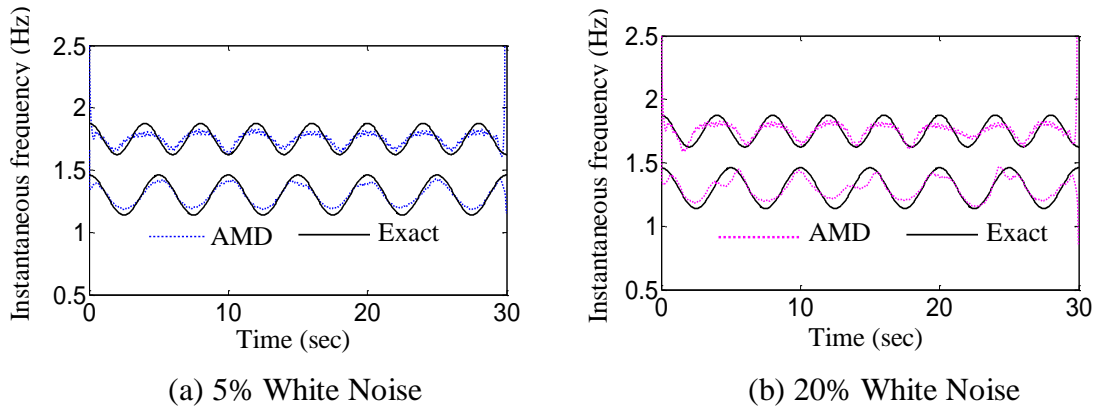
Figure 5.12. Instantaneous Frequencies with Different Noises

5.3. SIGNAL DECOMPOSITION WITH FREQUENCY AND AMPLITUDE MODULATED COMPONETS

5.3.1. Frequency Modulated Components. Consider a frequency-modulated signal $x(t) = x_1(t) + x_2(t) + x_3(t)$ with its three components defined by:

$$x_1(t) = \begin{cases} \cos[2\pi(6t)] & 0 \leq t \leq 10\ sec \\ \cos\left[2\pi\left(6t - \frac{(t-10)^2}{5}\right)\right] & 10 < t \leq 20\ sec \\ \cos[2\pi(2t + 60)] & 20 < t \leq 30\ sec \end{cases},$$

$$x_2(t) = \begin{cases} \cos[2\pi(8t)] & 0 \leq t \leq 10\ sec \\ \cos\left[2\pi\left(8t - \frac{(t-10)^2}{20}\right)\right] & 10 < t \leq 20\ sec \\ \cos[2\pi(7t + 15)] & 20 < t \leq 30\ sec \end{cases}, \text{ and}$$

$$x_3(t) = \begin{cases} \cos[2\pi(10t)] & 0 \leq t \leq 10\ sec \\ \cos\left[2\pi\left(10t - \frac{(t-10)^2}{10}\right)\right] & 10 < t \leq 20\ sec \\ \cos[2\pi(8t + 30)] & 20 < t \leq 30\ sec \end{cases}. \quad (5.3)$$

The original signal with a time interval of 0.01 sec. and a sampling frequency of 100 Hz is shown in Figure 5.13. The bisecting frequencies represented by the white solid lines in Figure 5.14 were selected from the wavelet transform scalogram using the simplified Morlet wavelet with a center frequency of 8 Hz and bandwidth parameter of 8

sec^2. Different parameters were used here to ensure that the wavelet ridges in time-frequency plane are visually identifiable from the scalogram.
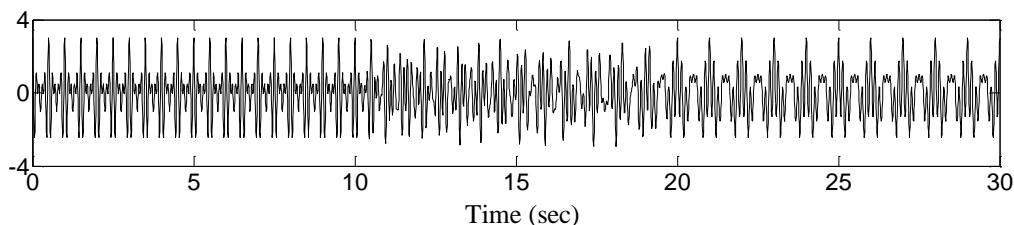
Figure 5.13. Original Signal
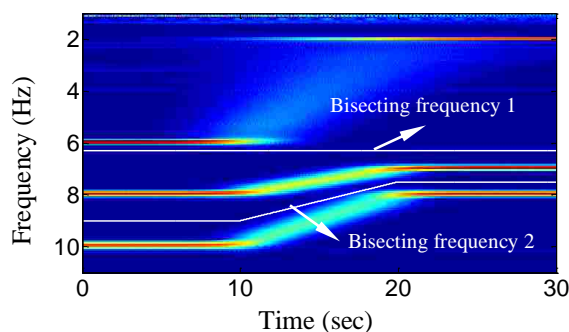
Figure 5.14. Continuous Wavelet Transform Scalogram and Bisecting Frequencies

In this case, EMD failed to separate the signal components since their frequencies are too close. However, the three individual components were accurately extracted by using AMD as shown in Figure 5.15. The modulated frequencies of three decomposed signals from AMD and wavelet scalogram ridges are compared with their exact values in Figure 5.16. It can be clearly seen that the instantaneous frequencies obtained by AMD are in excellent agreement with the exact values. As shown in Figure 5.16, those by wavelet ridges are sufficiently accurate in high frequency ranges but less so in low frequency ranges. The instantaneous frequency of the first component suddenly drops at 12 sec., and it cannot track the linear variation due to low resolution in time domain.
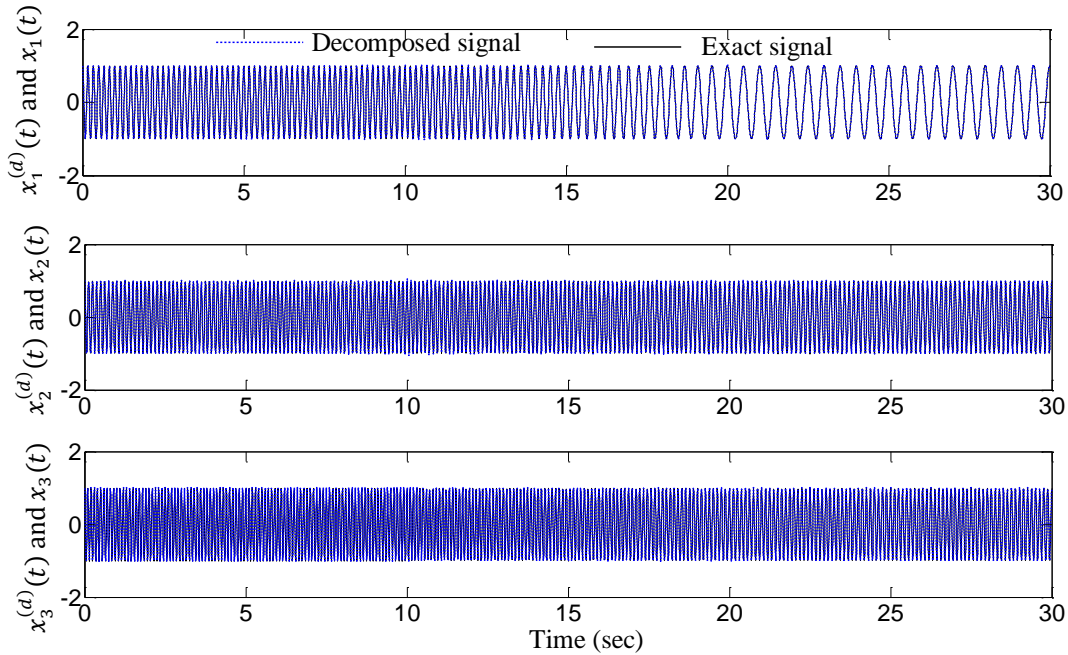
Figure 5.15. Decomposed Signals by AMD
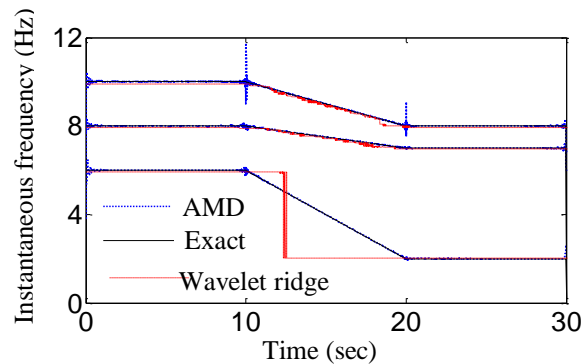
Figure 5.16. Instantaneous Frequencies Obtained from AMD and Wavelet Ridges

5.3.2. Frequency and Amplitude Modulated Components. Consider an amplitude and frequency modulated signal $x(t) = x_1(t) + x_2(t) + x_3(t)$ with three components defined by:

$$x_1(t) = \begin{cases} \cos[10\pi t + 2\sin(0.4\pi t)] & 0 \leq t \leq 10 \; sec \\ \cos\{10\pi t + 2\sin[0.5\pi(t-10)]\} & 10 < t \leq 20 \; sec \\ e^{-0.005[8\pi(t-20)]}\cos\{8\pi t + 2\sin[0.4\pi(t-20)]\} & 20 < t \leq 30 \; sec \end{cases}$$

$$x_2(t) = \begin{cases} \cos[16\pi t + 2\sin(0.4\pi t)] & 0 \le t \le 10 \ sec \\ \cos\{14\pi t + 2\sin[0.4\pi(t-10)]\} & 10 < t \le 20 \ sec \\ e^{-0.005[13\pi(t-20)]}\cos\{13\pi t + 2\sin[0.5\pi(t-20)]\} & 20 < t \le 30 \ sec \end{cases}$$

$$x_1(t) = \begin{cases} \cos[20\pi t + 2\sin(0.5\pi t)] & 0 \le t \le 10 \ sec \\ \cos\{18\pi t + 2\sin[0.5\pi(t-10)]\} & 10 < t \le 20 \ sec \\ e^{-0.005[16\pi(t-20)]}\cos\{16\pi t + 2\sin[0.5\pi(t-20)]\} & 20 < t \le 30 \ sec \end{cases}$$

$$(5.4)$$

The original signal with a time interval of 0.01 sec and a sampling frequency of 100 Hz is presented in Figure 5.17. The bisecting frequencies represented by the white solid lines in Figure 5.18 were selected from the wavelet transform scalogram using the simplified Morlet wavelet with a center frequency of 8 Hz and bandwidth parameter of 8 sec^2. Similar to the signal in Equation (5.3), EMD cannot separate the signal components in Equation (5.4) since their frequencies are too close. However, it can be seen from Figure 5.19 that the three individual components were extracted without any visible errors by AMD. The modulated frequencies of three decomposed signals from AMD and wavelet scalogram ridges are compared with their exact frequencies as presented in Figure 5.20. The instantaneous frequencies obtained by wavelet ridges are more accurate in high frequency ranges due to relatively high time resolution. However, for most parts, instantaneous frequencies cannot be separated as shown in Figure 5.20 since the required high time resolution is limited according to the Heisenberg-Gabor uncertainty principle. Overall, the instantaneous frequencies from wavelet transform are not a good representation of modulated frequencies; they look like straight lines representing the average of their respective exact frequencies. On the other hand, the instantaneous frequencies obtained from AMD, as shown in Figure 5.20, are in excellent agreement with the exact modulated frequencies.
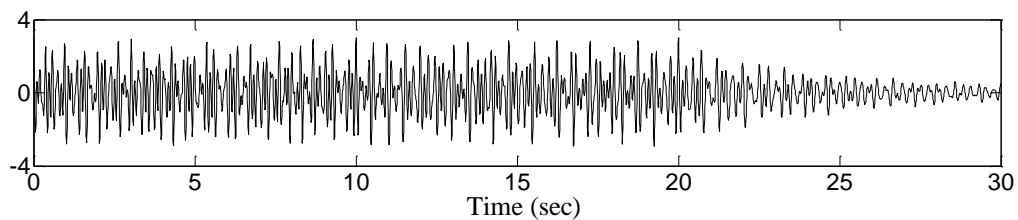
Figure 5.17. Original Signal
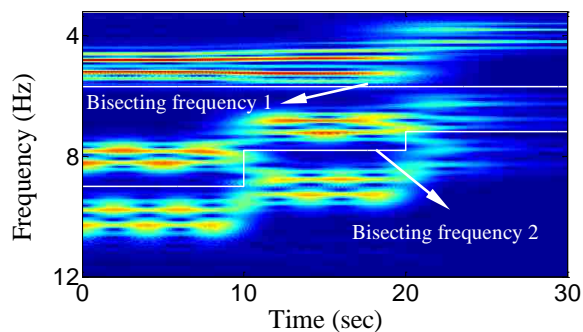
Figure 5.18. Continuous Wavelet Transform Scalogram and Bisecting Frequencies
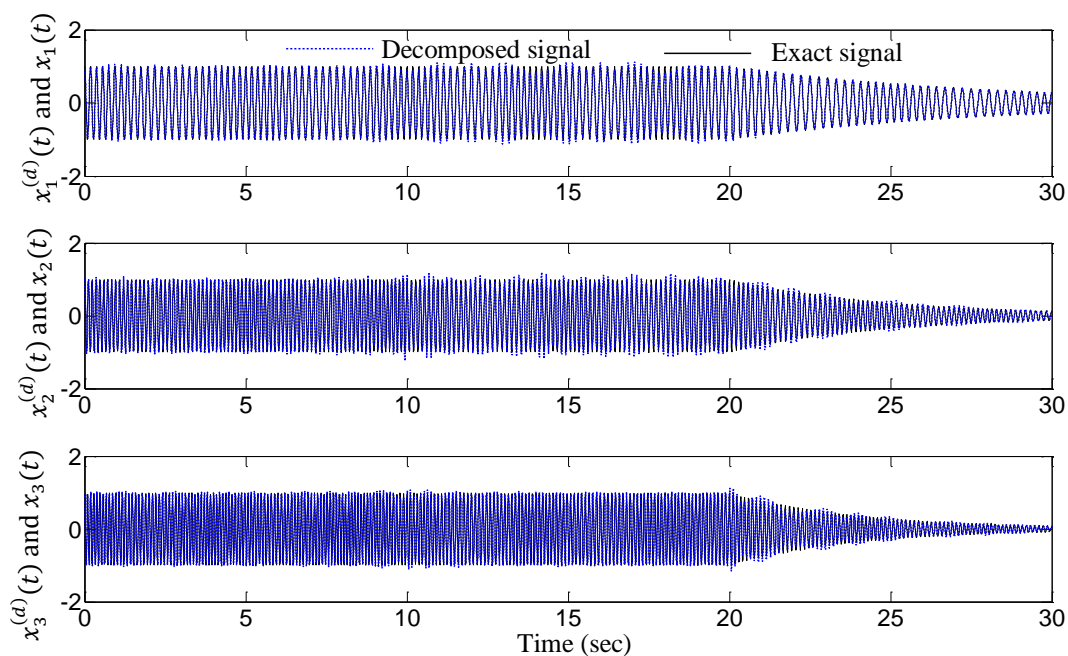
Figure 5.19. Decomposed Signals by AMD
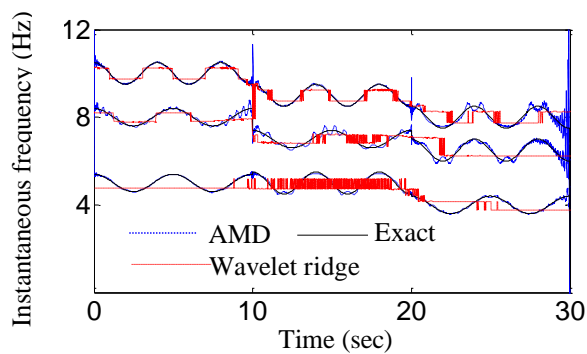
Figure 5.20. Instantaneous Frequencies Obtained from AMD and Wavelet Ridges

5.4. INSTANTANEOUS FREQUENCY IDENTIFICATION OF WEAKLY NONLINEAR SYSTEMS

5.4.1. Instantaneous Frequency and Damping Identification. As presented in Sections 5.1, the AMD-Hilbert spectral analysis is able to track the instantaneous frequencies and damping coefficients of a measured signal. In this section, it is applied to nonlinear systems that are often encountered in structural and mechanical engineering. In particular, interpreting measured responses for nonlinear behavior with the proposed AMD theorem is a main concern.

Consider a general system with nonlinear damping and restoring forces. Without knowing their specific physical model, the damping and restoring forces can be represented by the multiplications of a nonlinear damping coefficient and a nonlinear stiffness coefficient with the system velocity and displacement, respectively. Therefore, the free vibration of a single DOF nonlinear system with a unit mass can be represented by the following equation of motion:

$$\ddot{x}(t) + 2h_0(\dot{x})\dot{x}(t) + \omega_0^2(x)x(t) = 0 \tag{5.5}$$

in which $x(t)$ is the displacement of the system, $2h_0(\dot{x})$ is the velocity-related nonlinear damping coefficient and $\omega_0^2(x)$ is the displacement-related nonlinear stiffness coefficient or the squared of natural frequency. Through the system responses, both coefficients can be viewed as functions of time, $\omega_0^2(x) = \omega_0^2(t)$ and $2h_0(\dot{x}) = 2h_0(t)$. Depending on the degree of system nonlinearity, they may rapidly vary with time and have overlapping frequency spectra with the system responses (Feldman, 2011). Therefore, Equation (5.5) can be rewritten as:

$$\ddot{x}(t) + 2h_0(t)\dot{x}(t) + \omega_0^2(t)x(t) = 0 \tag{5.6}$$

And its Hilbert transform can be expressed into:

$$H[\ddot{x}] + 2h_{0L}H[\dot{x}] + 2H[h_{0H}]\dot{x} + \omega_{0L}^2H[x] + H[\omega_{0H}^2]x = 0 \tag{5.7}$$

in which h_{0L} and h_{0H} represent lowpass and highpass parts of the time-varying nonlinear damping coefficient $h_0(t)$; ω_{0L}^2 and ω_{0H}^2 are the lowpass and highpass part of the time-varying nonlinear stiffness coefficient or $\omega_0^2(t)$.

For a single DOF system, the displacement measurement $x(t)$ is assumed available. Its analytic signal $z(t)$ can be expressed into:

$$z(t) = x(t) + jH[x(t)] = A(t)e^{j \int \omega(t)dt} \tag{5.8}$$

in which $A(t)$ and $\omega(t)$ are the instantaneous amplitude and frequency of the analytic signal. The first and second derivatives of the analytic signal are then derived as:

$$\dot{z} = z(\frac{\dot{A}}{A} + j\omega) \text{ and } \ddot{z} = z(\frac{\ddot{A}}{A} - \omega^2 + 2j\frac{\dot{A}}{A}\omega + j\dot{\omega}) \tag{5.9}$$

Therefore, the velocity and acceleration as well as their Hilbert transforms can be expressed into functions of the displacement and its Hilbert transform. That is,

$$\dot{x}(t) = x(\frac{\dot{A}}{A}) - H[x]\omega, \text{ and } H[\dot{x}(t)] = x\omega + H[x]\frac{\dot{A}}{A} \tag{5.10}$$

$$\ddot{x}(t) = x\left(\frac{\ddot{A}}{A} - \omega^2\right) - H[x](2\frac{\dot{A}}{A}\omega + \dot{\omega}), \text{ and } H[\ddot{x}(t)] = x\left(2\frac{\dot{A}}{A}\omega + \dot{\omega}\right) + H[x](\frac{\ddot{A}}{A} - \omega^2) \tag{5.11}$$

Substituting Equations (5.10) and (5.11) into Equations (5.7) and (5.8) yields

$$x\left(\frac{\ddot{A}}{A} - \omega^2 + 2h_0\frac{\dot{A}}{A} + \omega_0^2\right) - H[x]\left(2\frac{\dot{A}}{A}\omega + \dot{\omega} + 2h_0\omega\right) = 0 \tag{5.12}$$

$$x\left(2\frac{\dot{A}}{A}\omega + \dot{\omega} + 2h_{0L}\omega + 2H[h_{0H}]\frac{\dot{A}}{A} + H[\omega_{0H}^2]\right) +$$

$$H[x](\frac{\ddot{A}}{A} - \omega^2 + 2h_{0L}\frac{\dot{A}}{A} - 2H[h_{0H}]\omega + \omega_{0L}^2) = 0 \tag{5.13}$$

Since any signal and its Hilbert transform have a 90° phase difference, they cannot be zero at the same time. As such, the determinant of the coefficient matrix of Equations (5.12) and (5.13) must be zero, leading to:

$$\left(\frac{\ddot{A}}{A} - \omega^2 + 2h_0\frac{\dot{A}}{A} + \omega_0^2\right)^2 + \left(\frac{\ddot{A}}{A} - \omega^2 + 2h_0\frac{\dot{A}}{A} + \omega_0^2\right)\left(-2h_{0H}\frac{\dot{A}}{A} - 2H[h_{0H}]\omega - \omega_{0H}^2\right)$$

$$+(2\frac{\dot{A}}{A}\omega + \dot{\omega} + 2h_0\omega)^2 + (2\frac{\dot{A}}{A}\omega + \dot{\omega} + 2h_0\omega)(-2h_{0H}\omega + 2H[h_{0H}]\frac{\dot{A}}{A} + H[\omega_{0H}^2] = 0 \tag{5.14}$$

If both $h_0(t)$ and $\omega_0^2(t)$ are slowly-varying functions of time, h_{0H}, $H[h_{0H}]$, ω_{0H}^2, and $H[\omega_{0H}^2]$ are approximately equal to zero. Under this condition, the instantaneous damping coefficient $2h_0(t)$ and the instantaneous natural frequency $\omega_0(t)$ can be evaluated from Equation (5.14) and expressed with:

$$\omega_0^2(t) = \omega^2 - \frac{\ddot{A}}{A} + 2\frac{\dot{A}}{A^2} + \frac{A\dot{\omega}}{A\omega} \text{ and } h_0(t) = -\frac{\dot{A}}{A} - \frac{\dot{\omega}}{2\omega} \tag{5.15}$$

Equation (5.15) relates the instantaneous damping coefficient and natural frequency of an engineering system to those of its measured signals. It can be proven

without difficulty that the instantaneous parameters of the signals are identical to those of a lightly-damped linear system, which has been used in almost all the system identification research to date. For a nonlinear system, Equation (5.15) becomes very important to establish one of the critical nonlinear characteristics – the relationship between its natural frequency and the amplitude of the system response. However, for a weakly nonlinear system, the amplitude and frequency often change slowly over time. As a result, the relationship becomes trivial as studied by Feldman (2011).

For a multi-DOF weakly nonlinear system, the AMD-Hilbert spectral analysis can be applied in a similar way as presented for linear systems. In addition to instantaneous frequency and damping, instantaneous mode shapes must be estimated as well.

5.4.2. Frequency Traction for Two-Story Shear Building. This example represents an engineering application of the proposed AMD for time-varying system identification. It is a two-story shear building as schematically shown in Figure 5.21. It has masses of $m_1=2.63\times10^5$ kg and $m_2=1.75\times10^5$ kg at the lower and upper floors, damping coefficients of $c_1=6.95\times10^2$ kN-sec/m and $c_2=1.86\times10^2$ kN-sec/m for the first and second stories, and initial stiffness of $k_1=2.10\times10^5$ KN/m and $k_2=1.05\times10^5$ kN/m for the first and second stories, respectively. The stiffness of the first story (k_1) was set to be periodically reduced from 2.10×10^5 kN/m to 1.40×10^5 kN/m from t=4 sec to 16 sec, $k_1=\{2.1-0.058(t-4)-0.131\sin[\frac{\pi}{2}(t-4)]\}\times10^5$ kN/m. The stiffness of the second story (k_2) was set to be linearly reduced from 1.05×10^5 kN/m to 0.70×10^5 KN/m over a period of t=4 sec to t=8 sec.
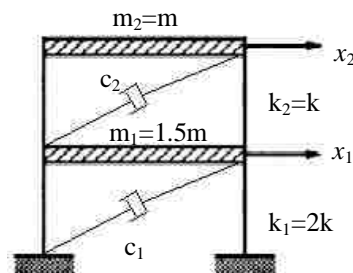
Figure 5.21. Two-Story Shear Building

The building was subjected to the 1940 El Centro ground acceleration record and a synthesized Gaussian white noise with zero mean and 0.1g (g is the gravitational acceleration) standard deviation. The displacement at first floor x_1 was considered as the dynamic response measurement with a time interval of 0.02 sec. From the wavelet scalogram of the displacement using the simplified complex Morlet wavelet function with a center frequency of 4 Hz and bandwidth parameter of 5 sec^2, a constant bisecting frequency of 4 Hz was selected. The decomposed signals of x_1 by AMD and their instantaneous frequencies are presented in Figures 5.22 and 5.23, respectively. It can be seen from Figure 5.22 that AMD can track the frequency modulation under earthquake and white noise excitations. The frequency identification is more accurate for the lower frequency component since the first mode dominates the first floor displacement as illustrated in Figure 5.22. In comparison with Figures 5.16 and 5.20, Figure 5.23 includes a significantly more fluctuation of the identified instantaneous frequencies. By filtering out the fast varying part of the instantaneous frequency, the average of the instantaneous frequency is accurate to represent the system time-varying frequency.
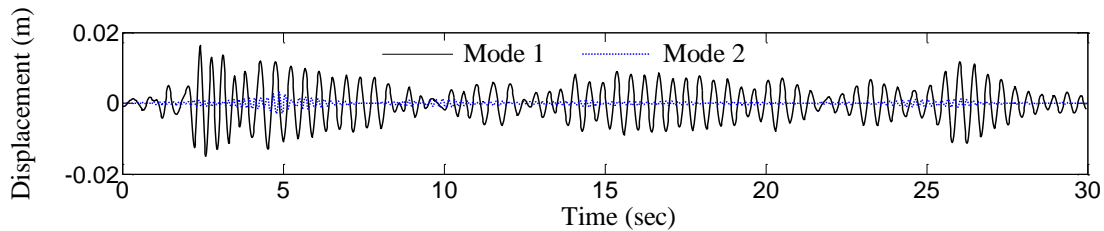
(a) EI Centro Earthquake Excitation
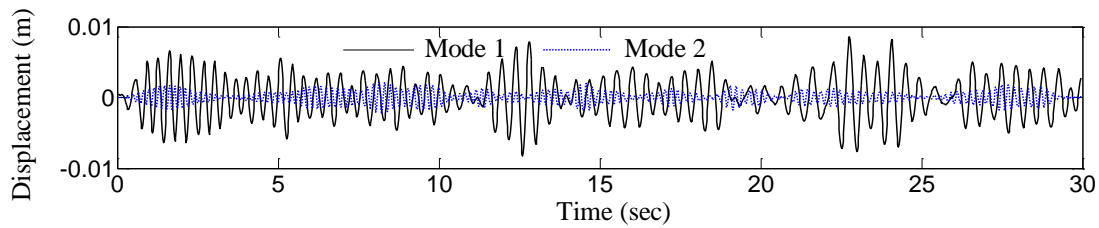
(b) White Noise Excitation

Figure 5.22. Decomposed Modal Responses by AMD

(a) EI Centro Earthquake Excitation (b) White Noise Excitation
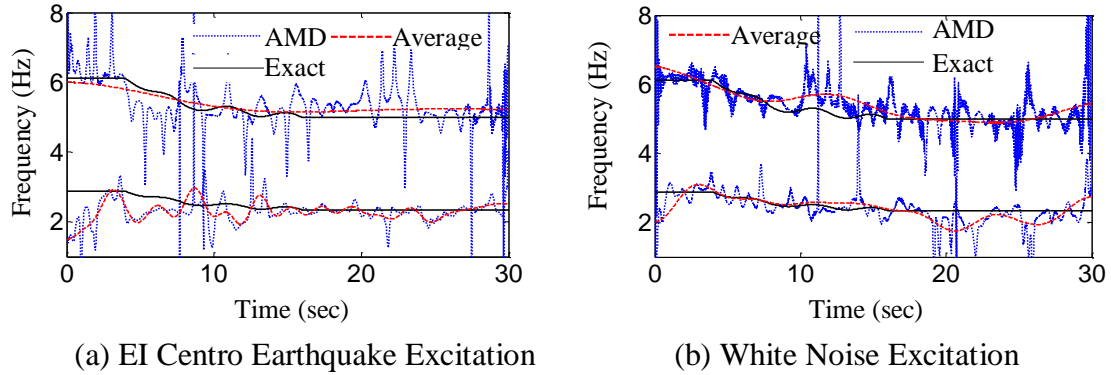
Figure 5.23. Instantaneous Frequencies by AMD

5.4.3. Frequency Traction for a Duffing System. A classic Duffing system with a hardening spring and a linear damping element is used as an example of a nonlinear elastic force. Specifically, the following equation of motion is considered (Feldman, 2007):

$$\ddot{x} + 0.05\dot{x} + x + 0.01x^3 = 0 \tag{5.16}$$

Under an initial displacement of 10 at rest, the free vibration response was simulated using the 4th Runge-Kutta method with 0.1 sec time interval and presented in Figure 5.24. By AMD-Hilbert spectral analysis of the response, the instantaneous frequency and damping coefficient as well as their average values can be obtained from the free vibration. They are presented in Figure 5.25 together with the amplitude-frequency relationship. It can be clearly seen from the average instantaneous frequency in Figure 5.25 that the cubic spring nonlinear effect is important in large amplitude. The instantaneous frequency decreased rapidly at the beginning of the free vibration and gradually approached to an asymptotic value of the corresponding linear system. Therefore, the average of the instantaneous frequency can accurately track the variation of a weakly nonlinear system. The average damping coefficient identified is 2.5%, which is exactly the same as the damping coefficient of the Duffing system.
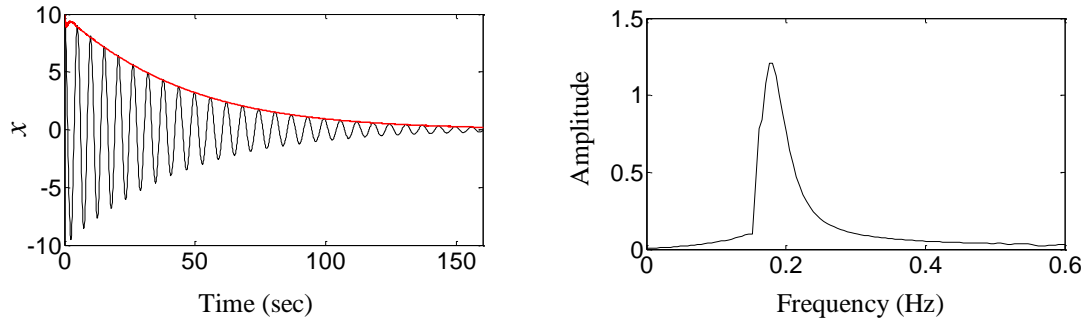
Figure 5.24. Free Response and Its Fourier Spectrum of a Duffing System
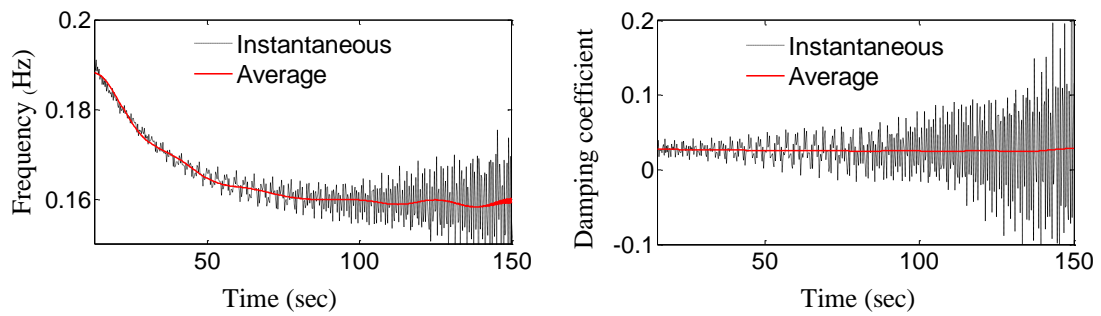
(a) Instantaneous Frequency

(b) Damping Coefficient
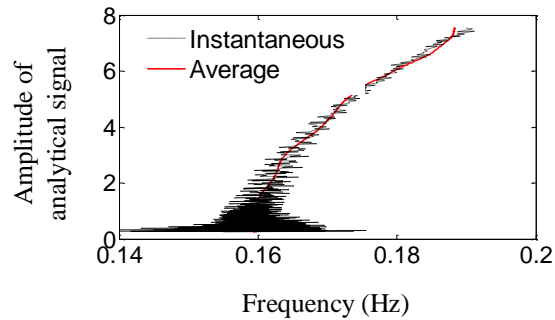
(c) Frequency-Amplitude Relation

Figure 5.25. Identified Dynamic Characteristics of the Analytic Signal

5.4.4. Frequency Traction for a Hysteretic Nonlinear Structure. A one-story shear building with a tuned mass damper as schematically shown in Figure 5.26 is considered as an example. It has masses of $m_1=100$ kg at the first floor and $m_2=10$ kg for the attached mass. The damping ratios of the first and second mode of the 2-DOF system at low amplitude are set to 1% and 5%, respectively. It has elastic stiffness of $k_1=100$ kN/m and $k_2=9.5$ kN/m for the first building story and the mass damper, respectively. The hysteretic behavior of the building is represented by a Bouc-Wen model (Wen, 1976). The equation of motion of the building and the mass damper can be described as:

$$m_1\ddot{x}_1 + c_{11}\dot{x}_1 + c_{12}\dot{x}_2 + (\alpha k_1 + k_2)x_1 - k_2 x_2 + (1-\alpha)\delta k_1 z = f_1 \quad (5.17a)$$

$$m_2\ddot{x}_2 + c_{21}\dot{x}_1 + c_{22}\dot{x}_2 + k_2 x_2 - k_2 x_1 = f_2 \quad (5.17b)$$

$$\dot{z} = A\dot{x}_1 - \beta\dot{x}_1|z|^n - \gamma|\dot{x}_1||z|^{n-1}z \quad (5.17c)$$

in which $\alpha = k_{\text{inelastic}}/k_1 = 0.5$, $\delta = 0.01$ m is the yield deformation, $A = 100$ 1/m, $\beta = 50$, $\gamma = 50$, $n = 1$, $c_{11} = 299.3$ N $\cdot$ sec/m, $c_{12} = c_{21} = -42.4$ N $\cdot$ sec/m, and $c_{22} = 14$ N $\cdot$ sec/m.
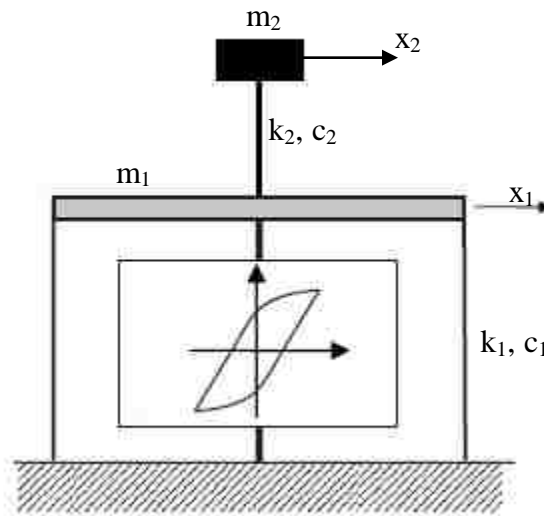
Figure 5.26. A One-Story Shear Building with a Tuned Mass Damper

5.4.4.1 Free vibration. A series of free vibration were simulated to verify the nonlinearity effects on the instantaneous frequency. The initial displacements at the first floor were set to 0.01, 0.02, 0.05, and 0.1 m. As discussed in Section 5.4, the instantaneous frequency of the decomposed response includes a slowly-varying part and

a rapidly-varying part. The rapidly-varying part can be filtered out by AMD with a suitable bisecting frequency. Another way to eliminate the rapidly-varying part is to integrate the instantaneous frequency over time duration. Therefore, the phase of the decomposed response can describe the structural nonlinearity during the vibration. The nonlinearity index E can be defined as (Liming et al., 2005):

$$E = \sqrt{\frac{\int [\theta_n(t) - \theta_l(t)]^2 dt}{\int [\theta_l(t)]^2 dt}} \tag{5.18}$$

where $\theta_n(t)$ and $\theta_l(t)$ represent the phase angles of the decomposed response from the nonlinear and its corresponding linear systems, respectively. The above nonlinearity index E also represents the damage severity of the structure during vibration. Therefore, E is also called as a damage index.

Again, the free vibration responses were simulated using the 4th–order Runge-Kutta method with time interval of 0.02 sec. When the initial displacement was set to less than or equal to 0.01 m, the structural system was considered to behave linearly. Otherwise, the structural system was considered as a nonlinear system. The responses of the linear and nonlinear systems and their Fourier spectra with initial displacement of 0.01 m and 0.05 m at the first floor are presented in Figure 5.27 and Figure 5.28, respectively. The identified instantaneous frequencies of linear and nonlinear systems from the simulated displacement at the first floor are presented in Figure 5.29. It can be clearly seen from Figure 5.29, the instantaneous frequency is significantly reduced at the beginning of the vibration when the amplitude of the response is significant. To further quantify the nonlinear effects on the phase, the free vibration with the initial displacements at the first floor of 0.02, and 0.1 m were simulated. The hysteretic loops are shown in Figure 5.30, and the phases of the first decomposed modal responses are presented in Figure 5.31. As demonstrated in Figures 5.30 and 5.31, a large initial displacement represents strong nonlinearity, and the phase angle is small for the strong nonlinear vibration. The damage indices with various initial displacements from 0.01 to 0.1 m are further presented in Figure 5.32. It can be seen from Figure 5.32 that the damage index is increased as the initial displacement increased.
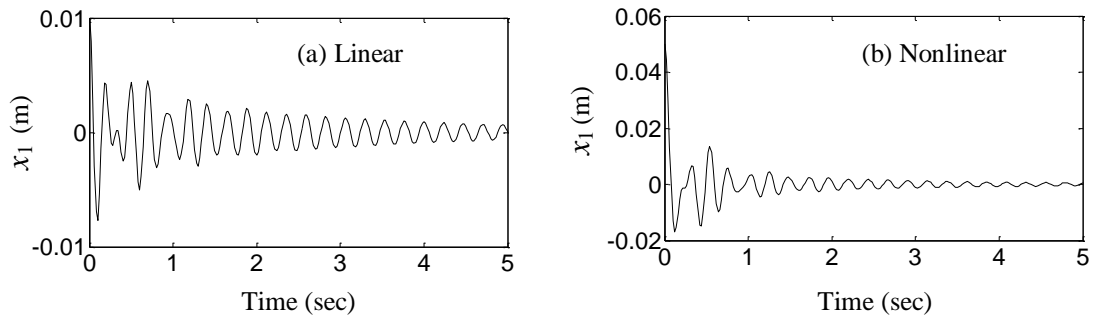
Figure 5.27. Free Vibration Responses of Linear and Nonlinear Systems
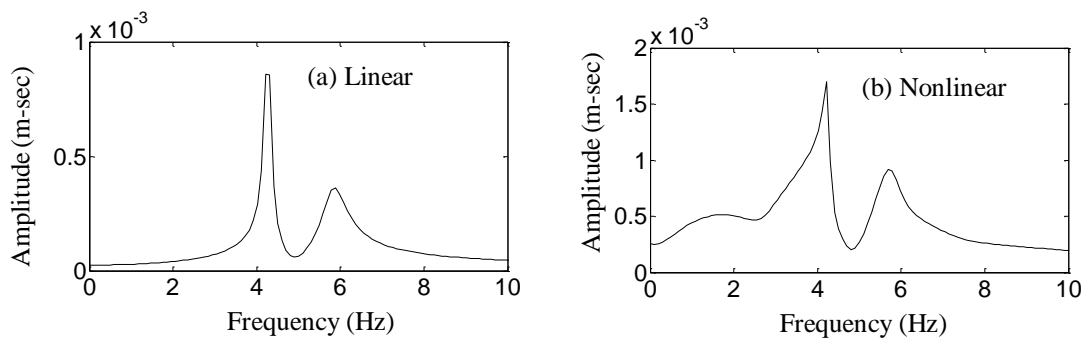
Figure 5.28. Fourier Spectra of Free Responses of Linear and Nonlinear Systems
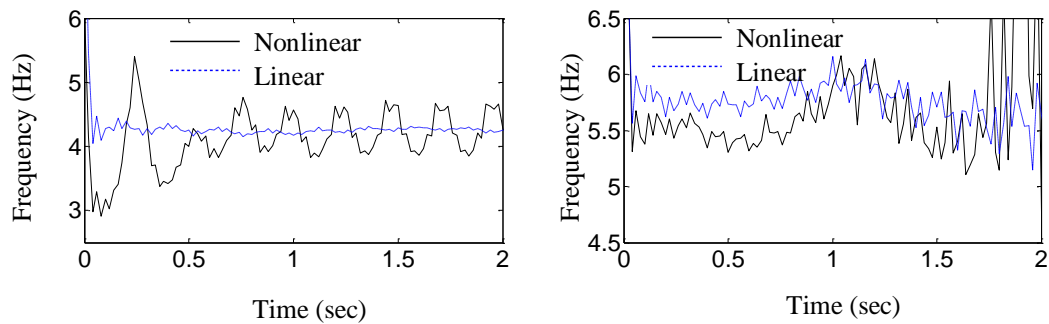
Figure 5.29. Instantaneous Frequencies of Mode 1 and 2 Responses from x_1
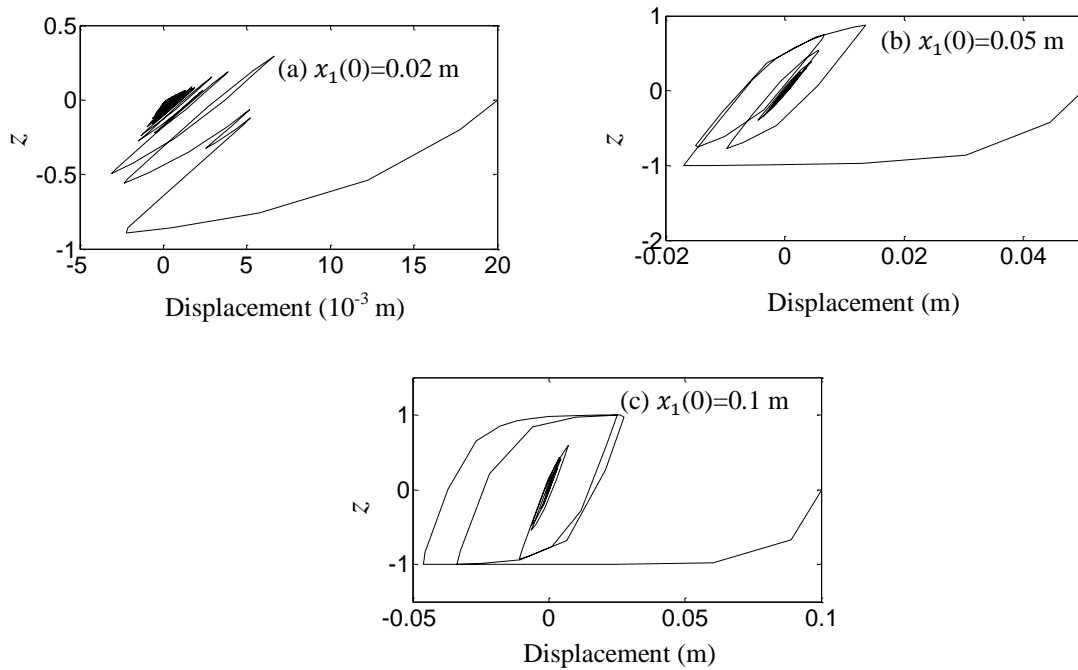
Figure 5.30. Bouc-Wen Hysteretic Loops with Various Initial Displacements
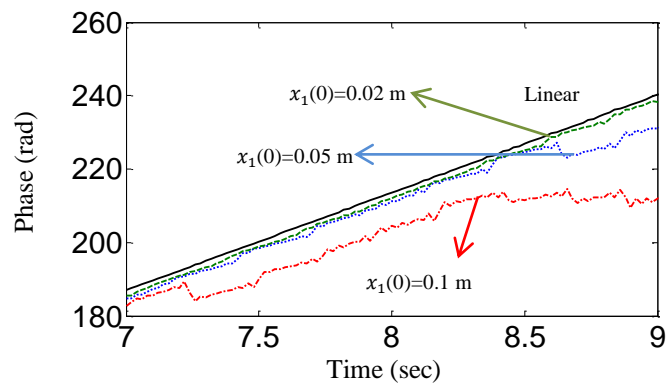
Figure 5.31. Phases of the Decomposed First Modal Response via AMD
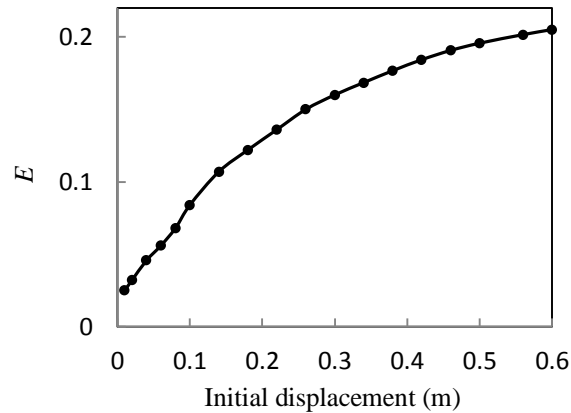
Figure 5.32. Damage Index E from Free Vibration

5.4.4.2 Ambient vibration. In this section, the one-story shear building with a tuned mass damper is subjected a Gaussian white noise excitation at its base.

Again, the responses were simulated using the 4th–order Runge-Kutta method with time interval of 0.02 seconds. The excitation for the linear simulation was set to $0.65f_0$ (f_0 is a mean-zero Gaussian white noise with a 1g standard deviation). For the linear simulation, the maximum displacement is less than the yield displacement; the structure was thus considered as a linear system. The excitation for nonlinear simulation was increased to $1.0f_0$, and the maximum displacement is larger than the yield displacement, the structure was considered as a nonlinear system. The displacement responses of the linear and nonlinear structure systems and their Fourier spectra are presented in Figure 5.33 and Figure 5.34, respectively. The instantaneous frequencies identified from the displacements of the first floor are presented in Figure 5.35. It can be seen from Figure 5.34 and Figure 5.35 that the frequency band of the nonlinear structure is wider than that of the linear system. To further study the nonlinear influences on the structure, an excitation level of $1.5f_0$, $2.0f_0$, $3.0f_0$ was considered. The Bouc-Wen hysteretic loops with various excitations are presented in Figure 5.36. Since the instantaneous frequencies for the ambient vibration fluctuate significantly, their integration (phase) are presented in Figure 5.37. It can be clearly seen that the structure performs like a linear structure when the excitation level is f_0; the phase and the nonlinearity index are close to those of the corresponding linear structure, respectively. However, when the excitation is increased to $3f_0$, the structure performs strongly

nonlinear. In this case, the phase is significantly reduced and the damage index increased. The defined damage indices for various excitations from f_0 to $3f_0$ are further presented in Figure 5.38. It demonstrates that the damage index is a nonlinear function of standard deviation of the excitation. It increases rapidly in a linear fashion at the beginning and then slowly increases over time.
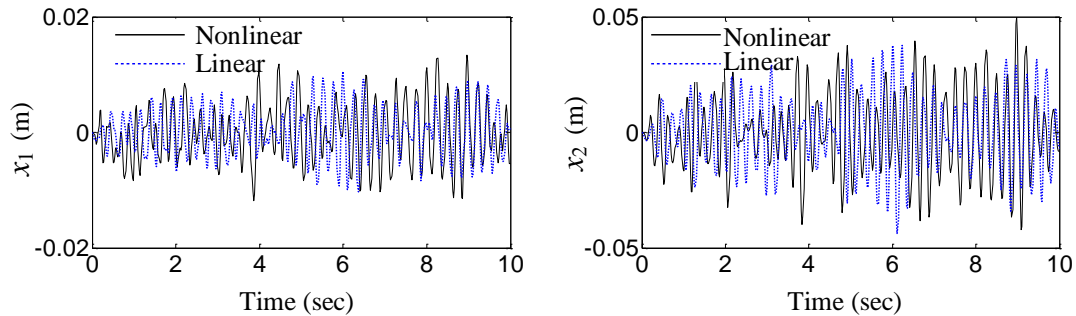
Figure 5.33. Ambient Responses of Nonlinear and Linear Systems
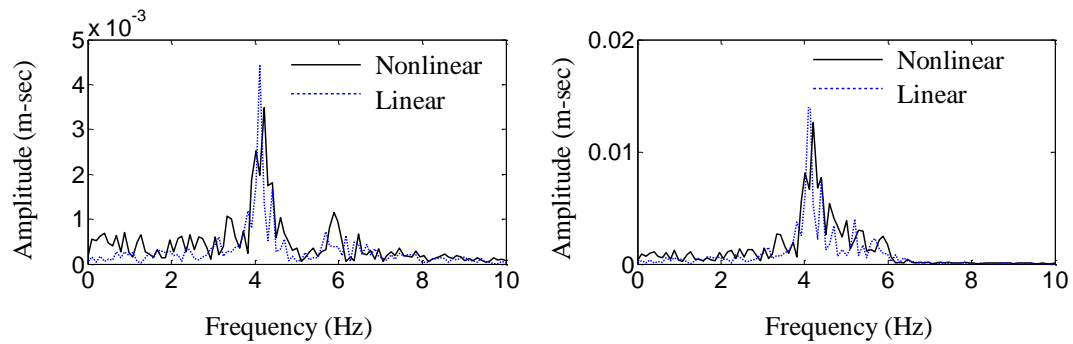
Figure 5.34. Fourier Spectra of Ambient Responses of Nonlinear and Linear Systems
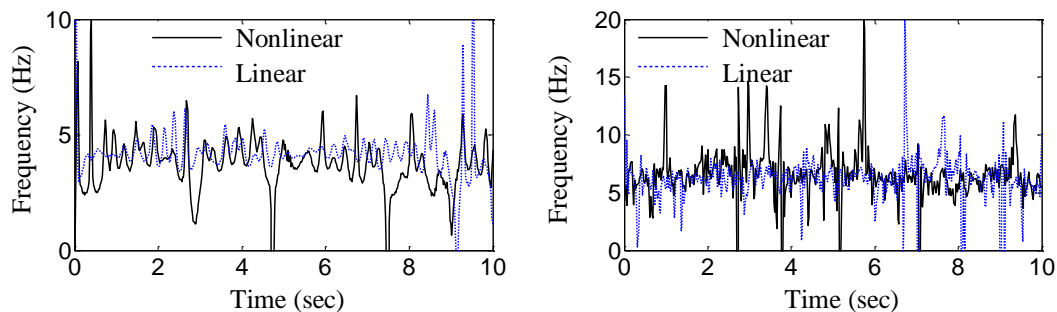
Figure 5.35. Instantaneous Frequencies of the Analytical Signal of Mode 1 and 2 Decomposed from x_1 via AMD
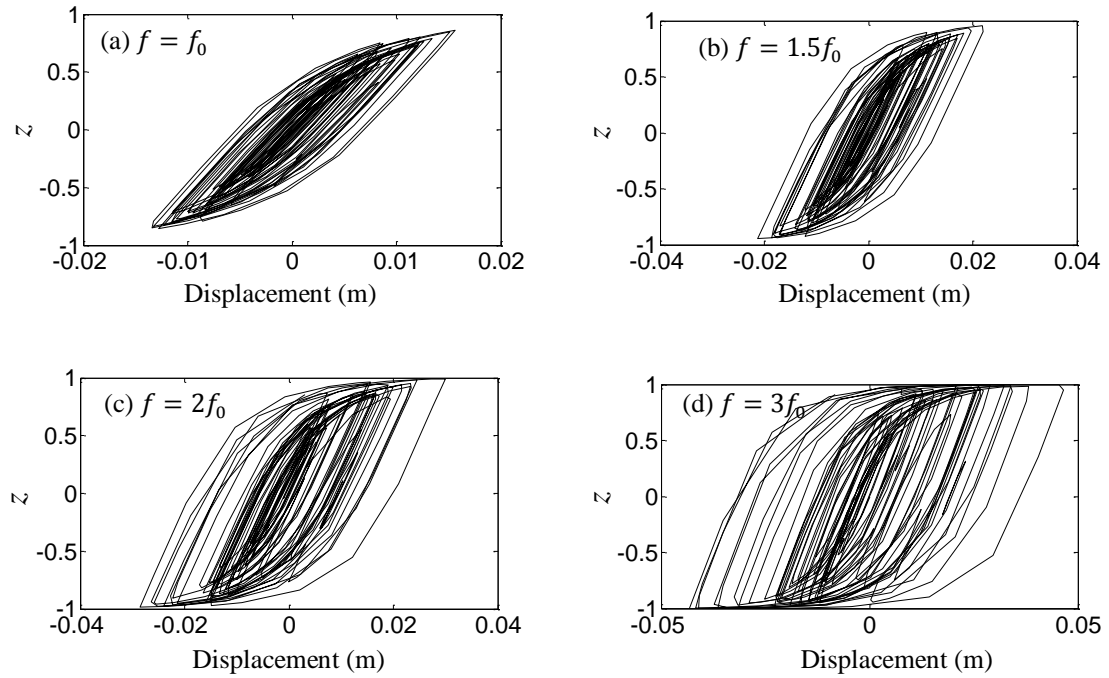
Figure 5.36. Bouc-Wen Hysteretic Loops with Various Excitations
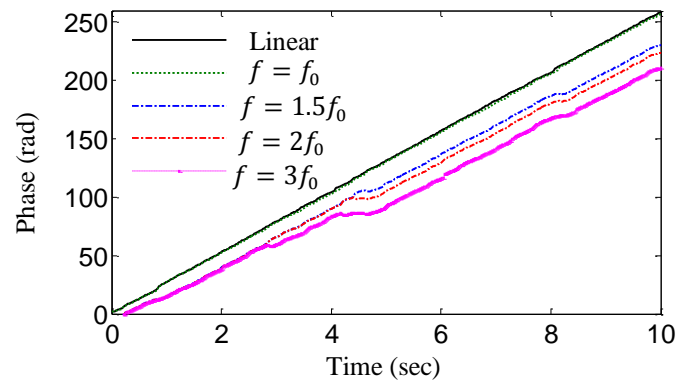
Figure 5.37. Phases of the Decomposed First Modal Responses via AMD
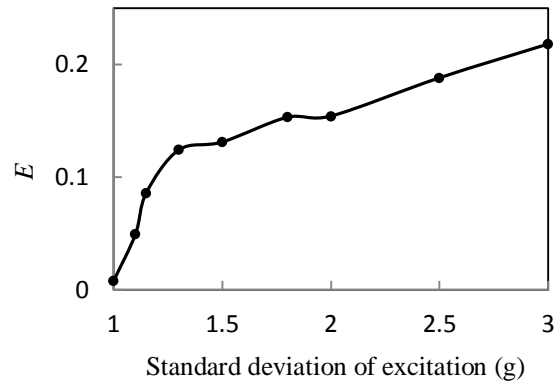
Figure 5.38. Damage Index *E* from Ambient Vibration

5.5. SUMMARY

The basis of the AMD theorem can be interpreted as an adaptive lowpass filter whose bisecting frequency varies with the time-varying frequencies of a non-stationary signal. By transferring the signal from time to phase domain, the frequency overlapping issue over the time duration of the signal can be alleviated or eliminated completely, thus giving more accurate decomposition of the signal in phase domain. The adaptive lowpass filter is effective for any slowly and rapidly modulated frequency components provided that time-varying bisecting frequencies are available. By repeating the process of lowpass filtering, AMD can be viewed as a suite of adaptive bandpass filters without brick wall effects associated with the conventional bandpass filters.

Time-varying bisecting frequencies can be estimated from the wavelet analysis with high frequency and low time resolution. The decomposed signals by AMD are insensitive to the selection of bisecting frequencies. For proper decomposition, a signal must be discretized or sampled according to the Nyquist-Shannon sampling criterion. The sampling frequency must be at least twice of the maximum frequency in the signal.

Each individual component with frequency modulations between two time-varying bisecting frequencies can be analytically extracted by AMD. The extracted component has well-behaved Hilbert transform; its instantaneous frequency and amplitude can be accurately evaluated by AMD-Hilbert spectral analysis. AMD-Hilbert spectral analysis is superior to HHT and wavelet analysis. It can accurately track rapid frequency modulations from a non-stationary signal with both amplitude and frequency

modulations, particularly when the frequencies are closely spaced. It is promising for the time-varying and nonlinear property identification of buildings from earthquake or white noise induced responses.

6. TIME-VARYING SYSTEM IDENTIFICATION UNDER KNOWN EXCITATIONS WITH HHT METHOD

6.1. HHT METHOD FOR TIME-VARYING SYSTEM IDENTIFICATION

To achieve the secondary objective of this study, this section presents a recursive Hilbert-Huang transform method for the time-varying property identification of shear-type buildings under base excitations. To overcome non-orthogonality and modal perturbation issues, all significant intrinsic mode functions of each signal and their Hilbert transforms were summed to track any variation of structural parameters of a multi-story building over time. Given floor masses, both the stiffness and damping coefficients of the building were identified one-by-one from the top to bottom story.

6.1.1. Identification of Parameter Variation. Consider a linear SDOF system with time-varying parameters. The equation of motion of the system under an external load $f(t)$ can be written as:

$$m(t)\ddot{x}(t) + c(t)\dot{x}(t) + k(t)x(t) = f(t) \tag{6.1}$$

where $m(t)$, $c(t)$, and $k(t)$ are the mass, damping and stiffness of the system, respectively. In this study, the mass is considered as constant m. The displacement of the system $x(t)$ can be decomposed into l IMFs as expressed as:

$$x(t) = \sum_{i=1}^{l} c_i(t) + r_l(t) \tag{6.2}$$

By applying Hilbert transform and introduced analytic signal $z_i(t) = c_i(t) + jH[c_i(t)] = a_i(t)e^{j\theta_i(t)}$, Equation (6.1) can be rewritten into:

$$m \sum_{i=1}^{l} \ddot{z}_i(t) + c(t) \sum_{i=1}^{l} \dot{z}_i(t) + k(t) \sum_{i=1}^{l} z_i(t) = g(t) \tag{6.3}$$

After the Bedrosian's theorem on the Hilbert transform of two signals has been introduced:

$$H[c(t)\dot{x}(t)] = c(t)H[\dot{x}(t)], H[k(t)x(t)] = k(t)H[x(t)] \tag{6.4}$$

when $c(t)$, and $k(t)$ change slowly compared to the oscillatory IMFs of the displacement in terms of frequency components, which is satisfied in most engineering applications. In Equation (6.3), $g(t)$ represents a summation of all analytical functions of the IMFs and their Hilbert transform of the loading function $f(t)$.

The first and second time derivatives of $z_i(t)$ are related to $z_i(t)$ by:

$$\dot{z}_i(t) = \alpha_i^c z_i(t), \quad \ddot{z}_i(t) = \alpha_i^m z_i(t) \tag{6.5}$$

in which $\alpha_i^m = \dfrac{\ddot{a}_i(t)}{a_i(t)} - \omega_i^2(t) + j[\dfrac{2\dot{a}_i(t)\omega_i(t)}{a_i(t)} + \dot{\omega}_i(t)]$ and $\alpha_i^c = \dfrac{\dot{a}_i(t)}{a_i(t)} + j\omega_i(t)$. Equation

(6.3) can then be further simplified into:

$$\sum_{i=1}^{l} \alpha_i^c z_i(t)c(t) + \sum_{i=1}^{l} z_i(t)k(t) = g(t) - m\sum_{i=1}^{l} \alpha_i^m z_i(t) \tag{6.6}$$

In matrix form, Equation (6.6) can be expanded into:

$$\begin{bmatrix} Re[\sum_{i=1}^{l} \alpha_i^c z_i(t)] & Re[\sum_{i=1}^{l} z_i(t)] \\ Im[\sum_{i=1}^{l} \alpha_i^c z_i(t)] & Im[\sum_{i=1}^{l} z_i(t)] \end{bmatrix} \begin{Bmatrix} c(t) \\ k(t) \end{Bmatrix} = \begin{Bmatrix} Re[g(t) - m\sum_{i=1}^{l} \alpha_i^m z_i(t)] \\ Im[g(t) - m\sum_{i=1}^{l} \alpha_i^m z_i(t)] \end{Bmatrix} \tag{6.7}$$

in which $Re[\ ]$ and $Im[\ ]$ represent the real and imaginary parts of the complex function in the bracket, respectively. Equation (6.7) will be used for the identification of time-varying damping $c(t)$ and stiffness $k(t)$ of the SDOF system at each time instant t. Note that this study used the summation of all significant IMFs in Equation (6.7) to eliminate the orthogonality requirements among IMFs.

6.1.2. A Recursive HHT Method for Multi-Story Shear Buildings. For a linear n-DOF system with time-varying parameters, the equation of motion under external loads is similar to Equation (6.1) but in matrix form as given by:

$$\mathbf{M}(t)\ddot{\mathbf{x}}(t) + \mathbf{C}(t)\dot{\mathbf{x}}(t) + \mathbf{K}(t)\mathbf{x}(t) = \mathbf{f}(t) \tag{6.8}$$

where $\mathbf{M}(t)$, $\mathbf{C}(t)$, and $\mathbf{K}(t)$ are time-varying mass, damping, and stiffness matrices, respectively; $\mathbf{f}(t)$ is the external load vector; $\mathbf{x}(t)$ is the displacement vector. Again, mass is considered to be constant in this study. Corresponding to Equation (6.3), Equation (6.8) can be rewritten into:

$$\mathbf{M}(t)\ddot{\mathbf{z}}(t) + \mathbf{C}(t)\dot{\mathbf{z}}(t) + \mathbf{K}(t)\mathbf{z}(t) = \mathbf{g}(t) \tag{6.9}$$

After the IMFs and Hilbert transforms of various displacement responses have been introduced. In Equation (6.9),

$$\ddot{\mathbf{z}}(t) = \left\{ \sum_{i=1}^{l_1} \ddot{z}_{1i}(t) \quad \sum_{i=1}^{l_2} \ddot{z}_{2i}(t) \quad \dots \quad \sum_{i=1}^{l_n} \ddot{z}_{ni}(t) \right\}^T,$$

$$\dot{\mathbf{z}}(t) = \left\{ \sum_{i=1}^{l_1} \dot{z}_{1i}(t) \quad \sum_{i=1}^{l_2} \dot{z}_{2i}(t) \quad \dots \quad \sum_{i=1}^{l_n} \dot{z}_{ni}(t) \right\}^T,$$

$$\mathbf{z}(t) = \left\{ \sum_{i=1}^{l_1} z_{1i}(t) \quad \sum_{i=1}^{l_2} z_{2i}(t) \quad \dots \quad \sum_{i=1}^{l_n} z_{ni}(t) \right\}^T,$$

$$\mathbf{g}(t) = \mathbf{f}(t) + jH[\mathbf{f}(t)] = \{g_1(t)\ g_2(t)\ \dots\ g_n(t)\}^T,$$

$$g_s(t) = \sum_{i=1}^{l_f} f_{si}(t) + j\sum_{i=1}^{l_f} H[f_{si}(t)] \quad (s = 1, 2, \dots, n),$$

l_s ($s = 1, 2, ..., n$) and l_f represent the total number of IMFs of the sth DOF displacement and the total number of the correlated external load functions. In this study, the base excitation of a structure was considered to simulate earthquake effects. Therefore, the external loads applied to all DOFs were correlated and the same number of IMFs was considered. The quantity $z_{si}(t)$ represents the analytical function of the ith IMF and its Hilbert transform of the sth degree of displacement. Similar to Equation (6.5), the first and second derivatives $\dot{z}_{si}(t)$ and $\ddot{z}_{si}(t)$ can be related to the displacement $z_{si}(t)$ by $\dot{z}_{si}(t) = \alpha_{si}^c z_{si}(t)$ and $\ddot{z}_{si}(t) = \alpha_{si}^m z_{si}(t)$. Given constant masses, Equation (6.9) can be used to identify the damping and stiffness coefficients of the general n-DOF system. In what follows, special formulations for shear-type buildings are derived.

For a shear-type building as schematically shown in Figure 6.1, interval damping and stiffness coefficients are to be identified. In this case, the damping and stiffness matrices in Equation (6.8) can be rearranged into two vectors:

$$\mathbf{c}(t) = \{c_1(t) \; c_2(t) \; ... \; c_n(t)\}^T, \text{ and } \mathbf{k}(t) = \{k_1(t) \; k_2(t) \; ... \; k_n(t)\}^T \quad (6.10)$$
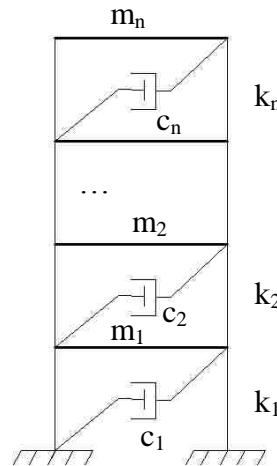
Figure 6.1. Multi-story Shear Building

Similar to Equation (6.7), the damping and stiffness coefficients can be identified from Equation (6.11):

$$\begin{bmatrix} Re[\mathbf{P}^c(t)] & Re[\mathbf{P}^k(t)] \\ Im[\mathbf{P}^c(t)] & Im[\mathbf{P}^k(t)] \end{bmatrix} \begin{Bmatrix} \mathbf{c}(t) \\ \mathbf{k}(t) \end{Bmatrix} = \begin{Bmatrix} Re[\mathbf{G}(t)] \\ Im[\mathbf{G}(t)] \end{Bmatrix} \quad (6.11)$$

For an *n*-story building, Equation (6.11) contains *2n* equations for the evaluation of *2n* time-varying parameters at any time instant *t*. The coefficient matrix and the right-hand term in Equation (6.11) are detailed in Equation (6.12) after *t* has been dropped for brevity:

$$\mathbf{P}^c = \begin{bmatrix} \sum_{i=1}^{l_1} \alpha_{1i}^c \mathbf{z}_{1i} & \sum_{i=1}^{l_1} \alpha_{1i}^c \mathbf{z}_{1i} - \sum_{i=1}^{l_2} \alpha_{2i}^c \mathbf{z}_{2i} & & & \\ & \sum_{i=1}^{l_2} \alpha_{2i}^c \mathbf{z}_{2i} - \sum_{i=1}^{l_1} \alpha_{1i}^c \mathbf{z}_{1i} & \sum_{i=1}^{l_2} \alpha_{2i}^c \mathbf{z}_{2i} - \sum_{i=1}^{l_3} \alpha_{3i}^c \mathbf{z}_{3i} & & \\ & & ... & & \\ & & & \sum_{i=1}^{l_n} \alpha_{ni}^c \mathbf{z}_{ni} - \sum_{i=1}^{l_{n-1}} \alpha_{(n-1)i}^c \mathbf{z}_{(n-1)i} \end{bmatrix}$$

$$\mathbf{P}^k = \begin{bmatrix} \sum_{i=1}^{l_1} \mathbf{z}_{1i} & \sum_{i=1}^{l_1} \mathbf{z}_{1i} - \sum_{i=1}^{l_2} \mathbf{z}_{2i} & & \\ & \sum_{i=1}^{l_2} \mathbf{z}_{2i} - \sum_{i=1}^{l_1} \mathbf{z}_{1i} & \sum_{i=1}^{l_2} \mathbf{z}_{2i} - \sum_{i=1}^{l_3} \mathbf{z}_{3i} & \\ & & ... & \\ & & & \sum_{i=1}^{l_n} \mathbf{z}_{ni} - \sum_{i=1}^{l_{n-1}} \mathbf{z}_{(n-1)i} \end{bmatrix}$$

$$\mathbf{G}(t) = \begin{Bmatrix} \mathbf{g}_1 - m_1 \sum_{i=1}^{l_1} \alpha_{1i}^m \mathbf{z}_{1i} \\ \mathrm{g}_2 - m_2 \sum_{i=1}^{l_2} \alpha_{2i}^m \mathbf{z}_{2i} \\ ... \\ \mathbf{g}_n - m_n \sum_{i=1}^{l_1} \alpha_{ni}^m \mathbf{z}_{ni} \end{Bmatrix} \tag{6.12}$$

Considering the sparse characteristics (diagonal and next upper diagonal non-zero elements) of its coefficient matrices, Equation (6.11) can be solved with a recursive algorithm to expedite the solution process. When the accelerations at all floors are measured, the floor displacements and then story drifts can be evaluated by double integrations. Therefore, the two algebraic equations for the real and imaginary components of responses associated with the top story of the building can be solved simultaneously to determine $c_n(t)$ and $k_n(t)$ at each time instant *t*, similar to an SDOF system. Once $c_n(t)$ and $k_n(t)$ are known, the damping and stiffness of the next story of

the building, $c_{n-1}(t)$ and $k_{n-1}(t)$ can be determined using the two algebraic equations in Equation (6.11) that are associated with the *n-1* story of the building. This process continues until all unknown coefficients are identified. The whole process can be described as:

Step 1: Identify damping and stiffness coefficients of the nth DOF. The equation of motion is described by:

$$\ddot{\mathbf{x}}_n m_n + (\dot{\mathbf{x}}_n - \dot{\mathbf{x}}_{n-1})c_n + (\mathbf{x}_n - \mathbf{x}_{n-1})k_n = \mathbf{f}_n \tag{6.13}$$

By introducing a drift displacement, $\mathbf{y}_n = \mathbf{x}_n - \mathbf{x}_{n-1}$, and a virtual excitation, $\mathbf{g}_n = \mathbf{f}_n - \ddot{\mathbf{x}}_n m_n$, Equation (6.13) can be rewritten as:

$$\dot{\mathbf{y}}_n c_n + \mathbf{y}_n k_n = \mathbf{g}_n \tag{6.14}$$

The damping and stiffness coefficients of the nth DOF can then be estimated as a SDOF system using the HHT method.

Step 2: Identify damping and stiffness coefficients of the sth DOF. The equation of motion for the sth DOF can be described as:

$$\ddot{\mathbf{x}}_s m_s + (\dot{\mathbf{x}}_s - \dot{\mathbf{x}}_{s-1})c_s + (\mathbf{x}_s - \mathbf{x}_{s-1})k_s = \mathbf{f}_s \tag{6.15}$$

By defining a drift displacement, $\mathbf{y}_s = \mathbf{x}_s - \mathbf{x}_{s-1}$, and a virtual excitation, $\mathbf{g}_s = \mathbf{f}_s - \ddot{\mathbf{x}}_s m_s - (\dot{\mathbf{x}}_s - \dot{\mathbf{x}}_{s+1})c_{s+1} - (\mathbf{x}_s - \mathbf{x}_{s+1})k_{s+1}$, after the system parameters c_{s+1} and k_{s+1} have been obtained, Equation (6.15) can be rewritten as:

$$\dot{\mathbf{y}}_s c_s + \mathbf{y}_s k_s = \mathbf{g}_s \tag{6.16}$$

Once again, the damping and stiffness coefficients can be identified as a SDOF system using the HHT method.

Step 3: Repeat Step 2 until all of the parameters are identified.

6.1.3. Evaluation of Identification Accuracy. An amplitude-based index is proposed to evaluate the accuracy of structural identification both for parameters and models. Since change in structural properties is mostly associated with the peak responses of a structure, an index of accuracy (*IA*) is defined as an amplitude-weighted root-mean-squared value over the duration of structural responses. That is,

$$IA = \frac{\sqrt{\sum_{s=1}^{n} \int_0^T \beta_{sm}^2(t)[x_{sp}(t) - x_{sm}(t)]^2 dt}}{\sqrt{\sum_{s=1}^{n} \int_0^T x_{sm}^2(t) dt}} \tag{6.17}$$

in which $\beta_{sm} = \dfrac{x_{sm}(t)}{\sqrt{\int_0^T x_{sm}^2(t)dt}}$ is the weighting factor based on the magnitude of the

structural response; the indices m and p denote the measured and predicted responses such as floor displacement in a multi-story building. The predicted structural responses were calculated based on the identified damping and stiffness coefficients.

6.2. APPLICATION OF THE RECURSIVE HHT METHOD

6.2.1. Single-Story Shear Building. A single-story shear building with mass $m=1.75\times10^5$ kg and damping ratio $\xi=0.02$ is subjected to the 1940 El Centro ground acceleration. The stiffness of the building is suddenly reduced from $k=2.76\times10^4$ kN/m. to 1.75×10^4 kN/m. at time instant t=4 sec. The natural frequency of the building from 0 to 4 sec is 12.6 Hz and reduced to 10 Hz after t=4 sec. Figure 6.2 shows the displacement time history of the building that was numerically calculated using the Runge-Kutta method.

Given the mass and damping ratio of the building, the stiffness of the building is to be identified based on the displacement response presented in Figure 6.2. Figure 6.3 presents the identified stiffness as a function of time when the numerical displacement in Figure 6.2 was used without noise, with 2% and 5% noise-to-signal ratio (NSR) Gaussian white noises, respectively. It can be seen from Figure 6.3 that the identified results are in good agreement with the exact stiffness values over time, regardless of the presence of noise, except for the times with low-amplitude responses. The presence of noise slightly decreases the accuracy of identified results. Indeed, the index of accuracy defined in Equation (6.17) is equal to 1.7%, 2.6% and 4.7% without, with 2%, and 5% white noises. They are all less than 5%, which seems quite satisfactory in engineering applications. Note that the identified stiffness results at the beginning when the external excitation is extremely low should be disregarded. In engineering applications, visual inspections can rule out this potentially false positive identification.
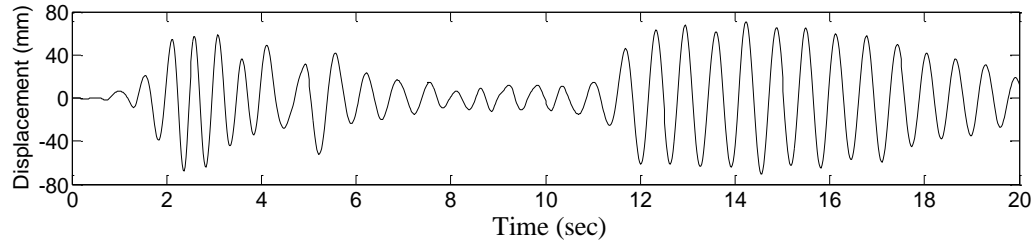
Figure 6.2. Displacement Time History of the Stiffness-Varying Building
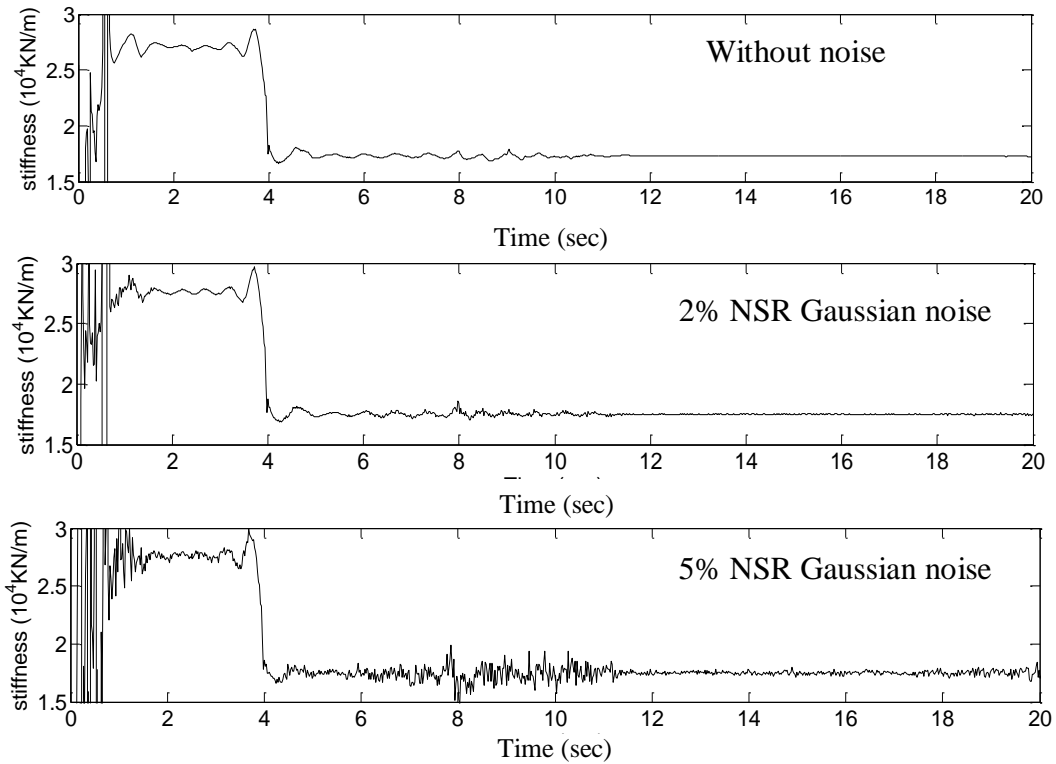
Figure 6.3. Identified Stiffness of the Single-Story Building

6.2.2. Two-Story Shear Building. A two-story shear building as shown in Figure 6.4 was subjected to the 1940 El Centro ground acceleration record. The masses of the building are $m_1=2.63\times10^5$ kg and $m_2=1.75\times10^5$ kg at the lower and upper floors, respectively. The damping coefficients of the first and second stories are $c_1=6.95\times10^2$ KN-sec/m and $c_2=1.86\times10^2$ kN-sec/m, respectively. The initial stiffness is $k_1=2.10\times10^5$ KN/m and $k_2=1.05\times10^5$ kN/m for the first and second story.
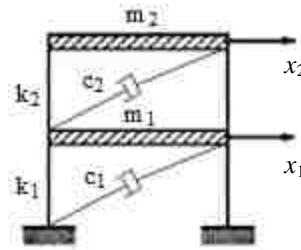
Figure 6.4. Two-Story Shear Building

6.2.2.1 Case 1: Abruptly reduction stiffness. In this case, the initial stiffness coefficients of the first story (k_1=2k) and second story (k_2=k) were respectively reduced to 1.40×10^5 kN/m and 0.70×10^5 kN/m at time instant t=4 sec. The exact displacement responses of the building as presented in Figure 6.5 were calculated using the Runge-Kutta method. For comparison, k_1 and k_2 identified from one IMF method (Shi and Law, 2009) are plotted in Figure 6.6 as a function of time. The corresponding k_1 and k_2 identified based on the proposed recursive method are shown in Figure 6.7. The damping coefficients c_1 and c_2 identified based on the proposed recursive method are shown in Figure 6.8. It is clearly observed from Figures 6.6 and 6.7, the k_1 and k_2 identified from the recursive method is in excellent agreement with the exact stiffness while the results from the one IMF method presented in Shi and Law (2009) are inconclusive for the identification of stiffness due to the non-orthogonal property between IMFs at any time instant. For Case 1, the index of accuracy is equal to 2.9%. In comparison with Figure 6.7, Figure 6.8 indicates that the identification of damping coefficients is less accurate likely due to the lower magnitude of damping force.

Figure 6.7 and Figure 6.8 also indicate that the accuracy of identified results is affected by the low amplitude responses used in the identification process. For example, the displacements immediately before 10 sec. and after 12 sec. are small, thus leading to local fluctuations of the identified stiffness.
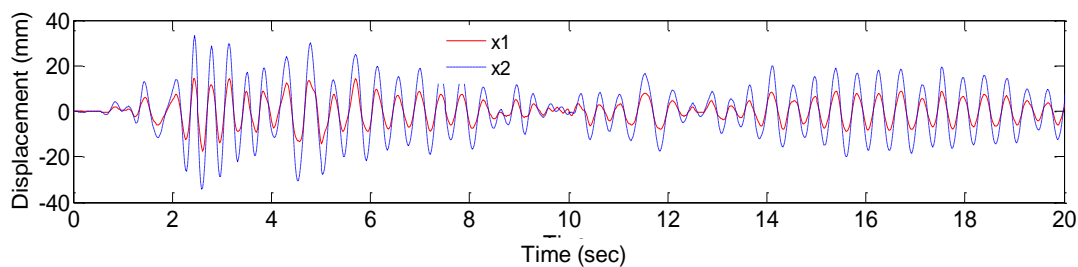
Figure 6.5. Exact Displacements of the Two-Story Shear Building
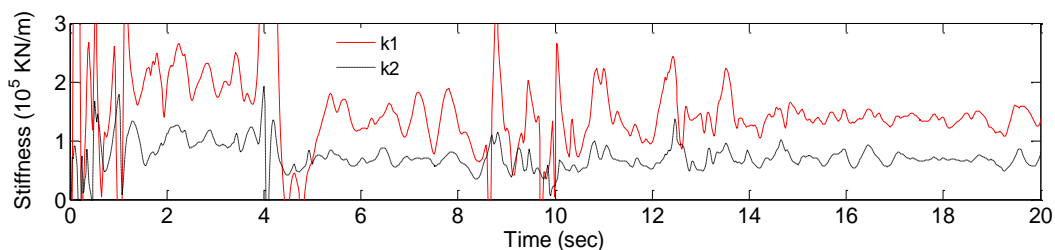
Figure 6.6. Identified Stiffness Based on One IMF
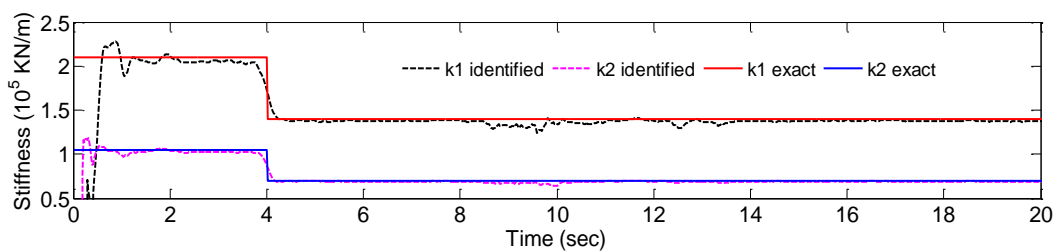
Figure 6.7. Identified Stiffness from the Recursive Method: Case 1
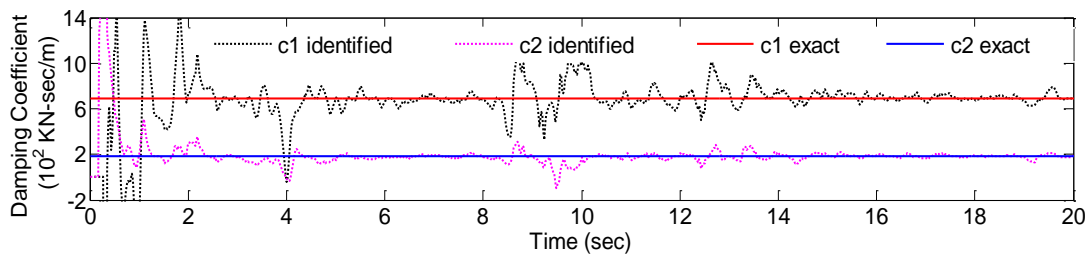
Figure 6.8. Identified Damping Coefficient from the Recursive Method: Case 1

6.2.2.2 Case 2: Gradually reducing stiffness. In this case, the stiffness of the first story (k_1) is linearly reduced from 2.10×10^5 to 1.40×10^5 kN/m. over a period of time t=4 sec to t=8 sec. The stiffness of the second story (k_2=1.05×10^5 kN/m.) remains unchanged over the duration of the earthquake. Again, the exact displacements were calculated using the Runge-Kutta method. The k_1 and k_2 values identified from the recursive method are shown in Figure 6.9. Clearly, the recursive method can accurately track the gradually varied parameter. For Case 2, the index of accuracy is 4.3%.
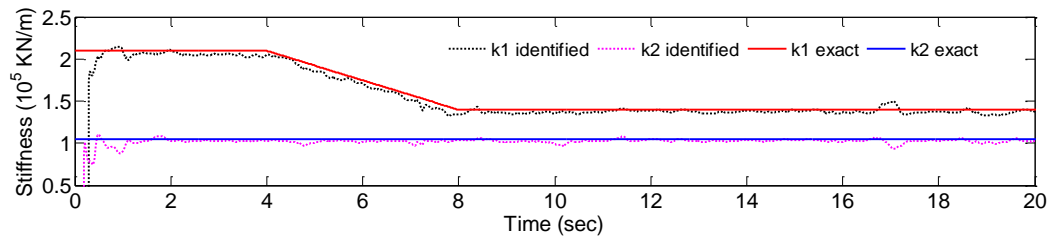
Figure 6.9. Identified Stiffness from the Recursive Method: Case 2

6.2.2.3 Case 3: Periodically reducing stiffness. In this case, the stiffness of the first story (k_1) is periodically reduced from 2.10×10^5 kN/m to 1.40×10^5 kN/m over a period of time t=4 sec to t=16 sec. That is, $k_1 = \{2.1 - 0.058(t-4) - 0.131\sin[\frac{\pi}{2}(t-4)]\} \times 10^5$ kN/m. The stiffness of the second story (k_2) is linearly reduced from 1.05×10^5 kN/m. to 0.70×10^5 kN/m over a period of time t=4 sec to t=8 sec. The k_1 and k_2 values identified from the recursive method are shown in Figure 6.10. Again, the proposed recursive method can accurately track both linear and periodical variations of stiffness. For Case 3, the index of accuracy is equal to 4.7%.
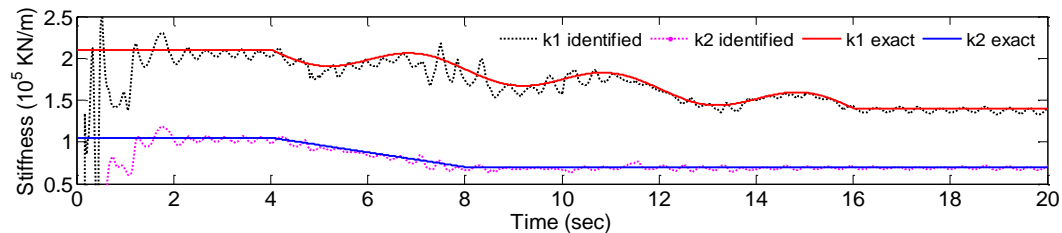
Figure 6.10. Identified Stiffness from the Recursive Method: Case 3

6.3. SUMMARY

In this section, a recursive HHT method was developed to track any variation of structural parameters of a multi-story building over time. The recursive HHT method allows the structural identification of a building story-by–story and thus computationally efficient in the determination of both stiffness and damping coefficients. The proposed HHT method uses a summation of all significant IMFs to address the non-orthogonality and model perturbation issues. It is robust in terms of the effect of noise and the consistency of identified results over time. With 5% noise in numerical data, the identified stiffness coefficients of a two-story building remained stable. For single- and multi-story building examples, the identified stiffness and damping coefficients are in good agreement with their exact values regardless of their abrupt, gradual and periodical variations over time.

7. TIME-VARYING SYSTEM IDENTIFICATION OF HIGH VOLTAGE SWITCHES OF A POWER SUBSTATION

7.1. INTRODUCTION OF THE SHAKE TABLE TEST

A power substation is comprised of interconnected components, such as bushings, interrupters, connectors, radiators, circuit breakers and surge arresters, most of which support fragile elements such as ceramic bushings or insulators. During earthquakes, some components of power substations, for example, porcelain insulators and bushings, were quite susceptible to earthquakes and easily broken during strong shaking. Typical damage caused during an earthquake is shown in Figure 7.1. These equipment items are usually connected to each other through conductor buses or cables. In the event of earthquakes, these connections may induce dynamic interaction between various items. Previous studies (Kiureghian et al., 1999a; 1999b) have indicated that the dynamic characteristics may have contributed significantly to the damage of power substations. However, design guidelines or analysis methods that account for this interaction effect are currently unavailable.

Electric switches play a critical role in the operation of a power substation. To ensure their functionality and safety during an earthquake event, shake table tests were conducted in the Structures Laboratory at the Missouri University of Science and Technology in order to understand the behaviors and potential failure modes of electric switches. Three full-size switches were provided by Turner Switches Company St. Louis, Missouri.

The unidirectional shake table used to excite each switch specimen. It is driven by one actuator that is activated by hydraulic power. It can operate in the frequency range from 0.01 Hz to 10 Hz with a maximum payload of 20 tons. The maximum stroke of the table is +/-25.4 mm. The MTS406 controller has a function generator such as sine and cosine waves. The table can also take external signals to simulate any earthquake ground motion.

(a) Broken Bushing of a Transformer

(b) Broken Bushing of a lightning rod

(c) Oil Leakage from the Bottom of Radiator   (d) Broken Support

Figure 7.1. Typical Damage Resulting from Earthquakes

7.2. TEST SETUP AND INSTRUMENTATION

To accommodate a three-pillar switch specimen, an "I" beam was designed and bolted onto the table to extend the support length for the switch, as illustrated in Figure 7.2. In this study, the switch was tested for the dynamic behavior in the plane formed by the three pillars. Three porcelain pillars are supported on a hollow square tube that was bolted to the I-beam. A wood truss was built and used as top transverse supports to the switch under testing. The top horizontal wood member along the excitation direction is

near the test specimen with a small gap in between. Figure 7.3 illustrates the truss system that was constructed to prevent any unwanted, potential lateral stability. Figure 7.4 shows the two data acquisition systems used for each test: Synergy Box and Orange Box. The Synergy Box was used to take accelerations and displacements. The Orange Box was used to take strain readings. Video images were also taken during some of the shake table tests. To enhance the video quality, a screen with marked strips was provided in the back of the test specimen. The accelerometers and linear variable differential transformers (LVDTs) are deployed as illustrated in Figure 7.2.
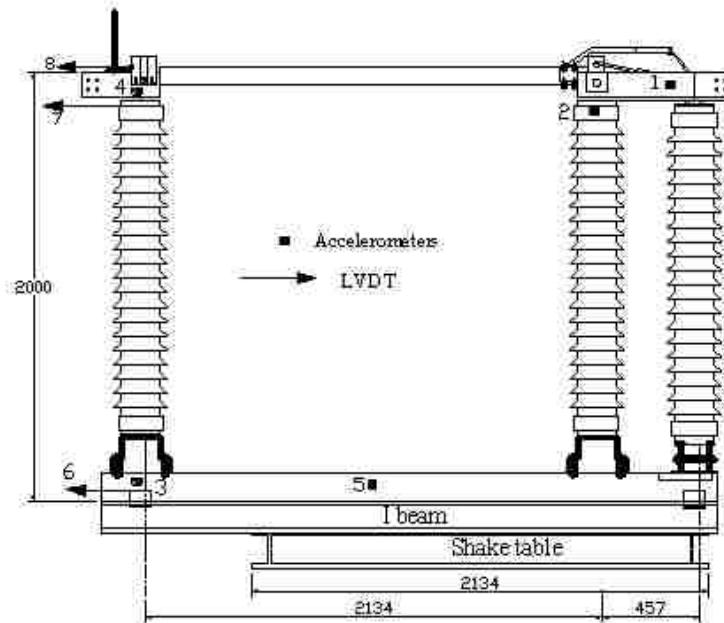
Figure 7.2. Test Setup of the High Voltage Switch on Shake Table (all units: mm)

Figure 7.3. Wood Truss System

Figure 7.4. Two Data Acquisition Systems

The specimen was excited with a sinusoidal motion in a frequency range 4 to 10 Hz in 0.2 Hz interval. For system identification, the amplitude of the sinusoidal wave of the first test was 1.27 mm, and the second test was 2.54 mm. For failure tests, the excitation amplitude was increased until the specimen collapsed. When the switch was in its closed position, the two LVDTs were set to zero prior to testing. As the hydraulic pump was turned on, the excitation frequency was recorded by the data acquisition. However, the stroke of the shake table was recorded manually and gradually set into a predetermined value, e.g., 2.54 mm to minimize a sudden jerk of the shake table system that could damage the specimen unintentionally. In its steady state, the maximum displacement can be applied for 15 sec. or longer to acquire adequate data. As a result, each run at any excitation frequency will last over 30 sec., which is governed by the lower bound of excitation frequency.

The main objectives of the test are to scan the fundamental frequency of the switch and understand its ultimate behavior. To achieve these objectives, the following vibration test procedure was used:

Step 1: Conduct a series of harmonic tests with constant amplitude and increasing excitation frequency for identification of the fundamental frequency.

Step 2: Repeat Step 1 with an increase in the amplitude of the excitation for the understanding of potential nonlinearity effects.

Step 3: Excite the structure at its fundamental frequency with increasing amplitude of the excitation for failure tests.

7.3. SYSTEM IDENTIFICATION WITH WEAK VIBRATION

The natural frequency and damping ratio of the switch were identified using the global least-squares estimation. The structure can be idealized as a linear SDOF system in the horizontal direction with the following equation of motion:

$$\ddot{x}(t) + 2\zeta\omega_n\dot{x}(t) + \omega_n^2 x(t) = -\ddot{x}_0(t) \qquad (7.1)$$

where ζ is the damping ratio of the system, ω_n is the natural frequency; $\ddot{x}(t)$ is the relative acceleration measured between accelerometer 4 and 3 in Figure 7.2, $x(t)$ is the relative displacement measured between LVDT 7 and 6, $\ddot{x}_0(t)$ is the base acceleration measured by accelerometer 3, and $\dot{x}(t)$ is obtained by the central difference method from the measured displacement $x(t)$.

Figure 7.5 and Figure 7.6 show the fundamental frequency and damping ratio identified using the global least-squares estimation for the first and second tests respectively. The fundamental frequency identified from the first test was 7.4 Hz and the average damping ratio was 4.8%, which are the same as those observed during testing. However, the natural frequency was suddenly reduced at resonance. The fundamental frequency identified from the second test was 7.2 Hz and the average damping ratio was 6.0%, except at resonance, when the natural frequency suddenly dropped.
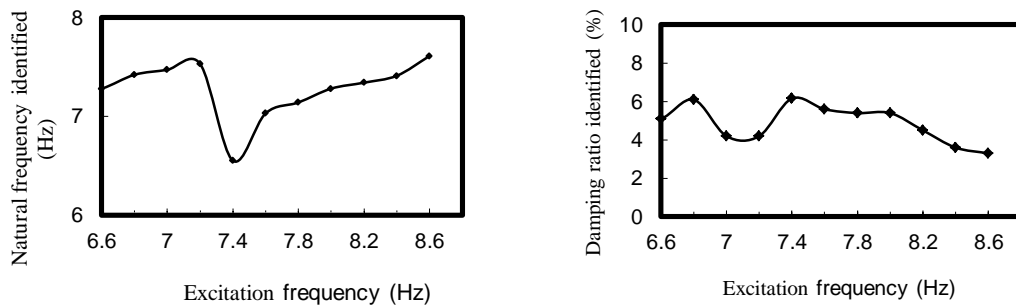
Figure 7.5. Fundamental Frequency and Damping Ratio Identified from the First Test
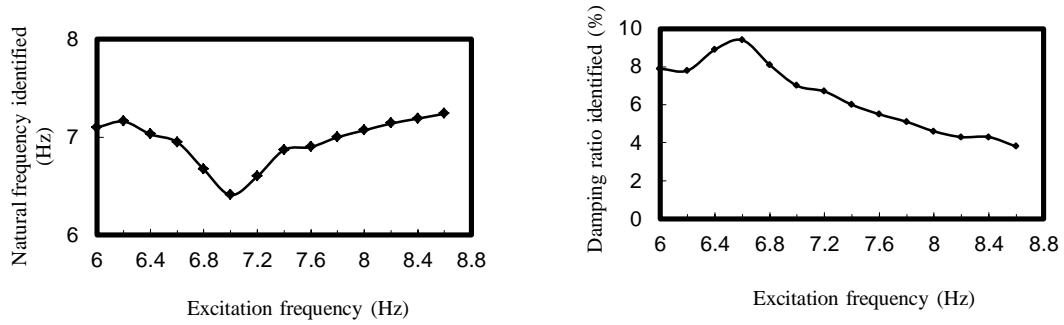
Figure 7.6. Fundamental Frequency and Damping Ratio Identified from the Second Test

The connection between the rigid bus (aluminum pipe) and the left pillar of the specimen can be open and close as an electric switcher. Therefore, friction mechanism was provided to make the mechanical connection. Under weak vibration, there is no sliding at the friction surface and the fundamental frequency was 7.4 Hz as originally identified as indicated in Figure 7.7. However, due to sliding between the bus and the pillar, the fundamental frequency dropped to approximately 7.0 Hz at resonance during the second test.
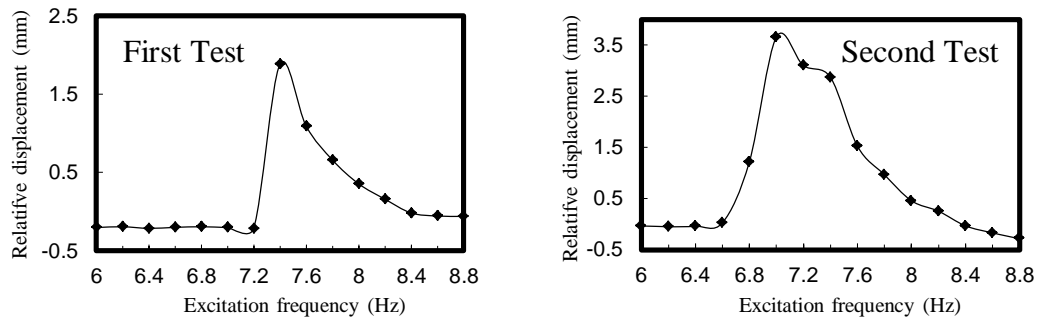
Figure 7.7. Average Relative Displacement from First and Second Tests

7.4. TIME-VARYING PARAMETER IDENTIFICATION WITH THE RECURSIVE HHT METHOD

As shown in Figure 7.7, the relative displacement suddenly changed near the excitation frequency 7.4 Hz for the second test. To find the variations of the fundamental frequency, the proposed recursive HHT was used.

The switch structure was considered as an SDOF system and identified using the proposed HHT method in Section 6. For the first series of tests, the relative displacement between top and bottom of the switch at an excitation frequency of 7.4 Hz is presented in Figure 7.8(a). Prior to EMD, a 4th-order Butterworth low-pass filter with a cutoff frequency of 30 Hz was employed to pre-process signals for noise reduction. The natural frequency identified from the HHT method and its lower and upper bounds identified by the conventional least-squares method are shown in Figure 7.8(b). The identified damping ratio of the switch is presented in Figure 7.8(c). It can be clearly seen from Figure 7.8(b) that the average values of the identified results by the proposed method basically lie between the lower and upper bounds. The natural frequency decreases with the increasing of excitation intensity due to the slip phase of the aluminum pipe against the supporting pillar. Around 6 sec., a significant slip may have occurred, resulting in a notable change in identified natural frequency and damping ratio. When the excitation is over, the natural frequency gradually resumed to its original value due to the stick phase of the friction mechanism. It can also be seen in Figure 7.8(b, c) that the identification of damping ratio is less accurate than that of natural frequency due likely to the error propagation of approximate natural frequency identified and the complex damping mechanism involved in switch vibration.

For the second series of tests, the relative displacement between the top and bottom of the switch structure at an excitation frequency of 6.8 Hz is shown in Figure 7.9(a). The natural frequency and damping ratio identified from the proposed HHT method are shown in Figure 7.9(b) and Figure 7.9(c), respectively. As one can see, the average values of the identified results are generally bound by the upper and lower natural frequencies (dashed lines in Figure 7.9) that were identified by the conventional least-square method. Again, the identified damping ratio is less accurate than the natural frequency.
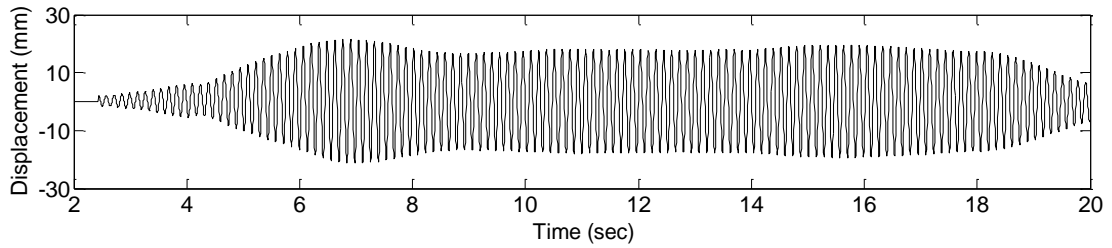
(a) Measured Relative Displacement at 7.4 Hz
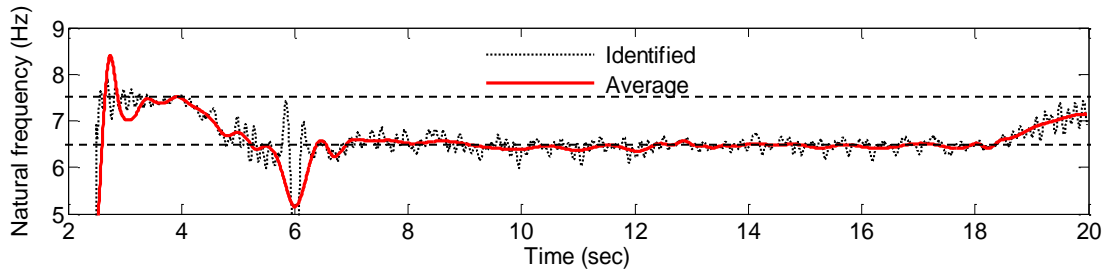
(b) Identified Natural Frequency
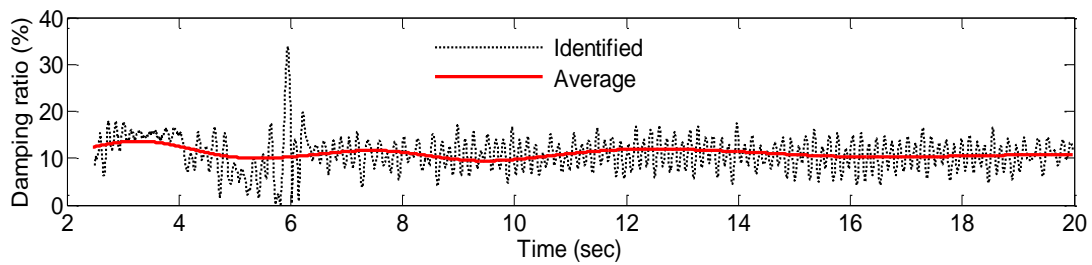
(c) Identified Damping

Figure 7.8. Measured Responses and Identified Parameters from the 1st Test
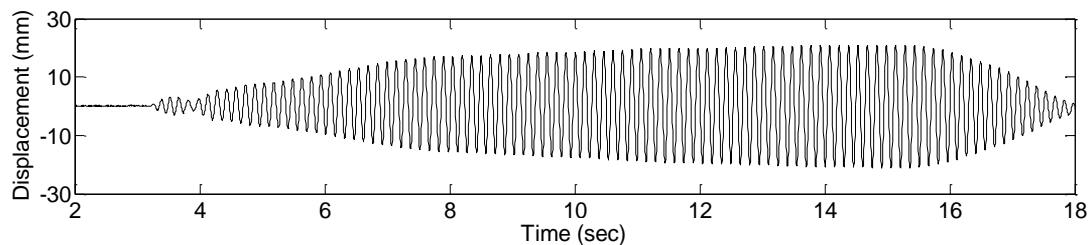
(a) Measured Relative Displacement at 6.8 Hz
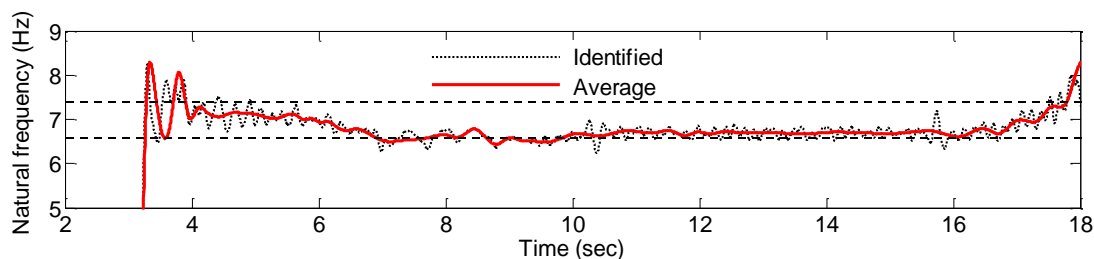
(b) Identified Natural Frequency
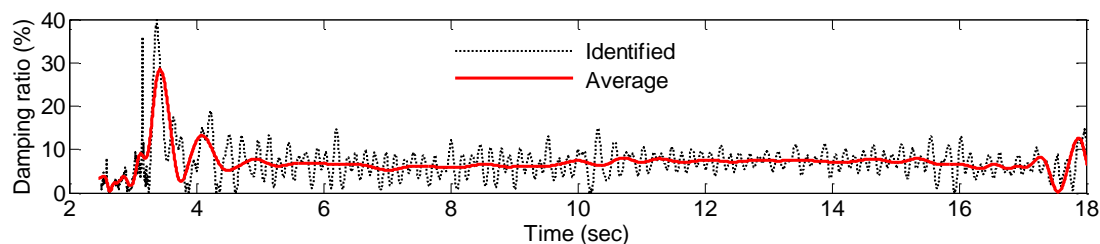
(c) Identified Damping Ratio

Figure 7.9. Measured Responses and Identified Parameters from the 2nd Test

7.5. ULTIMATE BEHAVIOR TEST OF THE STRUCTRUE

In order to understand the ultimate behavior of the switches, the level of excitations at their fundamental frequency was increased gradually. For the first ultimate test, the excitation frequency and amplitude were set to 7.2 Hz and 5.08 mm, respectively. Figure 7.10 presents the displacement on the top of the pillar from LVDT 7 and on the aluminum pipe from LVDT 8. The maximum displacement was 29.2 mm from LVDT 7 and 32.5 mm from LVDT 8. During the test, resonance was not observed at 7.2 Hz. The excitation frequency then dropped to 7.0 Hz. The displacement from LVDT 7 and LVDT 8 are shown in Figure 7.11. It indicates that the maximum displacement

reached at 55 mm. The specimen collapsed as fracture can be observed visually at the base of one pillar.
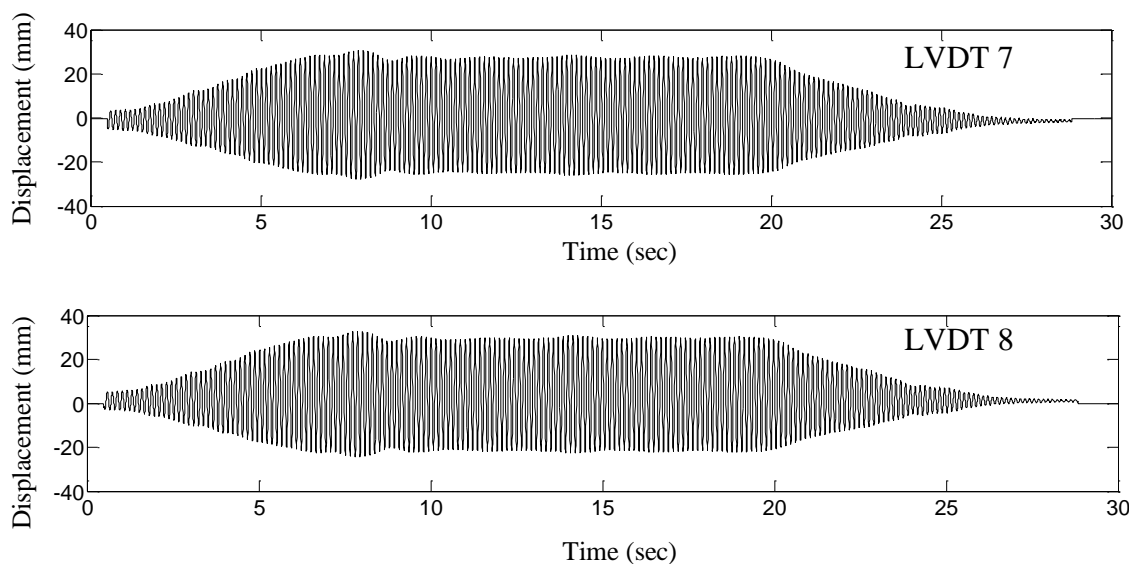
Figure 7.10. Displacements Measured from LVDT 7 and LVDT 8: First Test at 7.2 Hz
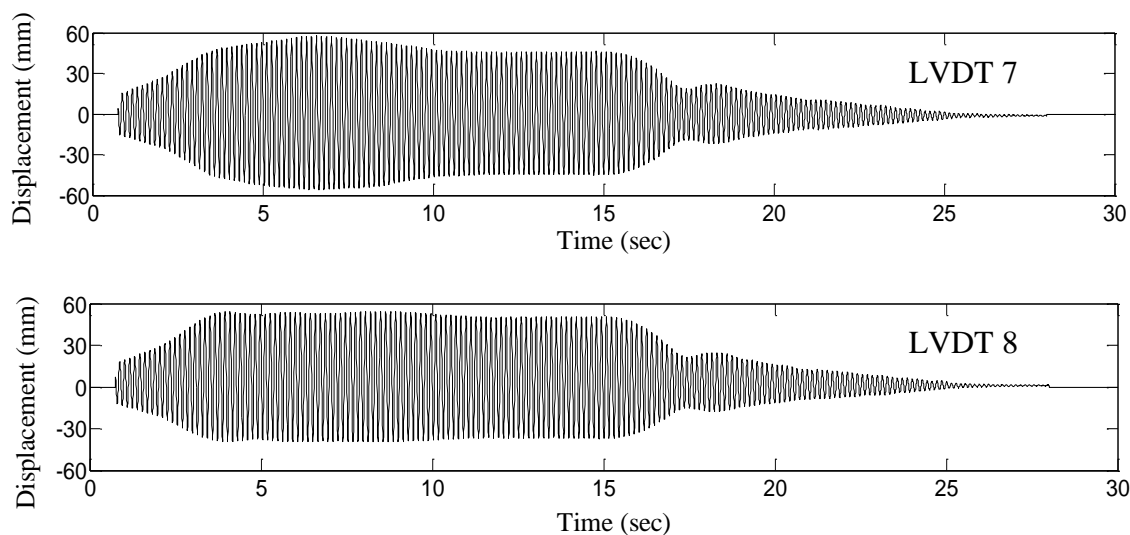
Figure 7.11. Displacements Measured from LVDT 7 and LVDT8: First Test at 7.0 Hz

For the third test, the excitation frequency was reduced to 6.7 Hz, and the amplitude increased to 7.62 mm. Figure 7.12 shows the displacements measured from LVDT 7 and LVDT 8. It was observed during the test that the structure failed at

approximately 23 sec. Visual inspection on the test specimen in Figure 7.13 confirmed that the bottom support of the mechanical open and close mechanism in a right pillar fractured likely due to fatigue. The fractured section had a prior defect (a portion of the cross section was cut) as observed in Figure 7.13 and Figure 7.14. Once the pillar fractured, the rigid bus was in open position, suddenly increasing the displacement at LVDT 8 as indicated in Figure 7.12. The left pillar was disconnected from the switch mechanism and continued to vibrate until the test stopped at approximately 25 sec.
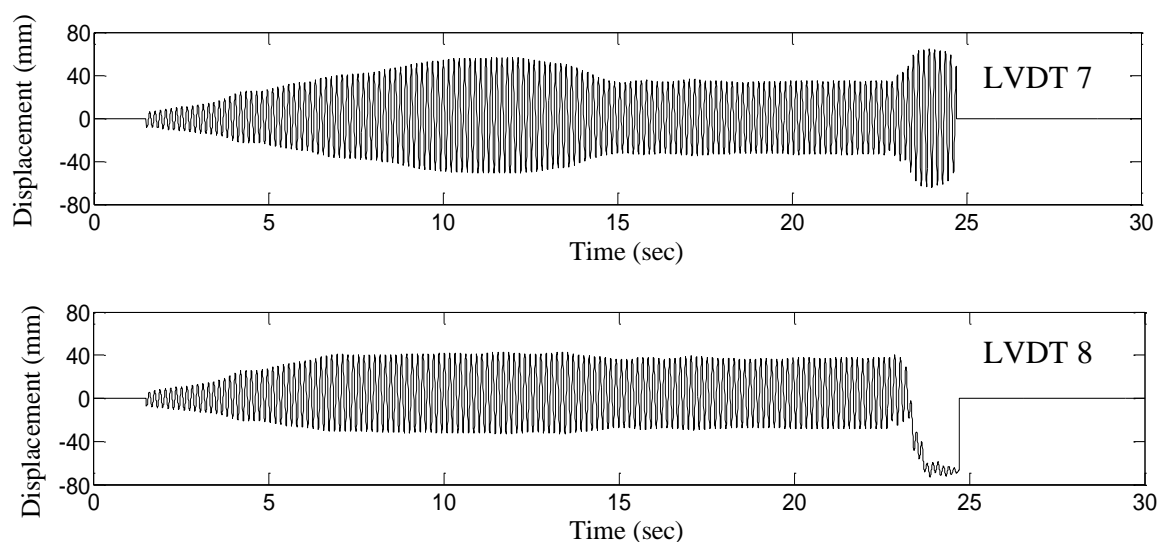
Figure 7.12. Displacements Measured from LVDT 7 and LVDT8: Third Test

Figure 7.13. Overall View of the Failed Structure

Figure 7.14. Fracture Detail and Failure Location

7.6. SUMMARY

Three power switches were tested at multiple excitation levels for system identification and the understanding of failure mechanism. The damping ratio and natural frequency of power switches were identified with conventional modal analysis and the recursive HHT method. The failure mechanism was investigated via visual inspection and data interpretation from displacement measurements.

Harmonic tests were conducted to identify the parameters of the structure. Under weak vibration, the fundamental frequency identified from the test was around 7.5 Hz and the average damping ratio was 4.8%. As the excitation level increased, the natural frequency was suddenly reduced at resonance due to potential sliding at the friction surface between the rigid bus and pillar. The time-varying structural parameters were then identified using the recursive HHT method. Depending on the level of excitations, the fundamental frequency decreased to as low as 7.0 Hz. Prior to the structural collapse, the fundamental frequency dropped to around 6.0 Hz.

The three tested switches consistently failed at the bottom of the open-and-close mechanical mechanism. Specifically, the rotary metal shaft for switch opening fractured at the bottom connection with prior defects as observed after the test. This is most likely attributed to fatigue effect.

8. CONCLUSIONS

In this dissertation, the state-of-the-art development of vibration-based parameter identification and damage detection methods has been reviewed with an emphasis on advanced time-frequency analysis, such as wavelet transform, Hilbert transform, and Hilbert-Huang Transform (HHT). Challenges and critical issues identified with the previous methods include the separation of coupled intermittent weak signal and continuous strong signal, simultaneous high resolution in time and frequency domains, decomposition of closely-spaced modes of vibration, decoupling of excitation and natural frequencies, and non-parametric identification of weakly nonlinear systems.

To address the above challenges and critical issues in structural health monitoring, a new signal decomposition theorem, called analytical mode decomposition (AMD), was discovered and mathematically proven based on the Hilbert transform of a harmonics multiplicative time series. AMD analytically decomposes a time series into many signals whose Fourier spectra are non-vanishing over mutually-exclusive ranges separated by predetermined bisecting frequencies based on the time-frequency characteristics of the time series. Therefore, it allows the decomposition of signal components with significant frequency overlapping over the duration of the signal by using time-dependent bisecting frequencies. Parametric studies have been extensively conducted for bisecting frequencies selection, sampling rate and noise effect. The AMD attributes and capabilities have been illustrated with representative signals, such as stationary, amplitude and frequency modulated, and low/high energy coupled processes.

AMD functions like a suite of "perfect" bandpass filters that are adaptive to the time-frequency characteristics of signals, thus achieving high resolution both in time and frequency domain. Unlike conventional bandpass filtering techniques where windows are applied in frequency domain, the adaptive filters are directly applied in time domain and require no windowing in frequency domain, eliminating the so-called brick wall effects at the edge of windows. AMD is simple in concept, efficient in computation, consistent in performance, and reliable in signal processing.

Due to high resolution in dual domains, AMD can accurately decompose closely-spaced modes of vibration in frequency domain and multi-scale components of signal in

time domain, which are encountered in structural and mechanical engineering. It has been successfully applied to the parameter identification and damage detection of single-degree-of-freedom (SDOF) and multi-degree-of-freedom (MDOF) systems from free vibration, harmonic vibration, and ambient vibration. Its accuracy, resolution, and efficiency have been validated either numerically or experimentally with a 36-story building with a 4-story appendage, a 3-DOF mechanical system, and a ¼-scaled three-story steel frame installed with a single tuned mass damper.

Modal parameters can be directly identified from free vibration or from the transient response under harmonic vibration extracted by AMD. The free vibration or transient response of a MDOF system can further be decomposed into many modes of free vibration by AMD. Each mode of free vibration has a well-behaved Hilbert transform and, by Hilbert spectral analysis, thus reveals the instantaneous natural frequency and damping ratio. This process is referred to as AMD-Hilbert spectral analysis.

Under ambient vibration, free vibration information of a structure was first extracted from the structural responses by the conventional random decrement technique (RDT), and then used to identify modal parameters by AMD-Hilbert spectral analysis like the case with free vibration. This procedure is referred to as RDT-AMD method. While RDT can eliminate modal overlapping effects as two natural frequencies approach each other, AMD can accurately separate two closely-spaced frequencies. Together, the new method provides a system identification tool of high accuracy from ambient vibration. Both the numerical analysis of the 36-story building and the shake table testing of the ¼-scale, 3-story steel frame have successfully demonstrated the effectiveness of the RDT-AMD method in practical applications.

For weakly nonlinear systems, a non-parametric identification method has been developed with AMD-Hilbert spectral analysis. Without knowing the physical model of a nonlinear system, the instantaneous frequency and damping coefficient of measured responses can be identified in the same way as for linear systems. By establishing the relationship between the instantaneous parameters of the responses and the nonlinear system, the parameters of a time-varying, associated linear system can be identified. Based on the AMD-Hilbert spectral analysis, the representative frequency-amplitude

nonlinear curve can be evaluated effectively based on the analysis of a classical Duffing oscillator. The AMD-Hilbert spectral analysis has been successfully applied to identify instantaneous parameters and detect damage in a hysteretic shear-type building with a single tuned mass damper.

In addition, a recursive HHT method has been developed to identify the time-varying structural parameters of shear-type buildings under harmonic excitations. When measured responses are available at every floor, the damping and stiffness coefficients of each story can be identified one by one from top to the bottom of buildings. The new method was validated with the shake table testing of a full-sized power switch system and the numerical analysis of 1- and 2-story buildings that have abruptly, gradually, and periodically changed stiffness coefficients.

While this study has demonstrated the accuracy, resolution, efficiency, and effectiveness of the AMD theorem in signal decomposition, parameter identification, and damage detection of linear and nonlinear systems, there are still several aspects that need to be addressed in future research work. They include:

1. The time-varying bisecting frequency was selected from the scalogram of a signal by wavelet analysis. This process adds a significant computational effort to the application of AMD-Hilbert spectral analysis. How time-varying bisecting frequencies can be extracted directly from the signal by AMD is a topic to explore.

2. AMD functions like an adaptive lowpass or bandpass filter. How it can be used for signal denoising is another topic to investigate.

3. AMD-Hilbert spectral analysis has been applied to weakly nonlinear systems. Whether it can be extended to moderately to strongly nonlinear systems is a topic of great interest to the earthquake engineering community.

4. The proposed recursive HHT method has been validated with complete measurements at all degrees of freedom. How this method performs with incomplete measurements is a question of practical importance for large scale civil engineering structures.

BIBLIOGRAPHY

Adhikari S., and Woodhouse, J., "Identification of Damping: Part 1, Viscous Damping," Journal of Sound and Vibration, 2001, Vol 243, pp. 43-61.

Alvin, K. F., Robertson, A. N., Reich, G. W., and Park, K. C., "Structural System Identification: from Reality to Models," Computer and Structures, Vol 81, 2003, pp. 1149-1176.

Bao, C., Hao, H., Li, Z. X., and Zhu, X., "Time-Varying System Identification using a Newly Improved HHT Algorithm," Computers and Structures, 2009, Vol 87, pp. 1611-1623.

Bedrosian, E., "A Product Theorem for Hilbert Transforms," Memorandum RM-3439-PR, U.S. Air Force Project RAND, 1962, 15 pp.

Bendat, J. S., and Piersol, A. G., "Engineering Applications of Correlation and Spectral Analysis," John Wiley & Sons, Inc., New York, 1993, 458 pp.

Benedettini, F., Capecchi, D., and Vestroni, F., "Identification of Hysteretic Oscillator under Earthquake Loading by Nonparametric Models," Journal of Engineering Mechanics, 1995, Vol 121, pp. 606–612.

Bodeux, J. B., and Golinval, J. C., "ARMAV Model Technique for System Identification and Damage Detection," European COST F3 Conference on System Identification and Structural Health Monitoring, Madrid, Spain, 2000, pp. 303–312.

Bodson, M., "An Information-Dependent Data Forgetting Adaptive Algorithm," Proceedings of the 1995 American Control Conference, June 1995.

Brandon, J. A., "Structural Damage Identification of Systems with Strong Nonlinearities: A Qualitative Identification Methodology, Structural Damage Assessment Using Advanced Signal Processing Procedures," Proceedings of DAMAS '97, University of Sheffield, UK, 1997, pp. 287–298.

Brandon, J. A., "Towards a Nonlinear Identification Methodology for Mechanical Signature Analysis, Damage Assessment of Structures," Proceedings of the International Conference on Damage Assessment of Structures (DAMAS 99), Dublin, Ireland, 1999, pp. 265–272.

Braun, S., and Feldman, M., "Decomposition of Non-Stationary Signals into Varying Time Scales: Some Aspects of the EMD and HVD Methods," Mechanical systems and Signal Processing, 2011, Vol 25, pp. 2608-2630.

Brincker, R., Zhang, L., and Andersen, P., "Modal Identification from Ambient Responses Using Frequency Domain Decomposition," Proceedings of the 18th IMAC, 2000, San Antonio, Texas, 2000, pp. 625-630.

Brincker, R., Zhang, L., and Andersen, P., "Modal Identification of Output-Only Systems using Frequency Domain Decomposition," Smart Materials and Structures, 2001, Vol 10, pp. 441-445.

Caicedo, J. M., Dyke, S. J., and Johnson, E. A., "Natural Excitation Technique and Eigensystem Realization Algorithm for Phase I of the IASC-ASCE Benchmark Problem: Simulated Data," Journal of Engineering Mechanics, 2004, Vol 130, pp. 49–60.

Carrasco, C., Osegueda, R., Ferregut, C., and Grygier, M., "Localization and Quantification of Damage in a Space Truss Model Using Modal Strain Energy," Smart Systems for Bridges, Structures, and Highways, Proceedings of SPIE, 1997, Vol 3,043, pp. 181–192.

Cawley, p., and Adams, A. C., "The locations of Defects in Structures from Measurements of Natural Frequencies," Journal of Strain Analysis, 1979, Vol 14, pp. 49-57.

Chance, J., Tomlinson, G. R., and Worden, K., "A Simplified Approach To The Numerical And Experimental Modeling Of The Dynamics Of A Cracked Beam," Proceedings of the 12th International Modal Analysis Conference, 1994, pp. 778–785.

Chen, G. D, and Wang, Z. C., "A Signal Decomposition Theorem with Hilbert Transform and its Application to Narrowband Time Series with Closely-Spaced Frequency Components," Mechanical systems and Signal Processing, doi: 10.1016/j.ymssp. 2011.02.002, 2011.

Chen, G. D, and Wu, J. N., "Optimal Placement of Multiple Tuned Mass Dampers for Reducing Seismic Responses of Buildings," Journal of Structure Engineering, 2001, Vol 127, pp. 1054-1062.

Chen, J, and Xu, Y. L., "Identification of Modal Damping Ratios of Structures with Closely-spaced Modal Frequencies," Structural Engineering and Mechanics, 2002, Vol 14, pp. 417-434.

Chen, Y., and Feng, M. Q., "A Technique to Improve the Empirical Mode Decomposition in the Hilbert-Huang Transform," Earthquake Engineering and Engineering Vibration, 2003, Vol 2, pp. 75-85.

Cheng, J. S., Yu, D. J., and Yang, Y., "Application of Support Vector Regression Machines to the Processing of End Effects of Hilbert-Huang Transform, Mechanical Systems and Signal Processing," 2007, Vol 21, pp. 1197-1211.

Choi, S., and Stubbs, N., "Nondestructive Damage Detection Algorithms for 2D Plates, Smart Systems for Bridges, Structures, and Highways," Proceedings of SPIE, 1997, Vol. 3,043, pp. 193–204.

Chopra, A. K., "Dynamics of Structures, 3rd Edition," Prentice Hall, Inc., New Jersey, 2006, 912 pp.

Chui, C. K., "Introduction to Wavelets," Academic Press, San Diego, CA, 1992, 266 pp.

Clough, R. W., and Penzien, J., "Dynamics of Structures, 2nd Edition," McGraw-Hill, Inc., Singapore, 1993, 768 pp.

Cohen, L., "Time-Frequency Analysis," Prentice-Hall PTR A Pearson Education Company Upper Saddle River, NJ, 1995, 299 pp.

Cole, H. A., On-the-Line Analysis of Random Vibrations, AIAA, 1968, paper NO. 68-288.

Doebling, S. W., Farrar, C. R., and Prime, M. B., "A Summary Review of Vibration-Based Damage Identification Methods," Shock and Vibration Digest, Vol 30, 1998, pp. 91-105.

Doebling, S. W., Farrar, C. R., Prime, M. B., and Shevitz, D. W., "Damage Identification and Health Monitoring of Structural and Mechanical Systems from Changes in Their Vibration Characteristics, A Literature Review," LA-13070-MS, UC-900, Los Alamos National Laboratory, Los Alamos, NM, 1996, 127 pp.

Ettouney, M., Daddazio, R., and Hapij, A., "Optimal Sensor Locations for tructures with Multiple Loading Conditions, Smart Structures and Materials 1999: Smart Systems for Bridges, Structures, and Highways," Proceedings of SPIE, 1999, Vol. 3,671, pp. 78–89.

Farrar, C. R., Baker, W. E., Bell, T. M., Cone, K. M., Darling, T. W., Duffey, T. A., Eklund, A., and Migliori, A., "Dynamic Characterization and Damage Detection in the I-40 Bridge Over the Rio Grande," Los Alamos Nationa Laboratory Report LA-12767-MS, 1994, 153 pp.

Feldman, M., "Hilbert Transform Applications in Mechanical Vibration," Wiley, 2011, 292 pp.

Feldman, M., "Theoretical Analysis and Comparison of the Hilbert Transform Decomposition Methods," Mechanical Systems and Signal Processing, 2008, Vol 22, pp. 509-519.

Feldman, M., "Time-Varying Vibration Decomposition and Analysis based on the Hilbert Transform," Journal of Sound and Vibration, 2006, Vol 295, pp. 518–530.

Feldman, M., "Consider High Harmonics for Identification of Non-linear Systems by Hilbert Transform," Mechanical Systems and Signal Processing, 2007, Vol 7, pp. 943-958.

Fink, D., "Coherent Detection Signal-to-Noise," Applied Optics, 1975, Vol 14, 689–690.

Flandrin, P., "Time-Frequency/Time-Scale Analysis," Academic press, San Diego, CA 1999, 386 pp.

Gabor, D., "Theory of Communication," Journal of the Institution of Electrical Engineers, Vol 93, 1946, pp. 429-457.

Gurly, K., and Kareem, A., "Application of Wavelet Transform in Earthquake, Wind, and Ocean Engineering," Engineering Structures, 1999, Vol 21, pp. 149-167.

Hahn, S. L., "The Hilbert Transform in Signal Processing," Artech House, 1996, 442 pp.

Hartmann, W., "Signal, Sound and Sensation," American Institute of Physics, 2004, 647 pp.

He X., and Roech G. D., "System Identification of Mechanical Structures by a High-Order multivariate autoregressive model," Computers and Structures, 1997, Vol 64, 341-351.

Hou, Z., Noori, M., and Amand, R. S., "Wavelet-based Approach for Structural Damage Detection," Journal of Engineering Mechanics, 2000, Vol 126, pp. 677-683.

Huang, D., Zhao, J., and Sun, J., "Practical Implementation of the Hilbert Transform Algorithm," Acta Oceanologica Sinica, 2003, Vol 25, pp. 1-11.

Huang, H. W., Yang, J. N., and Zhou, L., "Adaptive Quadratic Sum-Squares Error with Unknown Inputs for Damage Identification of Structures," Structural Control and Health Monitoring, 2010, Vol 17, pp. 404-426.

Huang, N. E., and Attoh-Okine, N. O., "The Hilbert Transform in Engineering," Taylor & Francis Group, LLC, FL, 2005, 313 pp.

Huang, N. E., and Shen, S. S. P., Hilbert-Huang Transform and Its Applications, Word Scientific Publishing Co. Pte. Ltd., Singapore, 2005, 311 pp.

Huang, N. E., Shen, Z., and Long, S. R., "A New View of Nonlinear Water Waves: The Hilbert Spectrum," Annual Review of Fluid Mechanics, Vol 31, 1999, pp. 417-457.

Huang, N. E., Shen, Z, Long, S. R., Wu, M. C., Shih, H. H., Zheng, Q., Yen, N. C., Tung, C. C., and Liu, H. H., "The Empirical Mode Decomposition and Hilbert Spectrum for Nonlinear and Nonstationary Time Series Analysis," Proceedings of the Royal Society of London-Series A, 454, 1998, pp. 903-995.

Huang, N. E., Wu, M. C., Long, S. R., Shen, S. S. P., Ou, W., Gloersen, P., and Fan, K. L., "A Confidence Limit for the Empirical Mode Decomposition and Hilbert Spectral Analysis," Proceeding of the Royal society of London, Series A, 459, 2003, pp. 2317-2345.

Ismail, F., Ibrahim, A., and Martin, H. R., "Identification of Fatigue Cracks from Vibration Testing," Journal of Sound and Vibration, 1990, Vol 140, pp. 305-317.

James, G. H., Carne, T. G., and Lauffer, J. P., "The Natural Excitation Technique (NExT) for Modal Parameter Extraction from Operating Structures," Modal analysis: The International Journal of Analytical and Experimental Modal Analysis, 1995, Vol 10, pp. 260-277.

James, G. H., Carne, T. G., and Mayes, R. L., "Modal Parameter Extraction from Large Operating Structures Using Ambient Excitation," Proceedings of the 14th IMAC Conference, Dearborn, MI, 1996, pp. 77-83.

Kerschen, G., Lee, Y. S., Vakakis, A. F., McFarland, D. M., and Bergman, L. A., "Irreversible passive energy transfer in coupled oscillators with essential nonlinearity," SIAM Journal on Applied Mathematics, 2006, Vol 66 pp. 648-679.

Kijewski, K., and Kareem, A., "Wavelet Transforms for System Identification in Civil Engineering," Computer-Aided Civil and Infrastructure Engineering, 2003, Vol 18, pp. 339-355.

Kijewski, T., and Kareem, A., "On the Presence of End Effects and Their Melioration in Wavelet-Based Analysis," Journal of Sound and Vibration, 2002, Vol 256, pp. 980-988.

Kiureghian, A. D., Hong, K. J., and Sackman, J. L., "Further Studies on Seismic Interaction in Interconnected Electrical Substation Equipment, Report No. PEER 2000/01," Pacific Earthquake Engineering Research Center, College of Engineering, University of California, Berkeley, November, 1999b, 112 pp.

Kiureghian, A. D., Sackman, J. L., and Hong, K. J., "Interaction in Interconnected Electrical Substation Equipment Subjected to Earthquake Ground Motions," Report No. PEER 1999/01, Report to Pacific Gas & Electric Co., San Francisco, California. February, 1999a, 94 pp.

Klein, L. A., "Sensor and Data Fusion: Concepts and Application, Second Edition SPIE, Press.," Vlo TT14, Bellingham, Washington, 1999, 252 pp.

Korpel, A., "Gabor: Frequency, Time, and Memory," Applied Optics, 1982, Vol 132, pp. 3624-3632.

Lardies, J., and Gouttebroze, S., "Identification of Modal Parameters using the Wavelet Transform," International Journal of Mechanical Science, 2002, Vol 44, pp. 2263-2283.

Lee C. G., and Yun C. B., "Parameter Identification of Linear Structural Dynamic System," Computers and Structures, 1991, Vol l40, pp. 1475–1487.

Leutenegger, T., Schlums, D. H., and Dual, J., "Structural Testing of Fatigued Structures," Smart Structures and Integrated Systems, Proceedings of SPIE, Vol 3, 1999, pp. 987-997.

Lin, J. W., Betti, R., Smyth, A. W., and Longman, R. W., "On-Line Identification of Nonlinear Hysteretic Structural Systems using a Variable Trace Approach," Earthquake Engineering and Structure Dynamics, 2001, Vol 30, 1279-1303.

Lin, J. W., Betti, R., Smyth, A. W., and Longman, R. W., "On-Line Identification of Nonlinear Hysteretic Structural Systems using a Variable Trace Approach," Earthquake Engineering and Structure Dynamics, 2001, Vol 30, pp. 1279-1303.

Loh, C. H., and Tou, I. C., "A System Identification Approach to the Detection of Changes in Both Linear and Nonlinear Structure Parameters," Earthquake Engineering and Structure Dynamics, 1995, Vol 24, pp. 85-97.

Loland, D. K., and Dodds, J. C., "Experience in Developing and Operating Integrity Monitoring System in North Sear," Proceedings of the 8th Annual Offshore Technology Conference, 1976, pp. 313-319.

Min, Z. H., Sun, L. M., Sun, Z., and Dan, D. H., "Structural Modal Parameter Identification using Wavelet Transform and Singular Value Decomposition under Ambient Excitation," Journal of Vibration Engineering, 2009, Vol 22, pp. 142-149.

Modena, C., Sonda, D., and Zonta, D., "Damage Localization in Reinforced Concrete Structures by Using Damping Measurements, Damage Assessment of structures," Proceedings of the International Conference on Damage Assessment of Structures (DAMAS 99), Dublin, Ireland, 1999, pp. 132–141.

Monaco, E., Calandra, G., and Lecce, L., "Experimental Activities on Damage Detection Using Magnetostrictive Actuators and Statistical Analysis," Smart Structures and Materials 2000: Smart Structures and Integrated Systems, Proceedings of SPIE, 2000, Vol 3,985, pp. 186–196.

Pandey, A. K., Biswas, M., and Samman, M. M., "Damage Detection From hanges In Curvature Mode Shapes," Journal of Sound and Vibration, 1991, Vol 145, pp. 321–332.

Peng, Z. K., Peter, W., and Tse, F. L., "An Improved Hilbert-Huang Transform and its Application in Vibration Signal Analysis," Journal of Sound and Vibration, 2005, Vol 286, pp. 187-205.

Qin, S. R., and Zhong, Y. M., "A New Envelope Algorithm of Hilbert-Huang Transform, Mechanical Systems and Signal Processing," 2006, Vol 20, pp. 1941-1952.

Ravindra V. Jategaonkar., "Flight Vehicle System Identification-A time Domain Methodology," American Institute of Aeronautics and Astronautics, Inc., Reston, Virginia, 2006, 534 pp.

Ruzzene, M., Fasana, A., Garibaldi, L., and Piombo, B., "Natural Frequencies and Damping Identification using Wavelet Transform: Application to Real Data," Mechanical Systems and Signal Processing, 1997, Vol 11, pp. 207-218.

Salvino, L. M., Pines, D. J., Todd, M., and Nichols, J. M., "EMD and instantaneous phase detection of structural damage," in: Huang, N. and Shen, S. S. P. (Eds), Hilbert-Huang Transform and Its Applications, World Scientific Publishing Co. Pte. Ltd. Singpore, 2005, pp. 227-262.

Schreier, P. J., and Scharf, L. L., "Statistical Signal Processing of Complex-Valued Data: The Theory of Improper and Noncircular Signals," Cambridge University Press, 2010, 330 pp.

Shi, Z. Y., and Law, S. S., "Identification of Linear Time-Varying Dynamical System using Hilbert Transform and EMD Method," Journal of Applied Mechanics, 2007, Vol 74, pp. 223-230.

Shi, Z. Y., and Law, S. S., and Xu, X., "Identification of Linear Time-Varying MDOF Dynamic Systems from Forced Vibration using Hilbert Transform and EMD Method," Journal of Sound and Vibration, 2009, Vol 321, pp. 572-589.

Skjaerbaek, P. S., Nielsen, S. R. K., and Cakmak, A. S., "Assessment of Damage in Seismically Excited RC-Structures from a Single Measured Response," Proceedings of the 14th International Modal Analysis Conference, 1996, pp. 133-139.

Smith, L., Chandler, P. R., and Patcher, M., "Regularization Techniques for Real-time Identification of Aircraft Parameters," Proceedings of the 1997 AIAA Guidance navigation and Control Confernece, New Orleans, LA, AIAA, 1997, Paper 97-3740.

Smyth, A. W., Masri, S. F., Chaassiakos, A. G., and Caughey, T. K., "On-Line Parametric Identification of MODF Nonlinear Hysteretic Systems," Journal of Engineering Mechanics, 1999, Vol 125, pp. 133–142.

Smyth, A. W., Masri, S. F., Kosmatopoulos, E. B., Chaassiakos, A. G., and Caughey, T. K., "Development of Adaptive Modeling Techniques for Non-Linear Hysteretic System," International Journal of Non-linear Mechanics, 2002, Vol 37, pp. 1435-1451.

Sohn, H., Farrar, C. F., Hemez, F. M., Shunk, D. D., Stinemates, D. W., Nadler, B. R., and Czarnecki, J. J., "A Review of Structural Health Monitoring Literature: 1996-2001," Report LA-13976-MS Los Alamos National Laboratory, Los Alamos, NM, USA, 2004, 301 pp.

Stanbridge, A. B., Khan, A. Z., and Ewins, D. J. "Fault Identification in Vibrating Structures Using a Scanning Laser Doppler Vibrometer, Structural Health Monitoring, Current Status and Perspectives," Stanford University, Palo Alto, California, 1997, pp. 56–65.

Staszewski, W. J., "Identification of Damping in MDOF Systems using Time-Scale Decomposition," Journal of Sound and Vibration, 1997, Vol 203, pp. 283-305.

Stubbs, N. and Osegueda, R., "Global Damage Detection In Solids–Experimental Verification," The International Journal of Analytical and Experimental Modal Analysis, Vol 5, 1990b, pp. 81–97.

Stubbs, N. and Osegueda, R., "Global Non-Destructive Damage Evaluation in Solids," Modal Analysis: The International Journal of Analytical and Experimental Modal Analysis, Vol 5, 1990a, pp. 67–79.

Teng, J., and Zhu, Y. H., "Parameters Optimization of Wavelet Transform in Modal Parameter Identification with Closely-Spaced Modes," Proceedings Of The Twelfth ASCE Aerospace Division International Conference On Engineering, Science, Construction, And Operations In Challenging Environments And The Fourth Nasa/Aro/Asce Workshop On Granular Materials In Lunar And Martian Exploration, Honolulu, Hawaii, 2010, pp. 2442-2450.

Titchmarsh, E. C., "Introduction to the Theory of Fourier Integral," Oxford University Press, 1950, 394 pp.

Trendafilova, I., "Damage Detection in Structures from Dynamic Response Measurements," An Inverse Problem Perspective, Modeling and Simulation Based Engineering, Technical Science Press, 1998, pp. 515–520.

Vakakis, A. F., McFarland, D. M., Bergman, L. A., Manevitch, L. I., and Gendelman, O., "Isolated Resonance Captures and Resonance Capture Cascades Leading to Single- or Multi-Mode Passive Energy Pumping in Damped Coupled Oscillators," Journal of Vibration and Acoustics, 2004, Vol 126, pp. 235–244.

Vakman,D., "Signals, Oscillations, and Waves," Artech House, Boston, London, 1998, 220 pp.

Vandiver, J. K., "Detection of Structural Failure on Fixed Platforms by Measurement of Dynamic Response," Journal of Petroleum Technology, 1977, pp. 305-310.

Wang, C., and Ren, W. X., "A Wavelet Ridge and SVD-Based Approach for Instantaneous Frequency Identification of Structure," Proceedings of the Second International Conference on Structural Condition Assessment, Monitoring and Improvement, Changsha, China, 2007, pp. 803-807.

Wang, C., and Ren, W. X., "A Wavelet Ridge and SVD-based Approach for Instantaneous Frequency Identification of Structure," Proceedings of the Second International Conference on Structural Condition Assessment, Monitoring and Improvement, Changsha, China, 2007, pp. 803-807.

Wang, W., "Decomposition of Wave Groups with EMD Method," in: Huang, N. and Attoh-Okine, N. O. (Eds), The Hilbert Transform in Engineering, Taylor & Francis Group, LLC, FL, 2005, pp. 267-280.

Wang, Z. C., and Chen, G. D., "A Moving-Window Curve Fitting Method for Crack Detection and Rigidity Identification in Multi-Span Bridges," Structural Control and Health Monitoring, (Accepted Paper), 2011.

Wen, Y. K., "Method for random vibration of hysteretic systems," Journal of Engineering Mechanics, 1976, Vol 102, pp. 249-263.

Xun, J., and Yan, S., "A Revised Hilbert-Huang Transformation based on the Neural Networks and its Application in Vibration Signal Analysis of a Deployable Structure," Mechanical Systems and Signal Processing, 2008, Vol 22, pp. 1705-1723.

Yan, B. F., and Miyamoto, A., "A Comparative Study of Modal Parameter Identification based on Wavelet and Hilbert-Huang Transforms," Computer-Aided Civil and Infrastructure Engineering, 2006, Vol 21, pp. 9-23.

Yang, J. N., Lei, Y., and Huang, N. E., "Identification of Natural Frequencies and Damping of in Situ Tall Buildings using Ambient Wind Vibration Data," Journal of Engineering Mechanics, 2004, Vol 130, pp. 570-577.

Yang, J. N., and Lin, S., "Identification of Parametric Variations of Structures based on Least Squares Estimation and Adaptive Tracking Technique," Journal of Engineering Mechanics, 2005, Vol 131, 290–298.

Yang, J. N., Huang, H. W., and Pan, S. W., "Adaptive Quadratic Sum-Squares Error for Structural Damage Identification," Journal of Engineering Mechanics, 2009, Vol 135, pp. 67-77.

Yang, J. N., Huang, H., and Lin, S., "Sequential Non-Linear Least-Square Estimation for Damage Identification of Structures," International Journal of Non-linear Mechanics, 2006, Vol 41, pp. 124-140.

Yang, J. N., Lei, Y., Pan, S., and Huang N. E., "System Identification of Linear Structures based on Hilbert-Huang Spectral Analysis, Part I: Normal Modes," Earthquake Engineering and Structure Dynamics, 2003, Vol 32, pp. 1443-1467.

Yang, J. N., and Lei, Y., "System identification of Linear Structures using Hilbert Transform and Empirical Mode Decomposition," Proceedings of 18th International Modal Analysis Conference: A Conference of Structural Dynamics, San Antonio, TX, Society for Experimental Mechanics, INC., Bethel, CT, 2000, Vol 1, pp. 213-219.

Yang, J. N., and Lin, S., "Identification of Parametric Variations of Structures based on Least Squares Estimation and Adaptive Tracking Technique," Journal of Engineering Mechanics, 2005, Vol 131, pp. 290–298.

Yang, J. N., Pan, S., and Lin, S., "Least-Squares Estimation with Unknown Excitations for Damage Identification of Structures," Journal of Engineering Mechanics, 2007, Vol 133, pp. 12–21.

Yongkyu S., "Online Parameter Estimation Techniques Comparison within a Fault Tolerant Flight Control System," Journal of Guidance, Control, and Dynamics, 2002, Vol 25, pp. 528-537.

Zheng, M., Shen, F., Dou, Y., and Yan, X., "Modal Identification based on Hilbert-Huang Ttransform of Structural Response with SVD Preprocessing," Acta Mechanica Sinica, 2009, Vol 25, pp. 883-888.

VITA

Zuocai Wang was born on December 08, 1982, in a small town of Hunan Province, P. R. China, where he received his elementary and secondary education. He received his Bachelor of Science (B.S.) degree in Civil Engineering in July 2005 and Master of Science (M.S.) degree in bridge engineering in December 2007, both from Central South University (CSU), Changsha, China. During his graduate study at CSU, his main research activities involved bridge stability and dynamics, bridge health monitoring, and finite element analysis. In December 2011, he received his Doctor of Philosophy (Ph.D.) degree in Civil Engineering at Missouri University of Science and Technology (Missouri S&T).

In 2008, he enrolled as a Ph.D. student in the Department of Civil, Architectural, and Environmental Engineering at Missouri S&T. In the course of his study, he has been involved in several projects, including "calibration of load and resistance factors in LRFD foundation design specifications" and "structural assessment of highway "N" power substation under earthquake loads", which were supported in part by Missouri Department of Transportation (MoDOT), by U.S. Department of Transportation (USDOT) under the auspices of Center for Transportation Infrastructure and Safety at Missouri S&T, and by Ameren Corporation, St. Louis, USA. His main research work was focused on bridge data analysis, engineering interpretation, system identification and damage detection. He published four international journal papers and has three additional papers under review.